APPLICATION OF PARALLEL TIME-IMPLICIT DISCONTINUOUS GALERKIN FINITE ELEMENT METHODS TO HYPERSONIC NONEQUILIBRIUM FLOW PROBLEMS

By

ANKUSH BHATIA

A DISSERTATION PRESENTED TO THE GRADUATE SCHOOL
OF THE UNIVERSITY OF FLORIDA IN PARTIAL FULFILLMENT
OF THE REQUIREMENTS FOR THE DEGREE OF
DOCTOR OF PHILOSOPHY

UNIVERSITY OF FLORIDA

2014

I offer this dissertation at the lotus feet of the Supreme Personality of Godhead, Sri Krishna; his dear most devotee, His Divine Grace A. C. Bhaktivedanta Swami Srila Prabhupada, by whose mercy I have gotten the opportunity to practice Krishna consciousness along with my Ph.D. work here in Gainesville, Florida; and my beloved spiritual master, His Grace Kalakantha Prabhu, who has very mercifully given shelter to me at his lotus feet.

ACKNOWLEDGMENTS

I especially thank all the devotees in Krishna House, for making this Ph.D. a very memorable experience. I also would like to express my gratitude towards so many other people who have helped me in this endeavor to do my dissertation work. These include, Manoj Parmar for always providing me with relevant guidance and encouragement in doing my Ph.D. I would also like to acknowledge consistent help of Dr. Ryan Gosse with my Ph.D. problems. His help has also been very crucial for my progress in the Ph.D. work, and thanks to all my labmates, including James, Arnob, Tomas, Navya, Ariel, Mark, Ryan, Jignesh, Moses for their companionship for my Ph.D. work. I would also like to express my gratitude towards my advisor Dr. Subrata Roy, for providing the necessary guidance and a platform to pursue my research interests through this Ph.D. program.

TABLE OF CONTENTS

LIST OF TABLES

LIST OF FIGURES

Abstract of dissertation Presented to the Graduate School
of the University of Florida in Partial Fulfillment of the
Requirements for the Degree of Doctor of Philosophy

APPLICATION OF PARALLEL TIME-IMPLICIT DISCONTINUOUS GALERKIN FINITE ELEMENT METHODS TO HYPERSONIC NONEQUILIBRIUM FLOW PROBLEMS

By

Ankush Bhatia

April 2014

Chair: Subrata Roy
Major: Mechanical Engineering

Discontinuous Galerkin (DG) methods are high order accurate methods, that have been proven to possess favorable properties for highly parallel systems, complex geometries and unstructured meshes. High-order accuracy in DG methods comes by increasing the order of polynomial approximation within the element, and the stencil does not extend beyond immediate neighbors. Thus, DG methods retain their compact nature, even for high-order stencils. This reduces the amount of effort required in coding a high-order accurate DG method, and once coded it only needs higher order basis functions for high order accurate solutions. The basis functions used for the DG method are also hierarchical, in that the lower order basis functions remain unchanged upon the addition of higher order basis. We have successfully introduced and demonstrated the application of DG methods to the fields of thermal ablation and hypersonic flow with the non-equilibrium air chemistry.

In addition to above, many challenges still plague heating predictions for hypersonic flow simulations. Surface heating predictions are found to be very sensitive to the mesh resolution in the shock. A slight misalignment of less than 1 $\%$ is seen to cause major changes in heating predictions. The cause for this is not well understood, but is known to come from the numerical errors associated with shock capturing. These errors propagate downstream of the shock and hence affect the solution in the shock layer and on the surface. Any kind of shock capturing methodology like slope limiter or

artificial viscosity, will have some errors in the shock region, and the goal of the different highlighted works have been to minimize this error, e.g., by capturing the shock in one or two elements.

As a different and unconventional approach for DG, we have attempted r-p adaptivity to accurately capture the shock. Herein, the shock is captured by using p = 0 elements (with first order of accuracy). Hence the solution methodology is stable. Implicit methods are also developed for solution advancement in time with high CFL numbers. The error in the shock is reduced by redistributing the elements outside of the shock to into the shock. Thus, extra number of elements, e.g. added by h-p adaptivity method, are not needed. The coding for this is also simple, as the total number of elements and their connectivity remain unchanged in the r-adaptivity iterations. We have successfully simulated examples in the area of inviscid and viscous hypersonic flows, with lesser number of elements in comparison to h-p adaptivity, getting the same level of accuracy. This methodology does not even require apriori knowledge of the shock′s location, and is suitable for detached shock type of problems, to the best of our knowledge.

Using r-p adaptivity method, we have also been successful in predicting surface heating rate for hypersonic flow over cylinder accurately. One issue that still remains is the performance of the method with arbitrary kind of meshes, wherein the variation of the mesh size is not smooth in between elements. This issue of, whether the r-p adaptivity method′s heating predictions are sensitive to mesh, still remains to be examined to determine the advantage of the r-p adaptivity methods in respect to other methods in the published literature.

This tool has also been used to solve for hypersonic flow with the non-equilibrium air chemistry and good comparisons are made with the published results. Finally, using this developed tool, we determine the effect of micro-second pulsed sinusoidal Dielectric Barrier Discharge (DBD) plasma actuators on the surface heating reduction

for hypersonic flow over cylinder. We find that the plasma actuators have significant effect on the surface heating and have also looked into several designs for optimum heat reduction.

CHAPTER 1
INTRODUCTION

Solving multi-physics problems is a daunting task. Specifically, our problems of interest include thermally ablative surface of a hypersonic vehicle (for example at re-entry condition) and simulation of thermo-chemical non-equilibrium flow field around this vehicle. We aim to simulate such problems using a high-order accurate, fully implicit method.

The current state of the art, for the Computational Fluid Dynamic or CFD simulations of these areas, includes using finite difference and finite volume codes, that are typically second order accurate. Moreover, their applications are more suitable for simple geometries [1]. For more complex shaped geometries and higher order accuracy ($>$ 2), finite element methods are more appropriate. Additionally, with advance in CFD techniques and expanding computational resources, the complexity of the problems is also increasing. This puts a great deal of strain on mesh resolution requirements for second order accurate methods, as the error is of order, $\mathrm{O}\left(\mathrm{h}^2\right)$ [2, 3].

To remedy this, we introduce Discontinuous Galerkin (DG), a high fidelity finite element based, method to the fields of thermal ablation [4, 5] and hypersonic flows with thermo-chemical non-equilibrium [6]. We also demonstrate, the usefulness and convenience of using the DG method for these problems, in terms of solution accuracy. For polynomial basis function of order p, the error convergence in DG methods is given as $\mathrm{O}\left(\mathrm{h}^{\mathrm{p}+1}\right)$, where h is the mesh size. Hence, with improved convergence rates, the solution error drops more rapidly, obviating the need for increasingly mesh resolved solutions. For complex problems and geometries, improving mesh resolution is a much more demanding task than enhancing the order of accuracy of the CFD method.

Another challenge in the field of hypersonic flows is capturing shocks. It is a well known fact, that applying a CFD method, with order of accuracy greater than one, directly to such a problem results in Gibbs oscillations around the shock. These

oscillations result in unphysical values of negative pressure and density, thus spoiling either the complete solution or causing convergence problems. Typical approaches in the literature, to deal with this problem, are applying slope limiters at the shock regions to eliminate oscillations in the solution, processed after a time step; or using artificial viscosity methods to supplement the numerical damping of the method, that smears out oscillations in the shock. However, these approaches are empirical and require a great deal of trial and error or experience for optimum shock capturing. The goal of such efforts is to capture the shock as finely as possible without generating oscillations in the solution.

Numerical errors, generated in the shock, are associated with the shock capturing methods employed. These have been known to corrupt solution downstream of the shock, especially in the field of hypersonic flows. This siginificantly affects the heating predictions at the surface of the vehicle in a hypersonic flow [7, 8]. Significant difference in the heating prediction, have been reported, for less than 1 % change in the mesh around the shock. Even recent methods like PDE based artificial viscosity methods do not give completely accurate results for surface heating prediction for hypersonic flow over cylinder [9].

This work uses r-p adaptivity, in conjunction with DG methods, both with and without the use of slope limiters, to capture the shock. This methodology identifies the shock location, using a pressure based sensor and uses first order solution (p = 0) in the shock and higher order solution in the smooth flow region. This approach, called p-adaptivity was first used in [10], in conjunction with h-adaptivity to finely capture the shock. However, its application was restricted to inviscid flows. We extend this p-adaptivity, along with r-adaptivity, to viscous hypersonic flows with and without full thermo-chemistry. This work is compared to other similar efforts in using DG method for solution of viscous hypersonic flows (without chemistry). Development of this tool

opens up more opportunities for us, in utilizing this tool, for performing plasma simulation problems (main focus area of our group), another area with complex physics.

The remainder of this chapter is written as follows. We elaborate on our motivation, by highlighting the thermal ablation and hypersonic flow physics in section 1.1. Sections 1.2 and 1.3 point out some test cases, that specifically illustrate the challenges faced by the state of the art codes in the fields of thermal ablation and hypersonic flows respectively. Section 1.4 highlights limitations, in general, for finite difference and finite volume methods that the DG scheme overcomes. Our specific contributions to the fields of DG methods, thermal ablation and hypersonic flow applications are discussed in section 1.5. The last section 1.6 draws out the structure of the rest of the thesis.

1.1 Motivation: Complex Physics of Thermal Ablation and Hypersonic Flow Problems

Problems of thermal ablation and hypersonic flow simulation deal with extreme physics of flow around the space vehicle and the thermal response of thermal protective system (TPS) on the vehicle's surface. These vehicles, mainly intended for inter-planetary missions, typically enter the atmosphere of a planet with very high speeds. The entry Mach numbers can vary between 20 and 50 (see [11]).

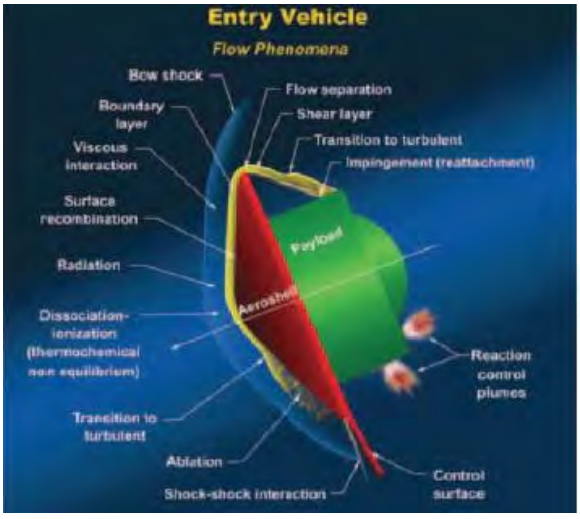

Figure 1-1. Hypersonic flow field around an entry vehicle, showing all the relevant physical processes that contribute to thermal ablation on the surface of the vehicle.

Their body shape is designed to generate high drag forces so they can decelerate sufficiently either for landing purposes or to transfer to an orbit around the planet (aerobraking). Thus, they experience a large amount of viscous dissipation on the surface. Various mechanisms of heat transfer like radiation, convective heating, shock/boundary layer viscous interaction, and recombination of the dissociated and ionized species in gas flow, are responsible for excessive amount of heat transfer to the vehicle′s surface that causes temperature rise of several thousand Kelvin. All these mechanisms are fully coupled to each other and complex in themselves. Thus their interaction is overwhelmingly difficult to accurately simulate the response of TPS to the given flow conditions.

Three main areas in analyzing the thermal ablation and hypersonic flow problem are the flight trajectory, the flow outside the space vehicle (interacting with the vehicle′s body) and the thermal response of the ablating material on the surface of the vehicle ([12]). As noted, all these mechanisms are complex and interact with each other in real time, and their proper understanding is essential to accurate modeling and numerical simulation of thermal ablation.

1.1.1 Flight Trajectory

Trajectory is the path of the vehicle during its flight with respect to Earth′s or a planet′s center. Flow environment around the vehicle can rapidly change as it descends. Gravitational, body and thrust forces acting on the vehicle′s body can change its direction of motion thus changing the flow environment around the vehicle. Flow environment in turn affects the response of thermal protection system, and thermal response of TPS decides the mass, shape and Lift-to-Drag (L/D) ratio of the vehicle. So, both trajectory and TPS response can be strongly inter-coupled.

It is quite obvious that for a good design study, that aims to reduce extra mass on the vehicle, it′s very essential to solve both flight trajectory and thermal response simultaneously. This is relevant for studies on design of TPS for future missions, and for

success of missions like Aero-assisted orbit transfer vehicles (AOTV), which are capable of on-orbit maneuvers [13, 14]. These studies focus on optimizing the solution space of trajectory for optimum mass, size and shape for TPS and fuel savings.

Studies aimed at understanding thermal ablation for an already made flight do not need to solve for flight trajectories in conjunction with thermal response of TPS and this can be calculated based on obtained data from the vehicle, during its flight, e.g. deceleration data sent from the accelerometer of Pioneer-Venus probes [15–18] was used to generate flight velocities during the entry of probes. Since, we focus on solving arc jet cases to establish solution capability for thermal ablation; solving for flight trajectory hence is not required in our work.

1.1.2 Flow Environment

As a space vehicle (on its entry) descends into atmosphere of increasing density, the flow around it makes a transition from free molecular to continuum flow. Collisions between impinging and reflected (from the surface) molecules are negligible in free molecular flow. This assumption is however not valid in transitional and continuum regime. A rapid rise in aerodynamic coefficient and heating rates are also observed at the end of transitional regime [11]. Free molecular and transitional flow regimes are a focus of DSMC (Direct Simulation Monte Carlo) schemes [19–21], we however focus on the continuum regime, where we can use the governing equations like Euler equations or Navier Stokes equations.

The flow chemistry can be characterized as frozen, non-equilibrium or equilibrium, depending on the intensity of collisions. Very few number of collisions ($\mathrm{K_{n,\infty}} = \lambda_\infty/\mathrm{D} \approx 100$) do not change the species distribution as the gas flows towards the surface (frozen chemistry). Moderate number of collisions ($\mathrm{K_{n,\infty}} \approx 1$) cause the species distribution to be a function of collision history of the molecules (chemical non-equilibrium), and very large numbers of collisions ($\mathrm{K_{n,\infty}} \approx 0.01$) overwhelm such dependence on previous collisions (chemical equilibrium), so that the distributions can be written as algebraic

functions of local temperature and pressure. Flows in general are chemically reactive and frozen or equilibrium models cannot be used.

Due to hypersonic flow velocities, a bow shock is formed in front of the vehicle and it can be either attached (at higher altitudes) or detached (at lower altitudes) from the surface of the vehicle. Flow away from vehicle surface is inviscid and there is a boundary layer formation, near the surface, due to the viscous nature of the flow. Boundary layer for the hypersonic flow can have large thickness, and a rapidly growing boundary layer interacts with the inviscid flow. If the inviscid flow is greatly affected by the boundary layer (due to large increase in pressure, skin friction and heating), then it may strongly feedback to the boundary layer itself [22], hence causing strong viscous interactions, which can cause severe local peaks in aerodynamic heating at the vehicle′s surface.

In addition to the above mechanism, shock wave may also impinge with boundary layer (due to its increasing thickness away from stagnation region, see Fig. (1-2)), resulting in adverse pressure gradient in that region of boundary layer. This causes the boundary layer to separate, which in turn produces induced and reattachment shock. Boundary layer becomes comparatively thin at the point of reattachment, and this again may cause severe local heating at the surface.

Due to strong shock, the gas species may also undergo dissociation and electronic excitation. Flow particles impinging on and also interacting with the vehicles surface (surface chemical reactions) cause convective heating. The dissociated species can also recombine (for high Damkohler numbers, or in other words chemical equilibrium) near the surface of the vehicle, due to lower temperatures, transferring their heat of formation to the surface, which results in additional convective heating. However since recombination is a three body reaction, Damkohler numbers usually tend to be small, and majority of the dissociated atoms flow into the wake and recombining far

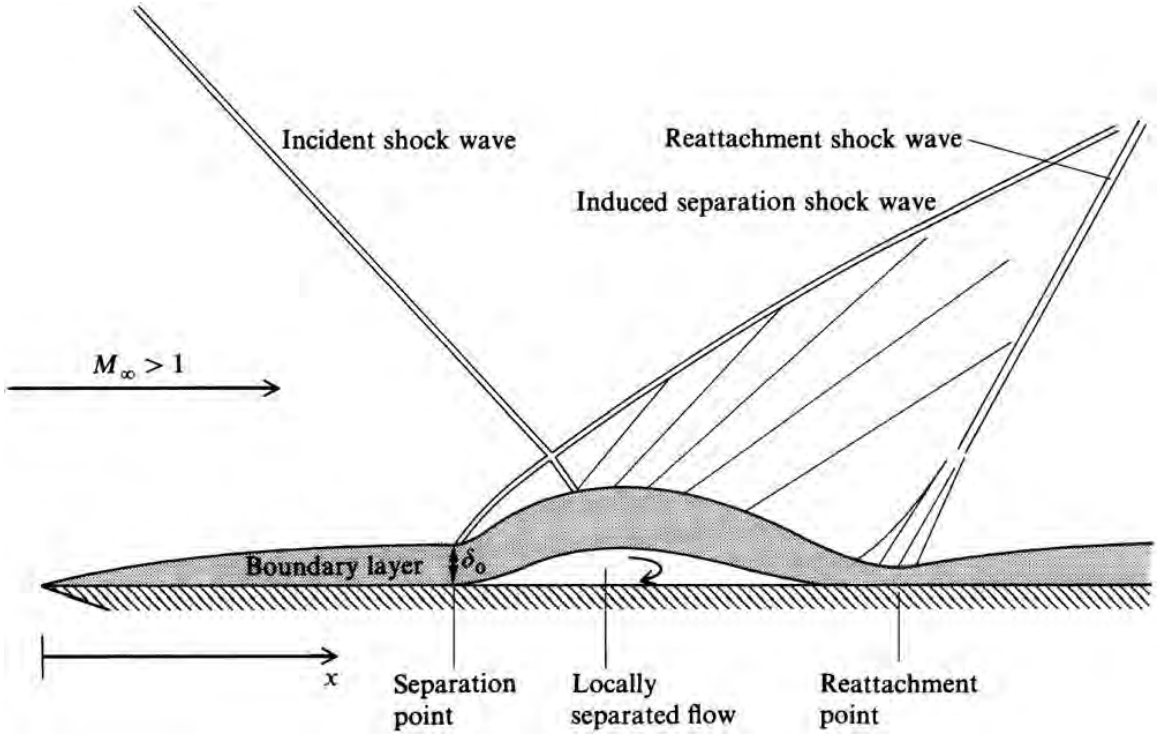

Figure 1-2. Hypersonic shock-wave boundary layer interaction. Adverse pressure gradient (due to interaction of shock and boundary layer) results in separation of boundary layer. Both induced separation shock and reattachment shock result from this interaction. Boundary layer especially tends to become thin at point of reattachment resulting in increased local heating at the surface. [22]

downstream they reduce net heat transfer to the surface. However, surface acting as a catalyst for the recombination can also offset this advantage [11].

We consider dissociation reactions in our study. Since charged particles require different treatment than neutrals, for this study we omit out ionization reactions. Excited species also cause high amount of radiation heat flux to the surface of the vehicle (radiative heating). Since calculation of radiation requires solving integro-differential equations and is more complex than solving differential equations, we use emissivity and Stefan Boltzmann′ law to incorporate radiation into the thermal ablation model.

1.1.3 Thermal Response of Ablating Material

Thermal protection systems are of two types, charring and non-charring [23]. Non-charring TPS (like carbon-carbon and silica) do not undergo chemical decomposition

at high temperatures. These materials may lose their mass by surface ablation, melting or fail mechanism. Surface ablation refers to removal of material from surface through chemical reactions, e.g. carbon in carbon-carbon may oxidize to form CO, or CO_2 and undergo nitridation to form CN [19].

Charring TPS like carbon phenolic is made of two components, fibrous component like graphitic carbon and a resin material. Resin component undergoes decomposition at high temperatures and releases mixture of gases called pyrolysis gas. Decomposition of resin material leads to formation of voids or pores in the material. Further gas generation and temperature rise leads to pressure build up in the pores, which causes the pyrolysis gas to leak out to the atmosphere. Leaking of pyrolysis gas into the boundary layer is called blowing phenomena and it acts to reduce the net amount of convective and radiative heat in flux to the surface [24]. Since, charring TPS provides better cooling mechanism, we will focus on these materials for our research. Important physics, that governs the thermal response of the material to the incoming heat flux, is described in the following sections.

1.1.3.1 Thermal conduction

Heat from hot gases is conducted into the TPS material. TPS material is a composite consisting of different materials. But still due to similar materials, thermal conductivity is fitted as one model for the overall material, by assuming that thermal conductivity is essentially isotropic [25]. These materials usually display low thermal conductivities and high specific heats, so that heat conduction process to inside material can be slowed down, and large amount of heat absorbed so that when some material is rejected at the surface it takes with itself substantial amount of thermal energy.

1.1.3.2 Material failure and thermal decomposition

The process of thermal decomposition was briefly mentioned in 1.1.3. A charring TPS upon decomposition leads to formation of three zones in the ablating medium [26, 27]. These zones are shown in Fig. (1-3). The zone with all the resin intact is the

virgin zone, the zone where material is undergoing decomposition is the pyrolysis zone and the last zone which has been depleted of all its resin content is the char zone.

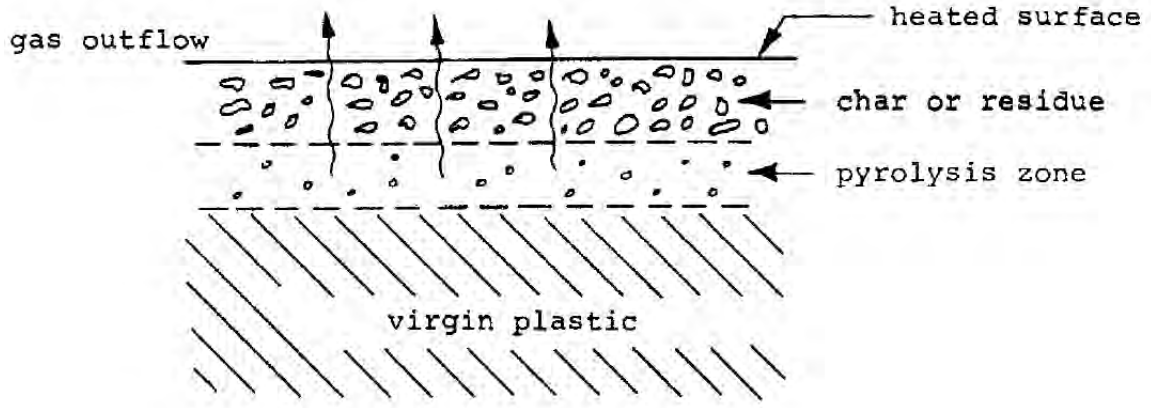

Figure 1-3. Schematic showing three zones in the charring ablator: virgin zone, which has all resin intact, pyrolysis zone, which is undergoing thermal decomposition and char zone, which has been depleted of all its resin content. Gas released is called pyrolysis gas and it leaves pores in the ablating zones, and also provides from blowing effect at the surface. [27]

Studies [16, 24, 28] have shown that the motion of pyrolysis gas through the porous media provides for extra cooling of the material, as it absorbs extra heat from the material, while exiting into the atmosphere. Some studies [15, 29–31] neglect this mechanism to avoid modeling of motion of pyrolysis gas through the porous media, but incorporating motion of pyrolysis gas is important for at least two reasons.

In low to moderate pressure and heating environment, thickness of both char and pyrolysis zone are substantial [16], so pyrolysis gas spends substantial amount of time traveling through this zone, hence absorbing sufficient energy from the solid. Second reason is to account for material failure due to development of high pressures within the porous media [16, 32, 33]. This phenomenon of material failure is referred to as spallation. In this work, we also include the modeling of the flow of the pyrolysis gases in our simulations for thermal ablation problems presented in [4, 5, 34] and for a Langley arcjet case. The model equations are taken from [16, 17, 35] and is presented in 2.4.

1.1.3.3 Surface ablation

Degradation and recession of surface is referred to as surface ablation. Surface can recede due to chemical reaction of surface with incoming gases from the flow field, or surface may also melt or vaporize due to high temperature. This is referred to as thermo-chemical ablation. Shear stress and pressure of impinging fluid may also remove micro particles from the surface [12], and thermal expansion strains and mechanical loads (due to aerodynamics or high pressure inside) may also cause material to be removed from the surface.

1.2 State of the Art of Numerical Simulations in Thermal Ablation

Thermal ablation is governed by many complex and inter-dependent physical processes, as already discussed. Goal of TPS design study is to predict the performance of a TPS (both of its material and shape) under given flight conditions. Such flight conditions are either simulated in an entry simulation facility, like arc-jet test facility, or are available through data obtained from actual flight missions (or planetary missions). Success of the design study depends on our understanding of all processes relevant to thermal ablation and their interactions.

Experimental facility, being both cost and time intensive, is not sufficient on its own to carry out an effective design study. Also, it does not offer sufficient insight into the mechanisms involved in a thermal ablation process. Thermal ablation turns out to be too complex for an analytical approach to be useful. In contrast, numerical tools actually serve the purpose of testing out formulations that model the processes in thermal ablation. Data from actual flights and experiments are useful for validation of these numerical procedures, and thus the postulated models can be tested.

Numerical efforts in the past have focused on hypersonic flow environment and thermally ablating material which interact with each other in real time in actual flights. Numerical models and simulations in both of these fields are very challenging and therefore developed independently as separate codes from the beginning. Later on,

however, as the interdependence of both these codes was better understood, attempts were made to provide some kind of coupling between them.

Current state of the art in thermal ablation is that both the domains are coupled to each other through a surface boundary condition (for either mass balance or energy balance or both of them). They are not solved simultaneously with each other in an iterative fashion. They are only solved at discrete trajectory points, where only one of the two codes may be run for the whole time between two trajectory points, while the other one is called into operation, only at the trajectory point itself. This solver then provides for boundary conditions for the other solver, which remain constant for that solver till the next trajectory point. Reason for not simultaneously running both the thermal response code and the flow solver is that the flow solver simulations tend to be expensive to run at every timestep. Additionally, with the loose coupling, the number of iterations for convergence per time step is also large, further increasing the simulation cost. Fewer trajectory points result in accuracy and convergence issues and more trajectore points lead to increase in both time and cost of computations.

Below we present a brief overview of past work highlighting their modeling and numerical aspects, as well as challenges that were overcome with time.

1.2.1 Past Development of Material Thermal Response Codes

Since thermal ablation is itself very complex problem, involving many complicated physical processes occurring simultaneously, past numerical efforts began with simplifying assumptions, and gradually level of complexity was increased with time. We look into major thermal response codes that brought some important change in the Industry and were used to solve thermal ablation problems of known space missions.

1.2.1.1 Charring Material Ablation (CMA) code

Charring Materials Ablation code or CMA was developed in late 1960′s by Moyer and Rindal [27]. It was developed as a one-dimensional finite difference based code with variable cross-section area, so it could be applied to 2-D geometries with 1-D energy

flow. There are three important equations involved, internal energy equation that solves for thermal response of the ablating material; material decomposition equation that specifies rate at which material inside will decompose at the given temperature and surface energy balance equation, which applies to outside of the vehicle for balancing all incoming and outgoing heat fluxes at the receding surface. Pyrolysis gas formed due to decomposition of resin is assumed to be in thermal equilibrium with char, i.e. no chemical reaction with char material, and any gas formed is assumed to leave the char immediately, i.e. no residence time in the char.

Two main limitations of CMA, as cited by works [29, 33] later on, were its explicit treatment of internal decomposition and surface energy balance with implicitly solved internal energy equations, which caused the code to have convergence issues, for high decomposition rate or high surface recession rates. The complete treatment of one-dimensional finite difference also becomes very complex due to node-dropping strategy employed for treating receding surfaces during ablation.

In one study [15], CMA was used to reconstruct the thermocouple data of 4 Pioneer-Venus probes that flew into the planet Venus in 1978. Both Wakefield heating [15] and Park heating [16] rate were used to assess the net heating rate at the surface of the probes during their flight. Comparison of their heating rates is given in Fig. (1-4). Flight data from the probes provided for velocity and atmospheric pressure, and thus surface heating rates were calculated.

It was noted in [36] that CMA did not account for motion of pyrolysis gas, which provided for cooling phenomena in the ablator, and thus Wakefield and Pitts [15] observed temperature rise to above the melting points of thermocouples (see Fig. (1-5)). Thus neglecting the flow of pyrolysis gas leads to unrealistically high temperature predictions. Also, by using finite-rate chemical reactions in both gas and gas-surface interactions, as opposed to Wakefield heating rate, which assumed thermo-chemical equilibrium at the surface, lower heating rates were predicted, and results of the

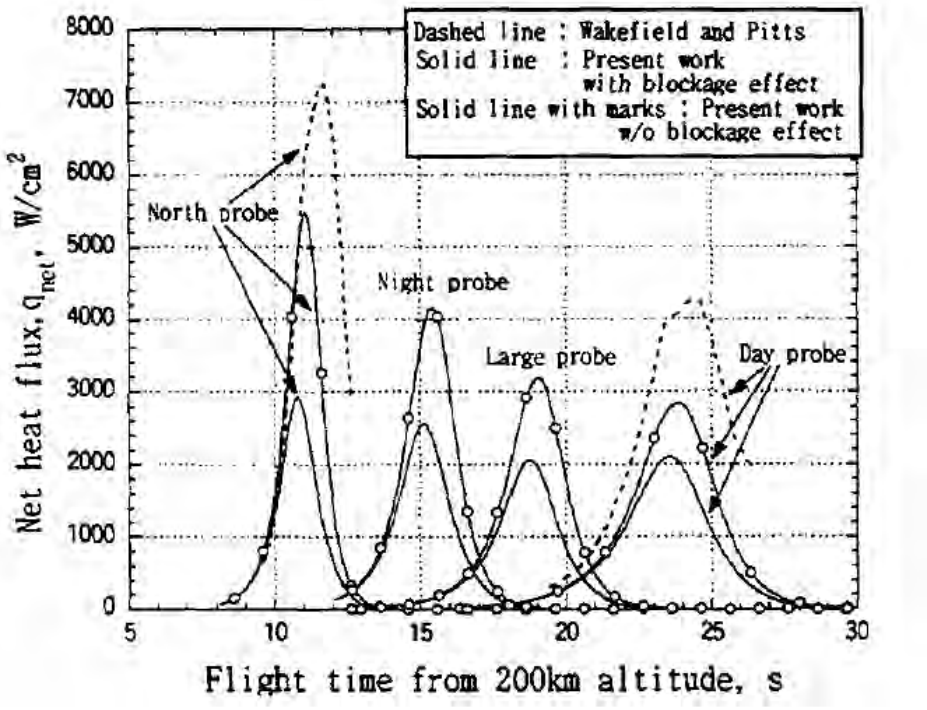

Figure 1-4. Comparison of net heating rates at the surface of four probes. ′Present work′ refers to Ahn et al. [36]. Comparison shows high heating prediction by Wakefield heating rate, which assumed thermo-chemical equilibrium assumption at the stagnation point, whereas heating rates predicted by Park′s method, which assumes finite rate chemical reactions, are lower. Injection of pyrolysis gas into boundary layer is called blowing phenomena and provides for convection blockage that further leads to lower heating rates predictions.

simulation as seen in figure above, lead to lower temperature predictions (with and without blockage effect). Though we still see that the temperatures do not entirely match and the reason for this is difficult to find unless full CFD flow simulation is done with material thermal response code. The methods used in this study are in general referred to as CFD approximation methods, which find the heating rate profile with time, and hence only material thermal response is run with heating rate provided as a function of time.

1.2.1.2 Fully Implicit Thermal response and Ablation program (FIAT)

Later on, to have more accurate TPS sizing programs, material thermal response code was coupled to flow solver code and both were iteratively solved. CMA due its

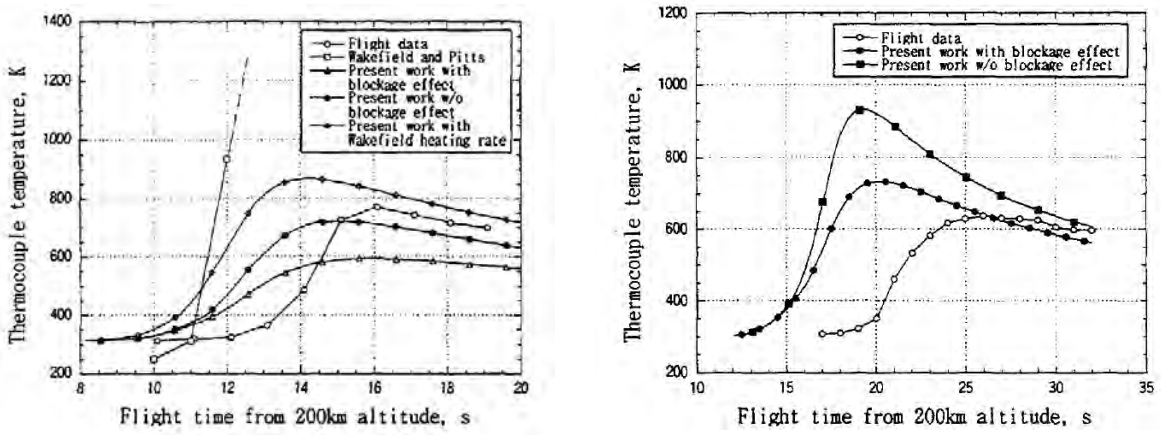

A B

Figure 1-5. Comparison of temperature histories as obtained from flight data and those predicted by Wakefield and Pitts [15] and Ahn et al. [36] (referred to as ′Present work′ in above plots) with Wakefield heating rates, Park heating rates with and without blockage effect. Results are shown for A) Day probe and B) North probe. Results show that Wakefield and Pitts predicted temperature rise to above melting point temperatures of thermocouple, since they used CMA which neglected flow of pyrolysis gas through the ablating material.

numerical instabilities caused the iterations process to slow down. Therefore FIAT, which is a fully implicit finite difference code based on the same governing equations as CMA, was developed by Chen and Milos [29] and was shown to be numerically stable for a wide range of TPS sizing problems. It also included other features like solving integro-differential equations (in explicit fashion, which did not cause any convergence issues, as internal radiation cools the surface) for internal radiation of the material, and coupling to CFD codes, like GIANTS [37, 38] and GASP [39, 40]. It was also used for thermal response analysis of materials like PICA (phenolic impregnated carbon ablator), and SIRCA (silicone-impregnated carbon ablator) for space missions like Stardust and Mars pathfinder. Here grid compression, rather than node-dropping strategy in CMA, was used to represent receding surfaces.

1.2.1.3 Control Volume Finite Element Method (CVFEM)

Moyer and Rindal [27] used upwind differencing scheme for apparent convection terms that appear due to translating grid (to account for surface recession) in CMA, and the same idea was also extended by Blackwell [41] in context of finite control volume using exponential differencing scheme by Spalding. The limitations with translating grids were that they were not easily applicable to multi-dimension problems. Therefore new concept of compressing grids was used in conjunction with Landau coordinates transformation by Blackwell and Hogan [42]. In comparison to CMA, where the last node at the ablating surface was dropped whenever the surface receded beyond the last node, total number of cells or elements remains constant in this method. Hence only the relative size of grid decreases. Therefore total number of elements or cells near the ablating surface always remains fixed.

Method of CVFEM in their initial publications was illustrated for one-dimensional problems, and later on in 1996 [43], it was extended to two-dimensional planar/axisymmetric geometries by assuming the mesh motion to be that of an elastic solid. This work, however did not consider effect of pyrolysis gas and coupling for both solid and fluid domains. In their recent works published in 2007 – 2010 [32, 33, 44], a code named MOPAR (Modeling of pyrolysis and ablation response), which is based on CVFEM, has been developed to deal with motion of pyrolysis gas flow within the ablating medium and also coupled [32] to a CFD flow solver, LeMANS [45, 46] developed for solving weakly ionized hypersonic flows with thermo-chemical non-equilibrium. They have enhanced the explanation of effects of pyrolysis gas on the ablation response of a material, but have been restricted to one dimensional ablation problems.

1.2.1.4 Two-dimensional Implicit Thermal response and Ablation program (TITAN)

Capability to simulate thermal ablation for an actual two or three dimensional geometry is essential for shape-change simulations, where the goal is to predict shape

change of the vehicle since that will affect the aerodynamics around the vehicle, and vice versa is also true. For this, a two dimensional thermal response code named TITAN was developed by Chen and Milos [47], which was solved in loose coupling with GIANTS, a CFD flow solver for simulating arc jet test models, and TITAN/MEIT, where MEIT [48] has engineering correlations developed for flow over slender body with small cone angles, and is thus less expensive as compared to GIANTS which is a full Navier Stokes solver. Here, they demonstrated how uncoupled simulations with TITAN and flow solvers would give unphysical results for their test cases of flat-faced cylinder test sample and slender body (see Fig. (1-6)).

It has been identified in [49] that TITAN/GIANTS solver divides the complete mesh into two, external grid and internal grid, where external grid contains thermally ablating media is a moving grid and internal grid, the inside vehicle structure is fixed. With this, TITAN/GIANTS can only solve simplified two-dimensional geometries. To overcome this limitation, TITAN/GIANTS were coupled with a third finite element based code, MARC [50], that deals with thermal and structural analysis of inside material, where the temperatures rise to levels at which no ablation or any decomposition effects are observed. It is mentioned in [49], that MARC cannot handle pyrolysis and ablation phenomena. So, now they have three integrated coupling of TITAN/GIANTS/MARC, and this coupling is in no way trivial (see Fig. (1-7)). Also, it is anticipated that such coupling will slow down computations and also present challenges for convergence.

1.2.1.5 COYOTE/SACCARA fully coupled simulations

Flow solvers with chemically reacting flow are computationally intensive (due to extra equations from chemical reactions) and in coupling with a thermal response code, the requirements become excessive, therefore it is a general practice to solve only for discrete trajectory points of an actual flight, and solve flow solver only at the trajectory points, which then provide fixed boundary conditions to the thermal response codes. Such simulation was run by [51], where they assumed flow to be in thermo-chemical

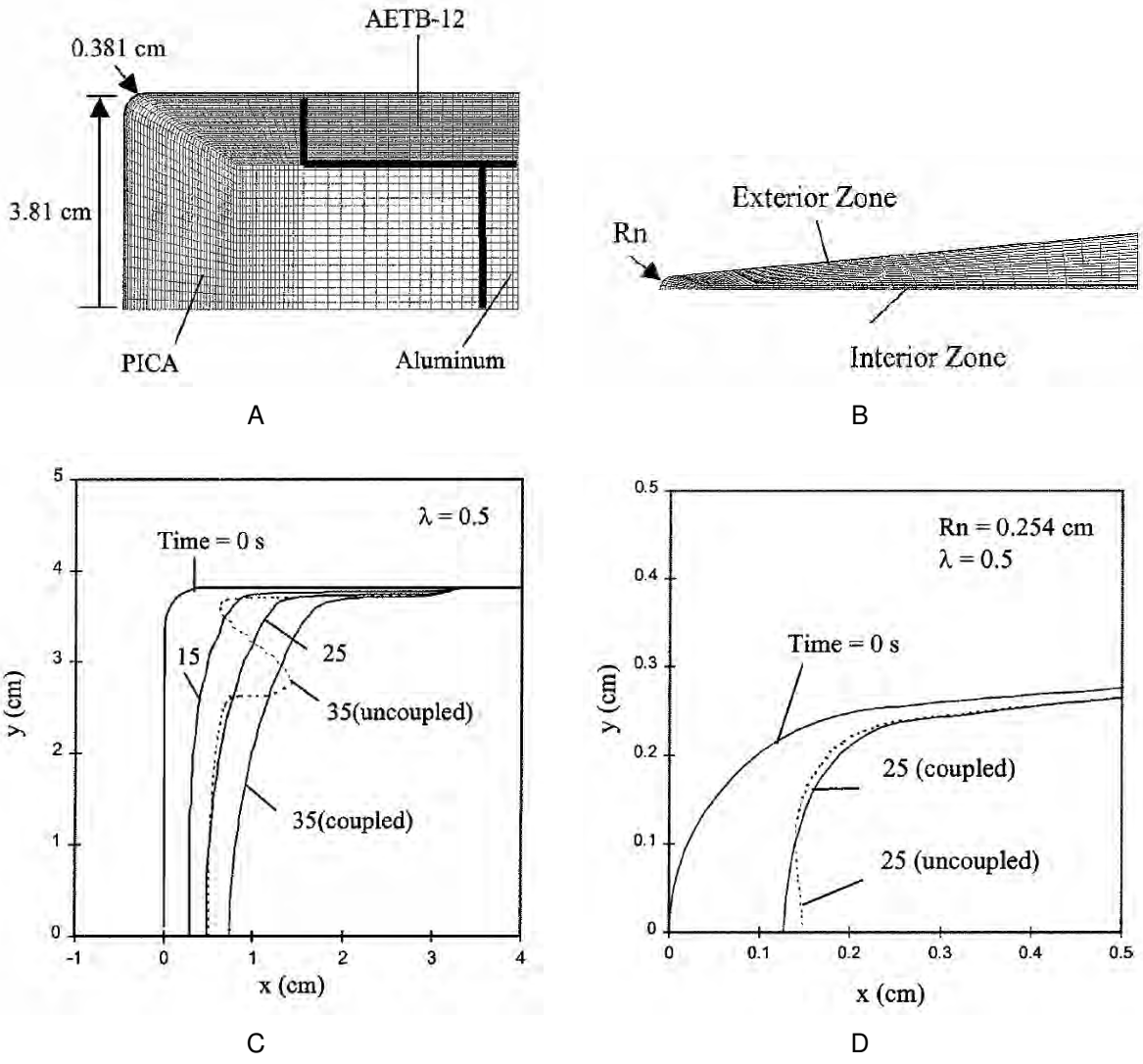

Figure 1-6. Results for shape change of both A) flat faced cylinder geometry and B) slender geometry shown in C) and D) respectively [47]. Results for both loosely coupled simulations as well uncoupled simulation of TITAN/GIANTS are shown in C (at 35 sec) and D (at 25 sec). It can be seen that unphysical results are obtained by an uncoupled simulation.

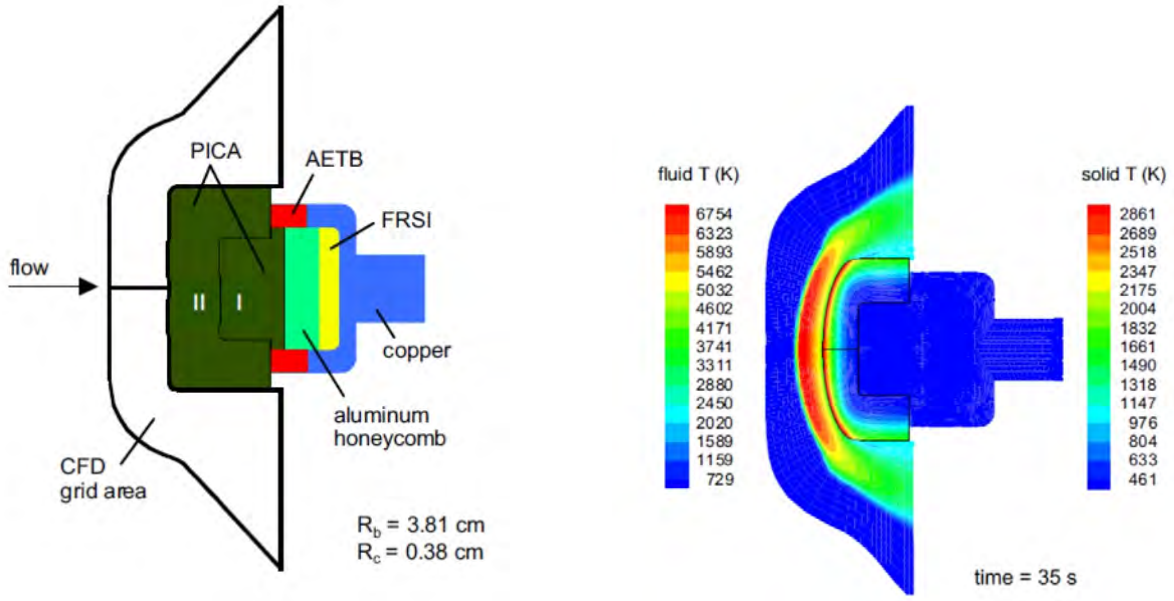

Figure 1-7. Arc Jet test model [49]. A) Shows different domains fluid, PICA (ablating media) and other structural components holding PICA, B) Fluid domain is solved by GIANTS and solid domain is solved by TITAN for PICA material and MARC for rest of structural components. Temperature distribution is shown at time of 35 sec.

non-equilibrium, and simulation was performed through SACCARA (Sandia Advanced Code for Compressible Aerothermodynamics Research and Analysis), which is a finite volume parallel code and can solve full 3D Navier Stokes equations for flows in thermo-chemical non-equilibrium. The code was coupled to COYOTE, a finite element based code developed to solve for heat conduction types of problems for complex geometries.

Both these codes are loosely coupled to each other. First, SACCARA code is run for a steady state flow at a trajectory point and it provides for convective heating rate, recovery enthalpy and pressure value at each surface node of the vehicle. These values are input to COYOTE, which then solves for temporal material response in and provides for ablation rate. Ablation rate and the pressure are used by ACE code to compute injected species mass fractions at the surface of the vehicle. Surface displacements

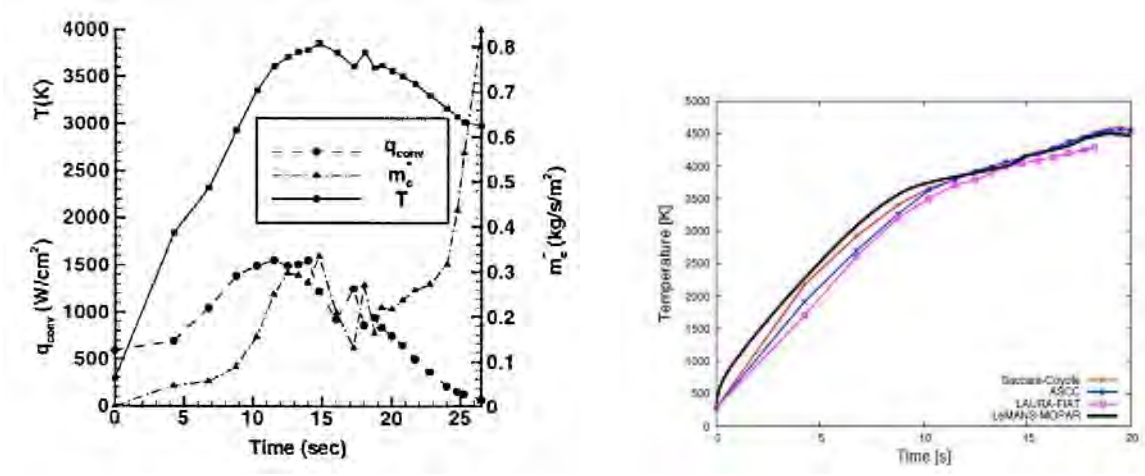

A B

Figure 1-8. Comparison of thermal prediction by Hassan et al. in their two papers [51, 52] for thermal response of IRV-2 vehicle, using COYOTE/SACCARA coupling. A) Results predict anomalous fall of stagnation point temperature after 14 seconds [51]. B) Improved results are shown as iterative coupling of COYOTE/SACCARA was implemented in [52]. Lack of coupling resulted in temperature lag between trajectory points (shown with dots in above plots), and this imprecision lead to highly inaccurate predictions.

from COYOTE are used to create new flow field mesh by a mesh generator, and the new mesh, surface species concentrations and surface temperatures (computed by COYOTE) are then fed in to SACCARA to for a new steady state simulation at the new trajectory point.

This coupling was tested out for an IRV-2 vehicle, and for its given trajectory its thermal response was studied. It was found in [51] that there were convergence problems in middle part of trajectory simulations, due to which a regular fall in stagnation point temperature was observed after nearly 14 seconds (see Fig. (1-8)), due to which net surface recession predicted was almost half of as predicted by ASCC, which was used to validate their results. It was also noted that computed heating rate by the flow solver was sensitive to convergence; hence calculated heating rate was also lower than ASCC (see Fig. (1-9)). In one of their papers [52] later on, they used iterative coupling

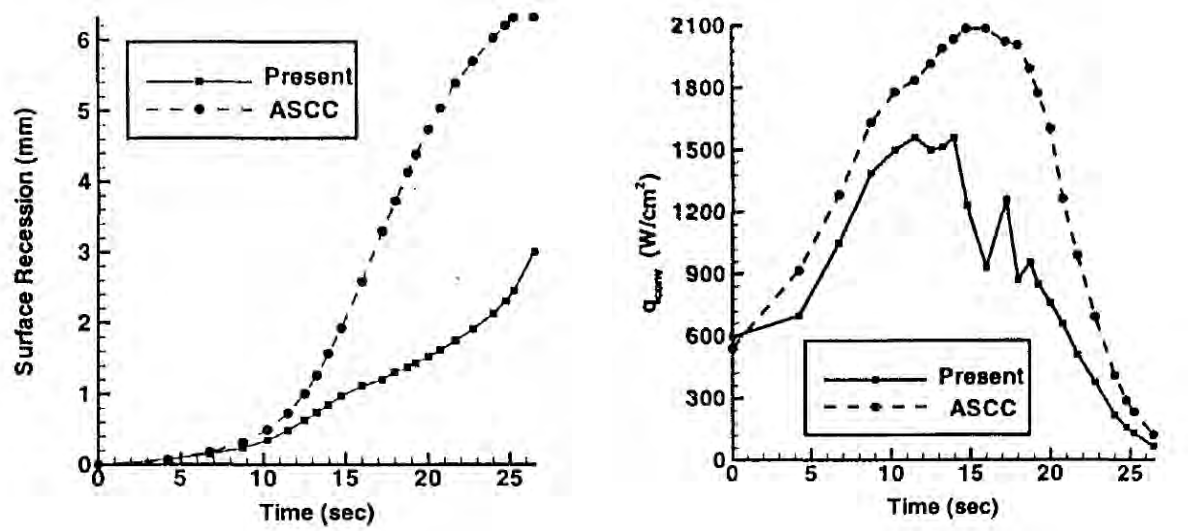

Figure 1-9. Comparison of A) net surface recession and B) net heating rate predicted by Hassan et al. [51] for thermal response of IRV-2 vehicle, using COYOTE/SACCARA coupling. Their results are compared with ASCC. For their simulations, ASCC updated heating flux value after every time step (of 1.0e-03 sec), but in [51] heating flux value was updated only after every 0.5 sec. Due to this, ASCC heating was predicted to be higher than COYOTE/SACCARA (denoted as ′Present′ in above plots), and hence anomaly in surface recession was observed.

between flow solver and thermal response code, and sufficiently accurate results were obtained (Fig. (1-8) B).

Many test cases are available in thermal ablation literature, which show instability in numerical simulations due to some inconsistency in modeling. Another example is [53], in which MOPAR, a one-dimensional implicit material response code with surface ablation and pyrolysis, was coupled to LeMANS, a CFD solver, and results for IRV-2 vehicle were shown. To implement a strong coupling between the material response code and the flow solver, modifications were made to the flow solver at the wall, where the ablated species were injected. This was done through adding blowing boundary conditions at the wall in flow solver by using first cell near the wall as a control volume.

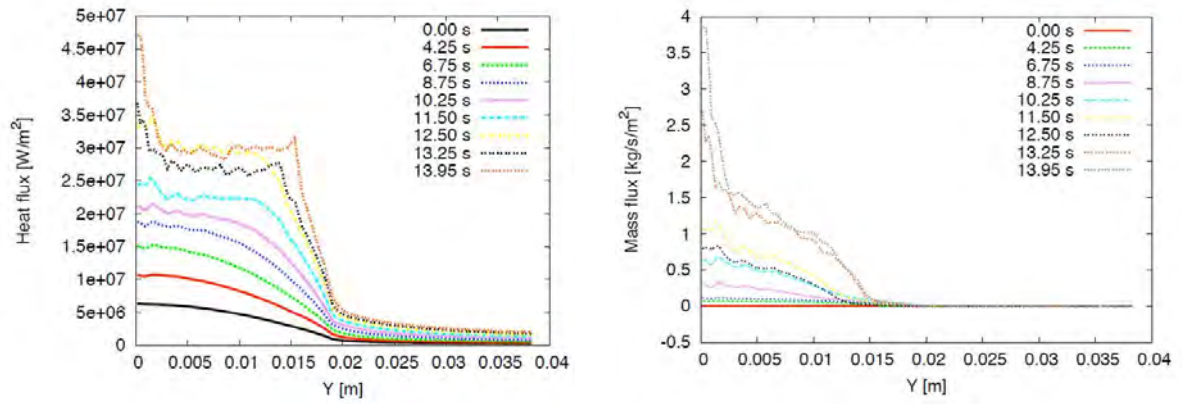

A B

Figure 1-10. Oscillations in solution of heat flux and mass flux in A) and B) respectively result from imprecision in modeling that is explained to result either from loss of assumption of perpendicularity of mesh to surface boundary as surface recedes, since 1-D thermal response code is used to treat a 2-D geometry or from use of coarse mesh. Imprecision from these factors is assumed to have been amplified at each discretized trajectory point, which can be attributed to the coupling between two domains. Such issues are not expected to occur where both problems are solved in one domain. [53]

In addition to this, mesh for the flow solver was also allowed to move as the surface the vehicle recedes for a complete strong coupling. For validation purposes, results were compared for IRV-2 vehicle. Both recession and stagnation point temperature was matched well to ASCC code and COYOTE/SACCARA, however their results for heat flux and blowing rate showed oscillations in the solution (see Fig. (1-10)). This was attributed to the imprecision in the solution, which was amplified in later trajectory points in solution of heat flux and blowing rates, which are very critical to measure thermal response of the vehicle.

1.3 State of the Art of Numerical Simulations in Hypersonic Flow

Various challenges in the field of hypersonic flow simulation are complex geometries of space vehicles, e.g. capsule-based entry vehicles and air-breathing launch systems; accurate simulation of the roughness-induced transition of turbulence on the surface of

the vehicle; new methods for coupling of radiation, chemistry and flow models; and need for automatic hybrid simulation methods for both continuum and rarefied flows [3].

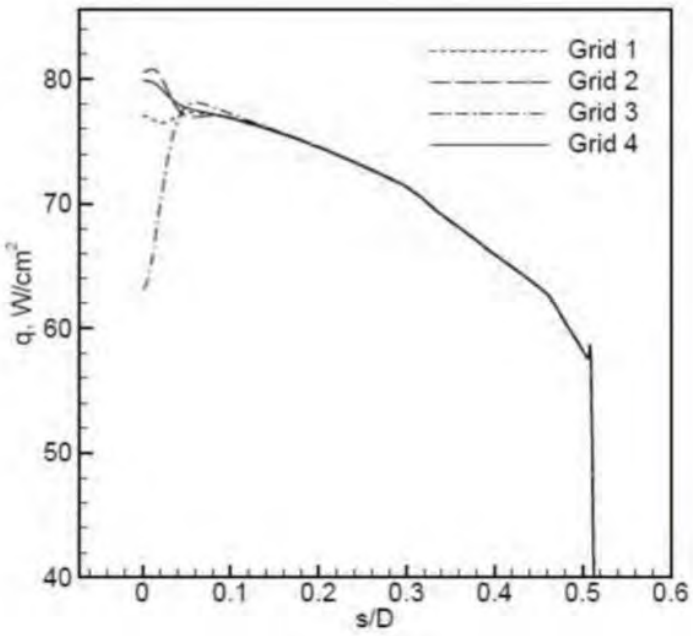

Figure 1-11. Effect of grid alignment at the shock on heating rate predicted at the surface of a capsule at an altitude of 70 km and flow Mach number of 26.2. The percentage difference in all of the four grids is within 1 % at the shock. Highest sensitivity is noticed at the stagnation point. [7]

Toughest of all challenges in hypersonic flows has been accurate and robust prediction of aerodynamic heating or the heat transfer at the surface of the vehicle ([3, 7–9, 54, 55]). Prediction of surface heat transfer coefficient is very sensitive to the mesh alignment along the shock. Even a slight misalignment of cells of a very small degree can cause tremendous changes in the surface heating prediction (see Fig. (1-11)).

The problem worsens for 3D simulations of an essentially 2D hypersonic flow over the cylinder, and large variations is seen to occur along the span-wise cells (in z-direction, perpendicular to the plane of the flow) [9], [8]. See Fig. (1-12).

Due to interest in the complex geometries, the use of unstructured meshes is desirable. Unstructured meshes are more convenient and less time-intensive to

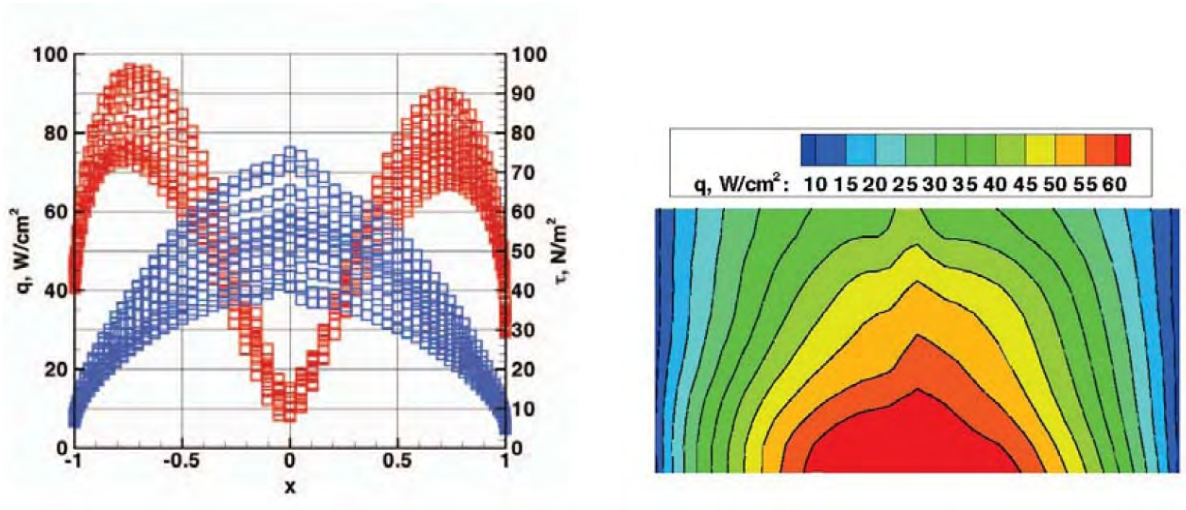

A B

Figure 1-12. Difference in heating prediction over ten spanwise elements in the z-direction for a 3D hypersonic flow over cylinder problem. Conventional reconstruction for the tetrahedral grids is used for this simulation. [8]

generate than the structured meshes. Furthermore, a lot of effort is still required, in the case of structured meshes, to align the elements along the shock and iterating for converged and accurate solutions.

To this end, solution adaptive methods are sought (in [3], [9], [2] and [10]) to enable output-guided grid adaptation, for accurate and efficient solutions. High-order methods are also essential for enhanced spatial accuracy to reduce the numerical error. In addition to all this, capturing complex physics further compounds the difficulty.

For more complex problems, there may also be multiple shock-shock interactions or shock-boundary layer interactions resulting in local flow separation and reattachment thus generating complex flow features. Further challenges, to capture accurate solutions are dearth of hypersonic flow test facilities, approximated physical models based on limited experimental data, and numerical errors associated with capturing high gradient solution.

[7] points out additional complexities associated with the hypersonic flow simulations of re-entry vehicles. Temperatures in shock reach several thousand Kelvin, and hence

the perfect gas model is no longer a valid assumption. Instead the flow is considered to be a mixture of ideal gases, and the flow chemistry accounts for production and destruction of all the species.

A wide range of density values varying almost by two orders of magnitude is encountered in the flow around a re-entry vehicle. Density increases by an order of magnitude across the shock and further even more significant increase is observed near the vehicle′s cold surface (relative to high temperatures in the shock and shock layer). As the flow goes around the vehicle, the density value falls to values significantly lower than the free-stream value. Thus the flow field of a re-entry vehicle may span a wide range of chemical equilibrium (near cylinder surface or shock layer), non-equilibrium (in shock) and frozen chemistry (in the wake region) (see Fig. (1-13)).

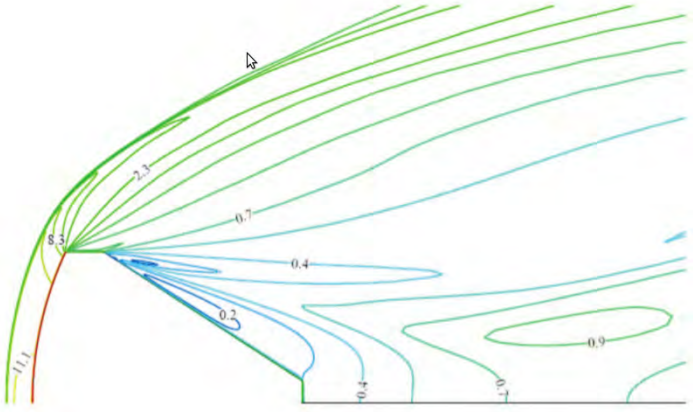

Figure 1-13. Contours of density for flow around re-entry capsule showing large variation of density values in the flow field. The Mach number for the flow is 16. [7]

Prediction of heat transfer is very sensitive, due to very high convective heat loads. For example, we found in our calculations for Mach 17 flow over cylinder, that a small error in temperature at the surface of the vehicle can cause significant differences in the heating predictions. If the temperature at the wall is fixed at 500^{o} C, and the element next to the wall has 0.45^{o} C error. Then this, apparently small error in the temperature, which is equal to 0.09 % error, will cause 3.125 % error in surface heating coefficient,

C_h, at the stagnation point. Thus, the value of C_h at the stagnation point may vary from 0.008, the desired value, to be 0.00825. This error is significanly visible in Fig. (1-14).

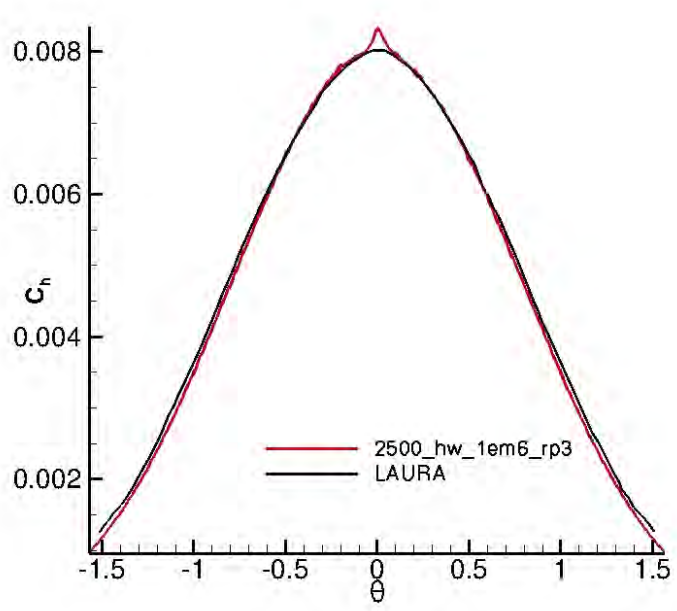

Figure 1-14. 3.125 % error in C_h profile (shown in red color, in reference to solution, shown in black, from LAURA) can come due to a small 0.09 % error in temperature prediction near the wall. This is our result from one of the r-p adaptive simulation that needed one more iteration of r-adaptation to remove the bump visible in C_h profile.

So, any amount of error in the prediction of the gas temperature close to the surface, will significantly affect the calculation of the net heat flux near the wall. This is dependent on few factors. Due to the cold wall, atomic gas species recombine at the wall (this recombination is exothermic), thus releasing heat to the wall. Hence accuracy of gas temperatures predicted near the wall depends on the uncertainty and errors associated with the modeling of chemical reactions rates. Additionally net thermal conductivity of the mixture also depends on its constituent gases, again affecting the net heat flux at the wall.

Strong shock wave forming in front of the vehicle is also prone to numerical errors thus causing that error to propagate downstream and affecting net surface

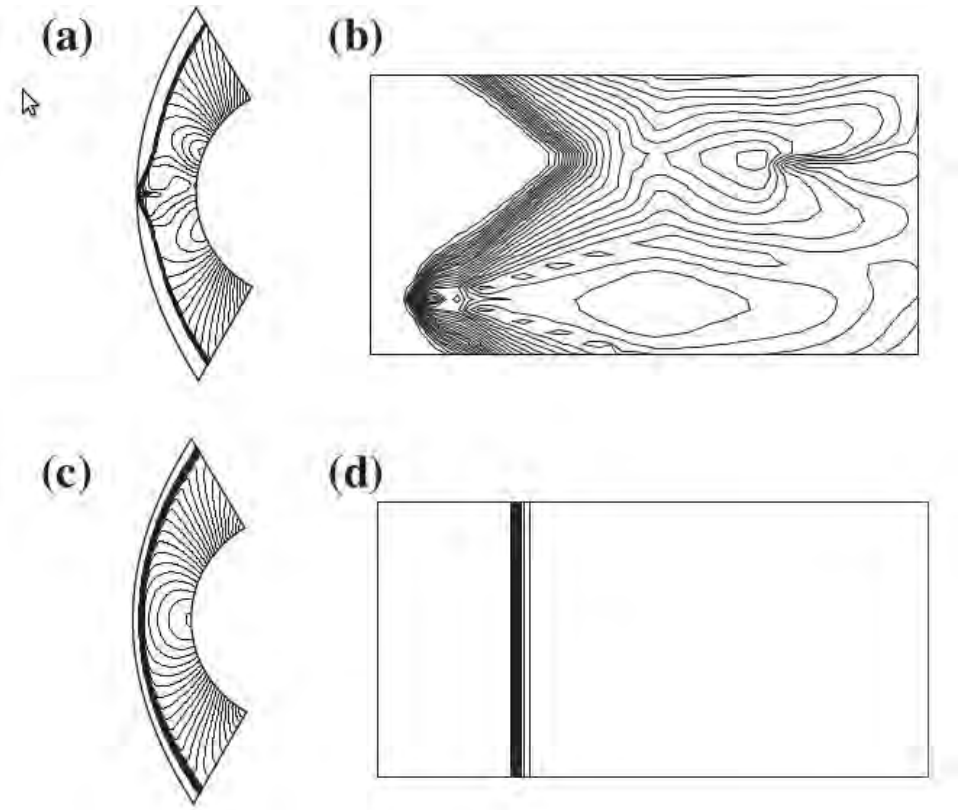

Figure 1-15. a) and b) solutions with carbuncle and c) and d) solutions without carbuncle for hypersonic flow over cylinder case. [54]

heat prediction. A fine grid is required to capture the shock to reduce the error, and the one set of grid has to be perfectly aligned with the shock to obtain accurate solution. Otherwise small misalignment can cause drastic differences in heating predictions as shown in Fig. (1-11). It is interesting to note that the main sensitivity arises at the stagnation point rather than elsewhere on the body.

Carbuncle effects frequently plague many CFD methods on very fine mesh close to the shock (see Fig. (1-15)). It is easy to identify such anomalies on simple geometries, but not so obvious in the case of complex geometries. In case of simple geometries, like cylinder, it will be obvious to identify the carbuncle effect as non-physical, but the same is not true for complex geometries ([54]).

In the field of DG methods, the PDE based artificial viscosity is applied to the shock region, to capture the shock in one element ([9]). The use of PDE based artificial

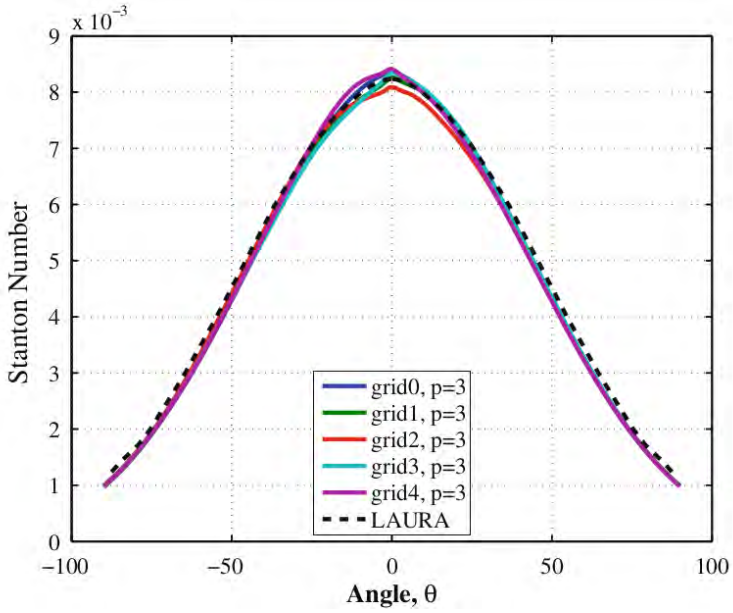

Figure 1-16. Result taken from [54] is solved with PDE based artificial viscosity applied to a 4^{th} order accurate DG method. $\mathrm{C_h}$ profiles with different meshes are compared to standard solution from LAURA. Minor asymmetry and a small bump can be seen in the $\mathrm{C_h}$ plots for even the well resolved finest grid solutions. ′grid4′ corresponds the finest grid used.

viscosity instead of a piecewise constant one, reduces the amount of numerical errors propagating downstream due to cells around shock not being completely aligned with the shock, thus minimizing the effect on surface heat transfer prediction. The problems in heat transfer prediction arises not only for unstructured meshes but also for symmetric meshes, producing incorrect and asymmetric heating profiles.

Element to element jumps in artificial viscosity causes oscillations in state gradients and hence corrupts the smoothness and accuracy of the downstream solution. By using the smooth PDE based artificial viscosity along with the high order accuracy, the dependence of shock capturing on grid orientation is significantly reduced. But, to illustrate the difficulty of getting accurate heating predictions, we can notice even in the well resolved case, with 4^{th} order accuracy and the finest mesh used in [9], the results for $\mathrm{C_h}$ do not exactly fall on the standard expected results (see Fig. (1-16)).

1.4 Industrial Standard Numerical Tools

Finite Difference (F.D.) and Finite Volume (F.V.) are industry standard methods used to solve both thermal ablation and hypersonic flow problems. These approaches have developed since 1960′s and are robust methods to solve both these problems of our interest. However there are certain limitations associated with these methods when it comes to higher order accuracy ($> 2^{\text{nd}}$ order) and complex geometries. A suitable alternative for handling complex geometries is Finite Element, F.E. method.

1.4.1 Finite Element Formulation for Thermal Ablation

[1] compares advantages of both finite element and finite difference procedures for thermal ablation problem. All the previous approaches to solve thermal ablation problem are briefly presented, and it is identified, therein that all of them used finite difference scheme. It is mentioned that finite difference is suitable to one-dimensional and two-dimensional simple geometry problems.

For complex geometry (see Fig. (1-17)) or complex/multifaceted boundary conditions, the scheme is no longer lucrative. It poses problems for a curved geometry, as the nodes which are supposed to be orthogonal to each other do not precisely lie on the curved boundary (see Fig. (1-18)), and hence an accurate boundary condition can no longer be applied to curved boundary. We have seen earlier that an imprecision leads to numerical instability and solution inaccuracy.

In finite element, use of elements however provide for curved edges which can exactly represent any complex, curved shapes. An example shown in Fig. (1-19) from [1] shows the comparison of two meshes of finite difference and finite element discretizations of a turbine blade profile.

1.4.2 Discontinuous Galerkin Method and its Benefits

Despite the important advantages of using Finite Element (FE) method as highlighted above with regard to the handling of complex geometries and curved boundaries, finite element method is still not widely used for thermal ablation or for high

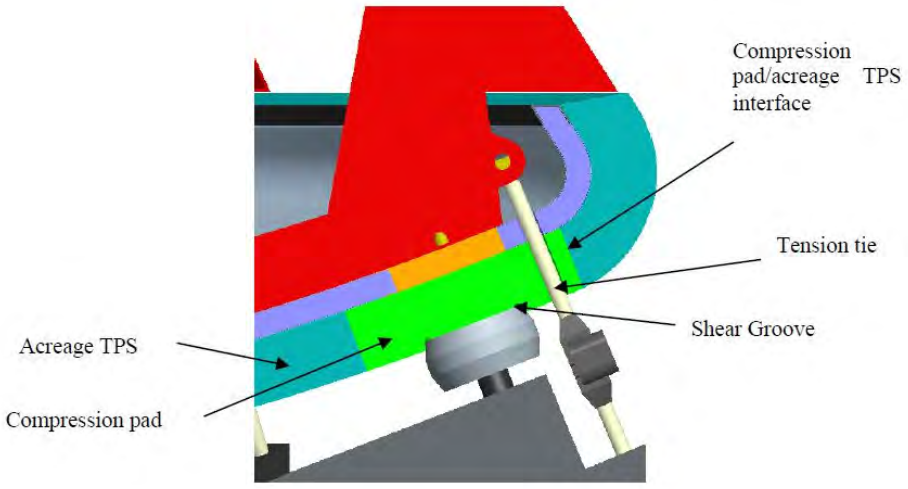

Figure 1-17. Generic heat shield penetration concept is shown [1]. Larger payloads increase the size and complexity of the entry vehicles. One single continuous piece of TPS can no longer serve as a heat shield material, thus isotropic material properties like thermal conductivity can no longer be assumed. To attach the launch load to primary vehicle or entry vehicle, tension tie rod penetrated through forebody TPS. This also consists of compression pad, which is inserted into acreage TPS. For such complex geometries, 1-D thermal response assumption will no longer work, and finite element will serve to analyze thermal response of such complicated structure of TPS.

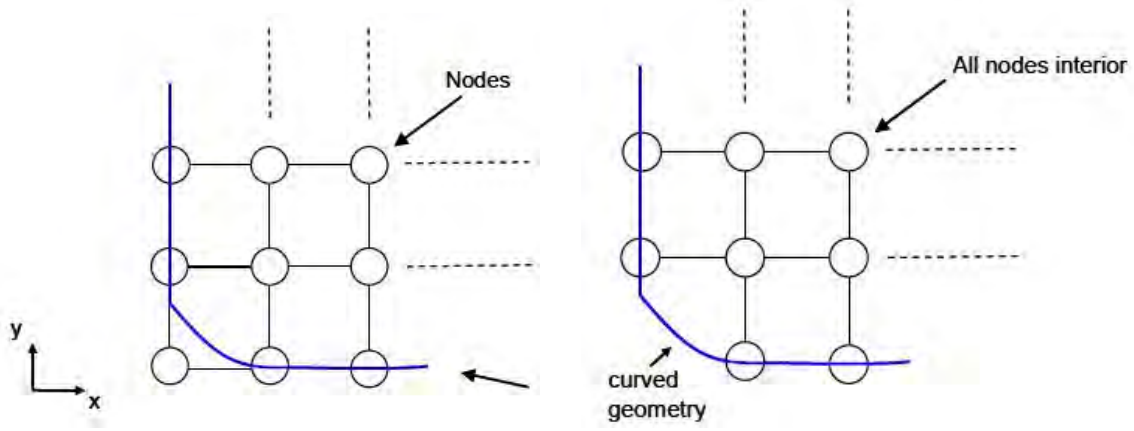

Figure 1-18. Finite difference uses grid points to approximate for the shape of a curved body [1]. Due to orthogonal nature of grid points, curved boundary cannot be correctly approximated. A) A node outside the boundary leads to incorrect boundary representation and B) node inside the boundary leads to incorrect boundary representation.

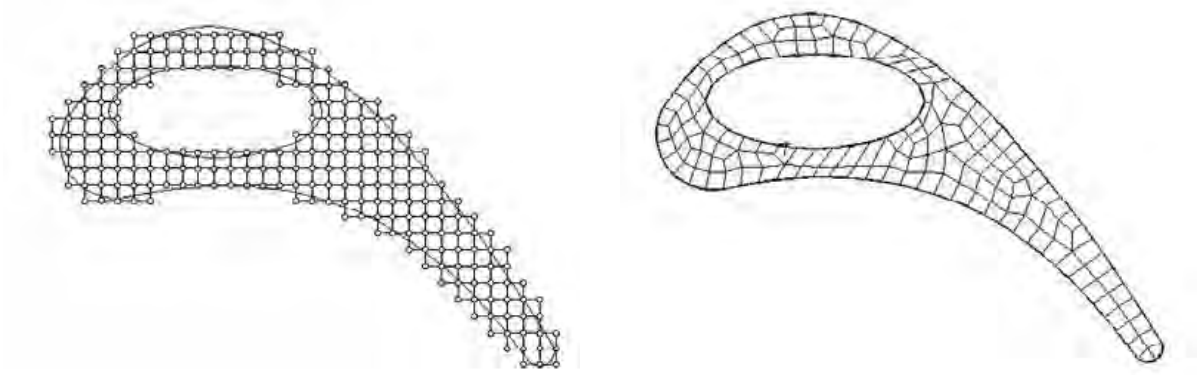

A B

Figure 1-19. Comparison of A) finite difference and B) finite element discretizations of a curved geometry, which is a turbine blade. As seen, boundary is correctly represented in finite element due to uses of elements which can have curved edges but still correspond to reference square elements in parametric space. [1]

speed flow simulation. Its serious limitation is handling high speed flows or convection dominated problems associated with it. It is very well known that finite element method will give spurious oscillations when solving a convection dominated problem, just like a central difference scheme in finite difference.

To overcome this limitation of finite element method, at the same time using its leverage for complex geometries, we turn to discontinuous Galerkin methods. Discontinuous Galerkin methods or DG methods are high order accurate methods, and this accuracy is afforded without any additional code complexity. All the advantages of DG method stem from the fact that it combines benefits of both finite volume and finite element methods. Being based in a finite element framework, it very conveniently allows for the increment of the polynomial accuracy without requiring any stencil support from the neighboring elements. This additional stencil support from the neighboring elements makes high order finite volume techniques (order of accuracy > 2) difficult to generalize for arbitrary meshes.

DG method also uses numerical fluxes for the inviscid terms in the governing equations, that gives it the capability to solve for the high speed or shock flow problems

with the high order resolution. These fluxes are approximations to Riemann solver and were originally developed for finite volume method, and later applied by Cockburn and Shu to DG methods.

Discontinuous Galerkin or DG method was first applied by Reed and Hill [56] in 1973 to solve neutron transport equation. Later on, it was developed in a series of papers by [57–61], Cockburn and Shu, into what came to be known in research community as Total Variation Diminishing Runge-Kutta Discontinuous Galerkin method (TVD RKDG). They presented a formal development of the method for hyperbolic system of equations for multidimensional systems. This used unstructured or triangular meshes for 2-D and tetrahedral meshes for 3-D.

Discontinuous Galerkin method differs from (continuous) Galerkin finite element method in that it allows solution to be discontinuous across the element boundaries. Therefore, the solution is local to its element alone, and hence formulation is compact overall and also near boundaries without any special treatment at the boundaries. Due to this, application of the boundary condition is more robust in DG method for any kind of boundary condition. In finite difference methods, high order accuracy for the internal nodes can be easily ruined by low order accuracy at the boundary nodes. So for this purpose one-sided and biased finite difference formulations are applied at the boundary and inside (close to boundary) nodes respectively. This is quite complex to deal with even for 1-D problems for high order accuracy (> 2), and also when discretizing higher order derivatives in governing equation, and situation further worsens for higher dimensions.

One price however that has to be paid is of computational cost, but because of its amenability to easy parallelization this cost can be overcome. We will now describe recent developments in DG methods.

1.4.2.1 Brief history of recent developments in discontinuous Galerkin methods

Extensive work has been done on discontinuous Galerkin (DG) methods to apply them to a variety of class of problems. Being first introduced in 1973, work was undertaken to develop these methods for linear and non linear hyperbolic systems. Major part of work was done by Cockburn and Shu for development of Runge-Kutta discontinuous Galerkin (RKDG) schemes. These were proven to be non-linearly stable for multi-dimensional hyperbolic systems, and shown later on to have favorable characteristics like high-order accuracy, high parallelizability and easy application to complicated geometries.

RKDG scheme was extended specifically to compressible Navier Stokes equations by Bassi and Rebay [62], where they rewrote second order governing equations as a set of first order equations by introducing new variables for first order derivative term. A simple average of viscous flux terms was taken from inside and outside of element at element boundaries. An important achievement of this work was that they used curved boundary and resolved the boundary layer within only a few elements. Their scheme became known as BR1 scheme in literature.

This caused the shift of focus of development of DG methods to convection-diffusion problems. Inspired by work of Bassi and Rebay, Cockburn and Shu applied RKDG methods to convection-diffusion problems and generalized the method of Bassi and Rebay into what came to be known as so called local discontinuous Galerkin methods (LDG) [63] in the literature. They showed that by proper choice of inter-element fluxes, additional variable could be eliminated locally and hence final discretization is solved only for original variable. But the problem with LDG method was that for multidimensional systems, the degree of freedoms for an element was connected to its neighbors neighbors. Hence the compactness which was afforded by DG methods for hyperbolic systems was lost in LDG for multidimensional systems.

Other two popular works in solving elliptic problems using discontinuous finite elements include BR2 scheme [64], which was extension of work on BR1 scheme by Bassi and Rebay and Interior Penalty or IP schemes [65] developed in 1970s and 1980s independent of work on DG methods. Both these schemes directly discretize the second order derivative terms and add an explicit stabilization term. Both these schemes are compact for elliptic problems unlike LDG for multidimensional problems. So, these schemes are useful for implicit solution of a problem. Peraire and Persson [66] derived a variant of LDG method, named CDG or Compact discontinuous Galerkin method, where the difference lies in how the derivative term across element boundaries is approximated. This scheme enables to achieve compactness for multidimensions, and is at par with LDG method in all respects, and even excelling in some, like stability.

Time-implicit DG methods are used where explicit methods pose very restrictive time-step limitation, e.g. high Reynolds number flows using spatially varying mesh, where CFL limit is decided by smallest spatial scale, and low Mach number flows, where time scales of wave propagation and fluid flows differ by orders of magnitude. Implicit DG methods for non-linear problems will give rise to a system of equations, by use of Newtons method and the matrix arising out has to be most probably solved by iterative solution techniques. Since, the matrices arising out of application of DG methods to thermal ablation problem can be highly ill-conditioned and in general block-wise structured, it is useful to look at previous works on preconditioners and parallelization for discretizations arising from DG method.

As mentioned in [67], the block structure of DG methods has been used in designing the block preconditioners which are more efficient than regular preconditioners. Here a multigrid method is used in conjunction with a block preconditioner as a smoother. They refer to use of various preconditioners as smoothers like block Jacobi smoother ([68]), block Gauss-Siedel (GS) smoother ([68, 69]), smoother based on solution of block tridiagonal systems [70] etc. In [67] itself, a new preconditioner

approach is proposed, called ILU0, where post-smoothing is performed based on block incomplete LU factorization with zero fill-in. The use of multigrid strategies in combination with block preconditioners mainly finds its use in elliptic problems; for convection dominated problems, there is not much to be gained by use of multigrid methods.

1.5 Contribution

- Solved wide range of problems from thermal ablation, high speed flows to hypersonic flows with thermo-chemistry
- Found r-p adaptivity approach to obtain same accuracy as h-p adaptivity methods for hypersonic flows solution, with lesser number of elements.
- Employed p = 0 solution in shock along with r-adaptivity to eliminate errors encountered with other methods like PDE based artificial viscosity methods.
- Introduced DG methods to the field of thermal ablation, opening avenues for high-order accurate simulations for complex geometries in thermal ablation.
- Successfully solved hypersonic flow problem with thermo-chemical non-equilibrium with DG methods, not yet done in published literature.
- Developed generalized approach for implicit methods, bringing the capability to solve any new physics without much effort. Used numerical approach to evaluate jacobians that evades the need and tediousness of evaluating analytical jacobians for a full implicit problem.
- Combined rp adaptivity + slope limiter for high order solution in shock.
- Found the effect of plasma DBD actuators on the reduction of surface heating for hypersonic flow over cylinder.

1.6 Thesis Layout

In chapter 1, we have described our motivation behind our work. We have pointed out several limitations of the current state of the art for numerical simulations in the field of thermal ablation and hypersonic flows. In addition, limitations and challenges associated with industry standard finite difference and finite volume codes were also pointed for complex geometries and high order solution. This laid the foundation for

using DG methods to open avenues for future work with more complex geometries and high order accurate solution.

Next in chapter 2, we layout governing equations for inviscid, viscous flows along with hypersonic flows with thermo-chemical non-equilibrium and thermal ablation problem. We present discontinuous Galerkin methods in chapter 3 along with our work on identifying the differences in BR1 and BR2 schemes. We also highlight our work on parallelization, implicit time integration and r-p adaptive methods to capture shock in chapter 3. Next, we present some validation examples in the field of inviscid and viscous flows in chapter 4. Chapter 5 presents three test cases for thermal ablation, chosen to solve using DG methods developed. Chapter 6 shows validation cases for inviscid, viscous hypersonic flows and hypersonic flows with thermo-chemical non-equilibrium. The effect of a DBD plasma actuator on surface heating for hypersonic flows over a cylinder is discussed in chapter 7. Finally, we conclude with chapter 8 highlighting our achievements and future work.

CHAPTER 2
GOVERNING EQUATIONS

In this chapter, we describe all important governing equations for different physics studied in this work. These include inviscid Euler equations (section 2.1), viscous Navier-Stokes equations (section 2.2), thermo-chemical non-equilibrium for a multi-species Navier Stokes equations (sections 2.3) and thermal ablation (section 2.4).

2.1 Inviscid Euler Equations

Neglecting both the viscous and thermal conduction effects, we can derive inviscid Euler equations, which can be written in following general form,

$$\frac{\partial \mathrm{U}}{\partial \mathrm{t}} + \nabla \cdot \mathrm{F_i} = 0 \tag{2–1}$$

Here, U is a conservative state vector given by,

$$\mathrm{U} = \begin{pmatrix} \rho \\ \rho \mathrm{u} \\ \rho \mathrm{v} \\ \rho \mathrm{w} \\ \rho \mathrm{E} \end{pmatrix} \tag{2–2}$$

and the inviscid flux tensor, $\mathrm{F_i} = (\mathrm{F_i^x}, \mathrm{F_i^y}, \mathrm{F_i^z})$ is given by,

$$\mathrm{F_i^x} = \begin{pmatrix} \rho \mathrm{u} \\ \rho \mathrm{u}^2 + \mathrm{P} \\ \rho \mathrm{uv} \\ \rho \mathrm{uw} \\ \mathrm{u}(\rho \mathrm{E} + \mathrm{P}) \end{pmatrix}; \qquad \mathrm{F_i^y} = \begin{pmatrix} \rho \mathrm{v} \\ \rho \mathrm{uv} \\ \rho \mathrm{v}^2 + \mathrm{P} \\ \rho \mathrm{vw} \\ \mathrm{v}(\rho \mathrm{E} + \mathrm{P}) \end{pmatrix}; \qquad \mathrm{F_i^z} = \begin{pmatrix} \rho \mathrm{w} \\ \rho \mathrm{uw} \\ \rho \mathrm{vw} \\ \rho \mathrm{w}^2 + \mathrm{P} \\ \mathrm{w}(\rho \mathrm{E} + \mathrm{P}) \end{pmatrix} \tag{2–3}$$

$\rho \mathrm{E}$ is the total energy which is the sum of the internal energy and the kinetic energy,

$$\rho \mathrm{E} = \rho \mathrm{e} + \frac{1}{2}\rho(\mathrm{u}^2 + \mathrm{v}^2 + \mathrm{w}^2) \tag{2–4}$$

Pressure is constructed from the internal energy, and thus can be found from the conservative variables in Eq. (2–2), in following way,

$$\mathrm{P} = (\gamma - 1)\left(\rho \mathrm{E} - \frac{1}{2}\rho\left(\mathrm{u}^2 + \mathrm{v}^2 + \mathrm{w}^2\right)\right) \tag{2–5}$$

Here γ is the specific heat ratio and is set equal to a constant value of 1.4 in this work.

2.2 Viscous Navier-Stokes Equations

With viscous effects and thermal conduction included, Eq. (**??**) become Navier-Stokes equations, which can be written in following general notation,

$$\frac{\partial \mathrm{U}}{\partial \mathrm{t}} + \nabla \cdot \mathrm{F_i} = \nabla \cdot \mathrm{F_v} \tag{2–6}$$

$\mathrm{F_v} = (\mathrm{F_v^x}, \mathrm{F_v^y}, \mathrm{F_v^z})$ is the viscous flux term, given by,

$$\mathrm{F_v^x} = \begin{pmatrix} 0 \\ \tau_{\mathrm{xx}} \\ \tau_{\mathrm{xy}} \\ \tau_{\mathrm{xz}} \\ \mathrm{u}\tau_{\mathrm{xx}} + \mathrm{v}\tau_{\mathrm{xy}} + \mathrm{w}\tau_{\mathrm{xz}} + \mathrm{q_x} \end{pmatrix}; \qquad \mathrm{F_v^y} = \begin{pmatrix} 0 \\ \tau_{\mathrm{yx}} \\ \tau_{\mathrm{yy}} \\ \tau_{\mathrm{yz}} \\ \mathrm{u}\tau_{\mathrm{yx}} + \mathrm{v}\tau_{\mathrm{yy}} + \mathrm{w}\tau_{\mathrm{yz}} + \mathrm{q_y} \end{pmatrix}; \tag{2–7}$$

$$\mathrm{F_v^z} = \begin{pmatrix} 0 \\ \tau_{\mathrm{zx}} \\ \tau_{\mathrm{zy}} \\ \tau_{\mathrm{zz}} \\ \mathrm{u}\tau_{\mathrm{zx}} + \mathrm{v}\tau_{\mathrm{zy}} + \mathrm{w}\tau_{\mathrm{zz}} + \mathrm{q_z} \end{pmatrix} \tag{2–8}$$

where τ is the viscous stress tensor given as follows,

$$\tau = \begin{bmatrix} \tau_{\mathrm{xx}} & \tau_{\mathrm{xy}} & \tau_{\mathrm{xz}} \\ \tau_{\mathrm{yx}} & \tau_{\mathrm{yy}} & \tau_{\mathrm{yz}} \\ \tau_{\mathrm{zx}} & \tau_{\mathrm{zy}} & \tau_{\mathrm{zz}} \end{bmatrix} \tag{2–9}$$

For flows with single species and without any thermo-chemical non-equilibrium we consider the working gas to be air. The viscous stress for air (being a Newtonian fluid) is given from Stokes hypothesis,

$$\tau_{\mathrm{ij}} = \mu \left(\frac{\partial \mathrm{u_i}}{\partial \mathrm{x_j}} + \frac{\partial \mathrm{u_i}}{\partial \mathrm{x_j}} - \frac{2}{3} \frac{\partial \mathrm{u_k}}{\partial \mathrm{x_k}} \delta_{\mathrm{ij}} \right) \tag{2–10}$$

In above, μ is the viscosity of the fluid and is given for a monoatomic gas by the semi-empirical Sutherland's Law. In this μ is function of temperature.

$$\frac{\mu}{\mu_{\mathrm{o}}} = \left(\frac{\mathrm{T}}{\mathrm{T_o}} \right)^{3/2} \frac{\mathrm{T_o + S}}{\mathrm{T + S}} \tag{2–11}$$

Here, the constants appearing in above equation are given as follows,

$$\mu_{\mathrm{o}} = 1.716.10^{-5} \frac{\mathrm{kg}}{\mathrm{ms}} \tag{2–12}$$

$$\mathrm{T_o} = 273.15\mathrm{K} \tag{2–13}$$

$$\mathrm{S} = 110.55\mathrm{K} \tag{2–14}$$

In addition to the viscous stress tensor which has already been defined above, the heat flux vector, q in the viscous flux tensor, $\mathrm{F_v}$ is given by Fourier's law,

$$\mathrm{q_j} = -\lambda \frac{\partial \mathrm{T}}{\partial \mathrm{x_j}} \tag{2–15}$$

λ is thermal conductivity coefficient given by molecular viscosity, μ, specific heat, $\mathrm{C_p}$ and Prandlt number, Pr,

$$\lambda = \frac{\mu \mathrm{C_p}}{\mathrm{Pr}} \tag{2–16}$$

For all cases considered in this thesis, wherever we use Navier-Stokes equations, Pr is chosen to be 0.72.

2.3 Multi-species Navier-Stokes Equations

Temperatures in a hypersonic flow field are typically few thousand Kelvin, up to 10,000 K or higher. Thus, Navier Stokes equations, described in section 2.2, for a monoatomic gas can no longer be used. The gas at such high temperatures undergoes chemical reactions and vibrational-electronic excitation. Thus, we consider multi-species Navier-Stokes equations for solving hypersonic flow with thermo-chemical non-equilibrium. Before giving the equations, we discuss the physics of the thermo-chemical non-equilibrium.

2.3.1 Thermo-Chemical Non-Equilibrium

A gas at very high temperature can undergo excitation of internal energy modes, molecular dissociation and thermal non-equilibrium wherein the gas state can no longer be specified by one single temperature. Total energy, e of a gas molecule can be considered to consist of four components namely translational, rotational, vibrational and electronic excitation.

$$\mathrm{e} = \mathrm{e_t} + \mathrm{e_r} + \mathrm{e_v} + \mathrm{e_e l} \tag{2–17}$$

Translational and rotational modes exist at room temperatures. Vibrational and electronic excitation modes are only significant contributors at high temperatures. The translational and rotational modes are given by following,

$$\mathrm{e_t} = \frac{3}{2}\mathrm{k_b T}\,, \tag{2–18}$$

$$\mathrm{e_r} = \begin{cases} 0 & \text{for atoms}\,, \\ \mathrm{k_b T} & \text{for diatomic molecules}\,. \end{cases} \tag{2–19}$$

Translational mode for a molecule or atom stands for kinetic energy due to its linear momentum and is same for both atom and polyatomic species as given above. Rotational modes on other hand represent kinetic energy due to the angular momentum of the molecule, and is zero for atoms and $\mathrm{k_b T}$ for diatomic molecules.

Vibrational energy mode is only relevant for polyatomic molecules, since it corresponds to the vibration of atoms within the molecule. In this work, we consider diatomic molecules (in addition to monoatomic molecules) which have two degrees of freedom. Since, this vibrational energy is not always fully excited, the molecule is represented by a harmonic oscillator and the vibrational energy of a (diatomic) molecule is given by,

$$\mathrm{e_v\,(T)} = \frac{\mathrm{k_b}\theta_\mathrm{v}}{\mathrm{e}^{\frac{\theta_\mathrm{v}}{\mathrm{T}}} - 1} \tag{2–20}$$

In above, θ_v is the characteristic temperature for vibration and is unique for each molecule. It is given in table below,

Electronic mode is the energy associated with excitation of electrons from ground state to higher energy states. This is valid for all species. The expression for electronic energy is given by,

Table 2-1. Vibrational temperatures for non-ionizing dissociating air

Species	θ_v
O_2	2239.0
NO	2817.0
N	0.0
O	0.0
N2	3395.0

$$e_{el} = k_b \frac{\sum_{\infty}^{i=1} g_i \theta_{el,i} e^{\frac{\theta_{el,i}}{T}}}{g_0 + \sum_{\infty}^{i=1} g_i \theta_{el,i} e^{\frac{\theta_{el,i}}{T}}} \tag{2–21}$$

Above, $\theta_{el,i}$ is the characteristic temperature and g_i is the degeneracy for each electronic transition. Table below (B-1) gives the values for first and second electronic transitions. As can also be noted from the table below, the characteristic temperatures for electronic transitions are much higher than those for vibrational modes. Hence, electronic transitions are only significant at very high temperatures, typically above 10,000 K.

Table 2-2. Electronic temperatures and degeneracies for non-ionizing dissociating air

Species	$\theta_{el,1}$	$\theta_{el,2}$	g_0	g_1	g_2
O_2	11,392.0	18,985.0	3	2	1
NO	55,835.0	63,258.0	4	8	2
N	27,665.0	41,495.0	4	10	6
O	22,831.0	48,620.0	9	5	1
N_2	72,233.0	85,744.0	1	3	6

We so far discussed thermal non-equilibrium, which uses definitions of two temperatures namely, T, for translational and rotational modes and T_v for vibrational and electronic modes. For chemical non-equilibrium we consider 5 species model in this work, consisting of O_2, NO, N, O and N_2. These 5 species are considered to undergo 5 chemical reactions, three dissociation of N_2, O_2 and NO and two exchange reactions described in detail in the later section in this chapter. Finite rate chemistry is considered for modeling chemical non-equilibrium in section 2.3.4.

2.3.2 Multispecies Navier Stokes Equations

Fluid flow in thermo-chemical non-equilibrium is represented by multi-species Navier Stokes equations. The gas undergoes molecular dissociation and exchange reactions between different species present. No ionization is considered in this model. We also assume the gas to be in equilibrium with itself. This means that every species can be described using its own species density, velocity and temperature for all energy modes. The equations can be written in following simple form,

$$\frac{\partial \mathrm{U}}{\partial \mathrm{t}} + \nabla \cdot \mathrm{F_i} = \nabla \cdot \mathrm{F_v} + \mathrm{S} \tag{2–22}$$

U again denotes the solution vector, $\mathrm{F_i}$ and $\mathrm{F_v}$ inviscid and viscous flux terms and S is the source term vector, and are given as follows,

$$\mathrm{U} = \begin{pmatrix} \rho_\mathrm{s} \\ \rho\vec{\mathrm{u}} \\ \rho \mathrm{e_t} \\ \rho \mathrm{e_v} \end{pmatrix}; \qquad \vec{\mathrm{F_i}} = \begin{pmatrix} \rho_\mathrm{s}\vec{\mathrm{u}} \\ \rho\vec{\mathrm{u}} \otimes \vec{\mathrm{u}} + \mathrm{P} \\ \rho\vec{\mathrm{u}}\mathrm{h_t} \\ \rho\vec{\mathrm{u}}\mathrm{h_v} \end{pmatrix}; \qquad \vec{\mathrm{F_v}} = \begin{pmatrix} -\rho_\mathrm{s}\tilde{\mathrm{V}}_\mathrm{s} \\ \underline{\tau} \\ \underline{\tau} \cdot \vec{\mathrm{u}} - \vec{\mathrm{q}} - \vec{\mathrm{q}}_\mathrm{v} - \sum_\mathrm{s} \mathrm{h_{t,s}}\rho_\mathrm{s}\tilde{\mathrm{V}}_\mathrm{s} \\ -\vec{\mathrm{q}}_\mathrm{v} - \sum_\mathrm{s} \mathrm{h_{v,s}}\rho_\mathrm{s}\tilde{\mathrm{V}}_\mathrm{s} \end{pmatrix}$$

$$\mathrm{S} = \begin{pmatrix} \omega_\mathrm{s} \\ 0 \\ 0 \\ \sum_\mathrm{s} \omega_\mathrm{s}\hat{\mathrm{e}}_\mathrm{v,s} + \mathrm{Q_{T-V}} \end{pmatrix} \tag{2–23}$$

In this work, we consider 2-D form of above equations and thus we have total 9 equations, considering 5 species. ρ_s is the species density, with s = 1,2, ...,5 and ρ is the total density which is the sum of all species density. $\rho\vec{\mathrm{u}}$ is the bulk momentum, $\rho \mathrm{e_t}$ and $\rho \mathrm{e_v}$ are the total energy and vibrational energy respectively. $\rho \mathrm{e_t}$ is equal to the sum

of ρe_v, translational rotational energy, kinetic energy and heat of formation of present species and h_t is the total enthalpy, the sum of internal energy and pressure.

$$\rho e_t = \rho e_v + \sum_s \rho_s C_{V,tr} T + \sum_s \rho_s h_s^0 + \frac{1}{2}\rho\left(u^2 + v^2\right) \tag{2–24}$$

$$h_t = e_t + \frac{P}{\rho} \tag{2–25}$$

For vibrational energy equation, h_v is considered equal to e_v, since there is no consideration of pressure term in the vibrational energy equation (for ρe_v), since kinetic energy is considered only in the total energy equation, for ρe_t.

$$h_v = e_v \tag{2–26}$$

Considering viscous flux term in continuity equation for 5 species density, ρ_s, we note that that $\tilde{V}_s$ is the diffusion velocity of species and is determined using Fick's law,

$$\rho_s \tilde{V}_s = -\rho D_s \nabla c_s \tag{2–27}$$

Shear stress, $\underline{\tau}$, and heat fluxes, $\vec{q}$ and $\vec{q}_v$ for translation-rotational modes and vibrational-electronic modes respectively are given by following formulas,

$$\underline{\tau} = \mu\left(\nabla\vec{u} + \vec{u}\nabla\right) - \frac{2}{3}\mu\nabla\cdot\vec{u}\underline{I} \tag{2–28}$$

$$\vec{q} = -k\nabla T \tag{2–29}$$

$$\vec{q}_v = -k_v \nabla T_v \tag{2–30}$$

Formulas for constants of diffusion, $\mathrm{D_s}$, viscosity, μ, conductivities k and $\mathrm{k_v}$ is given in section below. The terms, $\sum_{\mathrm{s}} \mathrm{h_{t,s}} \rho_{\mathrm{s}} \tilde{\mathrm{V}}_{\mathrm{s}}$, and $\sum_{\mathrm{s}} \mathrm{h_{v,s}} \rho_{\mathrm{s}} \tilde{\mathrm{V}}_{\mathrm{s}}$ in Eq. (2–23) in the viscous flux term denote the transport of total and vibrational energies respectively due to mass diffusion of the different species present. Finally, ω_{s} is the production rate of different species due to the chemical reactions between different species. $\sum_{\mathrm{s}} \omega_{\mathrm{s}} \hat{\mathrm{e}}_{\mathrm{v,s}}$ and $\mathrm{Q_{T-V}}$ in the source term, S in Eq. (2–23) are respectively, the production/destruction of vibrational energy (due to production/destruction of species) and energy exchange between translational-rotational and vibrational modes. The energy first of all is transferred to translational and rotational modes, where from it is transferred to vibrational modes depending on the translational-rotational temperature, T and the pressure, P. The details of these terms also follow in the later section.

2.3.3 Transport Properties

Fluid viscosity, μ is found from the species viscosities, μ_{s} using Wilke's semi-empirical mixing rule [71],

$$\mu = \sum_{\mathrm{s}=1}^{\mathrm{ns}} \frac{\mathrm{X_s} \mu_{\mathrm{s}}}{\phi_{\mathrm{s}}} \tag{2–31}$$

where,

$$\mathrm{X_s} = \frac{\mathrm{c_s M}}{\mathrm{M_s}} \tag{2–32}$$

$$\mathrm{M} = \left(\sum_{\mathrm{s}=1}^{\mathrm{ns}} \frac{\mathrm{c_s}}{\mathrm{M_s}} \right)^{-1} \tag{2–33}$$

$$\phi_{\mathrm{s}} = \sum_{\mathrm{r}=1}^{\mathrm{ns}} \mathrm{X_r} \left[1 + \sqrt{\frac{\mu_{\mathrm{s}}}{\mu_{\mathrm{r}}}} \left(\frac{\mathrm{M_r}}{\mathrm{M_s}} \right)^{\frac{1}{4}} \right]^2 \left[\sqrt{8 \left(1 + \frac{\mathrm{M_s}}{\mathrm{M_r}} \right)} \right]^{-1} \tag{2–34}$$

Here, $\mathrm{c_s}$ is the mass fraction of each species, s,

$$c_s = \frac{\rho_s}{\rho} \tag{2–35}$$

The individual species viscosities can be found from Blottner's model [72], which assumes the species viscosities to be a function of the translational-rotational temperatures, T,

$$\mu_s = 0.1 \exp\left[(A_s \ln T + B_s)\ln T + C_s\right] \tag{2–36}$$

Values of A_s , B_s and C_s are given in Appendix A. Model is valid for temperatures up to 30,000 K and is sufficient for our work.

The conductivities required for heat fluxes given in Eq. (2–30) are determined from Eucken relation [73],

$$k_t = \frac{5}{2}\mu_s {C_{Vs}}^{tr} \tag{2–37}$$

$$k_{rot} = \mu_s {C_{Vs}}^{rot} \tag{2–38}$$

$$k_{vib} = \mu_s {C_{Vs}}^{vib} \tag{2–39}$$

All the required specific heats in this section can be calculated by differentiation of the respective internal energies w.r.t. particular temperature, i.e.

$$C_{Vs} = \frac{\partial e_s}{\partial T} \tag{2–40}$$

Diffusion velocities are given by Fick's law, and depend upon gradients of concentration, pressure and temperature.

$$\rho_{\mathrm{s}}\tilde{\mathrm{V}}_{\mathrm{s}} = -\rho \mathrm{D}_{\mathrm{s}} \nabla \left(\frac{\rho_{\mathrm{s}}}{\rho} \right) \tag{2–41}$$

Here, $\mathrm{D_s}$ is the multi-component diffusion coefficient. In this work, $\mathrm{D_s}$ is replaced by single binary diffusion coefficient D, which is found using Lewis number, Le of 1.4 for all species,

$$\mathrm{Le} = \mathrm{D} \frac{\rho \mathrm{C_p}}{\kappa} \tag{2–42}$$

2.3.4 Source Term for Chemical Reactions

We are using 5 species model in this work, for the hypersonic flow simulation, consisting of $\mathrm{N_2}$, $\mathrm{O_2}$, NO, N and O. These species undergo following 5 chemical reactions, consisting of 3 dissociation reactions and 2 exchange reactions,

$$\mathrm{N_2 + M \longleftrightarrow N + N + M} \tag{2–43}$$

$$\mathrm{O_2 + M \longleftrightarrow O + O + M} \tag{2–44}$$

$$\mathrm{NO + M \longleftrightarrow N + O + M} \tag{2–45}$$

$$\mathrm{N_2 + O \longleftrightarrow NO + N} \tag{2–46}$$

$$\mathrm{NO + O \longleftrightarrow O_2 + N} \tag{2–47}$$

First three reactions are dissociation of $\mathrm{N_2}$, $\mathrm{O_2}$ and NO into their atomic species. M denotes the third body that can be any of the 5 species present, used to collide with the dissociating molecule that is required to conserve the energy of collision. These reactions are also known as third body reactions in the literature. Last two reactions are basically oxidation of $\mathrm{N_2}$ and NO species, resulting in formation of atomic Nitrogen species.

These reactions are governed by the forward and backward reaction rates. Forward reactions rate is given in Arrhenius form,

$$\mathrm{k_{f,r,m}} = \mathrm{C_{f,r,m}} \mathrm{T_{eff}^{\eta_{f,r,m}}} \exp\left(\frac{\theta_{\mathrm{f,r,m}}}{\mathrm{T_a}}\right) \tag{2–48}$$

Values of $\mathrm{C_{f,r,m}}$, $\eta_{\mathrm{f,r,m}}$ and $\theta_{\mathrm{f,r,m}}$ are given in Appendix A. $\mathrm{T_{eff}}$ is equal to following from Park's $\mathrm{TT_v}$ model, [74]

$$\mathrm{T_{eff}} = \sqrt{\mathrm{TT_v}} \tag{2–49}$$

The backward rate constant, $\mathrm{k_{b,m}}$ is determined from the equilibrium constant which is determined through curve fits to equilibrium experimental data given by McBride et al (2002) [75], and is in following form,

$$\mathrm{K_{eq,m}} = \mathrm{C_m} \exp\left(\mathrm{A_{1,m}} + \mathrm{A_{2,m}Z} + \mathrm{A_{3,m}Z^2} + \mathrm{A_{4,m}Z^3} + \mathrm{A_{4,m}Z^4}\right) \tag{2–50}$$

Here,

$$\mathrm{Z} = \frac{10,000\mathrm{K}}{\mathrm{T}} \tag{2–51}$$

The constants $\mathrm{A_{1,m}}$, $\mathrm{A_{2,m}}$, $\mathrm{A_{3,m}}$, $\mathrm{A_{4,m}}$ and $\mathrm{A_{5,m}}$ are also given in the Appendix A. These curve fits have been taken from [12].

The rates of each dissociation reaction is given by

$$\mathrm{R_c} = \sum_{\mathrm{m}=1}^{\mathrm{ns}} \left[-\mathrm{k_{f,c,m}} \frac{\rho_{\mathrm{r}}}{\mathrm{M_r}} \frac{\rho_{\mathrm{m}}}{\mathrm{M_m}} + \mathrm{k_{b,c,m}} \frac{\rho_{\mathrm{P1}}}{\mathrm{M_{P1}}} \frac{\rho_{\mathrm{P2}}}{\mathrm{M_{P2}}} \frac{\rho_{\mathrm{m}}}{\mathrm{M_m}} \right] \tag{2–52}$$

Here, c is the reaction number, m is the collison partner, r is the reactant and P_1 and P_2 are products. For exchange reactions, the rates can be written in following manner,

$$\mathrm{R_c} = -\mathrm{k_{f,c}} \frac{\rho_{\mathrm{r1}}}{\mathrm{M_{r1}}} \frac{\rho_{\mathrm{r2}}}{\mathrm{M_{r2}}} + \mathrm{k_{b,c}} \frac{\rho_{\mathrm{P1}}}{\mathrm{M_{P1}}} \frac{\rho_{\mathrm{P2}}}{\mathrm{M_{P2}}} \tag{2–53}$$

Finally the reaction rates of all species can be combined, to give production rates of all species, as follows,

$$\omega_{\mathrm{O_2}} = \mathrm{M_{O_2}} \left(\mathrm{R_2} - \mathrm{R_5} \right) \tag{2–54}$$

$$\omega_{\mathrm{NO}} = \mathrm{M_{NO}} \left(\mathrm{R_3} - \mathrm{R_4} + \mathrm{R_5} \right) \tag{2–55}$$

$$\omega_{\mathrm{N}} = \mathrm{M_N} \left(-2\mathrm{R_1} - \mathrm{R_3} - \mathrm{R_4} - \mathrm{R_5} \right) \tag{2–56}$$

$$\omega_{\mathrm{O}} = \mathrm{M_O} \left(-2\mathrm{R_2} - \mathrm{R_3} + \mathrm{R_4} + \mathrm{R_5} \right) \tag{2–57}$$

$$\omega_{\mathrm{N_2}} = \mathrm{M_{N_2}} \left(\mathrm{R_1} + \mathrm{R_4} \right) \tag{2–58}$$

2.3.5 Source Term for Vibrational Energy

Two terms in Eq. (2–23) that appear in the source term, S for the vibrational energy equation are respectively, $\sum_{\mathrm{s}} \omega_{\mathrm{s}} \hat{\mathrm{e}}_{\mathrm{v,s}}$, production and dissociation of polyatomic species that also affects total vibrational energy, and $\mathrm{Q_{T-V}}$, energy exchange between translational-rotational and vibrational modes of the gas. All different molecules are in vibrational equilibrium and thus a single vibrational temperature accounts for vibrational energy of all species. These exchange rates are combined into one single rate, $\mathrm{Q_{T-V}}$. Landau-Teller model is used and is given as follows,

$$\mathrm{Q_{T-V}} = \sum_{\mathrm{s}} \rho_{\mathrm{s}} \frac{\mathrm{e}^*_{\mathrm{vs}} - \mathrm{e_{vs}}}{\langle \tau_{\mathrm{s}} \rangle} \tag{2–59}$$

where $\mathrm{e}^{*}_{\mathrm{vs}}$ is the vibrational energy at thermal equilibrium $(\mathrm{T_v} = \mathrm{T})$ and $\langle \tau_{\mathrm{s}} \rangle$ is the molar averaged Landau-Teller relaxation time given by,

$$\langle \tau_{\mathrm{s}} \rangle = \frac{\sum_{\mathrm{r}=1}^{\mathrm{nd}} \mathrm{X_r}}{\sum_{\mathrm{r}=1}^{\mathrm{nd}} \frac{\mathrm{X_r}}{\tau_{\mathrm{sr}}}} \tag{2–60}$$

τ_{sr} is the Landau-Teller inter-species relaxation time given by Millikan and White (1953) [76],

$$\tau_{\mathrm{sr}} = \frac{101,325}{\mathrm{P}} \exp\left[\mathrm{A_{sr}}\left(\mathrm{T}^{-1/3} - 0.015\mu_{\mathrm{sr}}^{1/4}\right) - 18.42\right] \tag{2–61}$$

$$\mathrm{A_{sr}} = 1.16\mathrm{x}10^{-3}\mu_{\mathrm{sr}}^{1/2}\theta_{\mathrm{vs}}^{4/3} \tag{2–62}$$

$$\mu_{\mathrm{sr}} = \frac{\mathrm{M_s M_r}}{\mathrm{M_s} + \mathrm{M_r}} \tag{2–63}$$

2.4 Thermal Ablation

The governing equations for thermal ablation are taken from [16, 17] and are given as follows,

$$\frac{\partial \rho_{\mathrm{r}}}{\partial \mathrm{t}} = -\mathrm{R} \tag{2–64}$$

$$\frac{\partial \epsilon \rho_{\mathrm{g}}}{\partial \mathrm{t}} + \frac{\partial \epsilon \rho_{\mathrm{g}} \mathrm{u}}{\partial \mathrm{x}} = \mathrm{R} + \mathrm{D} \tag{2–65}$$

$$\frac{\partial \epsilon \rho_{\mathrm{g}} \mathrm{u}}{\partial \mathrm{t}} + \frac{\partial \epsilon \rho_{\mathrm{g}} \mathrm{u}^2 + \epsilon \mathrm{P}}{\partial \mathrm{x}} = -\epsilon \mathrm{f} + \mathrm{I} \tag{2–66}$$

$$\frac{\partial \rho_{\mathrm{c}} \mathrm{e_c} + \rho_{\mathrm{r}} \mathrm{e_r} + \epsilon \rho_{\mathrm{g}} \mathrm{e_g} + \frac{1}{2}\epsilon \rho_{\mathrm{g}} \mathrm{u}^2}{\partial \mathrm{t}} + \frac{\partial \epsilon \mathrm{u}\left(\rho_{\mathrm{g}} \mathrm{e_g} + \frac{1}{2}\rho_{\mathrm{g}} \mathrm{u}^2 + \mathrm{P}\right)}{\partial \mathrm{x}} = \frac{\partial}{\partial \mathrm{x}}\left(\mathrm{k}\frac{\partial \mathrm{T}}{\partial \mathrm{x}}\right) \tag{2–67}$$

First equation Eq. (2–67) describes the decomposition of resin material, second equation solves for conservation of mass for gas density, here ϵ is void fraction and is given by

$$\epsilon = \epsilon_{\max} - \frac{\rho_{\mathrm{r}}}{\rho_{\mathrm{p}}} \tag{2–68}$$

Here, $\epsilon_{\max}$ is the maximum void fraction that happens in the char state, and ρ_{p} is the intrinsic density of resin and both of their values are equal to 0.1788 and 1763.6 $\mathrm{kg/m^3}$ respectively. Term R appears in the gas and solid equations with opposite signs, indicating that resin decomposes to release the pyrolysis gas. Second term, D on right hand side of continuity equation is diffusion term that represents the rate of change of gas density due to the spatial variation of pressure, and is given by,

$$\mathrm{D} = \frac{\mathrm{K}}{\mu}\left(\epsilon\rho_{\mathrm{g}}\right)\frac{\partial^2 \mathrm{P}}{\partial \mathrm{x}^2} \tag{2–69}$$

Here, K is the permeability of gas, and μ is the gas viscosity. Momentum conservation for the gas describes that flow of gas is pressure driven. Here u is gas velocity and $\epsilon\rho_{\mathrm{g}}\mathrm{u}$ is the gas momentum. Since the gas is flowing through the porous media, the resistance to gas motion are given through f, friction and I, Inertia terms. These terms since they relate to pyrolysis gas motion in the ablating media are described in next section. Last equation solved for combined energy conservation of both solid (resin + char) and gas. $\mathrm{e_g}$, $\mathrm{e_c}$, and $\mathrm{e_r}$ are internal energies of the gas, char and resin material respectively. Terms $\mathrm{e_c}$ and $\mathrm{e_r}$ are evaluated using specific heats of both materials given in previous section. Eq. (2–71) gives the expressions for $\mathrm{e_c}$ and $\mathrm{e_r}$.

$$\mathrm{e_c} = \rho_{\mathrm{c}}\mathrm{Cp_c}\mathrm{T} \tag{2–70}$$

$$\mathrm{e_r} = \rho_{\mathrm{r}}\mathrm{Cp_r}\mathrm{T} + \rho_{\mathrm{r}}\mathrm{h_r^o} \tag{2–71}$$

Second term in energy equation is the derivative of the energy flux, similar to Euler equations, where the flux is decided by internal energy, kinetic energy and pressure

flow energy of gas. These terms were neglected in most thermal response codes since the gas was supposed to leave the material as soon as it was generated. Last term in energy equation is heat conduction within the material, through which we also apply net heat flux boundary condition at the surface.

CHAPTER 3
NUMERICAL METHODS

This chapter presents key ideas of DG formulation of all the terms presented in chapter 2. This will help us appreciate the numerical tool being used for this work, and also some very essential details for the numerics to be time and computational cost effective.

3.1 Why Discontinuous Galerkin?

In this work, we focus on the discontinuous Galerkin methods to solve all the problems. Several methods generally used for solving the computational fluid dynamics problems are finite difference, finite volume and finite element. There has been main focus on the use of finite difference and finite volume for problems of fluid flow. Even though finite element has a strong mathematical basis, its application to the fluid flow problems has rather been limited. Galerkin based finite element method, using same interpolation functions for both the test function and the solution vector, which are both continuous over the whole domain, is similar to a central difference method in its numerical properties. Thus it is very suitable for elliptic problems, like most problems in the solid mechanics, fluid flows with low Reynolds number and plasma. However, this method is not well suited for the high speed flow problems, which is a primary focus of this work.

Discontinuous Galerkin methods relax the requirement of solution continuity over the elements, and allows the solution to be piecewise continuous. This allows the problem within each element to be treated as a finite element domain in itself. Since the solution is discontinuous across the element′s faces, the fluxes are no longer uniquely defined on the element faces. This is similar to the case of finite volume method, and hence by extending the Riemann solvers, developed in the context of finite volume method, to the discontinuous Galerkin method, provides for the upwind mechanism in DG scheme. This provides an additional advantage for DG methods, that by increasing

the polynomial approximation within the element, high order accuracy can be achieved in the solution, without extending the stencil to more and more neighbor elements. This advantage specifically comes from finite element framework used for DG method.

With compact stencil, discontinuous Galerkin method is a very suitable candidate for high order accurate methods, since a compact stencil lends itself easily to convenient coding and parallel efficiency. These two advantages, however, come at the cost of increased computational resources required for discontinuous Galerkin method.

3.2 Inviscid Terms

Discontinuous Galerkin method was first applied to the first order systems, or inviscid systems. It was primarily brought into the field of research by Cockburn and Shu [57–61]. Later on, this method was applied to elliptic problems as well. In this section, we focus on describing implementation of DG methods to inviscid systems.

Inviscid terms as presented in Eq. (2–1), can be multiplied with the basis function, ϕ and integrated over the element domain, Ω ,

$$\int_{\Omega} \phi \left(\frac{\partial \mathrm{U}}{\partial \mathrm{t}} + \nabla \cdot \mathrm{F_i} \right) \mathrm{d}\Omega = 0 \tag{3–1}$$

Spatial integral term in Eq. (3–1) can be split into two by using integration by parts. Thus we get,

$$\int_{\Omega} \phi \frac{\partial \mathrm{U}}{\partial \mathrm{t}} \mathrm{d}\Omega - \int_{\Omega} \nabla \phi \cdot \mathrm{F_i} \mathrm{d}\Omega + \oint_{\partial\Omega} \phi \mathrm{F_i} \cdot \vec{\mathrm{n}} \mathrm{d}\sigma = 0 \tag{3–2}$$

In Eq. (3–2), $\partial\Omega$ denotes the boundary of the element's solution domain, Ω and $\vec{\mathrm{n}}$ is the outward going normal to the edge, $\mathrm{d}\sigma$.

We can split the whole domain, Ω into non-overlapping elements, E, consisting of lines in 1-D and quadrilaterals (linear or curvilinear) in 2-D.

$$\tau_{\mathrm{h}} = \mathrm{E} \tag{3–3}$$

Then, Eq. (3–2) can be written as follows,

$$\sum_{\mathrm{E}} \left[\int_{\mathrm{E}} \phi \frac{\partial \mathrm{U}}{\partial \mathrm{t}} \mathrm{d}\Omega - \int_{\mathrm{E}} \nabla \phi \cdot \mathrm{F_i} \mathrm{d}\Omega + \oint_{\partial \mathrm{E}} \phi \mathrm{F_i} \cdot \vec{\mathrm{n}} \mathrm{d}\sigma \right] = 0 \tag{3–4}$$

Here we choose the basis functions which are piecewise continuous within the element and discontinuous across the elements. These basis functions are given in Appendix B. The solution vector, U is also defined in terms of the same basis function, ϕ (Galerkin approach).

$$\mathrm{U} = \sum_{\mathrm{k}=0}^{\mathrm{p}} \phi_{\mathrm{k}} \mathrm{U}_{\mathrm{k}}^{\mathrm{h}} \tag{3–5}$$

Here, p denotes the polynomial order of approximation and ϕ_{k} and $\mathrm{U}_{\mathrm{k}}^{\mathrm{h}}$ denote k^{th} order basis functions and degrees of freedom respectively. For overall p degrees of freedom, we get (p+1)$^{\mathrm{th}}$ order of accuracy in DG method for inviscid terms.

Since the solution is discontinuous across element interfaces, we need numerical fluxes to uniquely define inviscid fluxes at the element interfaces. For our work, we use Local Lax-Friedrichs (LLF) solver [77] for the inviscid fluxes.

$$\mathrm{F_i} \cdot \vec{\mathrm{n}} = \mathrm{H}\left(\mathrm{U_n}, \mathrm{U_p}\right) = \frac{1}{2}\left(\mathrm{F_{in}} \cdot \vec{\mathrm{n}} + \mathrm{F_{ip}} \cdot \vec{\mathrm{n}} - \alpha\left(\mathrm{U_p} - \mathrm{U_n}\right)\right) \tag{3–6}$$

$\mathrm{U_n}$, $\mathrm{U_p}$ and $\mathrm{F_{in}}$, $\mathrm{F_{ip}}$ are respectively the solution vectors and inviscid fluxes belonging to the current element (n), being considered, and the neighboring element (p). $\vec{\mathrm{n}}$ is the normal pointing outside to a face of an element. α is the bigger of maximum

absolute eigenvalue of the jacobian matrices $\frac{\partial \mathrm{F_{i_n}}}{\partial \mathrm{U}}$ and $\frac{\partial \mathrm{F_{i_P}}}{\partial \mathrm{U}}$ evaluated at the face of an element.

As can be seen, for two neighboring elements, the normal to the common face is reversed in direction, and term $(\mathrm{U_p} - \mathrm{U_n})$ also changes sign. Hence, the numerical flux defined at the face of an element is conservative, i.e. the contribution is of opposite signs in the adjacent elements. This conserves the net flux going from one element into the neighboring one.

$$\mathrm{H_L}\left(\mathrm{U_n}, \mathrm{U_p}\right) = -\mathrm{H_R}\left(\mathrm{U_p}, \mathrm{U_n}\right) \tag{3–7}$$

α for both the elements retains same positive value, which is equivalent to the speed of wave propagation.

3.3 Viscous Terms

For the second order derivative terms, which are the viscous terms in Navier-Stokes equations, we present the numerical methodology in this section. Since, discontinuous Galerkin method was primarily developed for the first order systems, a common approach is to define an auxiliary variable for the second order derivative term. This gives rise to an additional auxiliary equation in addition to already existing governing equations. E.g., a discontinuous Galerkin formulation for 2-D Navier Stokes with 4 governing equations gives rise to 6 additional equations for x and y derivatives of x and y velocities and temperature, numbering a total of 10 equations.

Consider Eq. (2–6) in previous chapter,

$$\frac{\partial \mathrm{U}}{\partial \mathrm{t}} + \nabla \cdot \mathrm{F_i} = \nabla \cdot \mathrm{F_v}$$

$\mathrm{F_v} = \mathrm{F_v}\left(\mathrm{U}, \nabla \mathrm{U}\right)$ is the viscous flux term. Here, $\nabla \mathrm{U}$ can be replaced by auxiliary variable, θ, giving rise to the auxiliary equation,

$$\theta = \nabla \mathrm{U} \tag{3–8}$$

So, now Eq. (3–8) will be solved along with Eq. (2–6). Again as in above section, we multiply both these equations with the basis function, ϕ and again apply integration by parts to both the inviscid and viscous flux terms. We thus get,

$$\int_{\Omega} \phi \frac{\partial \mathrm{U}}{\partial \mathrm{t}} \mathrm{d}\Omega - \int_{\Omega} \nabla \phi \cdot \mathrm{F_i} \mathrm{d}\Omega + \oint_{\partial\Omega} \phi \mathrm{F_i} \cdot \vec{\mathrm{n}} \mathrm{d}\sigma - \int_{\Omega} \nabla \phi \cdot \mathrm{F_v} \mathrm{d}\Omega + \oint_{\partial\Omega} \phi \mathrm{F_v} \cdot \vec{\mathrm{n}} \mathrm{d}\sigma = 0 \tag{3–9}$$

Since we already dealt with the inviscid terms in the previous section, we only focus on the viscous terms. Viscous flux vector in the surface integral term is not uniquely defined on the element interface, therefore we define numerical flux which is the average of fluxes from both sides of the element's interface.

$$\mathrm{H_v} = \mathrm{F_v} \cdot \vec{\mathrm{n}} = \frac{\left(\mathrm{F_v^-}\left(\mathrm{U^-}, \theta^-\right) + \mathrm{F_v^+}\left(\mathrm{U^+}, \theta^+\right)\right) \cdot \vec{\mathrm{n}}}{2} \tag{3–10}$$

$\mathrm{F_v^-}$ and $\mathrm{F_v^+}$ belong to the current element and the neighboring element respectively. In a similar fashion, we also formulate the weak form of Eq. (3–8) by multiplying with basis function, ϕ, applying integration by parts and central averaging for the numerical flux.

$$\int_{\Omega} \phi \theta \mathrm{d}\Omega + \int_{\Omega} \nabla \phi \cdot \mathrm{U} \mathrm{d}\Omega - \oint_{\partial\Omega} \phi \mathrm{U} \cdot \vec{\mathrm{n}} \mathrm{d}\sigma = 0 \tag{3–11}$$

Numerical flux for the surface integral term will be averaged from both sides of the element,

$$\mathrm{U} \cdot \vec{\mathrm{n}} = \frac{\mathrm{U}^{-} + \mathrm{U}^{+}}{2} \tag{3–12}$$

This scheme in the literature is known as BR1 method and was first implemented by Bassi $\&$ Rebay [62]. This is a very simple and convenient method to use and implement, however it is computationally very intensive, due to extra auxiliary equations being solved. This increases the size of the matrix, to be solved for an implicit method, and hence hampers its speed considerably.

There are two ways to solve BR1 method in an implicit fashion. First is to solve the auxiliary equation in a coupled fashion along with the solution vector, U. This approach is computationally intensive, as already discussed, due to the size of the matrix. Other faster alternative is to first explicitly solve for the degrees of freedom of auxiliary variable, θ, in terms of U at a given time step and then substitute that in Eq. (3–9), so that U is then explicitly dependent on itself only and not on θ.

As can be seen from Eq. (3–11) and above equation, θ of the current element depends on U from current element as well as its neighbors.

$$\theta = \theta\left(\mathrm{U}^{-}, \mathrm{U}^{+}\right) \tag{3–13}$$

Through above relation and Eq. (3–9), we can see that since U is connected to θ of the immediate neighbors, it is also connected to U of neighbors′ neighbors. Hence the coupling in BR1 scheme is not compact, i.e. it extends beyond just the immediate neighbors. This has its ramifications on second alternative to BR1 discussed above to make the method faster. Second method (for implicit treatment), although with smaller matrix consisting only of the original governing equations, is more complicated to code because of extended stencil. This complication is discussed with more illustration in the following section.

The limitation to second method of BR1 for faster implementation is actually overcome by another method, also introduced by Bassi & Rebay, [62] called BR2 method.

3.3.1 BR1 vs BR2

In this section, we first discuss implementation of second alternative to solve BR1 method faster (presented above), followed by BR2 method.

For second alternative to solve BR1 method faster, we first express θ in terms of U, using the weak form of the auxiliary equation, Eq. (3–11), which can be modified using the following expression (from [62]),

$$\mathrm{U} \cdot \vec{\mathrm{n}} = \left(\frac{\mathrm{U}^- + \mathrm{U}^+}{2} \right) \cdot \vec{\mathrm{n}} = \left(\frac{\mathrm{U}^+ - \mathrm{U}^-}{2} \right) \cdot \vec{\mathrm{n}} + \mathrm{U}^- \cdot \vec{\mathrm{n}} \tag{3–14}$$

Substitute this expression in Eq. (3–11), we get

$$\int_\Omega \phi\theta \mathrm{d}\Omega + \int_\Omega \nabla\phi \cdot \mathrm{U} \mathrm{d}\Omega - \oint_{\partial\Omega} \phi \left(\frac{\mathrm{U}^+ - \mathrm{U}^-}{2} + \mathrm{U}^- \right) \cdot \vec{\mathrm{n}} \mathrm{d}\sigma = 0 \tag{3–15}$$

$$\int_\Omega \phi\theta \mathrm{d}\Omega + \int_\Omega \nabla\phi \cdot \mathrm{U} \mathrm{d}\Omega - \oint_{\partial\Omega} \phi \mathrm{U}^- \cdot \vec{\mathrm{n}} \mathrm{d}\sigma - \oint_{\partial\Omega} \phi \left(\frac{\mathrm{U}^+ - \mathrm{U}^-}{2} \right) \cdot \vec{\mathrm{n}} \mathrm{d}\sigma = 0 \tag{3–16}$$

First surface integral term can be combined with second domain integral term,

$$\int_\Omega \phi\theta \mathrm{d}\Omega - \int_\Omega \phi \cdot \nabla \mathrm{U} \mathrm{d}\Omega - \oint_{\partial\Omega} \phi \left(\frac{\mathrm{U}^+ - \mathrm{U}^-}{2} \right) \cdot \vec{\mathrm{n}} \mathrm{d}\sigma = 0 \tag{3–17}$$

$$\int_\Omega \phi\theta \mathrm{d}\Omega = \int_\Omega \phi \cdot \nabla \mathrm{U} \mathrm{d}\Omega + \oint_{\partial\Omega} \phi \left(\frac{\mathrm{U}^+ - \mathrm{U}^-}{2} \right) \cdot \vec{\mathrm{n}} \mathrm{d}\sigma \tag{3–18}$$

To speed up the BR1 method, the above equation can be solved for θ explicitly within every element. More specifically, we can express degrees of freedom of θ in terms of degrees of freedom of U.

Let, θ be defined using same basis functions as for U,

$$\theta = \phi^{\mathrm{T}} \{\theta\} \tag{3–19}$$

Then Eq. (3–18) becomes,

$$\left[\int_{\Omega} \phi\phi^{\mathrm{T}} \mathrm{d}\Omega\right] \{\theta\} = \left[\int_{\Omega} \phi \cdot \nabla\phi^{\mathrm{T}} \mathrm{d}\Omega\right] \{\mathrm{U}\} + \left[\oint_{\partial\Omega} \frac{\phi\phi^{+\mathrm{T}}}{2} \vec{\mathrm{n}} \mathrm{d}\sigma\right] \{\mathrm{U}\}_{\mathrm{nb}} - \left[\oint_{\partial\Omega} \frac{\phi\phi^{\mathrm{T}}}{2} \vec{\mathrm{n}} \mathrm{d}\sigma\right] \{\mathrm{U}\} \tag{3–20}$$

So in above, degrees of freedom of θ are expressed in terms of degrees of freedom of U. This is useful in finding θ and also for finding the derivative of θ w.r.t. U, which shall be useful for implicit methods later on.

Another important point with regards to saving some computational time, is to find θ as derivative of conservative variable rather than primitive variable. This way all the integrals in above equation, are constants throughout whole computation (for a given mesh) and not dependent on the solution, U. This advantage is not available if we choose θ as derivative of primitive variable.

This advantage adds on for implicit methods, since the jacobian matrices are also constant, and hence will not need to be re-evaluated, therefore saving computational time. The derivative of $\{\theta\}$ w.r.t. $\{\mathrm{U}\}$ (of current element) is given as,

$$\left[\int_{\Omega} \phi\phi^{\mathrm{T}} \mathrm{d}\Omega\right] \frac{\partial \{\theta\}}{\partial \{\mathrm{U}\}} = \left[\int_{\Omega} \phi \cdot \nabla\phi^{\mathrm{T}} \mathrm{d}\Omega\right] - \left[\oint_{\partial\Omega} \frac{\phi\phi^{\mathrm{T}}}{2} \vec{\mathrm{n}} \mathrm{d}\sigma\right] \tag{3–21}$$

and the derivative of $\{\theta\}$ w.r.t. $\{\mathrm{U}\}_{\mathrm{nb}}$ (of neighboring element) is given as,

$$\left[\int_{\Omega} \phi\phi^{\mathrm{T}} \mathrm{d}\Omega\right] \frac{\partial\{\theta\}}{\partial\{\mathrm{U}\}_{\mathrm{nb}}} = \left[\oint_{\partial\Omega} \frac{\phi\phi_{\mathrm{nb}}^{\mathrm{T}}}{2} \vec{\mathrm{n}} \mathrm{d}\sigma\right] \tag{3–22}$$

The disadvantage of faster version of BR1 method is that the matrix is no more compact (see section for implicit time integration 3.5.2 for more detail). This complicates the implementation of this method. The alternative to this is BR2 method. Original formulation of BR2 method is exactly same as the BR1 method just discussed. This was used in our code to debug implementation of BR2 method by comparing it to BR1 method. Both should perform exactly same, since the BR2 in its original formulation is derived from BR1 scheme. After this, other variations were introduced later on, to improve the performance of BR2 method and also to make it a compact scheme.

3.3.2 Original Formulation of BR2

Taken from [62], BR2 formulation defines θ being equal to (from Eq. (3–18)) a sum of $\nabla \mathrm{U}$ and a correction factor, $\mathrm{r_h}$,

$$\theta = \nabla \mathrm{U} + \mathrm{R_h} \tag{3–23}$$

where, $\mathrm{R_h}$ is defined by,

$$\int_{\Omega} \phi \mathrm{R_h} \mathrm{d}\Omega = \oint_{\partial\Omega} \phi \left(\frac{\mathrm{U}^{+} - \mathrm{U}^{-}}{2}\right) \vec{\mathrm{n}} \mathrm{d}\sigma \tag{3–24}$$

The way to solve for $\mathrm{R_h}$ from above equation is to express $\mathrm{R_h}$ again in terms of basis function, ϕ and degrees of freedom of $\mathrm{R_h}$,

$$\mathrm{R_h} = \phi^{\mathrm{T}} \{\mathrm{R_h}\} \tag{3–25}$$

Substituting above in Eq. (3–24),

$$\left[\int_{\Omega}\phi\phi^{\mathrm{T}}\mathrm{d}\Omega\right]\{\mathrm{R_h}\}=\left[\oint_{\partial\Omega}\frac{\phi\phi_{\mathrm{nb}}^{\mathrm{T}}}{2}\vec{\mathrm{n}}\mathrm{d}\sigma\right]\{\mathrm{U}\}_{\mathrm{nb}}-\left[\oint_{\partial\Omega}\frac{\phi\phi^{\mathrm{T}}}{2}\vec{\mathrm{n}}\mathrm{d}\sigma\right]\{\mathrm{U}\}\tag{3–26}$$

So, in the original formulation of BR2, $\mathrm{R_h}$ is defined for every element, and right hand side being the surface integral is summed over all the edges of the element. This $\mathrm{R_h}$ is then input in Eq. (3–9) in following fashion (excluding inviscid terms for space),

$$\int_{\Omega}\phi\frac{\partial\mathrm{U}}{\partial\mathrm{t}}\mathrm{d}\Omega-\int_{\Omega}\nabla\phi\cdot\mathrm{F_v}\left(\mathrm{U_h},\nabla\mathrm{U_h},\mathrm{R_h}\right)\mathrm{d}\Omega+\oint_{\partial\Omega}\phi\mathrm{F_v}\left(\mathrm{U_h},\mathrm{U_h^{nb}},\nabla\mathrm{U_h},\nabla\mathrm{U_h^{nb}},\mathrm{R_h},\mathrm{R_h^{nb}}\right)\cdot\vec{\mathrm{n}}\mathrm{d}\sigma=0\tag{3–27}$$

It is easily seen from above that an implicit method for Eq. (3–27) will need derivatives w.r.t. $\{\mathrm{U}\}$ from neighbors′ neighbors as well, just as in faster version of BR1 method. This is because, $\mathrm{R_h^{nb}}$ depends on the immediate neighbors of the neighbor of current element.

This is the problem with the original formulation of BR2 method. It also does not reduce the jumps in the solution, in between the elements, as shown in the next chapter. Solution to this problem comes, by replacing the global correction factor, $\mathrm{R_h}$ in the surface integrals in Eq. (3–27), with local correction factors, $\mathrm{r_h}$, which are defined only on their respective edges, i.e.,

$$\left[\int_{\Omega}\phi\phi^{\mathrm{T}}\mathrm{d}\Omega\right]\{\mathrm{r_h}\}=\left[\oint_{\partial\Omega}\frac{\phi\phi_{\mathrm{nb}}^{\mathrm{T}}}{2}\vec{\mathrm{n}}\mathrm{d}\sigma\right]\{\mathrm{U}\}_{\mathrm{nb}}-\left[\oint_{\partial\Omega}\frac{\phi\phi^{\mathrm{T}}}{2}\vec{\mathrm{n}}\mathrm{d}\sigma\right]\{\mathrm{U}\}\tag{3–28}$$

In the above definition, the surface integrals are not circular integrals, but line integrals on one edge at a time. There is local $\mathrm{r_h}$ defined for every edge, rather than one global $\mathrm{R_h}$ for all the edges. Hence, $\mathrm{r_h}$ for a particular edge depends only on the current element and its immediate neighbor sharing the concerned edge, whereas $\mathrm{R_h}$ depends

on current element and all its immediate neighbors. This way, first variation of BR2 can be written as,

$$\int_{\Omega} \phi \frac{\partial \mathrm{U}}{\partial \mathrm{t}} \mathrm{d}\Omega - \int_{\Omega} \nabla \phi \cdot \mathrm{F_v}\left(\mathrm{U_h}, \nabla \mathrm{U_h}, \mathrm{R_h}\right) \mathrm{d}\Omega \tag{3–29}$$

$$+ \oint_{\partial\Omega} \phi \mathrm{F_v}\left(\mathrm{U_h}, \mathrm{U_h^{nb}}, \nabla \mathrm{U_h}, \nabla \mathrm{U_h^{nb}}, \mathrm{r_h}, \mathrm{r_h^{nb}}\right) \cdot \vec{\mathrm{n}} \mathrm{d}\sigma = 0 \tag{3–30}$$

The main advantage is that the above scheme is compact, depending on current element and its immediate neighbors only. This scheme is also more stable and it reduces the jumps in the solution between the elements. As done for BR1 method, we can also define derivatives of $\{\mathrm{r_h}\}$ w.r.t. $\{\mathrm{U}\}$ and $\{\mathrm{U}\}_{\mathrm{nb}}$ respectively,

$$\left[\int_{\Omega} \phi \phi^{\mathrm{T}} \mathrm{d}\Omega\right] \frac{\partial \{\mathrm{r_h}\}}{\partial \{\mathrm{U}\}} = -\left[\oint_{\partial\Omega} \frac{\phi \phi^{\mathrm{T}}}{2} \vec{\mathrm{n}} \mathrm{d}\sigma\right] \tag{3–31}$$

$$\left[\int_{\Omega} \phi \phi^{\mathrm{T}} \mathrm{d}\Omega\right] \frac{\partial \{\mathrm{r_h}\}}{\partial \{\mathrm{U}\}_{\mathrm{nb}}} = \left[\oint_{\partial\Omega} \frac{\phi \phi_{\mathrm{nb}}^{\mathrm{T}}}{2} \vec{\mathrm{n}} \mathrm{d}\sigma\right] \tag{3–32}$$

3.4 Source Terms

For hypersonic flow, we have source terms corresponding to both chemical and thermal non-equilibrium. We can treat these source terms, with a source vector, S as in Eq. (2–22). Multiplying this equation with the basis function, ϕ and integrating over the element domain, we get (ignoring inviscid and viscous flux terms, which were discussed in previous two sections),

$$\int_{\Omega} \phi \frac{\partial \mathrm{U}}{\partial \mathrm{t}} \mathrm{d}\Omega = \int_{\Omega} \phi \mathrm{S} \mathrm{d}\Omega \tag{3–33}$$

For the problems we are dealing with, S is a function of U alone, hence its implementation is straightforward for our work.

3.5 Time Integration

We have already discussed the spatial discretization for all the spatial terms in Eq. (2–22). Now, we present the time discretization for the unsteady term in Eq. (2–22). We have considered two approaches in this work, namely explicit and implicit time integrations methods.

3.5.1 Explicit Time Integration

For explicit time integration, first order accurate forward Euler method is used,

$$\left[\int_{\Omega} \phi\phi^{\mathrm{T}} \mathrm{d}\Omega\right] \frac{\partial \{\mathrm{U}\}}{\partial \mathrm{t}} = \left[\int_{\Omega} \phi\phi^{\mathrm{T}} \mathrm{d}\Omega\right] \left(\frac{\left(\{\mathrm{U}\}^{\mathrm{n+1}} - \{\mathrm{U}\}^{\mathrm{n}}\right)}{\Delta \mathrm{t}} + \mathrm{O}\left(\Delta \mathrm{t}\right)\right) = \mathrm{R}\left(\{\mathrm{U}\}^{\mathrm{n}}\right) \quad \text{(3–34)}$$

Here, $\mathrm{R}\left(\{\mathrm{U}\}^{\mathrm{n}}\right)$ denotes all the spatial terms moved to the right hand side of Eq. (2–22). For explicit method, $\mathrm{R}\left(\{\mathrm{U}\}^{\mathrm{n}}\right)$ is known at previous time step, t^{n}, and hence solution procedure for explicit method is very easy and straightforward. Inviscid methods however, face time step restriction with CFL number restricted to $\frac{1}{2\mathrm{p}+1}$, where p is the polynomial order of the basis function [60]. Thus, for a fine mesh and higher order accuracy, the time step will be restricted for the explicit method for the inviscid terms.

Source terms, as in the chemistry terms in the hypersonic flows with thermo-chemical non-equilibrium, add on to the CFL time step restriction, which can be even more severe than the inviscid CFL restriction. This can be resolved by treating the source terms implicitly and the inviscid and the viscous terms explicitly.

For example, for one of the hypersonic flow problems over the cylinder (with M = 17.65), CFL was restricted to 0.005, with both thermal and chemical non-equilibrium on and a complete explicit method. However, with implicit treatment of only the source terms, we were able to come up to an inviscid time step restriction with CFL number of 0.5. As another example of the importance of implicit time integration methods, for the hypersonic and thermal ablation problems, $\Delta \mathrm{t}$ was restricted, for the thermal ablation problem, to 10^{-8} sec with an explicit method, however with a fully implicit method, we

were able to run the code at a time step of $10^{-3} - 10^{-2}$ sec. Total solution time for the thermal ablation problems can be typically few seconds and the presence of high source terms (for dealing with unsteady momentum equation of pyrolysis gas), makes explicit method very restrictive in its application. Implicit methods are thus very useful for the problems of our interest, namely thermal ablation and hypersonic flows.

3.5.2 Implicit Time Integration

Implicit methods overcome the severe time step restriction, by evaluating R at a current time step, i.e. $\mathrm{R}\left(\{\mathrm{U}\}^{\mathrm{n+1}}\right)$. Thus, the scheme can be written as,

$$\left[\int_{\Omega} \phi\phi^{\mathrm{T}} \mathrm{d}\Omega\right] \frac{\partial \{\mathrm{U}\}}{\partial \mathrm{t}} = \left[\int_{\Omega} \phi\phi^{\mathrm{T}} \mathrm{d}\Omega\right] \left(\frac{\left(\{\mathrm{U}\}^{\mathrm{n+1}} - \{\mathrm{U}\}^{\mathrm{n}}\right)}{\Delta \mathrm{t}} + \mathrm{O}\left(\Delta \mathrm{t}\right)\right) = \mathrm{R}\left(\{\mathrm{U}\}^{\mathrm{n+1}}\right)) \tag{3–35}$$

Since the above problem is non-linear, we need to use Newton method to obtain the solution of above equation system. With the Newton method, we want to drive $\mathrm{F}\left(\{\mathrm{U}\}^{\mathrm{n+1}}, \{\mathrm{U}\}^{\mathrm{n}}\right)$ in Eq. (3–36) to zero,

$$\mathrm{F}\left(\{\mathrm{U}\}^{\mathrm{n+1}}, \{\mathrm{U}\}^{\mathrm{n}}\right) = \left[\int_{\Omega} \phi\phi^{\mathrm{T}} \mathrm{d}\Omega\right] \left(\frac{\left(\{\mathrm{U}\}^{\mathrm{n+1}} - \{\mathrm{U}\}^{\mathrm{n}}\right)}{\Delta \mathrm{t}}\right) - \mathrm{R}\left(\{\mathrm{U}\}^{\mathrm{n+1}}\right) = 0 \tag{3–36}$$

For this, we need to evaluate jacobian matrices of $\mathrm{F}\left(\{\mathrm{U}\}^{\mathrm{n+1}}, \{\mathrm{U}\}^{\mathrm{n}}\right)$ w. r. t. $\{\mathrm{U}\}^{\mathrm{n+1}}$,

$$\mathrm{J}\left(\{\mathrm{U}\}^{\mathrm{n+1}}, \{\mathrm{U}\}^{\mathrm{n}}\right) = \frac{\partial \mathrm{F}\left(\{\mathrm{U}\}^{\mathrm{n+1}}, \{\mathrm{U}\}^{\mathrm{n}}\right)}{\partial\left(\{\mathrm{U}\}^{\mathrm{n+1}}\right)} = \frac{\left[\int_{\Omega} \phi\phi^{\mathrm{T}} \mathrm{d}\Omega\right]}{\Delta \mathrm{t}} - \frac{\partial \mathrm{R}\left(\{\mathrm{U}\}^{\mathrm{n+1}}\right)}{\partial \{\mathrm{U}\}^{\mathrm{n+1}}} \tag{3–37}$$

The term, $\frac{\partial \mathrm{R}\left(\{\mathrm{U}\}^{\mathrm{n+1}}\right)}{\partial \{\mathrm{U}\}^{\mathrm{n+1}}}$ includes derivative of all the terms, inviscid, viscous and source term w.r.t $\{\mathrm{U}\}^{\mathrm{n+1}}$. These derivatives include terms on domain and element interfaces. An element interface can either be inside the domain or on the boundary. In either case, finding the jacobians for all terms is a non-trivial task, and requires lot of careful

attention for the Jacobian matrices to work correctly for a good performance of the implicit method.

After finding this jacobian, J, the solution can be iterated for by finding the change in the solution vector, $\{\delta \mathrm{U}\}^{\mathrm{n+1,p}}$ at the $\mathrm{p^{th}}$ iteration of the $(\mathrm{n}+1)^{\mathrm{th}}$ timestep,

$$\left[\mathrm{J}\left(\{\mathrm{U}\}^{\mathrm{n+1,p}},\{\mathrm{U}\}^{\mathrm{n}}\right)\right]\{\delta \mathrm{U}\}^{\mathrm{n+1,p}} = -\mathrm{F}\left(\{\mathrm{U}\}^{\mathrm{n+1,p}},\{\mathrm{U}\}^{\mathrm{n}}\right) \tag{3–38}$$

At every iteration, this change is added to the initial guess $(\mathrm{p}=0)$ for $\{\mathrm{U}\}^{\mathrm{n+1}}$, which is set equal to solution from previous timestep,

$$\{\mathrm{U}\}^{\mathrm{n+1,0}} = \{\mathrm{U}\}^{\mathrm{n}} \tag{3–39}$$

$$\{\mathrm{U}\}^{\mathrm{n+1,p}} = \{\mathrm{U}\}^{\mathrm{n+1,p-1}} + \{\delta \mathrm{U}\}^{\mathrm{n+1,p}}, \qquad \mathrm{p} \geq 1 \tag{3–40}$$

3.6 Parallelization

For solution with a single processor, we use a serial-processor ILU-preconditioned GMRES solver. This is a very robust solver, for almost all the problems we have worked with in our lab including plasma, high speed fluid flow, hypersonic flow and thermal ablation. As an example, let us consider double Mach reflection (DMR) problem solved using 1 processor GMRES.

Table 3-1. Time taken for 1 processor GMRES for Double Mach Reflection

Mesh Details	Time for forming matrix (sec)	Time for solving global matrix, using 1 processor GMRES (sec)
330 X 100	18	62
660 X 200	72	242

As we see in Table 3-1, MIG takes large time to solve for one iteration. For convergence in 5 iterations/time-step, and a time-step value of of 10^{-3} sec for a total solution time of 0.2 sec, the program runs nearly 1000 iterations to give the final solution. This results in 22 hours run time for mesh 1 (330 $\times$ 100) and 3.6 days for mesh

2 (660×200). This necessitates the need for parallelization, which saves tremendous amount of time with more number of processors.

There are two components of the code, as shown in 3-1, that need parallelization. First part of the code assembles the global matrix and the second part solves the global system.

For the parallelization of the assembly of the global matrix, we have implemented domain decomposition. Herein, the total number of elements are divided almost equally amongst the total number of processors. This distribution is done based on element numbers. Thus, each processor forms only its own part of the global matrix. Currently to avoid any communication between the processors during the assembly part, we make complete domain′ solution available to all the processors. This way, even the terms, which come from jacobian of the flux terms w. r. t. the elements from other processors, are formed by the processors without any need of communication from other processors.

Price is paid, however, at the end of the solution process, when the solution values are passed from all processors to processor with rank zero, and then broadcasted from processor with rank zero to the rest of the processors. Time taken in this step can become a bottleneck for larger problems, and hence will need attention in future.

For solution process, we use HYPRE [78], a high performance parallel solver, to solve the matrix in parallel. Two methods have been implemented into MIG from HYPRE, DS (Diagonal scaling) + BiCGStab and Euclid (ILU preconditioner) + GMRES. Since the matrices for high speed flow problems and thermal ablation can be highly ill conditioned, hence a good preconditioner is required along with the use of Krylov iterative solvers. Curves for the performance of the solver, in terms of the time taken vs. the number of processors for two meshes containing 2780 and 33,000 elements (used for double Mach reflection problem) respectively are shown below.

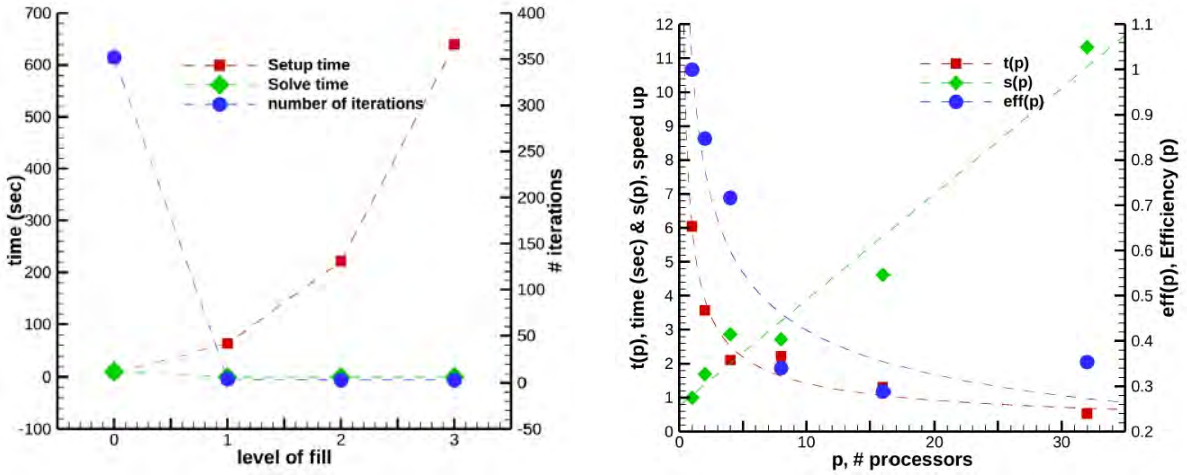

A B

Figure 3-1. A) Performance plot of Euclid + GMRES for 2780 elements with different levels of fill for ILU preconditioner. B) Performance plot with 0 level of fill showing linear speed up.

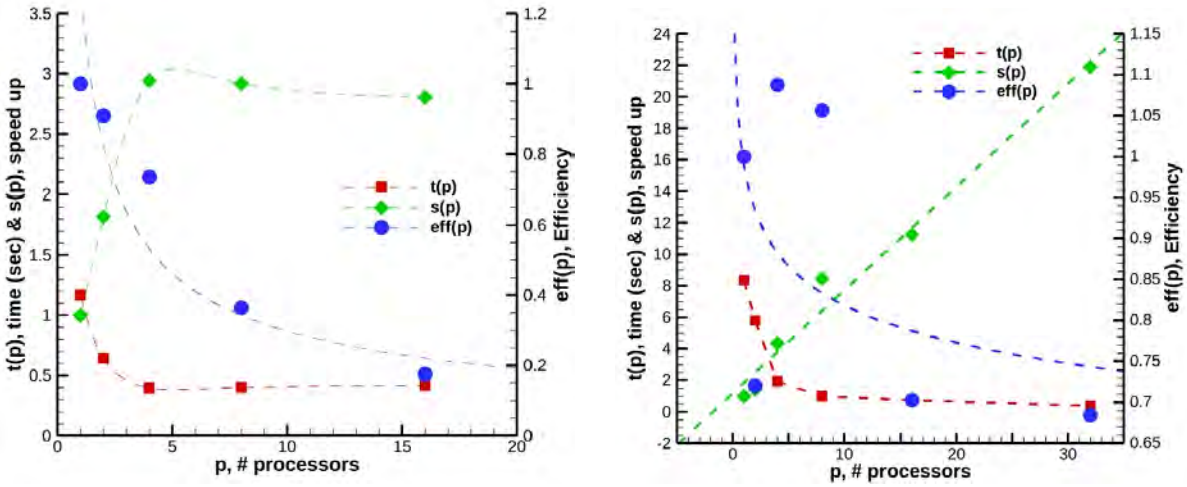

A B

Figure 3-2. A) Performance plot of DS + BiCGStab for 2780 elements with different number of processors. B) Performance plot of DS + BiCGStab for 33000 elements with linear speed up.

Fig. (3-1) A) shows performance plot of Euclid + GMRES for 2780 elements with different levels of fill for ILU preconditioner. Matrix size is 66,720 $\times$ 66,720. It can be seen that although level of fill $'0'$ takes lowest setup time (for ILU factorization), it also takes the largest number of iterations in solving the preconditioned system. This is probably due to ineffective factorization at the $'0'$ level. This results in 6 sec solve time, which is very significant, given the smaller size of the matrix. With increase in level of fill, setup time increases tremendously hence making this method impractical for our use.

Fig. (3-1) B) shows the performance plot of Euclid + GMRES for 2780 elements with 0 level of fill. We can see linear speed up (green curve). Use of 32 processors results in approximately 10 times speed up in comparison to 1 processor performance.

More useful method, so far for our purpose, has been DS + BiCGStab, another solver available in HYPRE. Fig. (3-2) shows performance plot of this method with different number of processors for A) 2780 elements and B) 33000 elements respectively. Matrices for these cases are of size (66,720 $\times$ 66,720) and (792000 $\times$ 792000) respectively. We notice saturation of speed up at a value of 3 for case A) for number of processors being more than 4. However DS + BiCGStab shows a promising performance with 33000 elements. Speed up is linear w. r. t. number of processors and a total 21 times speedup is achieved with 32 processors. Hence the performance improves with larger number of elements in the domain, which makes sense, since smaller number of elements will reach saturation faster.

3.7 r-p Adaptive Methods

Hypersonic flows have shocks which need to be captured with a given numerical method. Presence of the shocks is challenging for any high-order accurate method, since presence of shock like discontinuities leads to Gibbs oscillations. Naturally, amount of dissipation present in high order method is not sufficient to curtail these spurious oscillations. Therefore, a strategy is required for capturing the shock. Approaches, in the literature, used for capturing the shocks focus primarily on methods

of artificial dissipation [2, 79] and slope limiters [59]. However, we focus on a different approach in this work.

This method is called p-adaptivity and was first used in [10]. Since, it is well know that p = 0 (corresponding to first order accurate method) is sufficient to capture shock of any strength. So using an effective shock indicator technique, we can use p = 0 in the shock regions and higher order polynomial accuracy (p $\geq$ 1) in smooth flow regions. This approach avoids any use of slope limiters or artificial dissipation along with their complexities, and is thus more useful and convenient to use, especially in the case of DG methods. So far, this has been applied to only inviscid hypersonic flows [10], but in this work we further explore its application to viscous and thermo-chemical nonequilibrium hypersonic flows.

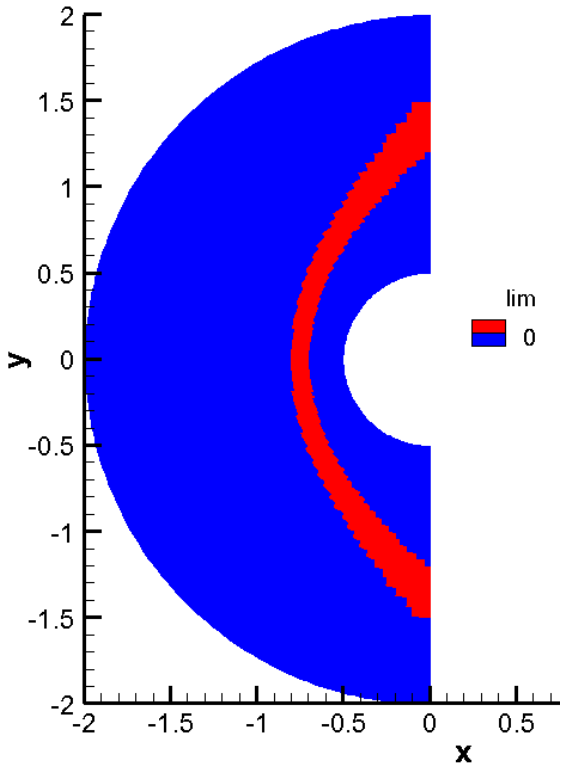

Figure 3-3. Use of shock indicator defined by Eq. (3–41) to identify shock region (shown in red) from smooth flow regions (shown in blue). This is an example of using p-adaptivity to capture shocks for inviscid hypersonic flow over cylinder with M = 17. As can be seen the shock indicator is very effective.

Shock indicator that's used in this work [10] is given as,

$$\mathrm{s_k} = \log_{10}\left(\frac{1}{|\partial\Omega_\mathrm{k}|}\int_{\partial\Omega_\mathrm{k}}\left|\frac{[\mathrm{P_h}]\cdot\vec{\mathrm{n}}}{\{\mathrm{P_h}\}}\right|\mathrm{ds}\right) \tag{3–41}$$

$[\mathrm{P_h}]$ in Eq. (3–41) denotes the jump in the pressure across the edges of an element, Ω_k, and $\{\mathrm{P_h}\}$ denotes the average of pressure across the edge. $\mathrm{s_k}$ is evaluated for all the elements in the domain, and the following criteria is used to identify the regions of the shock from the smooth flow regions,

$$\begin{cases} \mathrm{s_k} > 0.3, \quad \mathrm{p} = 0 \quad (\mathrm{shock} \quad \mathrm{region}) \\ \mathrm{s_k} < 0.3, \quad \mathrm{p} \geq 1 \quad (\mathrm{smooth} \quad \mathrm{flow} \quad \mathrm{region}) \end{cases} \tag{3–42}$$

This shock indicator is very effective in identifying regions of shock from smooth flow regions. This can be used for transient problems, where the location of shock may change with time or problems where hypersonic flow develops beginning with a uniform flow solution to steady state solution e.g., around a cylinder. A switch, 'lim' is used to identify shock regions, and an example is shown below for hypersonic flow around a cylinder. p = 0 is red regions indicating shock and $\mathrm{p} \geq 1$ is used in blue regions indicating smooth flow regions.

Solution accuracy in smooth flow regions can be improved by increasing the order of polynomial approximation, p in those regions, without changing the mesh resolution there. This is the advantage afforded by DG method. But, the shock region is limited to p = 0 and hence first order accuracy only. Only possibility to improve solution accuracy in shock region is to refine the mesh there. One approach taken in [10] is applying h-refinement in shock regions. This improves solution accuracy in shock regions. However, this also results in large number of elements in the region around the shock, which may not lie in the shock. For this purpose, we use r-adaptivity approach, where

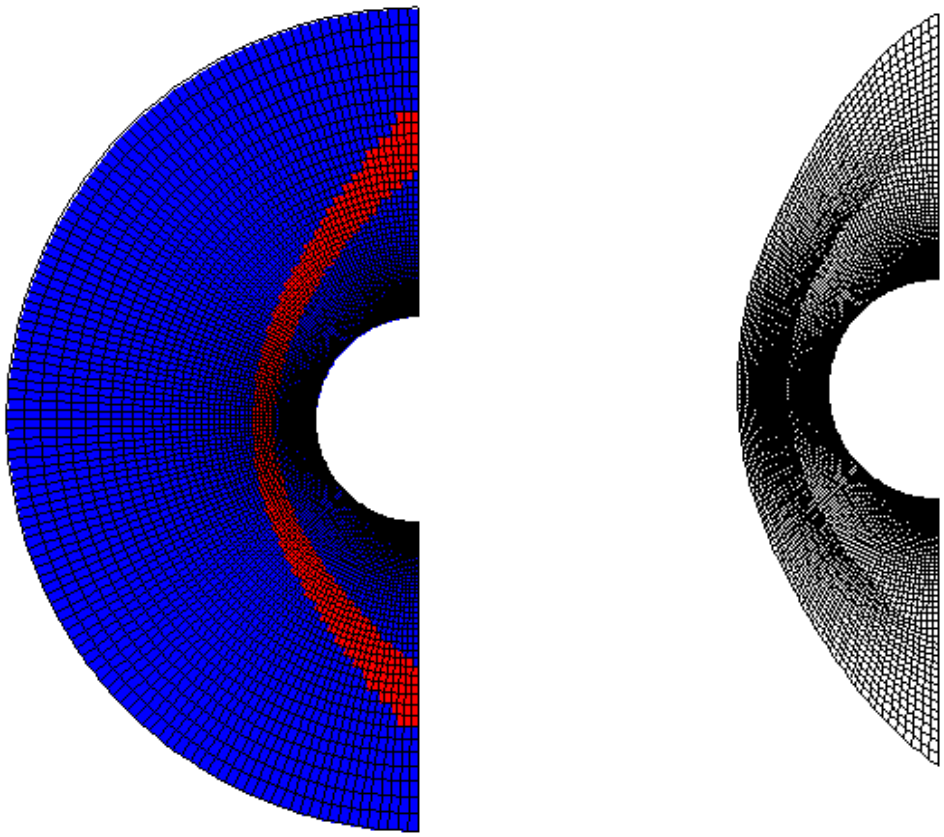

A Before r-p adaptivity B After r-p adaptivity

Figure 3-4. A) Mesh before r-p adaptivity. Elements outside the shock are brought closer to shock B) Mesh after r-p adaptivity. More elements are packed in region of shock. Thus shock mesh resolution is improved without increase in total number of elements.

we cluster the elements in the domain outside of the shock, to region very close to shock. An example of this is shown below in Fig. (3-4).

This application is also not dependent on the shape of the body, but is the shock based refinement, hence applies to all body shapes.

CHAPTER 4
CODE VALIDATION EXAMPLES

In this chapter, we present some example problems to test the inviscid and viscous sections of the code. In each section, a simple example problem leads to more and more complex ones. Each of these, tests the basic machinery of the code to see if the correct physics is captured in every section. This is a very effective way to solve a very tough problem like non-equilibrium hypersonic flow or thermal ablation, i.e. to test smaller sections of the code by isolating them in a sample problem.

Along with presenting the results, we will also show solution capability for high order polynomial accuracy.

4.1 Inviscid Flow

In this section, we isolate the inviscid phenomena that primarily deals with the pressure variation resulting in flow features. First problem is the potential flow around a cylinder (at very low Mach number of 0.01) where in the beginning, there develops a high pressure and low pressure regions in front and back of cylinder respectively, causing acceleration of fluid close to cylinder from front to back of cylinder. This effect is also connected to Bernoulli′s equation (defined for incompressible and inviscid flow). As the flow speed increases, the flow at the top of the cylinder reaches sonic condition (M = 1) for free stream Mach number, M_∞ of 0.38 approximately.

As the flow speed further increases, we get what we call transonic flows, with flow Mach numbers increasing above unity at the top of cylinder. Presence of higher pressure downstream causes the shock to appear on the surface of the cylinder. Shocks move from back of the cylinder to the front, and weaken in strength since they can not sustain for Mach numbers below unity. A more complex problem of steady, but moving shock is then solved. This is double Mach reflection problem having is a Mach 10 flow that hits the wedge at an angle α. Complex inviscid interactions of shock with Mach stem giving rise to complex features is also noticed in this case.

4.1.1 Potential Flow Around the Cylinder

At very low Mach numbers, for the potential flow problem, only the inviscid effects are important. The problem of 2-D uniform flow, being suddenly exposed to the cylinder, is equivalent to a cylindrical particle being impulsively started in a quiescent flow field. The forces acting on the particle, till the flow achieves a steady state behavior, have been theoretically derived in [80].

Hence, we can test our inviscid part of the code for the transient effects, as the flow develops from initial uniform flow solution to the potential flow solution. We consider Mach number of 0.01, that tests our code for the unsteady forces, the convection and the pressure terms. Important details for the problem setup are as follows,

$$\mathrm{M} = 0.01 \tag{4–1}$$

$$\rho = 1.17659 \ \mathrm{kg/m^3} \tag{4–2}$$

$$\mathrm{u} = 3.47224 \ \mathrm{m/s} \tag{4–3}$$

$$\mathrm{P} = 101325 \ \mathrm{Pa} \tag{4–4}$$

$$\mathrm{Radius} = \mathrm{R} = 0.1 \ \mathrm{m} \tag{4–5}$$

$$\mathrm{Domain\ size} = 20\,(\mathrm{R}) = 2 \ \mathrm{m} \tag{4–6}$$

$$\mathrm{Acoustic\ time\ scale} = \tau = \frac{\mathrm{R}}{\mathrm{a_o}} = \frac{0.1 \ \mathrm{m}}{347 \ \mathrm{m/s}} = 2.88\mathrm{x}10^{-4}\mathrm{s} \tag{4–7}$$

The drag force on the cylindrical case for the inviscid problem is calculated from,

$$\mathrm{D} = \int \mathrm{P n_x d\Gamma} \tag{4–8}$$

The values for this drag force are compared to the exact solution from [80] and the code was tested for different orders of accuracy.

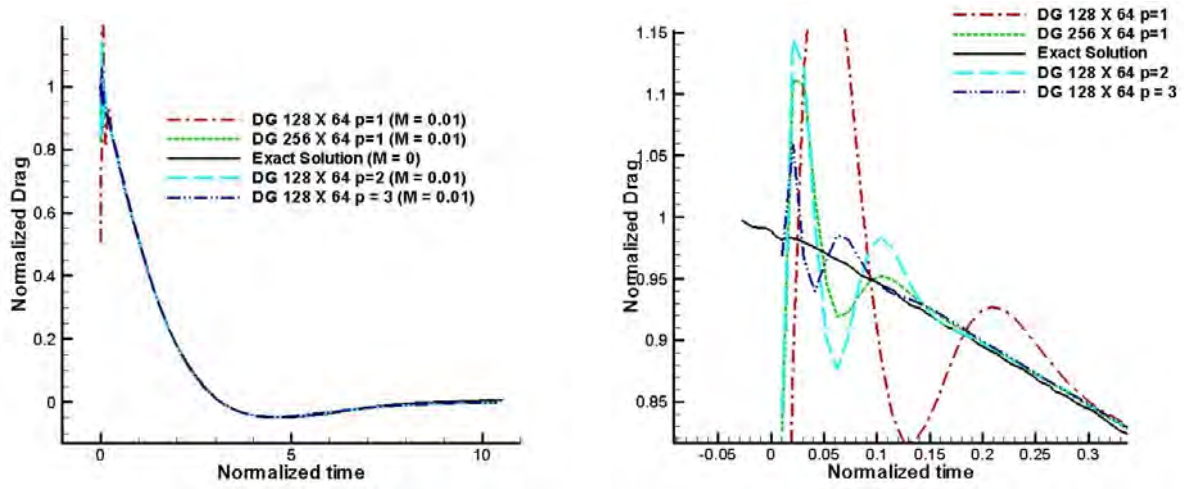

A Drag Vs. time for all p′s

B Zoom in

Figure 4-1. A) Normalized Drag vs. Normalized time response of fluid to sudden presence of cylindrical particle. B) Zoom in of the initial transients.

We show the comparison of the exact solution to the results obtained using DG method in Fig. (4-1). The solution is obtained with polynomial order of accuracy, p = 1, 2 and 3 for 128 X 64 mesh and p = 1 for 256 X 64 mesh. We see a good comparison of drag with the exact solution, and the more subtle differences for initial transients are also showed in a zoomed in section. We notice that p = 3 and 128 X 64 mesh gives the best comparison for the initial transient prediction of the drag.

After comparing the transient solution, for the drag prediction of the potential flow, we also compare the steady state solution given by the code, MIG to the potential flow solution.

4.1.2 Subsonic Flow Around the Cylinder

Now we consider the case of subsonic flow around the cylinder, with M = 0.38. The viscous viscous effects are ignored in this case, which shall be true for high Reynolds number cases, away from the wall. This Mach number of 0.38 is considered critical Mach number for flow over cylinder, since the flow Mach number reaches unity at the top of the cylinder. Thus, there is still no shock in the solution. For Mach numbers greater than 0.38 (discussed in the next section, 4.1.3 titled ′Transonic flow around cylinder′),

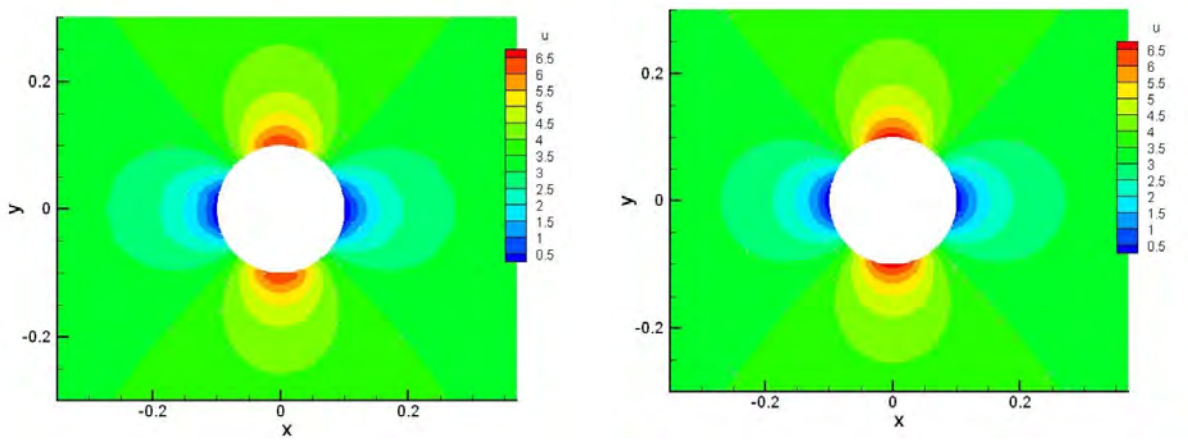

Figure 4-2. A) Steady state solution for x-velocity contours, obtained using P1Q2 approximation in MIG, and its comparison to B) steady state potential flow solution.

there is a shock that develops in the rear of the cylinder and travels towards the front. Thus we get some interesting flow physics, which is discussed in the next section.

For the inviscid flow simulations in the previous, current and the following sections, we choose a circular domain around the cylinder and use the quadrilateral mesh elements. Curved boundaries, with quadratic geometric interpolation function, are used at the circular body of the cylinder, giving an exact fit . For this purpose, we use Gordon Hall transformation, which gives the mapping of the complete physical element from the reference square element, by mapping the edges.

For boundary conditions for all inviscid cylinder flow cases, we use slip boundary condition for the wall, and far-field boundary condition at the outside domain. Left side of this domain uses inlet boundary condition, and right side interpolates the boundary from inside, except we make sure that pressure is 1 atm at the right side of outside domain. We show a comparison of these meshes in Fig. (4-3). Bassi & Rebay [81] use 128 x 32 triangular elements mesh, and we use 64 x 50 quadrilateral elements mesh.

The steady solution is compared by matching Mach number contours provided in [81] and these comparisons are given in Fig. (4-4). Our results match well to their

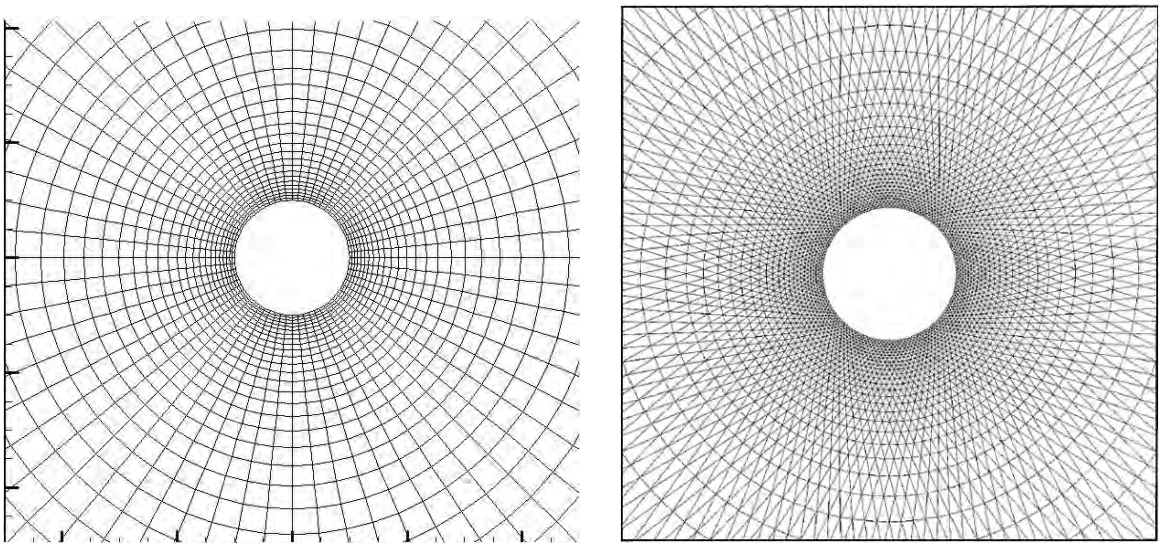

A 64x50 mesh, MIG B 128x32 mesh, Bassi & Rebay

Figure 4-3. A) 64x50 mesh used in MIG. Uses quadrilateral elements and P1Q2 approximation. B) 128x32 mesh from Bassi & Rebay. Uses triangular elements and P1Q2 approximation.

result, except behind the cylinder. This asymmetry for front and back of cylinder was also noticed for results by Bassi, Rebay ([81]) for coarser meshes.

The asymmetry in the flow, behind the cylinder is due to use of coarser meshes behind the cylinder. Also, the number of triangular elements are higher than compared to the number of the quadrilateral elements we use in MIG.

4.1.3 Transonic Flow around the Cylinder

Subsonic flows with free stream Mach numbers being lower than the critical value of 0.38, can be captured without the use of limiters, as there are no shocks developed in the flow. But, for flows with M $>$ 0.38, the flow achieves Mach numbers greater than 1 over the cylinder top and hence the solution develops transient radial shocks. Ideal handling of these flows requires the use of a good limiter. However, in our simulations we have attempted the solution without employing the limiters.

The fluid accelerates to a maximum velocity over the cylinder top. Seeing an adverse pressure gradient, downstream of the cylinder top, the flow develops a

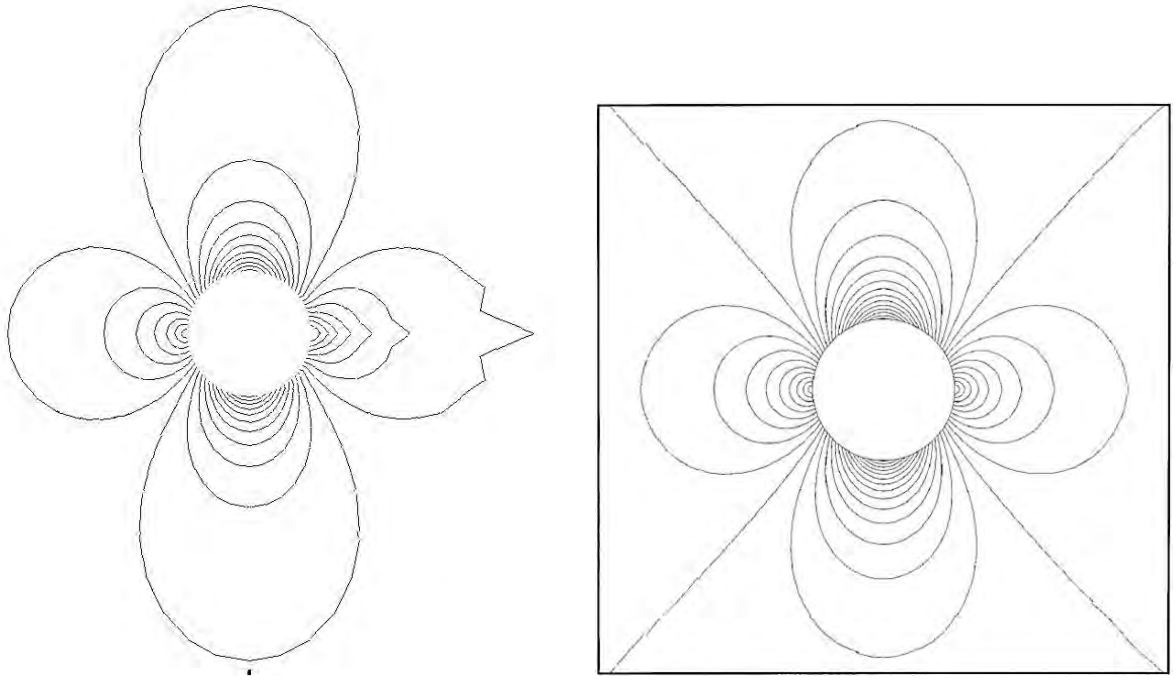

A 64x50 mesh, MIG

B 128x32 mesh, Bassi & Rebay

Figure 4-4. Mach contours shown for M = 0.38 for (a) MIG and (b) Bassi & Rebay ([81]). Results differ at the back of the cylinder, where the mesh is coarser for MIG in comparison to Bassi & Rebay.

transient radial shock that propagates upstream. As the shock propagates upstream the shock weakens in strengths and hence eventually fades away. The complete mechanism of shock development, its propagation upstream along the cylinder surface, formation of the recirculation zone behind the cylinder subsequently leading to vortex shedding phenomena behind the cylinder is explained below (Fig. (4-5)) with the figure illustrations.

This case was run for P1Q2 i.e. linear basis function and quadratic approximation for the circular cylinder boundary. Time step of 10^{-5} sec was used along with the mesh of 128 x 50 elements. 128 elements were used along the circumferential direction and 50 along the radial direction. For this case as mentioned, no limiters were used, but since the density and energy values can become zero or negative; to avoid the solution to either diverge or crash, we have limited density to not fall below the value of 0.1 $\mathrm{kg/m^3}$

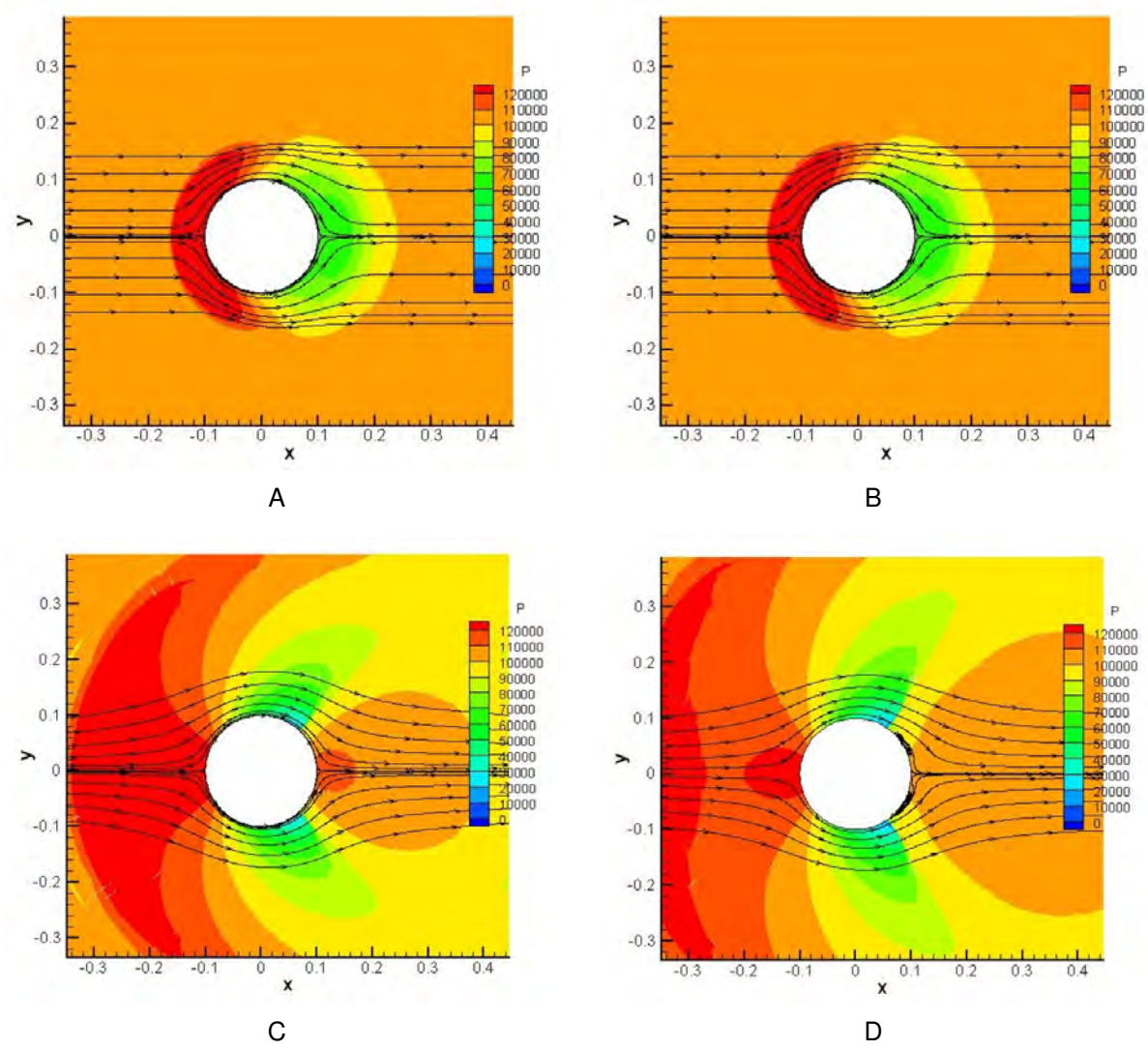

Figure 4-5. Figure Illustration for development of radial shocks and vortex shedding phenomena for transonic flow around the cylinder, with M = 0.5. A. & B. Initial development of high and low pressures across front and back respectively that causes flow acceleration from the front of the cylinder to the back of the cylinder. C. & D. Development of radial shock and its motion towards the front end of the cylinder. Adverse pressure gradient is formed after the shock that causes recirculation and flow separation after the shock.

(the freestream value of density being 1.17659 $\mathrm{kg/m^3}$). We see initial development of high and low pressure zones on the front and back portions of the cylinder respectively (Fig. (4-5) A, B). This leads to the fluid accelerating from front to the back portion of cylinder hence resulting in the formation of radial shocks (two shocks in Fig. (4-5) C, D are symmetric to the x-axis). These shocks move towards the front portion of the cylinder. They weaken as they move and fade away before reaching the front portion of the cylinder.

These shocks reappear again as the flow conditions again develop similar to the initial phase, causing acceleration of fluid from front portion to the end. The recirculation zone that is formed due to flow separation behind the shocks, creates two prominent counter-rotating vortices behind the cylinder (Fig. (4-6) A, B). These vortices are stretched in the front direction and eventually leads to vortex shedding phenomena (Fig. (4-6) C, D). The simulation is run for a total time of 7 ms.

There is a sudden pressure increase after the shock, which causes the shock to move more towards the front portion of the cylinder. We also see that after the shock, the pressure increases along the direction of the flow. This is adverse pressure gradient and causes the flow to decelerate after the shock. This is also referred to as the rotational effect produced by the shock, or isentropy deviation. Due to this deceleration, close to the surface of the cylinder, the flow starts to recirculate and separate from the cylinder surface.

As the radial shock moves towards the front portion of the cylinder, recirculation zone increases in size. But then the pressure again increases in the front of the cylinder, resulting in appearance of one more shock, and high velocities result in convection or stretching of the vortex. This will then cause the shedding of the vortices.

We also show comparison of Mach contours structure (in Fig. (4-7), with the published result from [82] at a time of 100 ms.

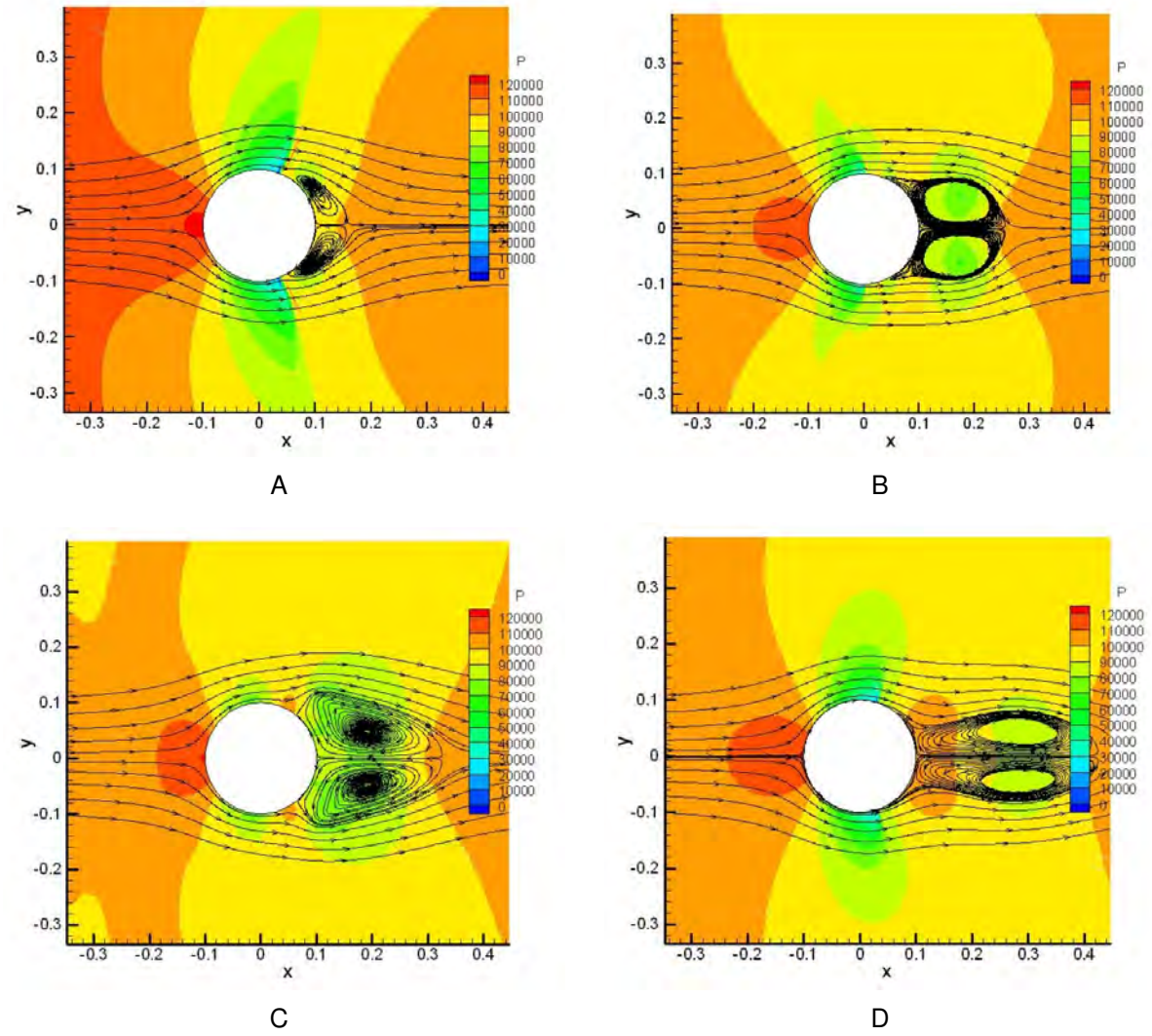

Figure 4-6. Figure Illustration for development of radial shocks and vortex shedding phenomena for transonic flow around the cylinder, with M = 0.5. A. & B. Radial shocks are seen to move towards the front portion of the cylinder. Recirculation region forms behind the shock due to flow separation. As the radial shock continues to move towards the front portion, the recirculation region increases in size. C. & D. Increase in the size of recirculation zone behind the cylinder results in the increase of pressure in the front portion of the cylinder thus causing higher velocities over the cylinder. This causes redevelopment of radial shock and the stretching of the recirculation zone thus preparing for the vortex shedding phenomena observed for transient shock problems.

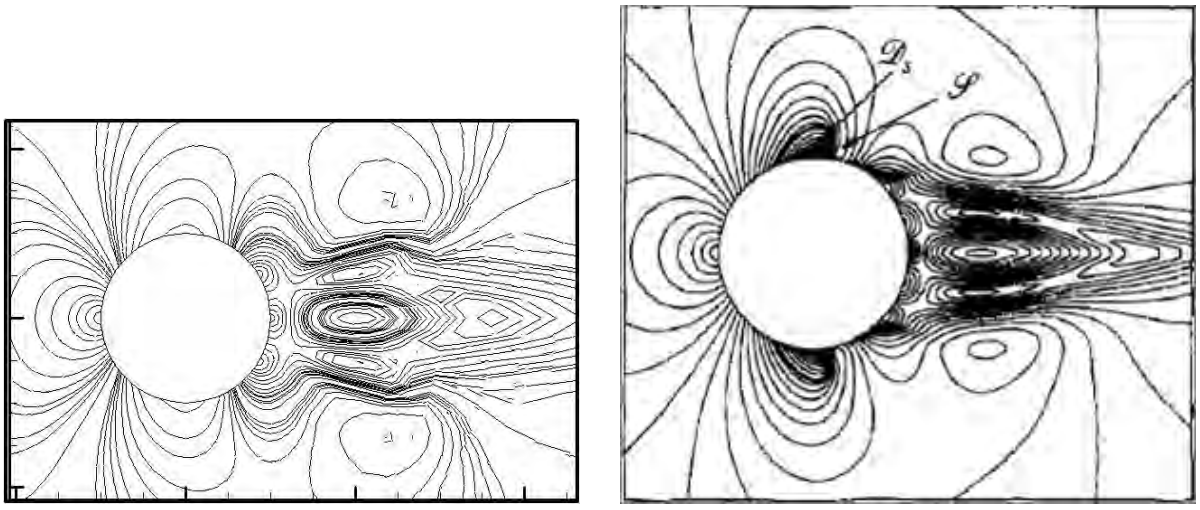

A MIG, t = 5.4 ms

B Botta et al., t = 100 ms

Figure 4-7. Mach contours comparison for M = 0.5 flow over cylinder for A) MIG at t = 5.4 ms and B) Botta et al. [82] at t = 100 ms.

In above results, we have used DG method and Botta et al. uses Finite Volume or FV method, which is DG method with p = 0 (or first order approximation). Mesh used in [82] is also finer than ours close to cylinder. Botta et al. shows a solution at 100 ms in comparison to our solution at 5.4 ms. The features are closest to the reported results at this time, though not exactly the same. Contours on front portion are similar, but at the back end, we see some differences in the solution.

4.1.4 Double Mach Reflection

So far we have tested the code for weak shocks of Mach number less than 2. To test the code for a strong shock problem, we choose to do double Mach reflection problem. In this problem the Mach number of the traveling shock is 10. This shock hits a wedge inclined at an angle, α with the x-axis. The wedge acting as a reflecting wall, causes the shock to reflect off the leading edge of the wedge, resulting in a complex interaction of Mach stem, reflected shock and the incident shock.

The cartesian grid can be fixed to the wedge, and hence in rectangular domain as shown below (Fig. (4-8)), the shock is now at an angle of alpha with the x-axis as shown

in the figure below. Thus the incoming flow hits the wedge also at an angle of $-\alpha$ and will reflect off at the incident point.

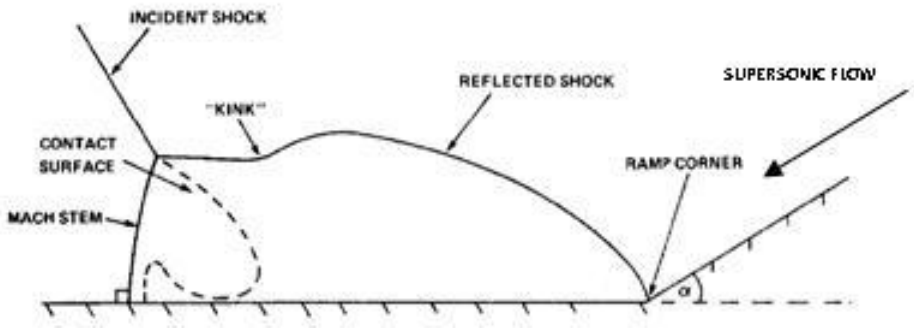

Figure 4-8. Schematic of 2-D double mach reflection problem

For boundary conditions, and domain information please refer to [83]. Since this problem has a strong shock, and we are not using artificial dissipation in our scheme, we get overshoots and undershoot across the shock; this causes the density and total energy to take negative values near shock. In our code, we limit values of density and total energy to their minimum physically possible values. By this, we have been able to get results for p = 1 (linear polynomial approximation) for DG method. For higher p ($\geq$ 2), the jumps across shock become steeper and causes convergence problems.

Below, we show results obtained with $\mathrm{p} = 0$ and 33000 element that gives us good physical understanding of different flow features in this problem. The domain size considered is 3.3 m $\times$ 1 m, and the solution is seen at t = 0.2 sec. Details of this problem can also be found in our 2011 AIAA publication [4].

Looking at contour plots in Fig. (4-9), we find that the high speed flow is highly compressed at the intersection of reflected shock and the reflecting wall. This is seen from Fig. (4-9) A) with higher density of nearly 18 units in comparison to 8 units. This density slowly merges into free-stream density value at the region between contact discontinuity and Mach stem. This high compression is also seen in pressure contour in Fig. (4-9) B), where the pressure value is nearly 460 units compared to 116.5 units value in the free stream. Uniformly decreasing pressure in the x-direction for the fluid

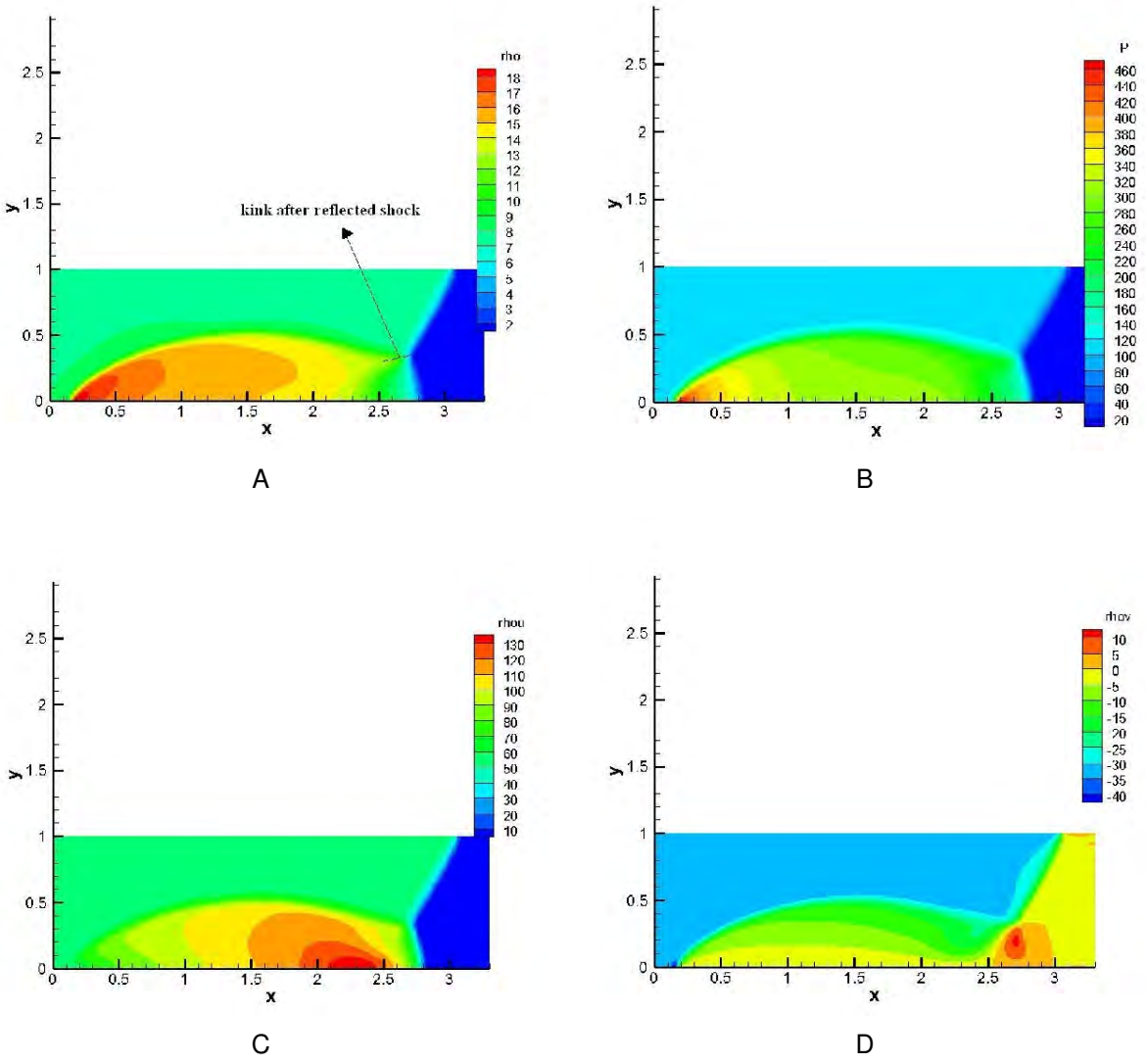

Figure 4-9. Results for 33000 elements case with p = 0. These results give basic insight into the physics of DMR problem. A) Density contours at t = 0.2 sec shows that density is compressed when high speed flow hits the reflecting wall, and high pressure region (in B)) is thus created which leads to formation of jet (seen in C)) with high velocity (higher than shock speed) that impinges the Mach stem resulting in convexly shaped Mach stem. The high speed jet impinging on the fluid at rest after Mach stem leads to a recirculation of fluid in reference to the incident shock (in D)).

close to the wall causes a wall jet Fig. (4-9) C) with maximum speed of nearly 13 units. This is higher than the speed of shock in line with the bottom boundary, which comes to be equal to 11.547 units. Thus, we see that the high speed fluid is impinging the Mach stem, resulting in a convex Mach stem.

The recirculation region as seen in Fig. (4-9) D), results from lifting of fluid close to the wall by the wall jet hitting the fluid at rest. The recirculation region is defined in relation to the fluid velocity in the free stream. We also note that the results for p = 0 have large numerical diffusion, as can be noticed from the results above. The kink after reflected shock in Fig. (4-9) A) is also not finely resolved. In addition, the contact discontinuity between the kink and the Mach stem is also not clearly visible. These results are improved with p = 1 method which has low numerical diffusion in relation to the case with p = 0. Below (Fig. (4-10)), we show zoomed-in sections of density and pressure contours noticing the clearly visible and well resolved kink and contact discontinuity.

We also found during the simulations of this problem for $\mathrm{p} \geq 1$, that the order of Gaussian quadrature for performing area integration of a 2-D elements has to be the same to the order of Gaussian quadrature for doing the edge integration of the same 2-D element. If this is not followed, then the error in integration can cause the solution to grow unbounded and cause unphysical features that can destroy the solution.

Contact discontinuity is visible in density plot but not in pressure plot, which is how it is identified. Whether the feature seen in Fig. (4-10) is purely numerical or has some physical significance has to be further investigated. This feature is due to higher x-velocity produced (Fig. (4-10) C)), with value around 16 units higher than 13 units for fluid close to the wall (where jet velocity is maximum) for p = 0 case presented above.

We also show how our results have improved with finer mesh in comparison to results presented with p = 0. Top three results in Fig. (4-11), are three contour results published in [4], and bottom two results are for mesh sizes obtained with finer mesh.

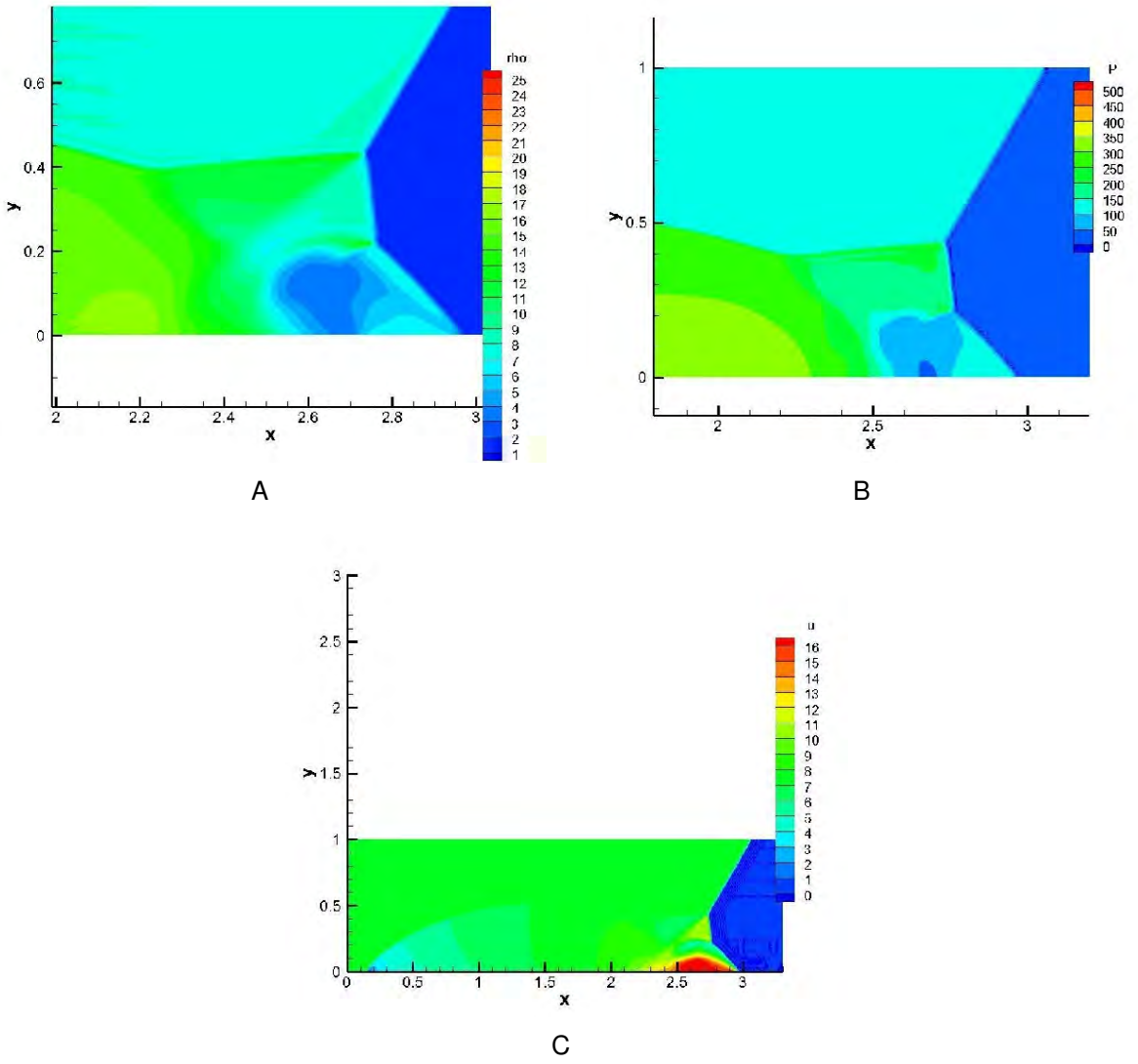

Figure 4-10. A) & B): Zoomed sections of density and pressure contours at t = 0.2 sec with 33000 elements and p = 1. Contact discontinuity can be identified by seeing the discontinuity in density in the region between the kink after reflected shock and Mach stem, and continuity in pressure in that region. We also find that the Mach stem is convexly curved close to the incident shock and the high speed fluid impinges Mach stem producing the feature that we see above. The maximum velocity in the region of fluid jet is nearly 16 units, which is higher than previous case with p = 0 (Fig. (4-9) C)).

We definitely see much better mesh resolution, and all the features of reflected shock, incident shock, Mach stem and especially the region between kink after reflected shock and Mach stem are very well resolved with the finer mesh of 132000 elements and p = 1.

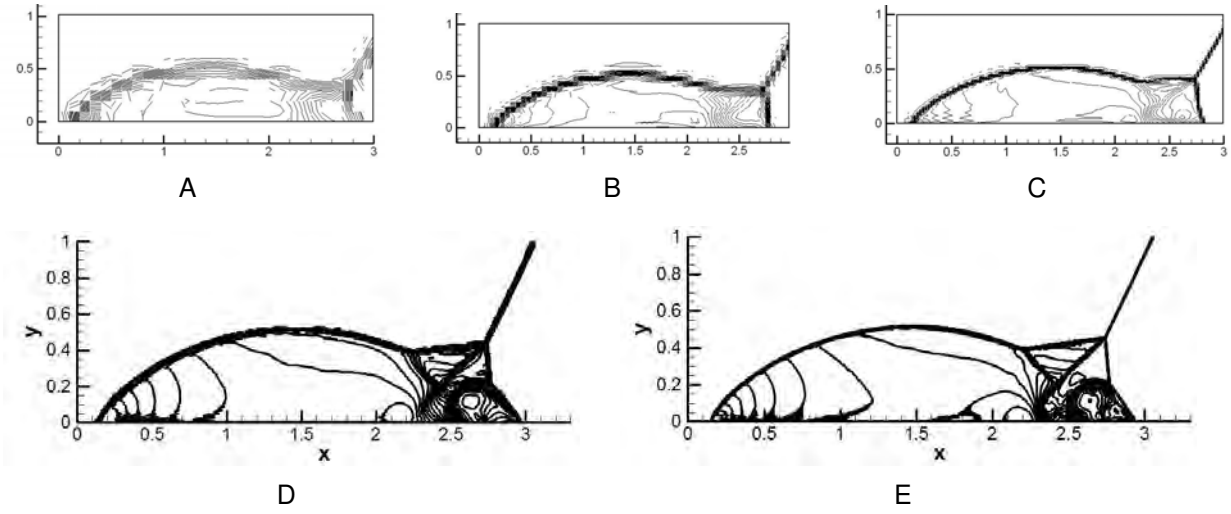

Figure 4-11. Density contours are shown for A) 40 10, B) 80 20, C) 160 40, D) 330 100 and E) 660 200 meshes (from top left to bottom right) and p = 1. We observe that the regions of reflected shock, incident shock, Mach stem, and the region between kink and Mach stem becomes better resolved as the mesh is made finer. Total 30 levels of contours are shown. They are equally spaced between density values of 2 and 20 units.

4.2 Viscous Flow

After testing the inviscid cases with some of the standard cases for the inviscid terms, we now test viscous terms in this section. For this purpose we pick standard problems to test the viscous terms. Our first problem deals with the dampening of the amplitude of two counter-rotating vortices. Here the inviscid terms have no role to play and hence the whole shear effect has to come from viscous terms. So, this is the basic testing for the viscous terms.

After this, we test our code for problems with gradually increasing complexity. Next problem is Rayleigh flow in an impulsively started plate. This problem reduces to a very simple diffusion equation (which has an exact solution) and hence tests the code for

viscous terms in the x and y directions separately. This problem has solution variation only in one direction, i.e. y. Next problem, the flat plate flow, is more complex in that it has solution variation in both x and y directions, and hence tests the capability to capture the phenomena correctly in x and y directions. This problem also has an exact solution.

4.2.1 Taylor Vortex

This is a problem of counter rotating vortices present everywhere. It has periodic boundary conditions and thus we can avoid boundary conditions. So, we simply test the basic scheme of the DG method for the viscous terms.

Domain for this problem is 1 $\times$ 1. Initial condition for this problem is as follows,

$$\mathrm{U} = \begin{pmatrix} \rho \\ \rho\mathrm{u} \\ \rho\mathrm{v} \\ \rho\mathrm{E} \end{pmatrix} = \begin{pmatrix} 1 \\ -\cos\left(2\pi\left(\mathrm{x}+0.25\right)\right)\sin\left(2\pi\left(\left(\mathrm{y}+0.25\right)\right)\right. \\ \sin\left(2\pi\left(\mathrm{x}+0.25\right)\right)\cos\left(2\pi\left(\mathrm{y}+0.25\right)\right) \\ \frac{\mathrm{P}}{\gamma-1}+\frac{1}{2}\rho\left(\mathrm{u}^2+\mathrm{v}^2\right) \end{pmatrix} \tag{4–9}$$

Here, P is given by,

$$\mathrm{P} = 101325 \quad \mathrm{Pa} - 0.25\rho\cos\left(4\pi\left(\mathrm{x}+0.25\right)\right)\cos\left(4\pi\left(\mathrm{y}+0.25\right)\right) \tag{4–10}$$

and, γ is 1.4. From this problem, we found that explicit treatment of correction terms in BR2 is not effective for running the problems at a high timestep. Hence we worked on making our BR2 code totally implicit, which was good amount of work. With earlier explicit treatment of correction terms, $\mathrm{r_h}$, when we ran the Taylor vortex problem with viscosity coefficient of 0.1 (for heavier damping of the vortex amplitudes), we ran into divergence issues for the code. In order to just check the BR2 scheme in the code, not worrying about the implicit jacobian terms, we first ran this problem explicitly with

$\triangle t = 10^{-6}$ sec. Below (Fig. (4-12)) we show result at a total time of 0.1 sec, compared to initial solution at t = 0 sec,

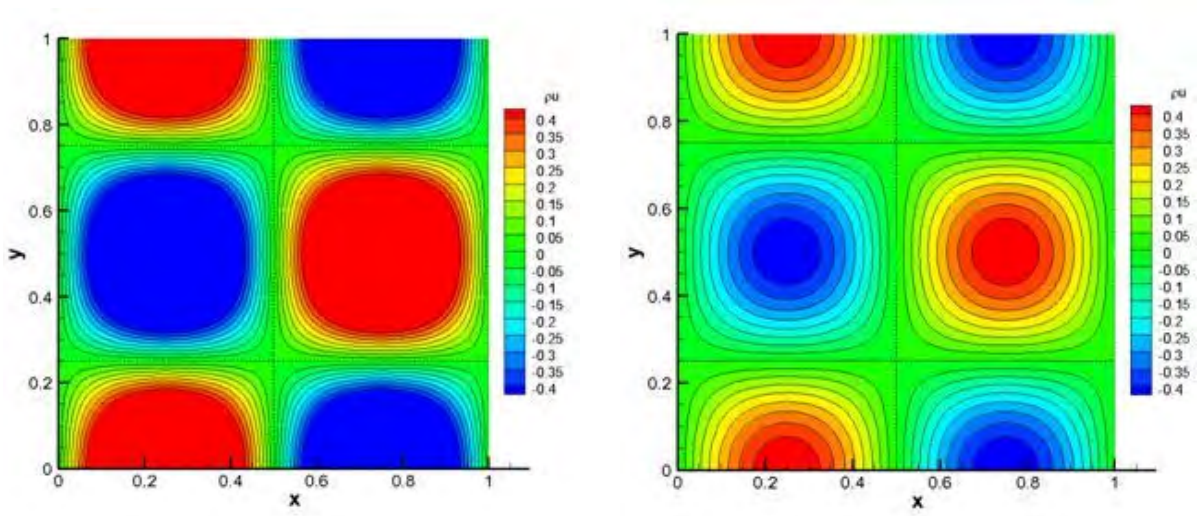

A t = 0 sec

B t = 0.1 sec

Figure 4-12. Taylor Vortex problem: Contours of ρu, shown at t = 0 sec (initial solution), and at t = 0.1 sec. Above results are obtained using explicit time integration scheme with $\triangle t$ = 1.0 $\times 10^{-6}$ sec.

The above mesh uses 100 $\times$ 100 elements, and no dispersion effect is seen in above results. Net analytical dissipation of velocity amplitudes should be $\exp(-8\pi^2 \nu t)$ = 0.45404, and our amplitude is 0.451324. Additional amplitude damping can be attributed to numerical dissipation of the scheme. It is to be noted that this BR2 scheme is with global corrections, hence is exactly same as BR1 scheme, only with a faster performance. We can also see small effect that inviscid terms have on the solution.

By running the simulations without the inviscid terms, and seeing the 3D plots for solution of ρu with and without inviscid terms (in Fig. (4-13)), we understand that inviscid terms are acting in this problem, and without inviscid terms, there are jumps in solutions in between elements.

Also amplitude of ρu in Fig. (4-13) A) above is 0.453815, as opposed to 0.451324 in comparison to the exact solution of 0.45404. Thus we find theres very minimal

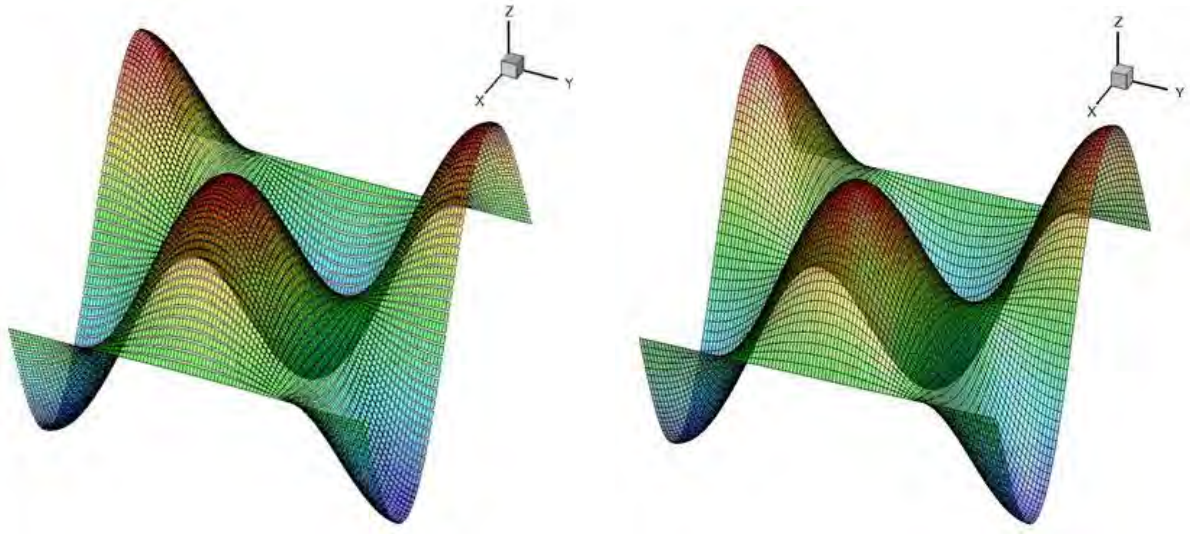

A Without inviscid terms B With inviscid terms

Figure 4-13. Taylor Vortex problem: 3D plots for solution of ρu, run with A) no inviscid terms activated and B) inviscid terms activated. Jumps in the solution (seen as gaps) between elements in A) are visible in comparison to B), where jump terms are not visible.

numerical dissipation of viscous terms themselves, and the BR2 scheme as proposed is very similar to BR1 scheme.

Dissipation error of viscous terms is very minimal close to central difference scheme in finite difference, and dispersion error is not visible. For inviscid terms, nothing is happening in the solution to see any dispersion error in the solution, but it is clear there is no dispersion error for viscous formulation.

To be able to run the simulations with higher time step, we then worked on BR2 scheme, and we use fully implicit BR2 with local corrections in the test cases shown below. BR2 with local corrections has much better performance than BR1 scheme.

4.2.2 Rayleigh Impulsively Started Flow

This problem tests the code for viscous terms in presence of the inviscid terms. An impulsively started plate in a quiescent viscous fluid causes fluid particles near the plate, at t = 0, to accelerate under the effect of shear forces. With time, this effect is felt farther

and farther away from the plate, which induces more and more fluid to move along with the plate.

As the plate moves at t = 0, the fluid (being ideal), next to the wall, also moves along with the plate at speed u of the wall. Assumption of incompressible fluid and no dependence of fluid motion on x, leads to v = 0 (y-velocity). Thus examining y-momentum equations, we find that pressure is not a function of y direction. Hence the pressure is a constant. Under these conditions, the fluid equations simplify to following parabolic equations.

$$\frac{\partial \mathrm{u}}{\partial \mathrm{t}} = \nu \frac{\partial^2 \mathrm{u}}{\partial \mathrm{y}^2} \tag{4–11}$$

The exact solution for this problem is a self similar solution given by,

$$\frac{\mathrm{u}}{\mathrm{U}} = \mathrm{erf}\,(\eta) \tag{4–12}$$

$$\eta = \frac{\mathrm{y}}{\delta} \tag{4–13}$$

$$\delta = 2\sqrt{\nu \mathrm{t}} \tag{4–14}$$

For the simulation purpose, we considered the plate to be stationary wall at y = 0, and the fluid was considered to be uniformly moving at a given velocity, U at t = 0. We choose a rectangular domain, with left and right sides having periodic boundary conditions. Bottom wall has wall boundary conditions (i.e. u = v = 0) and top edge of the domain is considered to have floating boundary condition (i.e. no gradient in y-direction at the top edge). Thus this problem is exactly the Rayleigh impulsively started flat plate problem, where the frame of reference is attached to the moving plate.

We examined our results with BR1 and BR2 schemes for the viscous terms, and also did a mesh convergence study with different orders of accuracy. The flow Mach number considered is M = 0.3.

For starting mesh, we consider 3 $\times$ 60 elements, with finest mesh at the wall having 10^{-5} m thickness. Having a coarser element than this at the wall led to convergence problems at the start of the solution. Flow solution (u = U) immediately sees the wall (u = 0) and develops strong discontinuity, that causes convergence problems in the beginning of the simulations. Below, we show results for BR1 scheme both with and without inviscid terms included in the formulation.

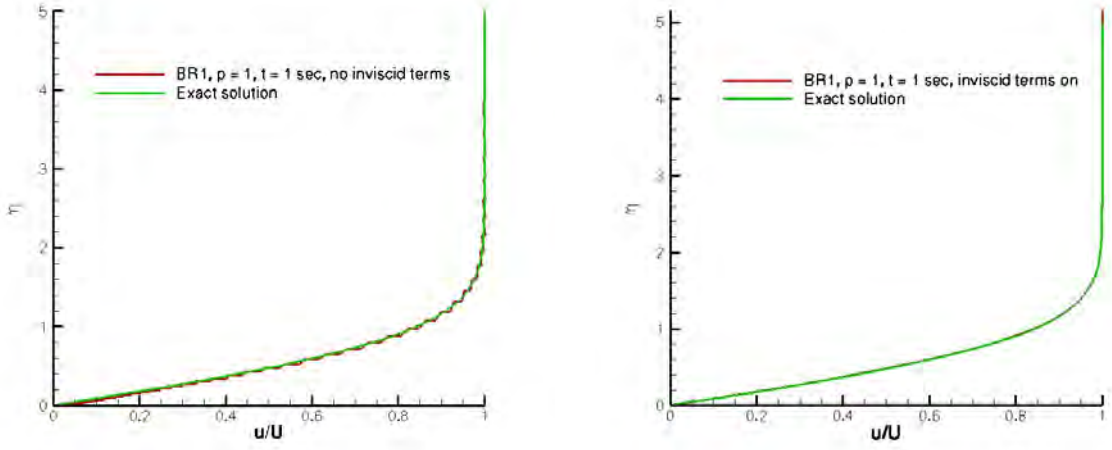

A Without inviscid terms B With inviscid terms

Figure 4-14. Rayleigh problem with BR1 scheme: Effect of inviscid terms on the final solution for BR1 scheme. The simulation are run to a total time of 1 sec. With A) no inviscid terms activated, the solution with BR1 scheme has inter-element jumps and B) with inviscid terms activated, these jumps are no longer seen.

It is seen in Fig. (4-14), that BR1 scheme with p = 1 is not able to remove inter-element jumps which are incorrectly taken care of by inviscid terms. This problem is purely viscous in nature, and hence inviscid terms acting is an incorrect mechanism, that affects both inside and the solution at boundary. This is already taken care of at boundary by using the pressure normal contribution at the boundary, but at the inside, the viscous scheme is expected to smooth out such inter-element jumps. These inter-element jumps are found to disappear when using BR2 scheme (with local

contribution for r_h) and p = 1. For BR1 scheme, this happens when using p = 2 (the quadratic basis function) (see Fig. (4-15)).

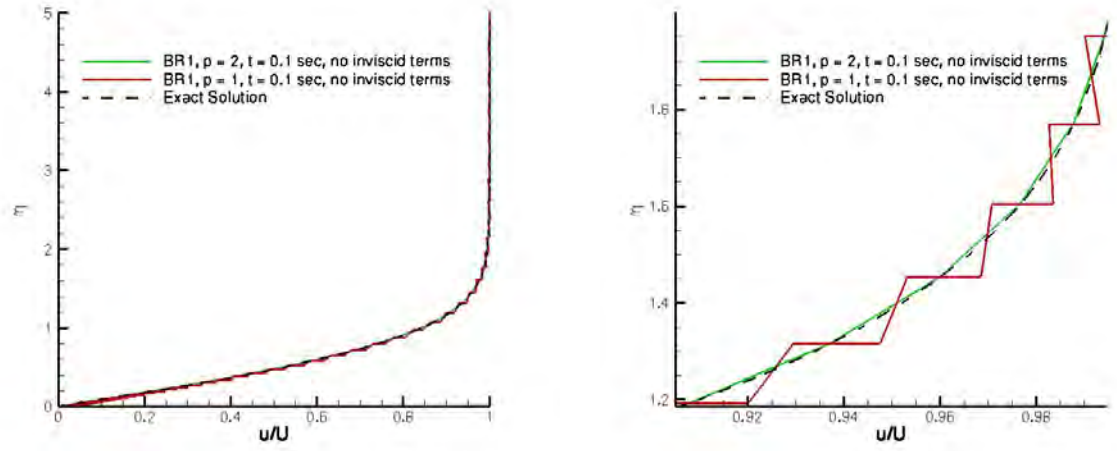

A Comparison of p = 1 and p = 2

B Zoomed in section

Figure 4-15. Rayleigh problem with BR1 scheme: A) Comparison of solutions with p = 1 and p = 2. The simulation's run time is 0.1 sec. Inviscid terms are turned off in this case to isolate the effect of BR1 scheme on the solution. Inter-element jumps observed with p = 1 are no longer observed with p = 2. A more clear picture of this is seen in B), the zoomed in section of figure in A).

4.2.3 Flat Plate

Flat plate is a typical problem to check the viscous part of the code. The problem details are given in Fig. (4-16),

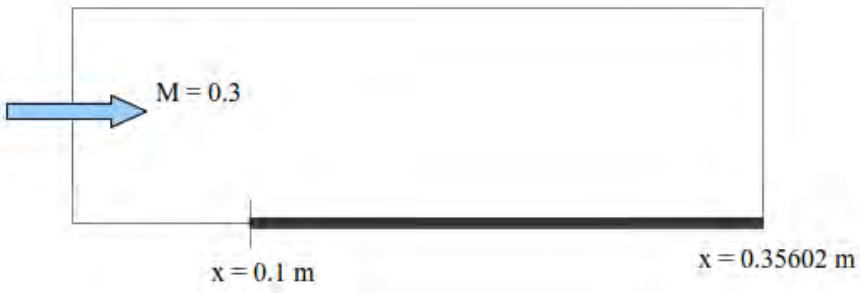

Figure 4-16. Schematic of flat plate problem. Total domain size is 0.35602 m, the plate begins at x = 0.1 m, and the total plate length is 0.25603 m. The flow Mach number is 0.3 providing all the problem details

This is Mach 0.3 flow over flat plate. The freestream density is 1.17659 kg/m^3 and the freestream velocity is 104.165 m/s. The boundary conditions are as follows,

Left side: Freestream inlet boundary condition

top and right side: Pressure outflow condition, with fixed freestream pressure = 101325 Pa

bottom side (before plate): symmetric in y direction

bottom side (after plate): wall boundary with u = v = 0 and density taken from inside element and total energy fixed at $\mathrm{P}/(\gamma - 1)$

For inviscid terms at bottom boundary we use pressure normal contribution. We present results with both BR1 and BR2 schemes. If we do not use pressure normal contribution for the inviscid flux, but instead use $\alpha\,(\mathrm{U_b} - \mathrm{U_n})$ for inviscid flux at bottom boundary, we get results that do not match up with Blasius profile given in Fig. (4-17).

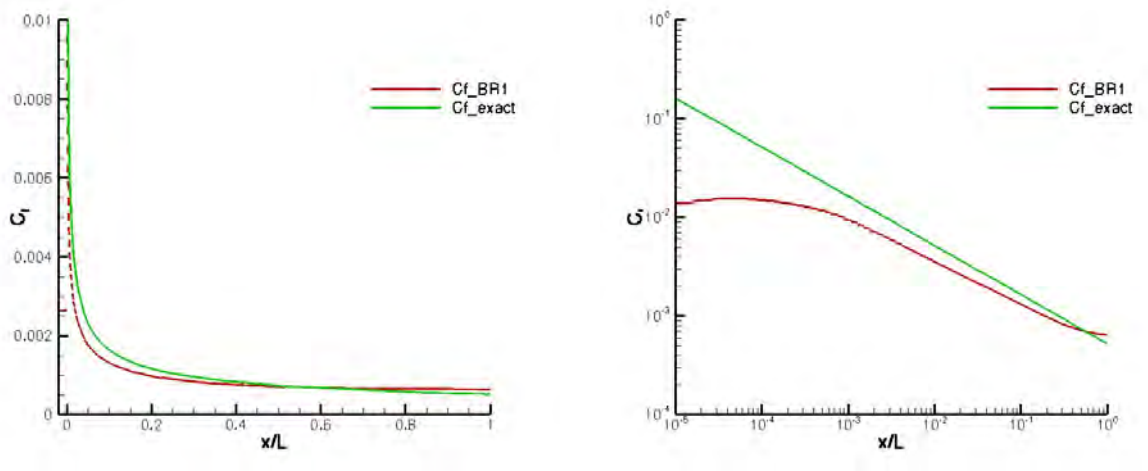

A regular scale B log scale

Figure 4-17. Flat plate solution with BR1 scheme and incorrect boundary condition. $\mathrm{C_f}$ plots in A) regular scale and B) log scale are compared with the exact Blasius solution. As is clear the deviation from exact solution is significant because of incorrect application of boundary condition for inviscid terms.

Using correct application of boundary conditions at the wall for inviscid terms, we get more accurate comparisons of $\mathrm{C_f}$ profiles shown in Fig. (4-18).

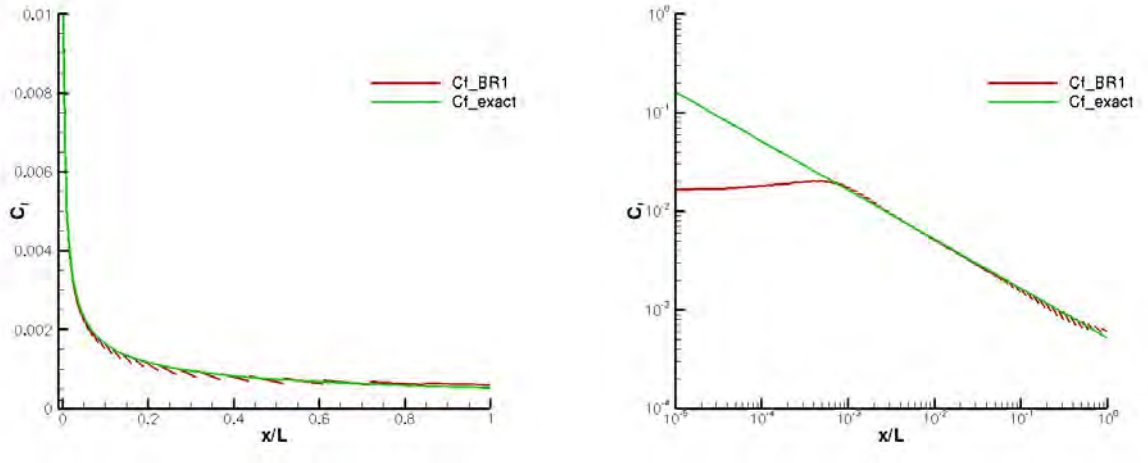

A regular scale B log scale

Figure 4-18. Flat plate solution with BR1 scheme and correct application of boundary conditions for the inviscid terms. C_f plots in A) regular scale and B) log scale compare well with the exact Blasius solution.

Using BR2 scheme, we obtain much accurate C_f profiles (see Fig. (4-19)).

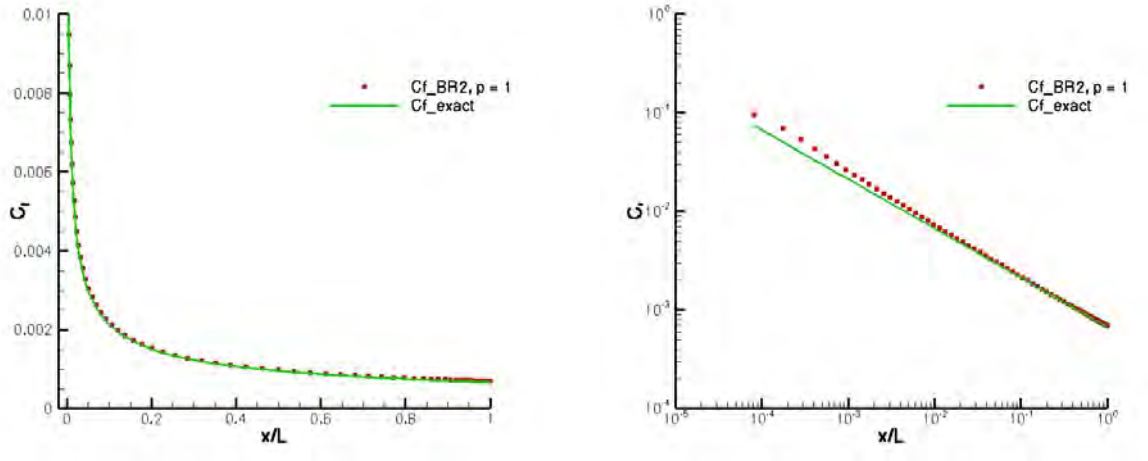

A regular scale B log scale

Figure 4-19. Flat plate solution with BR2 scheme and correct application of boundary conditions for the inviscid terms. C_f plots in A) regular scale and B) log scale compare very accurately to the exact Blasius solution.

CHAPTER 5
THERMAL ABLATION TEST CASES

In this chapter, we present some test cases that were attempted with DG method after having demonstrated solution capability for inviscid and viscous flow problems in the previous chapter. Our attention herein, is on solving the thermal response of a charring ablator. We choose three test cases,

- An arc-jet case by Ahn & Park ([15]), with carbon phenolic as TPS material
- Ablation test sample from 4^{th} AF/SNL/NASA Ablation Workshop, Albuquerque, NM
- Langley arc-jet test case

A charring ablator like carbon phenolic leads to generation of pyrolysis gases, which flows through through the porous ablating material and affects overall heating of the material.

As mentioned earlier, one of the first material thermal response codes, CMA does not take the flow of pyrolysis gas through the ablating material into account. This assumption is valid for high heating rate entries, but not for low to moderate heating rate environments. This was the case for Pioneer Venus probes which went on their mission in 1978 [15]. This mission had 4 probes, which all entered the atmosphere of Venus, and sent back the data of thermocouple temperatures back to Earth. Wakefield and Pitts, 1980 [15] tried to reconstruct this data using CMA. They first tested the code with some arc jet cases, which accurately matched the experiment results.

When, however the temperature plots for actual probes were attempted to reconstruct, their results showed very high temperature rise for thermocouples, contrary to the data from thermocouples (see Fig. (1-5)). This anomaly in results was attributed in 1998 by Ahn et al. [36] to be connected to the lack of modeling of the flow of pyrolysis gas through the ablating media. As already noted, codes like CMA consider pyrolysis gas to leave the material as soon as it is generated. Their thermocouple temperature reconstruction came closer to actual data points received from the probes.

We try to compare our results with 1-D arc jet data that was obtained experimentally by Wakefield and Pitts and numerically solved by both [15] and [36].

5.1 1D Arc Jet Cases from Ahn & Park

Wakefield and Pitts, tested CMA code for carbon phenolic material by running some test cases in an arc jet heating facility, also known as Ames Advanced Entry Heating Simulator [84]. In this test facility, a test sample is exposed to a combined, yet mutually independent convective and radiative heating. Test sample is placed in centerline of a supersonic flow heated by an electric arc, and radiative heating is focused at the test sample by using argon arc radiation source and arc-imaging optics. A schematic from [84] is shown in Fig. (5-1).

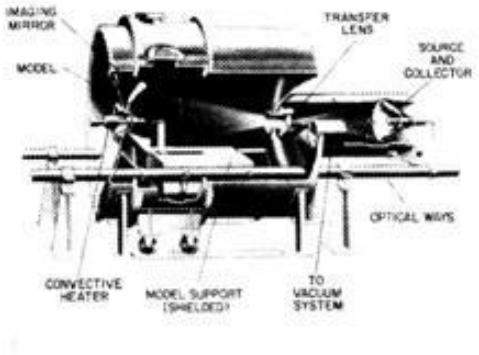

Figure 5-1. Advanced Entry Heating Simulator [84]. Test sample is placed in the center line of supersonic flow from left side, heated by electric arc, and radiative heating from right side is focused on test sample using argon arc radiation source and arc-imaging optics.

Here, the test sample is made of carbon phenolic and is exposed to a series of tests, (i) convective heat transfer of 1400 $\mathrm{W/cm^2}$, (ii) combined convective heat transfer of 1400 $\mathrm{W/cm^2}$ and radiative heat transfer of 2300 $\mathrm{W/cm^2}$, and (iii) radiative heat transfer alone of 600 $\mathrm{W/cm^2}$. Total time for exposure for these tests is 4-5 sec. For convective heating of 1400 $\mathrm{W/cm^2}$, surface pressure on the test sample is 0.22 atm and flow enthalpy is 23.3 KJ/g. These tests were close to actual flight heat fluxes and served to test the working of code by Wakefield and Pitts.

5.1.1 Material Properties of Carbon-Phenolic

Carbon phenolic has two components, phenolic resin and graphitic carbon. The resin component undergoes decomposition with rise in temperature, and releases a mixture of gases called pyrolysis gas. The rate of decomposition of the resin component, R, expressed as an Arrhenius equation is written in terms of temperature, T and resin density, ρ_{r} in Eq. (5–1),

$$\mathrm{R} = \sum_{\mathrm{k}=1}^{\mathrm{N}} \left(-\frac{\mathrm{B_k}}{\mathrm{T}} \right) \rho_{\mathrm{v}} \left(\frac{\rho_{\mathrm{r}}}{\rho_{\mathrm{v}}} \right)^{\mathrm{n}} \tag{5–1}$$

Here, ρ_{v} is the density of virgin material. This expression was evaluated in many previous works and also given in [36]. Here N = 2, and n is also taken to be a constant equal to 2. Activation Energy, $\mathrm{B_k}$ is taken to be 3544 and 19680 K for k = 1 and 2 respectively and constants $\mathrm{A_k}$ are 677 and $1.64 \times 10^{9} \mathrm{s}^{-1}$ for k = 1 and 2 respectively.

Thermal conductivity and specific heat were measured experimentally in [15], and are given in Fig. (5-2). The expressions were curve fitted and are given in Eq. (5–4). As indicated in [15], these properties are measured for virgin material from 250 K to 480 K and for the char material from 250 K to 3000 K. The temperature range for virgin material was taken before the onset of pyrolysis.

$$\mathrm{Cp_c\,(T)} = \mathrm{c_1 z^4 + c_2 z^3 + c_3 z^2 + c_4 z + c_5 J/kg - K} \tag{5–2}$$

$$\mathrm{Cp_r\,(T)} = 1174 \mathrm{J/kg - K} \tag{5–3}$$

$$\log_{10}\left(\mathrm{k\,(T)}\right) = -6.5 \times 10^{-8} \mathrm{T}^2 + 5 \times 10^{-4} \mathrm{T} - 0.1 \tag{5–4}$$

The virgin and char density are given to be 1490 $\mathrm{kg/m^3}$ and 1240 $\mathrm{kg/m^3}$ respectively. The elemental composition of resin material is given as C: 1.3527, H: 6.4557, O: 1 by mole. Heat of formation for carbon-phenolic was given to be 372 J/g. Governing equations for 1-D thermal ablation are used for the results shown.

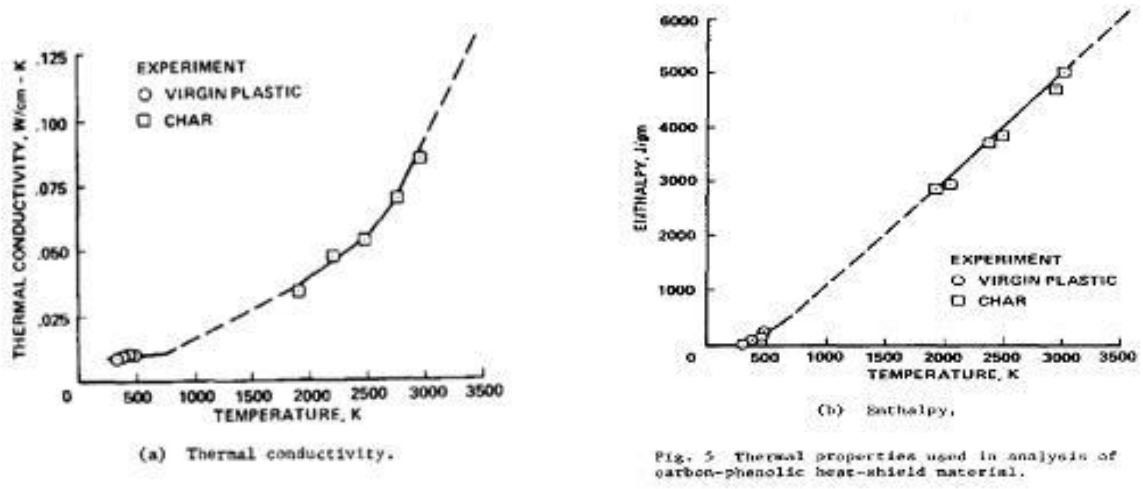

A B

Figure 5-2. Thermal conductivity and enthalpy of carbon phenolic for virgin plastic and char material as given in [15]. Properties for virgin plastic were measured from 250 K to 480 K and for char from 250 K to 3000 K.

5.1.2 A Comment on Governing Equations Used in This Work

Here, we use governing equations used by Ahn et al. in their two papers [36] and [17]. We will refer to them as 1998 and 2002 paper respectively, in this work to highlight the modeling differences in both the papers. These equations include decomposition of the resin material and energy balance in both the char and resin material. This is the norm in many thermal response codes as noted in chapter 1. Most thermal response codes with exception of SCMA (by Ahn et al.) and a series of papers by Martin et al. and Amar et al. [32, 33, 44, 53], do not take into account the flow of pyrolysis gas through the ablating medium.

Hence, any cooling by flow of pyrolysis gas will be neglected resulting in over-prediction of temperature distributions in the ablating material. This will result in a conservative design of TPS, which will not be cost effective. Papers by Martin et al., consider the role of pyrolysis gas in Energy equation, but the flow velocities are evaluated using Darcys equation or Forchheimer correction (for non-Darcy flows). But, for our work, we solve for

a conservation equation for mass, momentum and energy balance for the pyrolysis gas. The governing equations are given in chapter 2.

5.1.3 Pyrolysis Gas Modeling

Resin material undergoes decomposition and produces a mixture of gases, known as pyrolysis gas. 14 gas species are considered, $\mathrm{C}, \mathrm{CH}, \mathrm{CH_2}, \mathrm{CH_3}, \mathrm{CH_4}, \mathrm{CO}, \mathrm{CO_2}, \mathrm{C_2}, \mathrm{C_3}$, $\mathrm{H}, \mathrm{HO}, \mathrm{H_2O}, \mathrm{O}$, and $\mathrm{O_2}$. These are assumed to be at thermal equilibrium at solid material's temperature and pressure inside, i.e. the gas gets sufficient time to absorb all possible energy from the solid, after it exits to atmosphere.

CANTERA [85], a thermochemical solver is used to evaluate thermodynamic properties of gas like molecular weight, internal energy, pressure etc as a function of temperature and gas density. Initial composition of the gas for calculation purposes is taken to be same as resin material, C: 1.3527, H: 6.4557, O: 1. The input to CANTERA for all thermodynamic calculations is through a CTI file, and properties like specific heat, enthalpy, and entropy are specified as functions of temperature, in terms of NASA polynomials, for each of the components of the pyrolysis gas. For non-equilibrium analyses, reactions and their rates (in Arrhenius coefficients) can also be specified in this CTI file. An equilibrium criterion is set to be at constant temperature and pressure. Fig. (5-3) shows the plots of internal energy, $\mathrm{e_g}$, as a function of temperature and molecular weight, MW, as function of gas density and temperature.

The data points for both $\mathrm{e_g}$ and MW are exponentially fitted and their expressions are given in Eq. (5–6). It's essential to get a plot that grows monotonically and avoid any discontinuity in the gradients of these properties. The expression of $\mathrm{e_g}$, was obtained using TECPLOT, while 3D data for MW (in terms of temperature and density) was curve fitted using an online software [86]. We used second order polynomial in logarithm (of base 10) in density and fourth order polynomial in temperature. X-axis in Fig. (5-3) B) is from 2.952 to 9.288, which stands for temperature, y-axis is from -2.2 to 2.2, which stands for $\log_{10}(\rho_\mathrm{g})$ and z axis is from 4.872e-3 to 1.8317e-2, which is for molecular

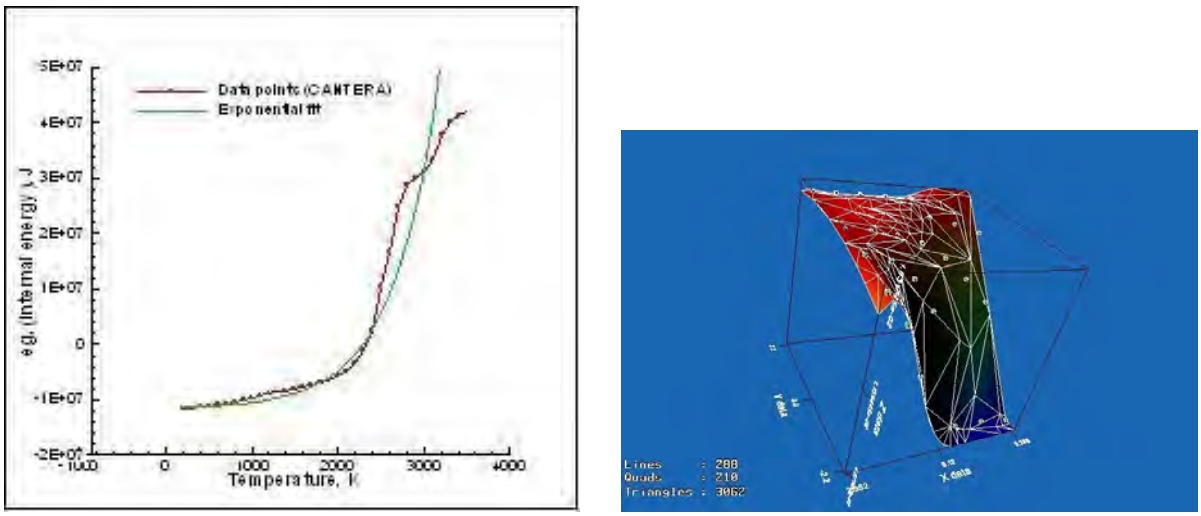

A B

Figure 5-3. Plots for A) internal energy, $\mathrm{e_g}$ as a function of temperature, T where red line indicates data points from CANTERA and green line is curve fitting using TECPLOT. B) Molecular weight of gas, MW represented by z-axis in terms of gas density, ρ_g represented by y-axis and temperature, T represented by x-axis. The data was obtained from CANTERA [85], and surface fitting for right plot was done through online software [86].

weight, MW of gas in kg/mol. CANTERA can also be used for including effects of chemical reactions in the flow solver.

We have used two curve fits for internal energy, $\mathrm{e_g}$. In Fig. (5-3) A), we fitted the data points with one single exponential curve for whole range between temperatures of 200 K and 3400 K, but this curve under predicts internal energy for temperature range of 2400 K to temperature range of 3000 K and then over predicts. For temperature range below 3000 K, this under-prediction of internal energy is significant, and will result in lower cooling provided by the flow of gas, therefore for more accurate prediction we choose second curve as shown in Fig. (5-4).

$$\mathrm{e_g} = \exp\left(\mathrm{A_1 T} + \mathrm{A_2}\right) - \mathrm{A_3} \tag{5–5}$$

$$\mathrm{MW} = \mathrm{B_1}\exp\left(\mathrm{y}\right) + \mathrm{B_2}\exp\left(\mathrm{x}\right) + \mathrm{B_3}\exp\left(\mathrm{x}\right)\exp\left(\mathrm{y}\right) + \mathrm{B_4} \tag{5–6}$$

Here, $A_1 = 1.869 \times 10^{-3}, A_2 = 11.98$ and $A_3 = 1.156 \times 10^{7}$. For the expression of the molecular weight, MW in Eq. (5–6), x and y depend on the temperature and the gas density respectively as, $x = (T/1000)^2$ and $y = \log_{10}(\rho_g)$, and constants are $B_1 = 1.7981 \times 10^{-4}$, $B_2 = -1.333 \times 10^{-6}$, $B_3 = 2.0159 \times 10^{-7}$, and $B_4 = 1.678 \times 10^{-2}$.

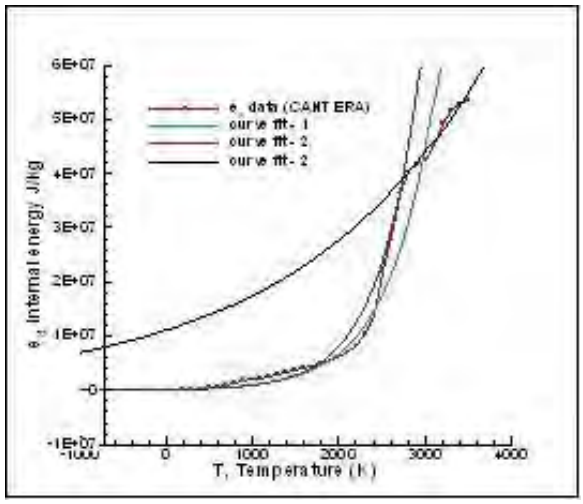

Figure 5-4. Second curve-fitting for internal energy, e_g in terms of temperature, T. Black curve is used from 2800 K to 3400 K and blue curve is used from 200 K to 2800 K.

5.1.4 Boundary and Initial Conditions

Total grid size is taken to be 1 cm, and the inner boundary is fixed at x = 0 cm and outer boundary at x = 1 cm. Boundary conditions are as follows. No boundary conditions are needed for first equation of Eq. (2–67), since it's a pure unsteady differential equation. For second equation of Eq. (2–67), no boundary conditions for $\epsilon\rho_g$ are specified at x = 0 cm. At x = 1 cm, $\epsilon\rho_g$ is found by solving the state equation, i.e. molecular weight as a function of $\epsilon\rho_g$ and T, which basically relates pressure, gas density and temperature. Pressure at x = 1 cm, is given to be 0.22 atm (Arc jet case in [15] and [36]), and temperature will be known by solids temperature. For third equation of Eq. (2–67), u is taken to be 0 m/s and adiabatic boundary condition for temperature exists at x = 0 cm for fourth equation.

At x = 1.0 cm, first equation of Eq. (2–67), as mentioned, doesn't need a boundary condition. Boundary condition for second equation has already been specified above. No boundary condition is applied on velocity at x = 1.0 cm. For temperature, an incoming heat flux (in negative X direction) of 1400 $\mathrm{W/cm^2}$ is specified. Initial conditions are uniform throughout the domain for all 4 variables; ρ_r is 250 $\mathrm{kg/m^3}$, $\epsilon\rho_\mathrm{g}$ is $6.05 \times 10^{-3}\mathrm{kg/m^3}$ (evaluated at P = 0.22 atm, and T = 300.0 K), u is 0 m/s and T is 300.0 K.

5.1.5 Results

Wakefield and Pitts conducted an arc jet wind tunnel experiment with the carbon-phenolic sample, which was exposed to a heat flux of 1400 $\mathrm{W/cm^2}$. They compared their results with CMA simulation, and these results were also published by Ahn and Park. Total run time for the problem is 5 sec, and surface pressure and enthalpy at the exit are 0.22 atm and 23300 J/g. Total thickness of model domain is 1 cm.

Here we consider two cases, by Ahn and Park in their 1998 and 2002 papers. Differences in both cases were noted in chapter 1. First we present results for case with D = 0, which was considered in the 1998 paper. In Fig. (5-5) A) and B), we show spatial distribution of solution variables at a time of 4 sec. From Fig. (5-5) B), we can see from plot of resin density that pyrolysis zone extends from 2 mm to 4 mm. Other two regions that can be identified are virgin plastic ($\rho_\mathrm{r} = 250\mathrm{kg/m^3}$) and char zone ($\rho_\mathrm{r} = 0\mathrm{kg/m^3}$).

Pressure varies from a value of nearly 8 atm in the region of virgin plastic, where it is flat, to as low as 0.1 atm on the right side of domain. High pressure gas gradient is observed at the pyrolysis zone, but the gas flow is actually driven by the gradient of product of gas pressure, P and void fraction, ϵ. This is seen in the jump of velocity magnitude at the pyrolysis zone, and higher velocities are attained at the right boundary due to a steeper gradient of $\epsilon\mathrm{P}$. We also observe some numerical artifacts on solution of gas momentum, since gas momentum has friction which acts as a dominant source term. We also observe cooling effect of pyrolysis gas from these plots.

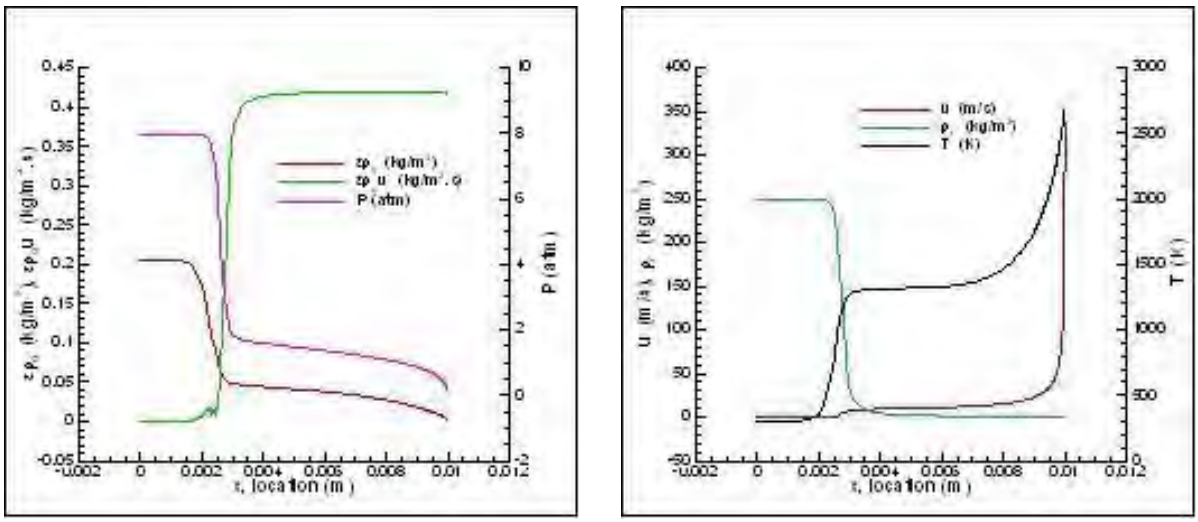

A B

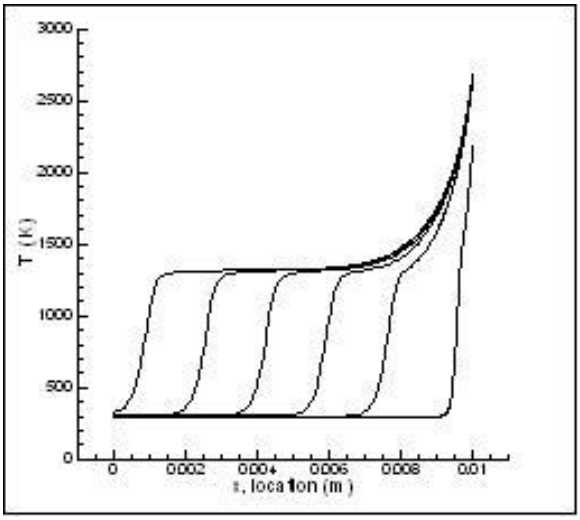

C

Figure 5-5. DG Simulation results for thermal ablation problem with diffusion coefficient, D = 0. A) Plots of gas density, flux and pressure are shown at t = 4 sec, B) Plots of gas velocity, resin density and total temperature are shown at t = 4 sec and C) temperature distribution plotted at time = 0.1, 1, 2, 3, 4, and 5 sec to show the cooling effect of pyrolysis gas.

In Fig. (5-5) B), temperature profile of the material has a steeper gradient at the beginning of pyrolysis zone at around 2 mm, as compared to elsewhere in domain. There are two heating mechanisms in the domain, thermal conduction and convection cooling. In beginning of pyrolysis zone, we only observe thermal conduction, whereas at other places we observe both convection cooling and conduction. This explains the observed temperature distribution and the trend of thermal response can be seen in Fig. (5-5) C), where we see that a steep rise in temperature is slowed down by the convection cooling of the exiting pyrolysis gas.

And, based on our calculations, we observe that increase in the pyrolysis gas density in the virgin plastic zone is due to the resin decomposition term, R, which also leads to corresponding gas generation. But temperature at virgin zone is 300 K, so value of R should be very close to zero, which is not the case with model chosen in Ahn et al. This tells that gas generated due to pyrolysis primarily leaves out to the atmosphere.

Both friction and inertia terms in 2002 paper provide resistance to gas flow, so if their values are higher than in 2002 paper (this is exactly the case with 1997 paper) they would provide sufficient resistance to the flow, which would lead to significant rise in values for gas density in virgin plastic domain. We also observed a difference in results shown in Ahn and Park in their two papers for the result of gas pressure for the day probe. Pressure in the virgin plastic domain for 1997 paper is nearly 75.67 atm, and that in 2002 paper is nearly 30 atm at flight time = 27 sec. We are investigating this difference in two models between 2 papers.

In the above plot, Fig. (5-6), we compare our results for temporal variation of surface temperature (on right side of domain). We provide results for our simulation for both curve fit 1 and curve fit 2 for internal energy, $\mathrm{e_g}$. As we have already mentioned that curve fit 2 is more accurate than curve 1, we find that our results match the experimental results for initial 1 sec, and after that due to high gas velocity, there′s no further rise in the observed temperature. High gas velocity leads to high cooling

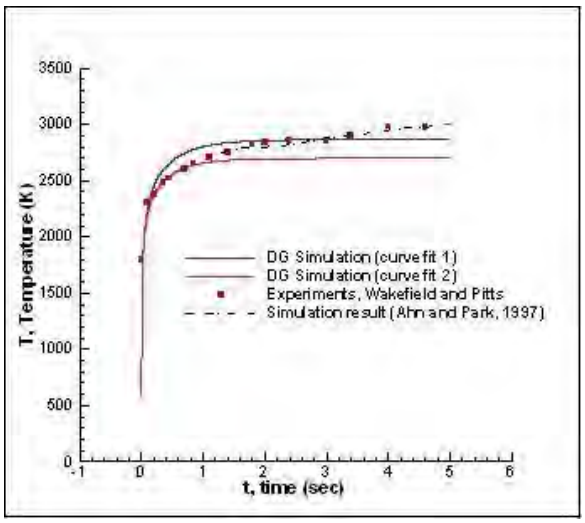

Figure 5-6. Temporal variation of surface temperature for DG simulation with D = 0, and comparison with Ahn and Park simulations [60] and experimental results [5].

at the surface, which exactly balances out net heat influx to the surface and thermal conduction.

Second case that we present is with nonzero diffusion term in Eq. (2–67). This case is exactly similar to Ahn and Park, 2002. Shown below in Fig. (5-7), are the results for solution variables at time of 4 seconds, to highlight the differences in both the models of 1998 and 2002 paper. Diffusion term in momentum equation is related to the second derivative of pressure, and results in more diffused profile for gas density. Pressure is related to gas density and temperature, and both are more diffused out, which causes a lower pressure (actually $\epsilon \mathrm{P}$) gradient that drives the flow, and therefore we get lower gas momentum near exit, as compared to case D = 0. Therefore we find these results are consistent with basic gas dynamics.

Due to the diffusion term, gas velocity is lower, hence lower cooling as compared to case with D = 0. Therefore we observe diffused temperature profile in this case. This in turn affects the decomposition of resin material and we see a broader pyrolysis zone in this case, which extends roughly from 3 mm to 7 mm. This diffusion mechanism is in general better for the vehicles body since it provides for more time that the vehicle gets before its temperature starts to increase. E.g. temperatures above 500 K are observed

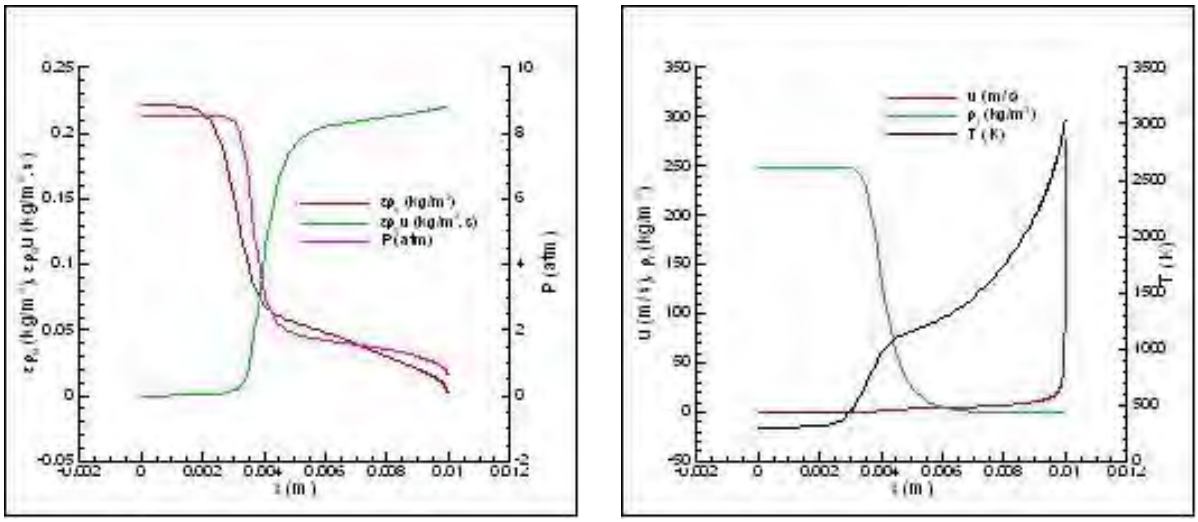

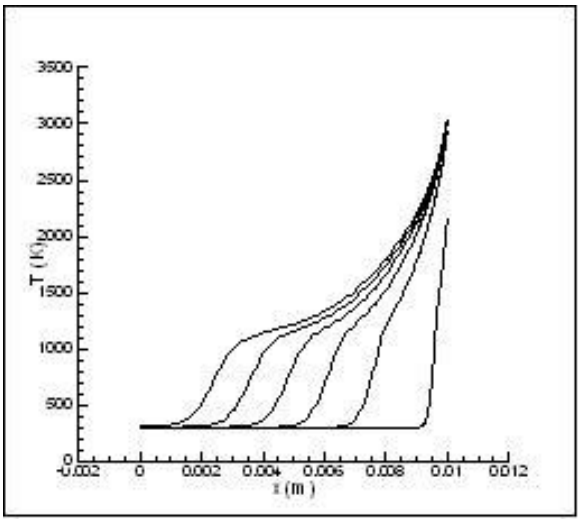

Figure 5-7. DG Simulation results for thermal ablation problem with nonzero diffusion term, A) Plots of gas density, flux and pressure are shown at t = 4 sec, B) Plots of gas velocity, resin density and total temperature are shown at t = 4 sec and C) temperature distribution plotted at time = 0.1, 1, 2, 3, 4, and 5 sec to show the cooling effect of pyrolysis gas. As compared to case with D = 0, we see that all the profiles appear to be more diffused, and the pyrolysis front also travels with slower speed than compared to D = 0 case.

at location of 2.25 mm for earlier case (D = 0) and for this case at location of 3.17 mm at time of 4 sec. Theres no significant difference in pressure for both cases, pressure in this case is approximately 0.5 atm higher than that of case-1. Velocities in the domain for this case are lower as compared to case with D = 0, therefore we have lower cooling within the domain, and since conduction heat conduction is a diffusion mechanism, we observe more diffused profiles of temperature. So, from looking at temperature profile we can tell which effect is dominant, conduction or convective cooling.

Below we compare (Fig. (5-8)) the temporal variation of surface temperature with simulation results by Ahn and Park, 2002 and experimental results by Wakefield and Pitts, 1980. Again we plot the results for both curve fits-1 & 2 for internal energy. Our surface temperature shoots to higher value at later time than experimental results. Reason for this as already explained is lower cooling for this case. Given our lack of clarity about some aspects of their model, our plot is close to experiment results.

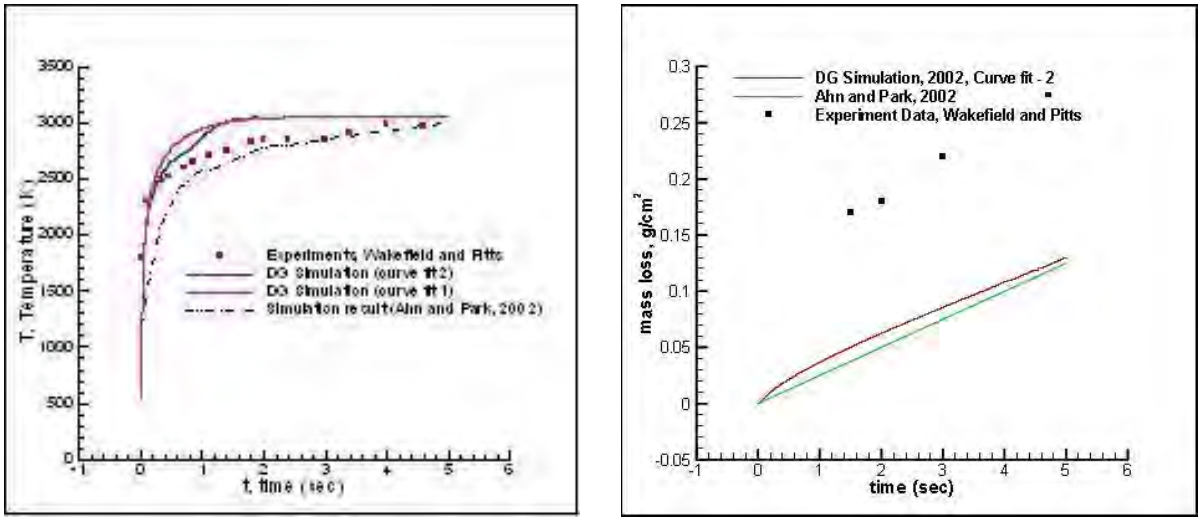

A B

Figure 5-8. A) Temporal surface temperature variation for non zero D and 2002 paper, B) mass loss comparison with 2002 paper and experimental results. Mass loss in our simulations is over-predicted by an error of 3.2 %

We also compare result for mass loss of TPS material with the simulation results shown in 2002 paper, and our results are close to their results with an over prediction

error of 3.2 % . The experiment results differ from simulation results by a constant. The reason for this is ascertained to be mass loss that occurred while the test sample was moved from edge of the stream (in arc jet wind tunnel) to center of the streamline and while removing the sample from the center of streamline. The fact that both experiment and simulations have same slope, indicates that mass loss predicted by the model is accurate.

5.2 Ablation Workshop Cases

In this section we present results for a TACOT case, presented in 4^{th} AF/SNL/NASA Ablation Workshop, Albuquerque, NM for an Inter-code comparison exercise carried out in the workshop. In this workshop, an ablation test case was designed and compared on different ablation codes worldwide. The purpose of the exercise was two folds, to inter-calibrate the similar type codes (code types being identified as type 1, 2 and 3 in the workshop) to compare the numerical methods, their respective merits and weaknesses and how the same input data (provided by the organizers) is interpreted and fed into their respective codes, by the participants.

Second purpose was to compare the outcome of modeling differences used in the different types of codes. Three types of codes were identified as type 1, 2 and 3. Type 1 codes considered basic heat transfer analysis, decomposition of the resin, equilibrium chemistry for pyrolysis gas and simplified transport for the gas. Type 2 added an average momentum equation for the pyrolysis gas, where type 3 considered high-fidelity physics like non-equilibrium thermochemistry for the gas, in-depth ablation etc.

A theoretical ablative model, titled, TACOT or Theoretical Ablative Composite for Open Testing, was developed with thermo-chemical properties close to those of low density ablators, for meaningful model comparison. Architecture of the material is chosen such that the material can be easily manufactured but is good only for ground testing, and not for actual re-entry flights, so that the scope of this exercise could be

broadened to international participation. The material selected for the model was highly porous (80 % porosity), and consisted of 10 % (by vol. fraction) of ex-cellulose carbon fibers coated by a matrix of ex-novolac/formaldehyde polymer, which constitute another 10 % of the volume fraction.

The material densities for both carbon fibers as well as matrix are 1600 $\mathrm{kg/m^3}$ and 1200 $\mathrm{kg/m^3}$ respectively. Thermal conductivity and specific heat of the virgin and char materials, were taken from [34] in this exercise and are plotted with temperature in Fig. (5-9) below. Enthalpies of the char and virgin materials can be calculated from integration of the specific heats, along with formation enthalpies of char and virgin material being 0 J/kg and -2×10^6 J/kg respectively (at 298 K). Enthalpy of the material at any time can be calculated by considering the material to be mixture of both virgin and char at temperature of the solid.

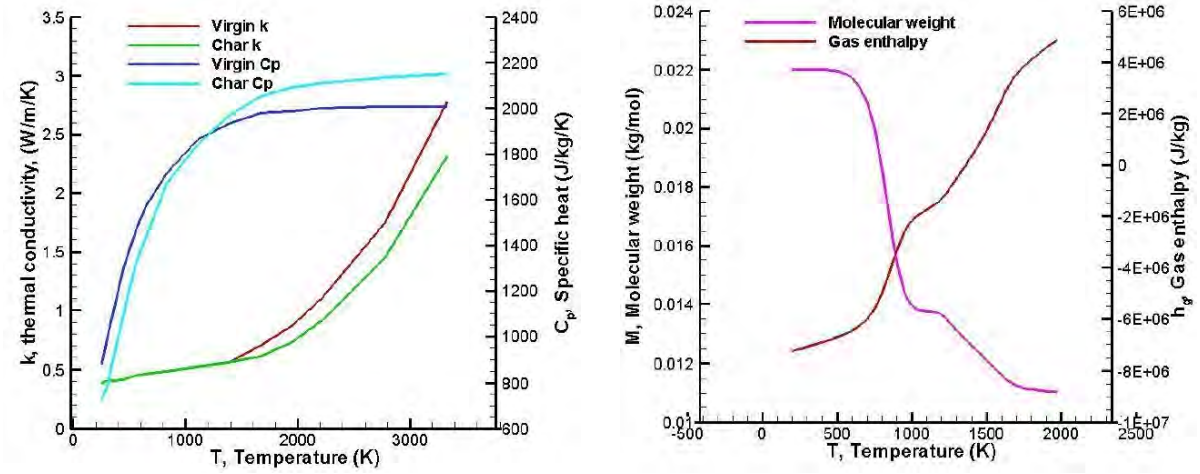

A B

Figure 5-9. A) Thermal conductivity and specific heat for virgin and char material plotted with temperature, B) Molecular weight and gas enthalpy of the gas using thermo-equilibrium assumption

For type 2 codes, the porosity of the material is taken to be 0.8 for virgin and 0.85 for char material. Permeability for virgin and char are 1.6×10^{-11} and 2.0×10^{-11} respectively, and were evaluated from the DNS simulation. The products of pyrolysis

gas from decomposition of phenolic were obtained from [87] by George F. Sykes, and elemental composition of C, H and O was determined from this to be, 0.206, 0.679 and 0.115 respectively (in mole fraction). This elemental composition of the pyrolysis gas products is used to evaluate thermal properties for pyrolysis gas assuming thermo-chemical equilibrium of the gas at the temperature of solid material. Above in Fig. (5-9) B), we provide the plots for molecular weight, M and the gas enthalpy for the pyrolysis gas, $\mathrm{h_g}$, based on the thermo-chemical equilibrium assumption. The above pyrolysis gas properties are a function of temperature at the pressure of 1 atm.

The domain for the problem is 5 cm; Boundary conditions on right side are known temperature as a function of time, and outside pressure of 1 atm. The right side temperature as a function of time is given below in Fig. (5-10). Left side of the domain is adiabatic and no flow condition (i.e. u = 0) is also considered.

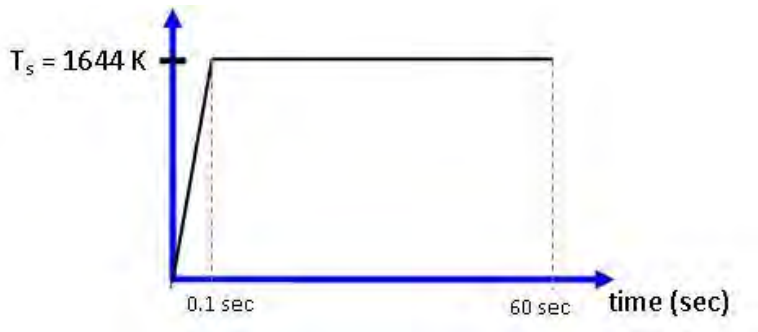

Figure 5-10. Boundary condition at the right side of the domain, with temperature varying as a function of time.

The total run time for simulation is 1 min, and the results from MIG-DG are plotted against the baseline case, run by FIAT, a commercially used NASA material response code. Fig. (5-11) shows comparison of the temporal variation of temperatures at the surface and at hypothetical thermocouple locations at depths of 1, 2, 4, 8, 16 and 50 mm. We observe that temperature increases at all depths except 50 mm, which is the left end of the domain and is considered adiabatic. So, we observe that over a period of 1 min, the effect of high surface-temperature boundary condition doesnt reach the left

end, which is assumed to be connected to the vehicles body. Our results are very close to the results of FIAT, for outside thermocouple locations, however we under-predict the temperatures by around 5 % errors at the more inside thermocouples (at 8 and 16 mm depths). We also show our results for the mass loss rate of the pyrolysis gas at the exit of the domain, and virgin and char depths with time in Fig. (5-11) B).

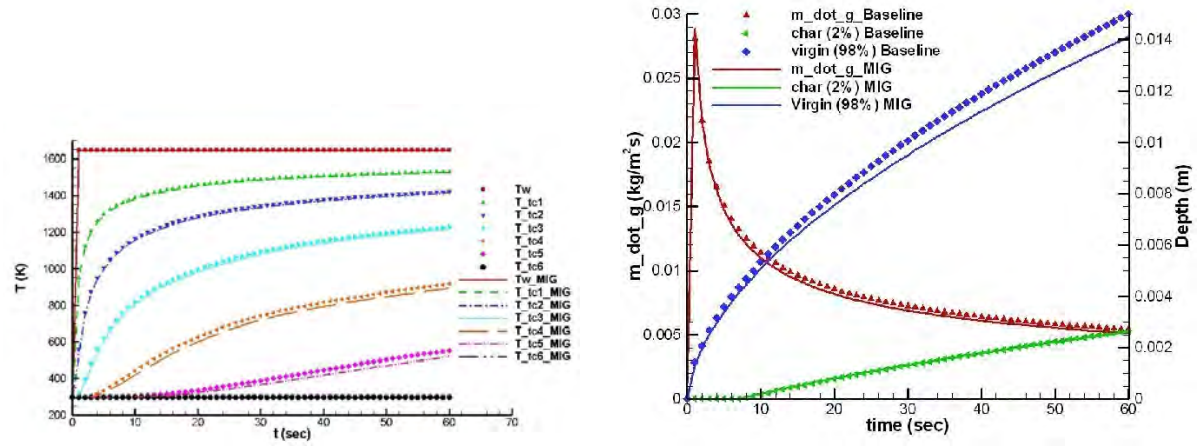

A B

Figure 5-11. Comparison of results for A) temporal variation of surface temperature and thermocouples at the depth of 1 mm, 2 mm, 4 mm, 8 mm, 16 mm and 50 mm, with reported results from FIAT in the ablation workshop, results from MIG agree very closely to the reported results from FIAT, and B) mass loss rate from the exit of the sample to outside and comparison of char and virgin material depths with time varying from 1 sec to 60 sec.

Next, we solve Langley arc jet test case to match the experiment results given in [88]. This way we demonstrate our capability to solve for both thermal ablation and hypersonic flow problems in one single framework.

5.3 Langley Arc Jet Test Case

The test sample used in this work, is shown in Fig. (5-12). The sample has 1.27 cm of thickness at its centerline, it is axisymmetric with nose radius of 7.98 cm at the stagnation point [88].

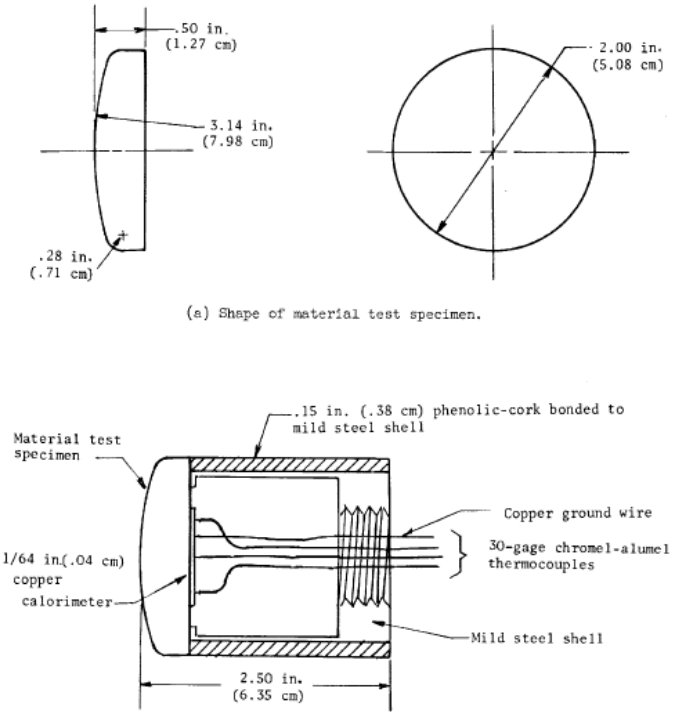

Figure 5-12. Test Sample from Sutton.[88]

We have used different sources for identifying the material properties of the test sample and the pyrolysis gas. We setup this case by using Fay Riddell model, to find heat flux at the surface, described in the next section.

The test sample′s geometry allows the problem to be analyzed as 1-D, 2-D and 3-D. The problem nature is essentially 2-D and 1-D is a good approximation as well.

5.3.1 1-D Ablation Test Case with Fay Riddell Model

For 1-D ablation test case, we take the sample size of 1.27 cm (size of the sample at the stagnation point). Fay Riddell model describes the surface heat flux for given amount of dissociation of the air at the boundary layer edge. Sutton [88] gives the cold heat wall stagnation surface heat flux for this particular test to be 1.45 $\mathrm{MW/m^2}$. Using the expression for surface heat flux, given below.

$$\mathrm{q"_s} = \frac{0.768}{\mathrm{Pr}^{0.6}} \left(\rho_\mathrm{e}\mu_\mathrm{e}\right)^{0.4} \left(\rho_\mathrm{w}\mu_\mathrm{w}\right)^{0.1} \left(\mathrm{H_e} - \mathrm{H_w}\right) \left(1 + \left(\mathrm{Le}^{0.52} - 1\right) \frac{\mathrm{h_d}}{\mathrm{H_s}}\right) \left(\frac{\mathrm{du}}{\mathrm{dx}}\right)_\mathrm{e}^{0.5} \tag{5–7}$$

In above formula, index $'\mathrm{e}'$ denotes the edge of boundary layer formed on the body in the hypersonic flow, and $'\mathrm{w}'$ denotes the wall or the surface of the body at the stagnation point. Fay Riddell model is only valid at the stagnation point, hence is useful to predict heat flux at the stagnation point when a flow solver to solve the hypersonic flow outside the body is not present. In our case, Fay Riddell model serves as a useful first step before doing both the flow solver and the ablation in a single framework.

To use the Fay Riddell model, our first objective is to predict the amount of dissociation present in the air at the boundary layer edge, after the flow has moved through the shock into the shock layer. This will be done by matching $\mathrm{q_s^"}$ found from Eq. (5–7) to the cold wall heat flux given from the experiment (= 1.45 $\mathrm{MW/m^2}$). It is also given that the wall is super-catalytic, hence all species present in the flow, close to the wall, must combine into free stream species. Hence at the wall, we will only have $\mathrm{O_2}$ and $\mathrm{N_2}$. The cold wall temperature is 300 K. The temperature of the gas at the boundary layer edge is found by dividing the stagnation enthalpy by the specific heat for the composition of air at the boundary layer edge. Hence we can find out the amount of composition of gas in the boundary layer edge for which the heat flux from the Fay Riddell model will match the cold wall heat flux provided from the experiments. Thus, knowing the air composition at the boundary layer, we can employ the Fay Riddell model to predict wall heat flux for the 1-D ablation test case.

In this section, we will give graphs of material properties for both solid and gas, taken from different references. Also given are curve fits fitted to these graphs, along with their equations.

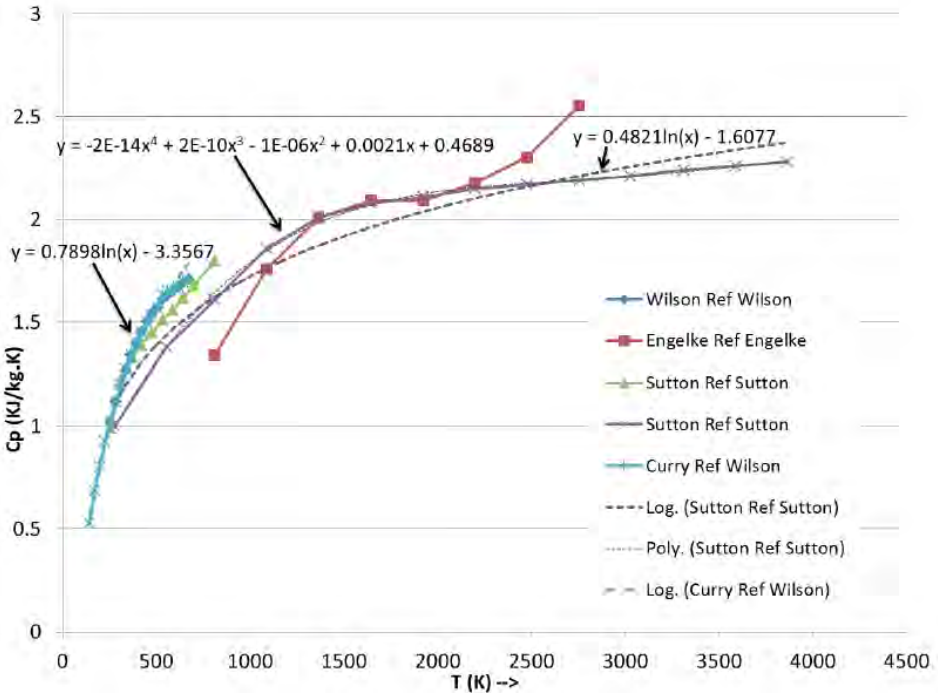

Figure 5-13. Specific heat plots for Narmco 4028 gathered from different sources. Curve equations were fitted to these data points for use in MIG.

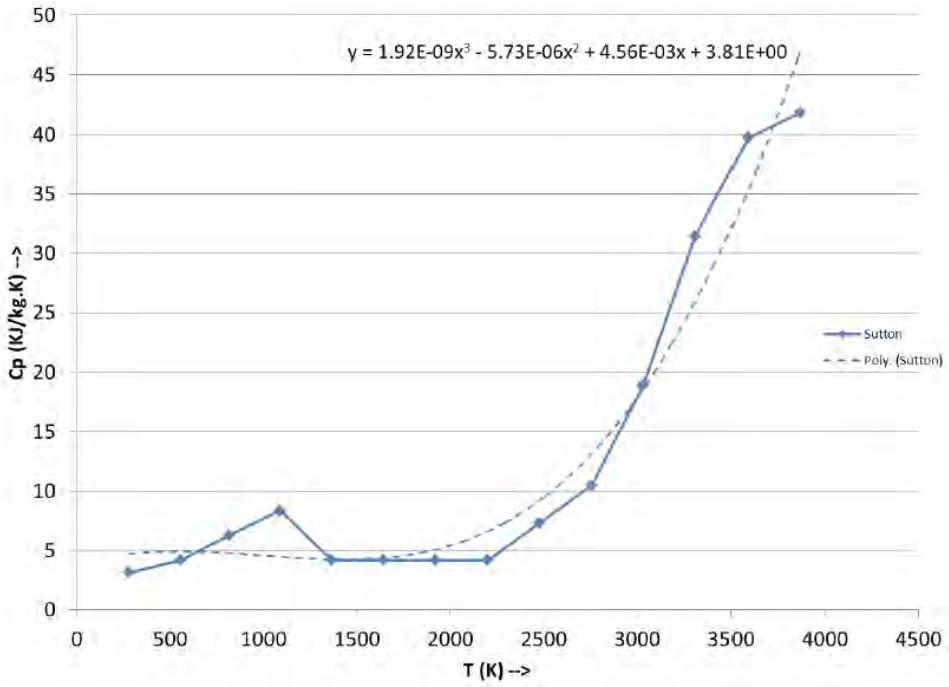

Figure 5-14. Specific heat plot for gas gathered from Sutton. Curve equation is fitted to these data points for use in MIG.

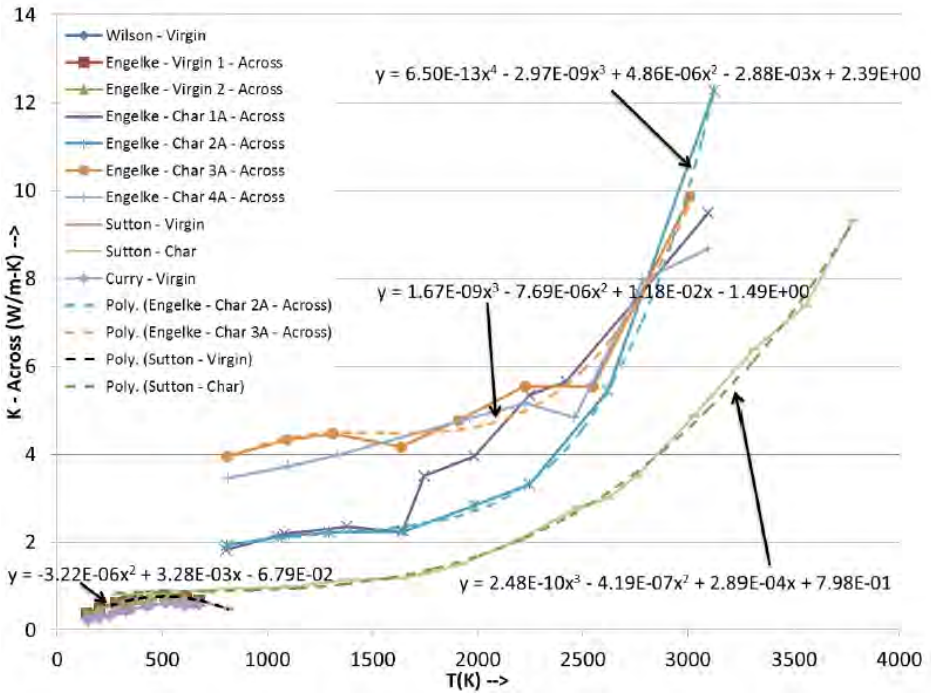

Figure 5-15. Thermal conductivity plots for Narmco 4028 with perpendicular fibers gathered from different sources. Curve equations were fitted to these data points for use in MIG.

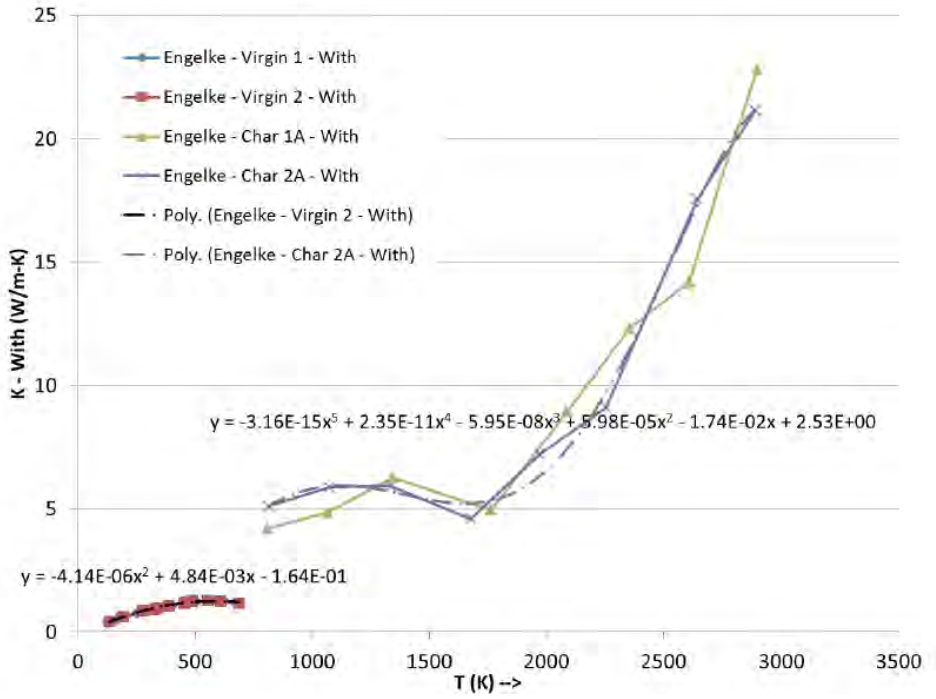

Figure 5-16. Thermal conductivity plots for Narmco 4028 with parallel fibers gathered from different sources. Curve equations were fitted to these data points for use in MIG.

5.3.2 Simulation Results

After working on hypersonic flow cases to have a working code for chemically reacting flow in thermal non-equilibrium, we now present our results for thermal ablation problem for Langley arc jet test case. We consider first data point in Table IV in Suttons work [88]. Here the pressure at the stagnation point of the test sample is 0.07 atm (7091 Pa) and the cold wall heat flux is 1.45 $\mathrm{MW/m^2}$. Mass fraction of atomic oxygen therein is given to be 0.23, which implies that all of $\mathrm{O_2}$ in the boundary layer edge is oxidized to O. Using this information and varying the mass fraction of atomic N and $\mathrm{N_2}$ at the boundary layer edge, we determine the amount of N in boundary layer edge that gives the Fay-Riddell heat flux at the stagnation point (at 300 K surface temperature of the stagnation point) to be equal to the given value of the cold wall heat flux of 1.45 $\mathrm{MW/m^2}$. We get mass fraction of N and $\mathrm{N_2}$ to be 0.47 and 0.3 respectively. Thus for these given values of gas composition in the boundary layer, we now can use Fay-Riddell heat flux to provide for heat flux due to outside hypersonic flow at the wall as a function of wall temperature.

Using this, we ran 1-D thermal ablation problem and got following results in comparison to experimental temporal variation of surface and back-surface temperatures published in [88].

We see that we very closely match the results for temporal variation of surface and back-surface temperatures for the Langley arc jet test case with the experiments (see Fig. (5-17)).

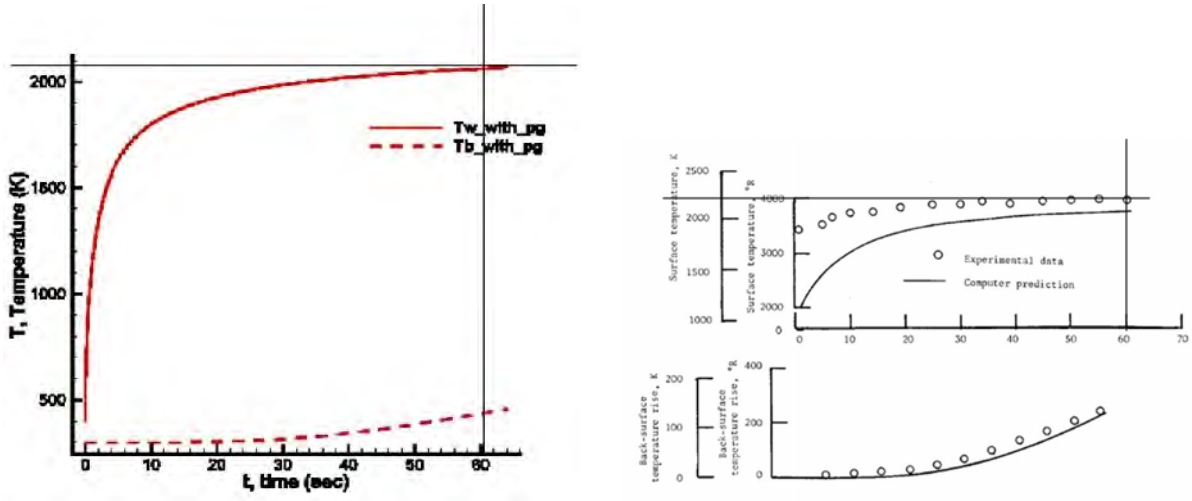

A B

Figure 5-17. Temporal variation of surface and back-surface temperatures for the Langley arc jet test case is shown. Comparison is made between results we obtained in MIG to those given in [88]

CHAPTER 6
HYPERSONIC FLOW CASES

This chapter focuses on hypersonic flow simulation outside a given body. Even though, numerical effort at simulating hypersonic flows began a few decades before, this is still a challenging problem, as has been demonstrated from examples presented in chapter 1. In this chapter we consider, hypersonic flow over cylinder and demonstrate solution capability for inviscid and viscous hypersonic flows, followed by hypersonic flows with full thermo-chemical non-equilibrium.

As mentioned in chapter 3, we employ two methods to capture shocks in the hypersonic flows, r-p adaptivity with p = 0 for shock regions and r-p adaptivity along with slope limiter to capture shock with higher (≥ 1) order of accuracy. We also implement time-implicit solutions for higher CFL numbers and hence faster solution turn around time.

Previous applications of DG method were limited to viscous hypersonic flows ([2, 10]). Here we extend DG to chemically reacting hypersonic flows with thermal non-equilibrium. Use of p-adaptive method, allows us to interpolate non-smooth shock region with piecewise element-averaged polynomial (p = 0) and with higher order polynomials (p $\geq$ 1) where the flow features are mathematically smooth.

Also by redistributing (r) elements in critical regions about shock, we get accurate solutions without employing excessive mesh elements (h). Specifically we study the flow over a stationary cylinder using (i) inviscid, (ii) viscous, and (iii) thermo-chemical non-equilibrium flow regimes. We compare our simulations with published results.

6.1 Hypersonic Flow Over Cylinder

Approaches, available in the literature, have so far focused on using either the slope limiters [59] or the artificial dissipation scheme [2, 79] to capture the shocks especially for the hypersonic flows. An approach to capture the shocks without using either a slope limiter or artificial dissipation was attempted earlier in [10]. We think that this approach

is useful and more convenient to use in the case of DG methods and further explore its application to the viscous and thermo-chemical nonequilibrium hypersonic flows.

It is well known that p = 0 (the first order accurate method) is sufficient to capture a shock of any strength. Hence, using an effective shock indicator technique, we can apply p = 0 in the shock regions and higher order polynomial accuracy, p $\geq$ 1 in the smooth flow regions. We can focus on reducing the mesh size in the shock and increasing the order of accuracy in the smooth flow regime to increase the over all accuracy of the solution.

A recent work in DG methods, [2] has demonstrated that the sub-cell shock capturing (i.e. capturing the shock within an element using the artificial dissipation and a shock sensor) lacks robustness and may not be more accurate than super-cell shock capturing or refinement (capturing the shock within few elements of reduced size for more accurate shock capturing).

We also look into the shock refinement option rather than the shock capturing for high order DG method. We employ p-adaptivity to use p = 0 for shock region and p $\geq$ 1 for smooth flow. For refining the mesh near the shock, rather than going for h-adaptation, we choose r-adaptation in order to selectively refine only the cells near the shock. This can be implemented to hypersonic flow over any general body shape, with special interest for problems with detached shock.

In this work, we validate the steady state solutions, though for thermal ablation, its essential to obtain a time accurate solution response. Our implicit time scheme is first order accurate. We present validation of our results for inviscid, viscous and thermo-chemical non-equilibrium hypersonic flow problems. Here, we present results for p = 0 and 1.

Now we present the results for three cases of hypersonic flow over a circular cylinder. (i) Inviscid flow simulation for a freestream Mach number of 6 (compared with results from [10]), (ii) viscous hypersonic flow freestream Mach number of 17 (with

results compared from [2]), and (iii) flow with the thermo-chemical non-equilibrium for freestream Mach number of 17. These test cases serve as benchmark cases to validate our code for solution capability to solve hypersonic flow problems of varying degree of complexities.

6.1.1 Inviscid Hypersonic Flow

Here we solve for inviscid hypersonic case, using r-p adaptivity. First we simulate the problem with p = 0 everywhere to steady state (see Fig. (6-1)). Then this solution is taken, and by using shock sensor and p-adaptivity method, we apply p = 1 solution in regions with smooth flow features and p = 0 in regions of shock (see Fig. (6-2)).

The jump indicator based on pressure jump values (see 3.7) over each edge of the element is used to distinguish between shock and smooth flow regions. This jump indicator ([2, 10]) is found to be more robust in comparison to the smoothness indicator in [79]. Also for time accurate simulations, starting from uniform flow as initial solution, when the shock moves along the elements, smoothness indicator fails to provide distinction between regions with p = 0 and p $\geq$ 1. Shock indicator based on pressure jump does not face this issue.

After we obtain a steady state solution with p = 0 and p = 1 using p-adaptivity, we apply r-adaptivity, where using the shock location, we compress the domain bringing it closer to shock. This results in clustering of all the elements on domain outside shock and within shock, close to the shock. The elements can also be clustered in a fashion so that elements closer to shock are finer than elements away from the shock. Thus the shock can be accurately captured, with small mesh elements. This can be repeated several times to get shocks location accurately. After we obtain steady solution on this mesh, we can proceed to p-adaptivity method with p = 2 in smooth flow region and p = 0 in shock regions. This can be extended to higher values of p to increase order of accuracy within smooth region.

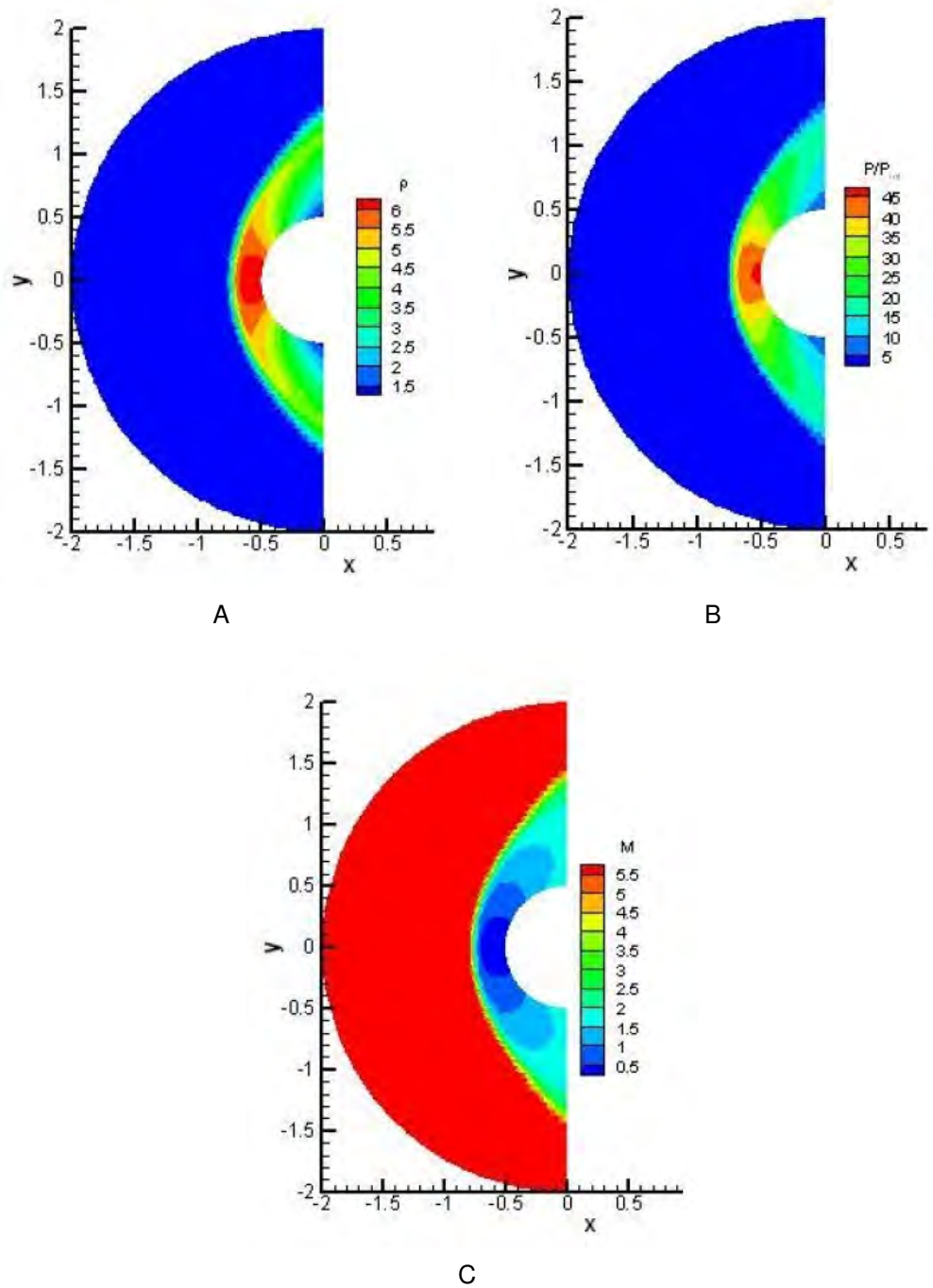

Figure 6-1. Inviscid Hypersonic case (p = 0 results). A) Density contours, B) P/P contours, and C) Mach number contours are shown. Mesh is 128 100 elements, 128 in circumferential direction and 100 in radial direction, with finer mesh close to cylinder. Pressure and Mach contours compare well with results published in [10].

In Fig. (6-1), we show steady state solution obtained with p = 0 for the inviscid hypersonic problem. We show density, pressure (P/P_∞) and Mach number contours. These contours are comparable to the contours given in [10]. Our next step is to obtain contours with p-adaptivity using p = 1 in regions of shock and p = 0 in smooth flow regions. For this, we take the steady state solution obtained from above figure, using only p = 0 everywhere, and using shock detector based on pressure jump, apply p = 1 in smooth regions and p = 0 in shock regions. Shock location is evaluated at every time step, and p = 0 and p = 1 accordingly applied and the solution is run up to steady state. In Fig. (6-2), density contours along with indicated shock is shown. Density contours are more stretched out in smooth flow regime due to using p = 1 there, but there is also some waviness in the solution near the shock. Reason for waviness is coarse mesh near the shock and higher threshold value used for shock indicator which shows some oscillations. These oscillations persist in solution, although not causing any stability problems. These oscillations in the shock region are shown in 3-D plot of density contours in Fig. (6-3). We can get rid of the oscillations by lowering the shock indicator threshold value (see Fig. (6-3) B)) or by refining the mesh by redistribution of elements in the rest of the domain outside the shock in close proximity to shock (see Fig. (6-4)), thus reducing the mesh size. We do not see oscillations in Fig. (6-3) B), but then the region of p = 0 is very wide and includes regions from top and bottom of cylinder as well in addition to shock. This may not be useful since we will have poor accuracy in regions above and below shock. Shock indicator which exactly identifies shock and not other regions without shock, will be useful. For this purpose, value of 0.1 was seen to best serve the purpose with least oscillations for this particular mesh.

For finer shock resolution, we apply r-p adaptivity, bringing the domain elements close to shock region as shown in Fig. (6-4). All the domain elements outside the shock are clustered into the shock uniformly. Thus, as we can see the mesh in Fig. (6-4), we get finer elements within the shock region. It is clearly seen (in Fig. (6-5)) that shock

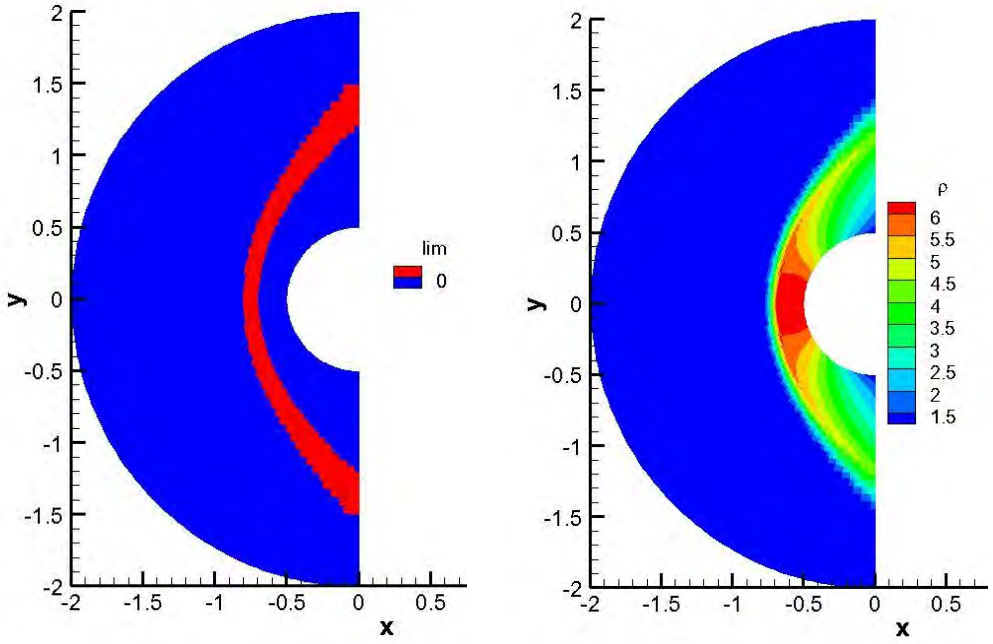

Figure 6-2. A) shows shock location as indicated from pressure jump shock indicator. Threshold value of 0.3 is used for the shock indicator. Red region indicates shock (p = 0 is used by setting the limiter to a value of 1) and blue region indicates smooth region, (p = 1 is used by setting limiter to a value of 0). B) shows density contours with contour levels set same as those with only p = 0. Density contours are more stretched out here in comparison to p = 0, but we can see some waviness in solution near shock.

thickness has reduced as compared to results shown in Fig. (6-1)). We still observe some waviness in solution profiles. These solutions have not yet reached steady state (from the perspective of norm of residual), but the shocks location is stationary. Solution seems to have effect of error wave propagation from shock to the flow in the shock layer, which can be very easily seen in contour plots of Mach number and density. This error wave may be due to difference in accuracy of scheme in shock with p = 0 and shock layer with p = 1. In these simulations, shock location is being evaluated at every time step, and thus this may cause delay for solution reaching steady state from residual perspective. It will be of interest to find out if the error waves go away when solution reaches steady state, or is it dependent on oscillations near shock which are controlled

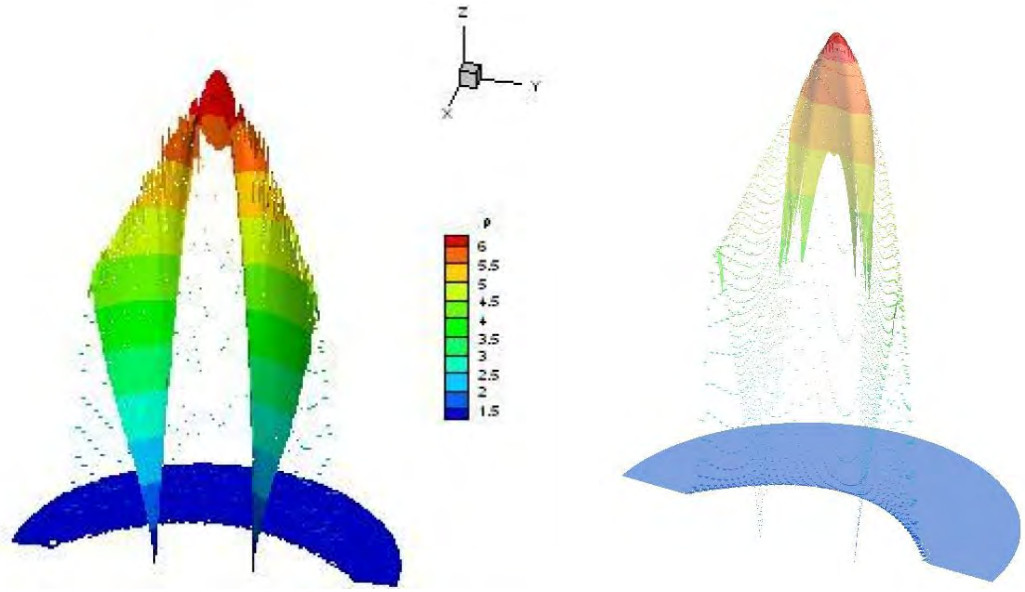

A B

Figure 6-3. Density contour plots in 3-D with shock indicator threshold values of A) 0.3 and B) 0.04. Decreasing threshold value removes oscillations, but it doesnt much serve the purpose for having high order approximation in the smooth region.

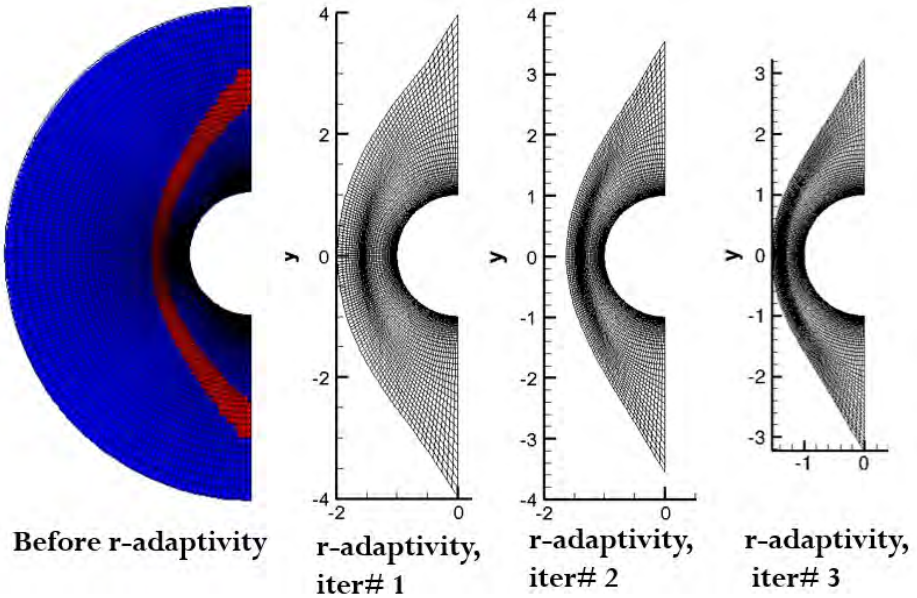

Figure 6-4. Application of r-p adaptivity, to original mesh with shock location, identified using pressure based shock sensor. First iteration gives new mesh with elements outside the shock clustered closer to the shock region. Further iterations of r-p adaptivity lead to improved mesh resolutions around shock region.

by adjusting threshold value for shock indicator and also by refining the shock region more and more.

Using r-p adaptivity, we get following results compared to results by Wang et al. (see Fig. (6-5)).

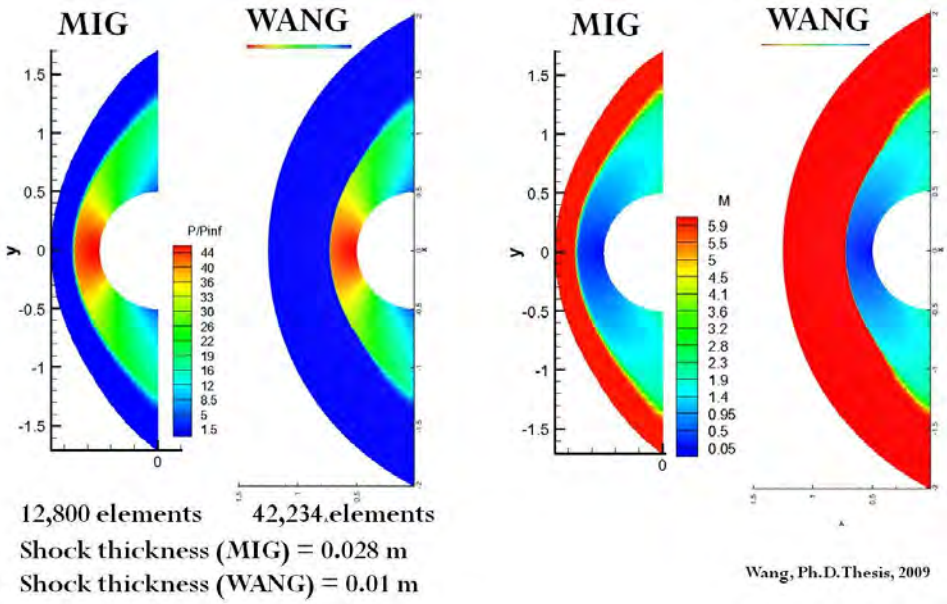

Figure 6-5. Better shock resolution obtained by using r-p adaptivity and higher order polynomial approximation in MIG (DG method). Shock is finely captured with approximately a third of the elements used in Wang. The solution focuses on refining the mesh near the shock and increasing polynomial order of accuracy in smooth flow regions to improve solution resolution everywhere.

To finalize the accuracy of our inviscid hypersonic flow results we show the shock standoff distance as predicted by our code compared to that presented in Wang (see Fig. (6-6)). We note that despite using $1/3^{\mathrm{rd}}$ of number of elements in Wang, we accurately predict shock stand-off distance to be 0.726 m. This is due to using r-p adaptivity where the elements outside the shock are redistributed to cluster near the shock, thus providing enhanced mesh resolution at the shock.

The advantages of r-p adaptivity, over h-p adaptivity used in [10], is that it is more suitable for transient problems, and does not lead to the increase in number of elements. Hence this is very suitable for problems of coupled simulation of hypersonic flow and

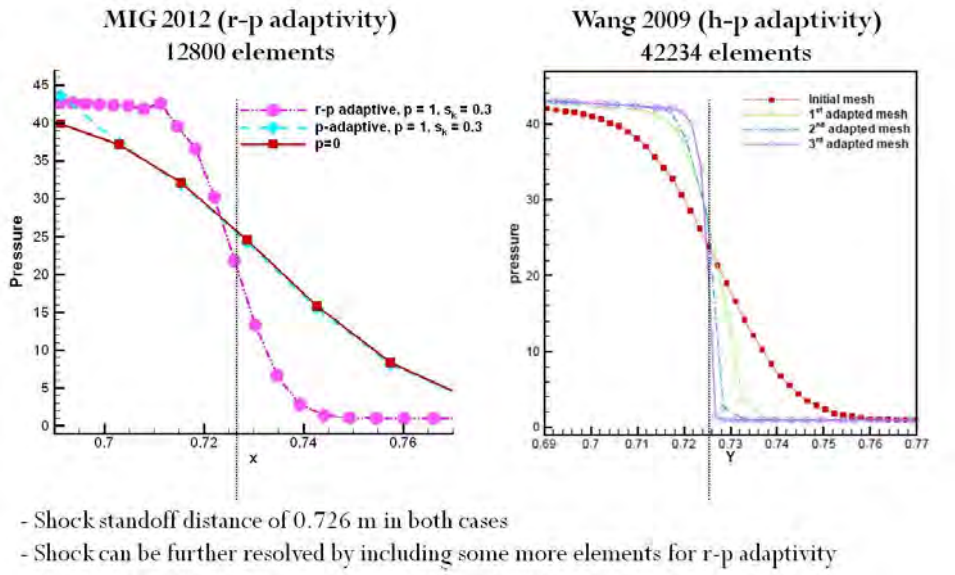

Figure 6-6. Shock location is identified and shock standoff distance is 0.726 m in both cases. These results are again compared to those in Wang. The method used in Wang is h-p adaptivity for refining mesh close to shock.

thermal ablation since shock′s location can vary upon blowing of pyrolysis gases from solid domain into fluid domain. Hence this adjustment can be made using r-p adaptivity.

6.1.2 Viscous Hypersonic Flow

In this section, we present results obtained for viscous hypersonic flow. Here, the Mach number for the flow is 17, and the results are compared to one of the results given in [2]. As seen in Fig. (6-7), temperature contours for both results match well. Shock standoff distance is also 0.4 m in both cases.

These results are again improved by further applying r-p adaptivity to the obtained solution and re-rerunning the simulations. This r-p adaptivity changes the mesh to readjust the elements outside the shock to in the shock (see Fig. (6-8)).

The improved results for viscous hypersonic flow are hence seen in Fig. (6-9),

We also conducted mesh convergence study, wherein, we refined the mesh both near the wall and in the θ direction. The plots for heat coefficient is given in Fig. (6-10).

$'1x'$ corresponds to the base mesh, which 128 $\times$ 100 elements. $'2x'$ refers to the mesh with twice the number of elements in θ direction, i.e. 256 $\times$ 100 elements. Two

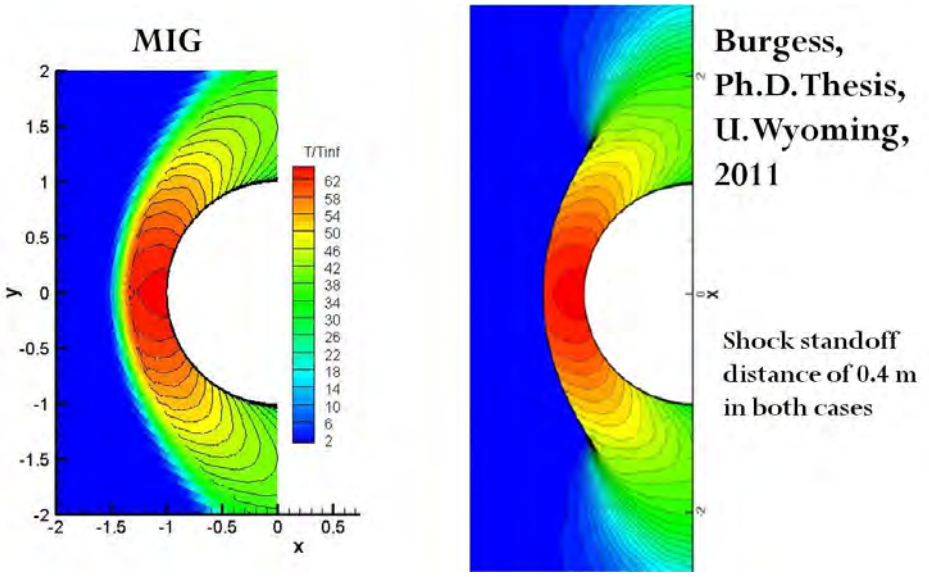

Figure 6-7. Viscous hypersonic flow simulation results for M = 17 flow over cylinder, compared to Burgess. Both results show same shock standoff distance of 0.4 m.

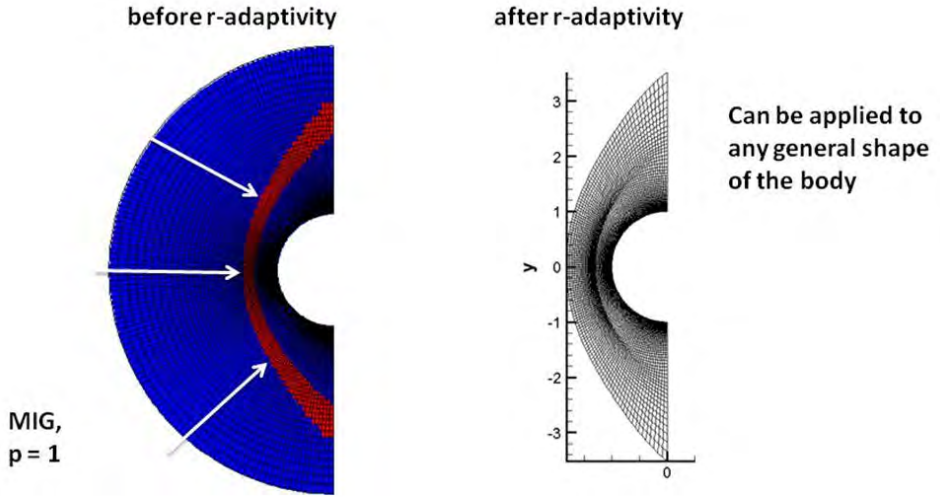

Figure 6-8. r-p adaptivity applied to the steady state solution obtained from the initial mesh. Shock location is identified using the shock indicator based on the ratio of average pressure to the jump in pressure across current element and its neighbors. The advantage of this approach is that it can be applied to any shape of the body.

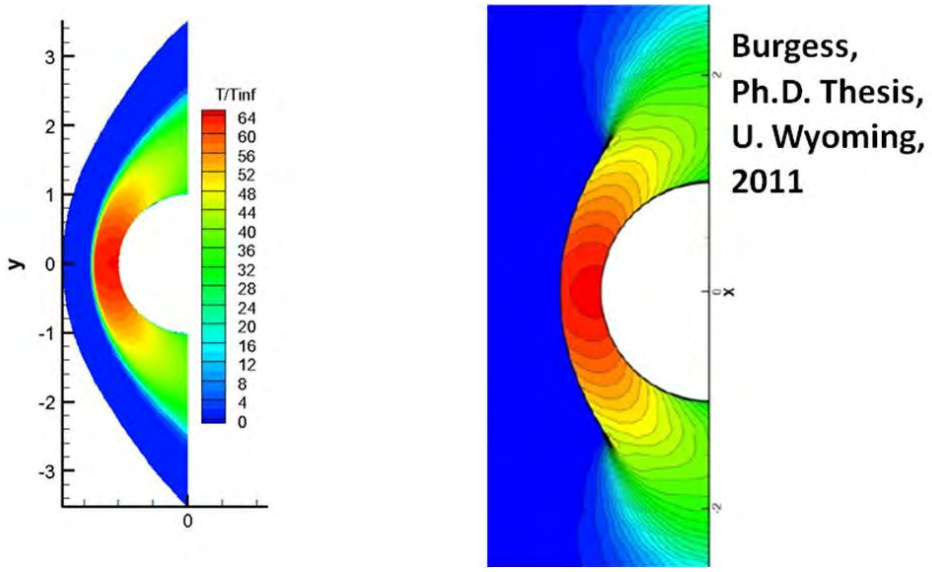

Figure 6-9. Results after applying r-p adaptivity to viscous flow simulations obtained from p = 1. Our code uses 12,800 elements as compared to 37575 elements in Burgess.

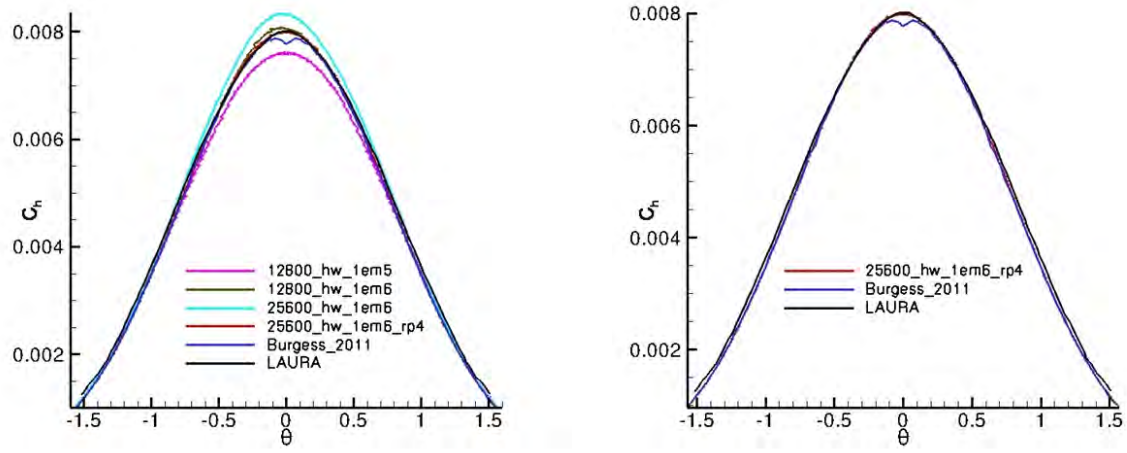

A B

Figure 6-10. Surface heating coefficient profile is shown for different meshes and r-adaptivity. Wall thickness certainly affects the results in addition to refinement of mesh in θ direction. But this is not sufficient, even r-adaptivity which refines the mesh in shock is seen to affect the result significantly.

wall thicknesses are used in the simulations, 10^{-5} m and 10^{-6} m. A finer wall thickness certainly improves the results for $\mathrm{C_h}$. We compare our results to Burgess, [2] and LAURA [89], and note that result reported in [2] has small kink in the profile at stagnation point which may be due to not having fine enough mesh for the shock. In Fig. (6-10), B) we show our best case (with 4^{th} r-adaptive iteration) to match the standard LAURA result very accurately.

6.1.3 Hypersonic Flow with Thermo-Chemical Non-Equilibrium

After benchmarking our results for inviscid (M = 6) and viscous (M = 17) hypersonic flows, we present the results for hypersonic flow in thermo-chemical non-equilibrium. We consider 5 species model with over all 5 chemical reactions (described in chapter 2), and compare our results with those obtained from US3D by Dr. Gosse.

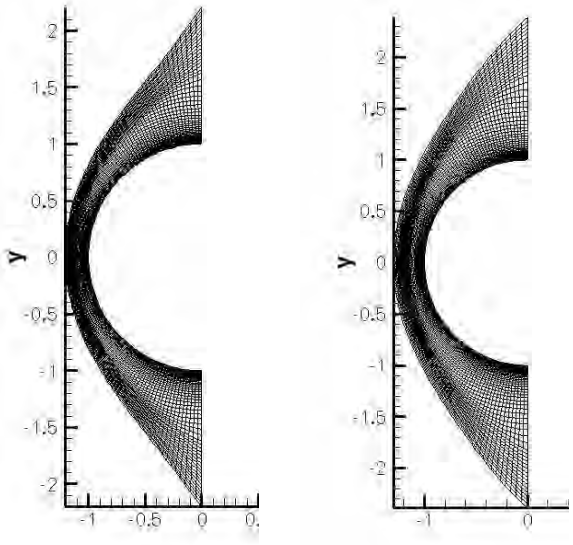

A only $\mathrm{O_2}$ B $\mathrm{N_2}$ + $\mathrm{O_2}$

Figure 6-11. Final r-p adapted meshes for non-equilibrium cases for A) only $\mathrm{O_2}$ in freestream and B) both $\mathrm{O_2}$ and $\mathrm{N_2}$ in freestream. In the 4^{th} and final iteration of r-p adaptivity, the meshes are fine at the identified shock locations of 0.15 and 0.2 m (away from cylinder's surface) respectively.

The governing equations for this problem are the multi-species Navier-Stokes equations with elaborate transport, chemistry and vibrational models, which requires

diligent and tedious book keeping. First case is with only oxygen, O_2 in the freestream flow. This test case was crucial for us to debug the code, as the simulations for the full problem (the second test case), N_2 + O_2 in freestream with full thermo-chemical non-equilibrium, did not match in the initial attempt. Not being able to match MIG results for the full problem to US3D initially, we compared our code to US3D for models other than chemistry, i.e. viscous, inviscid and thermal non-equilibrium models. Each model was tested in isolation of other to find out the difference in models. Thus, we were able to eliminate all the models and only model that caused the difference was thermo-chemistry model.

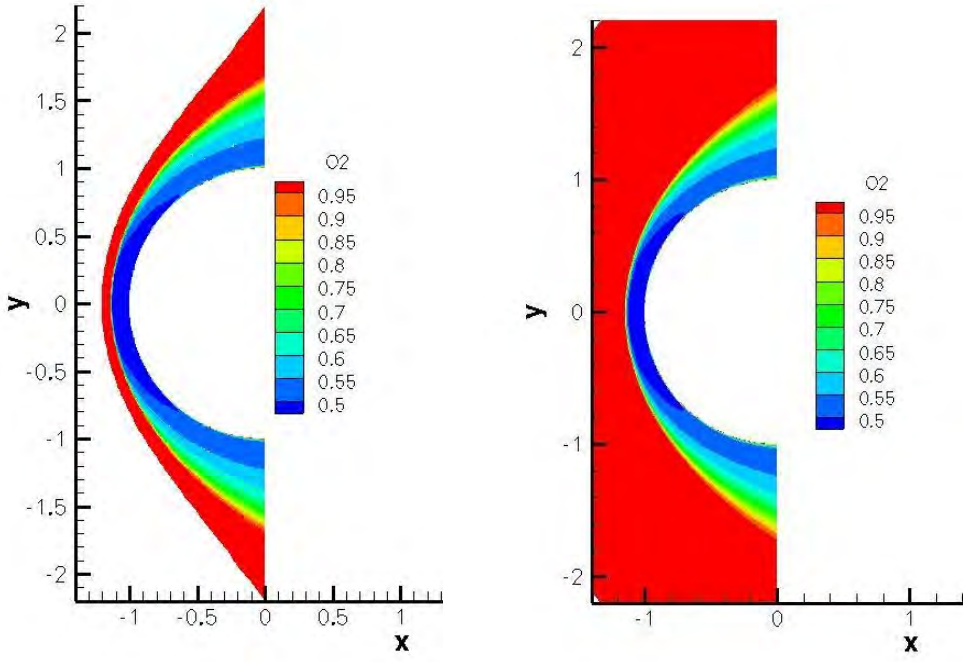

A MIG B US3D

Figure 6-12. Contours of mass fraction of O_2 for A) MIG and B) US3D. Both are steady state results. Significant dissociation of O_2, nearly 55 % is observed in both cases. Dissociation follows immediately after the flow passes the shock.

For this purpose, we tested the first case with only O_2 in freestream. This case has only one reaction, i.e. dissociation of O_2 into O, and is much easier to debug than the

second test with $N_2 + O_2$ in freestream and full thermo-chemical non-equilibrium. Thus we found the reason for the discrepancy in the results, to be in chemistry coefficients. Park's model provides values for coefficients for both forward and equilibrium rate constants. In this, the density and molecular weight are to be used in g/cm^3 and g/mol. Thus, the expressions for reaction rates given in Eq. (2–52) and Eq. (2–53), have to have a factor to properly account for using SI units for density and molecular weight.

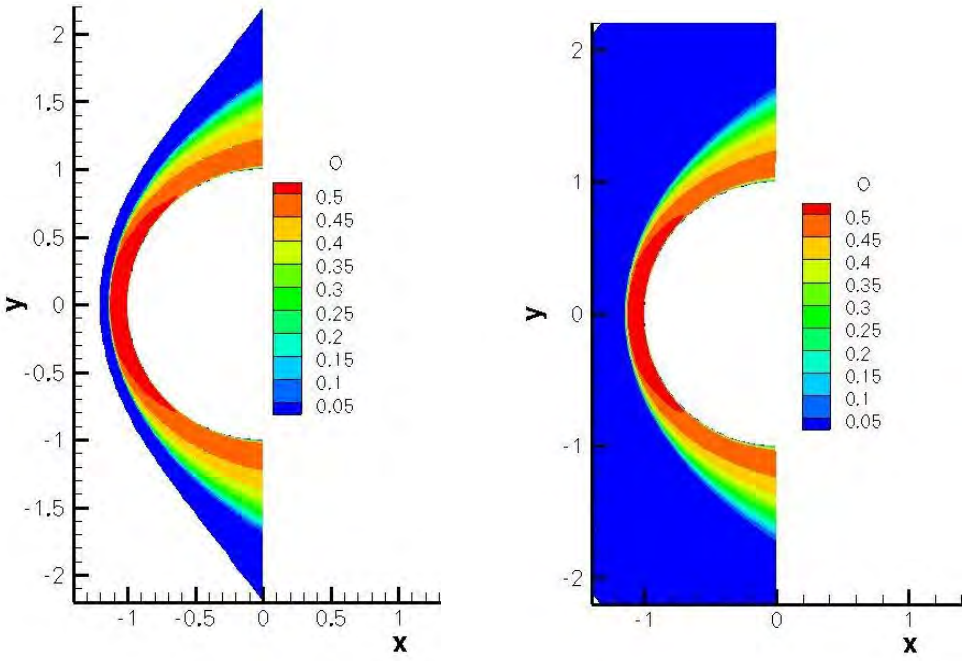

A MIG B US3D

Figure 6-13. Contours of mass fraction of O for A) MIG and B) US3D. Both are steady state results. Significant production of O, nearly 55 % is observed in both cases. Reason for this production follows exactly from the dissociation of O_2 explained in Fig. (6-12).

For this simulation, a mesh with circular outer domain was taken for first set of runs and a steady state solution obtained with p-adaptivity (i.e. p = 0 in shock). Highest timestep that we used in this case was 10^{-6} sec, which corresponds to maximum CFL number of 500 at the wall where the wall thickness is 10^{-5} m. Then applying

r-p adaptivity to this solution we rerun the simulation again to steady state. After 4 iterations, we achieve the final r-p adapted mesh with shock location identified at approximately 0.15 m and 0.2 m (for test-case 1 and 2 respectively) away from the cylinder at the stagnation line. Meshes for both the test cases are given in Fig. (6-11).

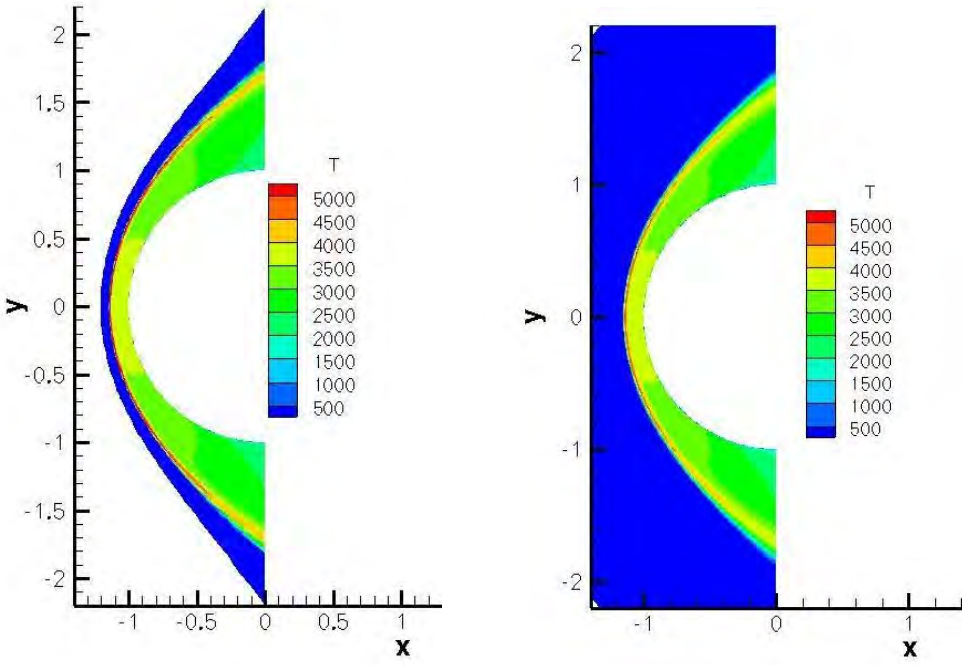

A MIG B US3D

Figure 6-14. Contours of temperature, T for A) MIG and B) US3D. Both are steady state results. Contours match well for both MIG and US3D. Nature of temperature contours can be understood based on the amount of dissociation of O_2 observed in the shock.

The final solution on these meshes are now presented. First for only O_2 case, the comparison is shown for MIG and US3D. Shock standoff distance in both cases is predicted to be 0.15 m, and other properties like density, pressure and velocity also compare well.

Contours for mass fractions of O_2, O, T and T_v are given in Fig. (6-12), Fig. (6-13), Fig. (6-14) and Fig. (6-15) respectively.

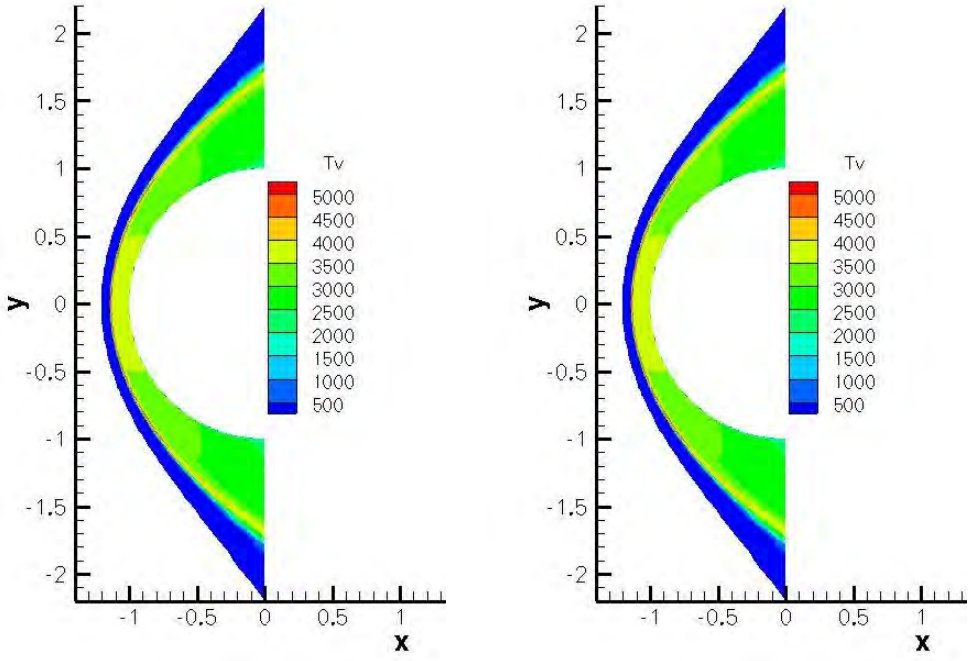

A MIG B US3D

Figure 6-15. Contours of vibrational temperature, $\mathrm{T_v}$ for A) MIG and B) US3D. Both are steady state results. Contours match well for both MIG and US3D. Nature of vibrational temperature contours can be understood similar to the explanation given in Fig. (6-14) for translational-rotational temperature, T.

In Fig. (6-12), significant dissociation of $\mathrm{O_2}$ into O is observed. High temperatures in shock of nearly 5000 K are responsible for this dissociation, at which the forward reaction rates for $\mathrm{O_2 + M \Leftrightarrow 2O + M}$ dominate the backward rates. Away from the stagnation region, temperatures in the shock are lower, hence lesser amount of dissociation is observed. Therefore, higher mass fraction of $\mathrm{O_2}$ is seen in shock and shock layer away from the stagnation region. Based on same arguments, we can explain the corresponding contours for mass fraction of atomic oxygen, O. Comparisons between MIG and US3D are very similar.

As can be seen in Fig. (6-17), a significant drop in temperatures occur right after the shock, due to dissociation processes, which are endothermic in the forward direction. The species (both diatomic and monoatomic oxygen) equilibrate (on stagnation line),

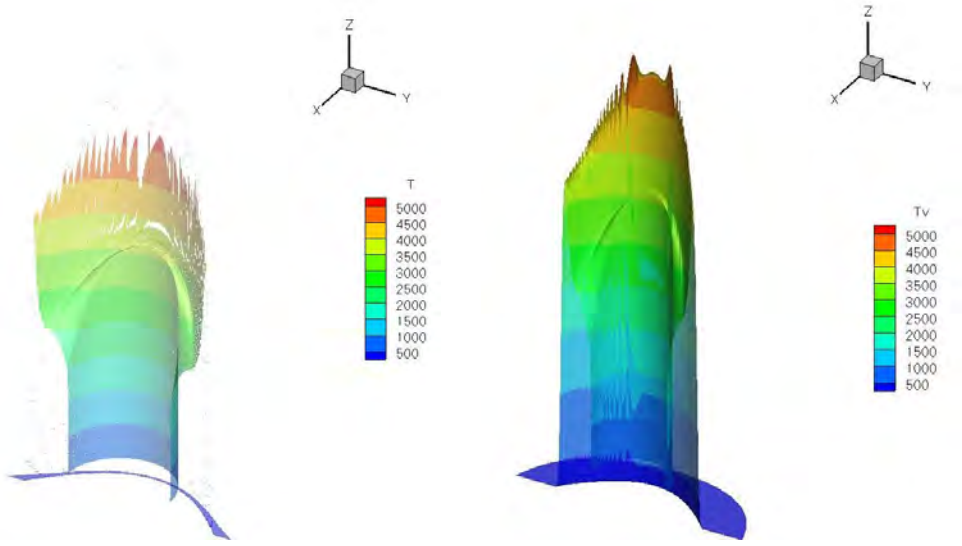

A MIG B US3D

Figure 6-16. 3D Contours of temperature, T for A) MIG and B) US3D. High temperature observed in MIG is at the shock and is due to oscillations observed near shock. Method used in MIG for results presented in Fig. (6-12) - Fig. (6-16) is r-p adaptivity with p = 0 for shock regions.

a small distance after the shock. Hence, no further drop in temperature is observed along the stagnation line after the initial drop. However, away from stagnation line, due to lower temperatures in shock, O_2 continues to dissociate causing further decrease in temperature as the flow moves closer to the cylinder surface. This explains the nature of contours seen for both T and T_v in Fig. (6-14) and Fig. (6-15) respectively.

Although the temperature contours in Fig. (6-14) compare well, the maximum temperatures encountered in the shock in MIG and US3D are 6680 K and 5380 K respectively. This results from oscillations in temperature around the shock, as shown in Fig. (6-16). Hence this difference is purely related to p-adaptivity approach employed in MIG to capture the shock and may be improved by the use of slope limiter.

The stagnation line properties are also plotted for mass fractions of O_2 and O, and T and T_v and compared for both MIG and US3D codes in Fig. (6-17).

Stagnation plots in Fig. (6-17) show a higher temperature rise (for T) in the shock for MIG in comparison to US3D. This has already been discussed and may

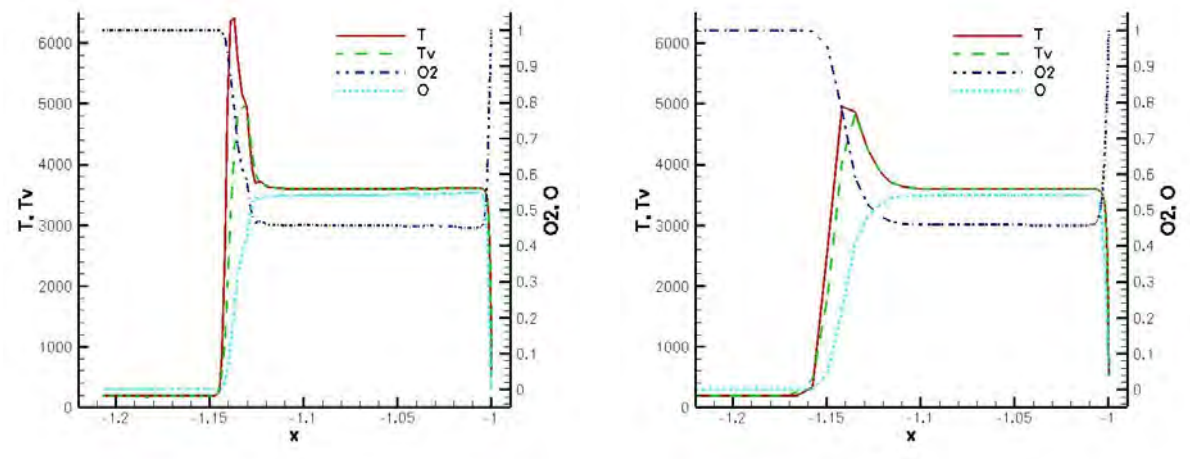

A MIG B US3D

Figure 6-17. Stagnation line plots for both temperatures, T and $\mathrm{T_v}$, and mass fractions of $\mathrm{O_2}$ and O shown for A) MIG and B) US3D. High temperature rise at the shock in MIG is observed relative to US3D. Several other important conclusions are made from these two plots.

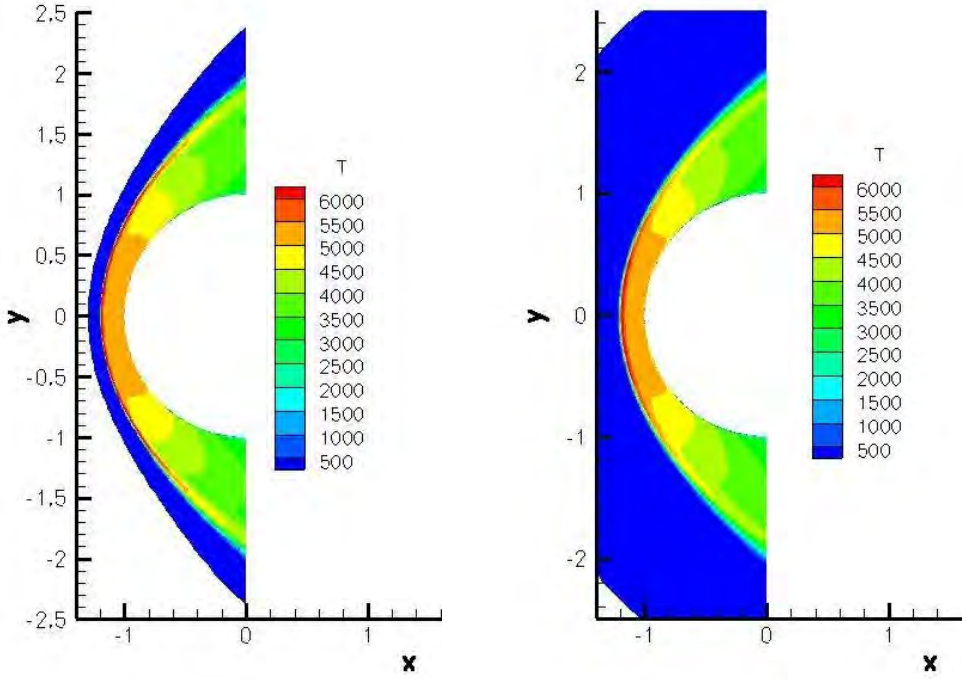

A MIG B US3D

Figure 6-18. Temperature contours for $\mathrm{N_2}$ + $\mathrm{O_2}$ case for both A) MIG and B) US3D. Both results compare very well to each other. Maximum temperature in MIG is 7700 K and in US3D is 6500 K, and the difference is attributed to p-adaptivity as before explained.

be connected to p-adaptivity approach used in this work. Thermal non-equilibrium is seen to be predominant in the shock and some distance (nearly 0.02 m) after the shock. Elsewhere, thermal equilibrium is predominant.

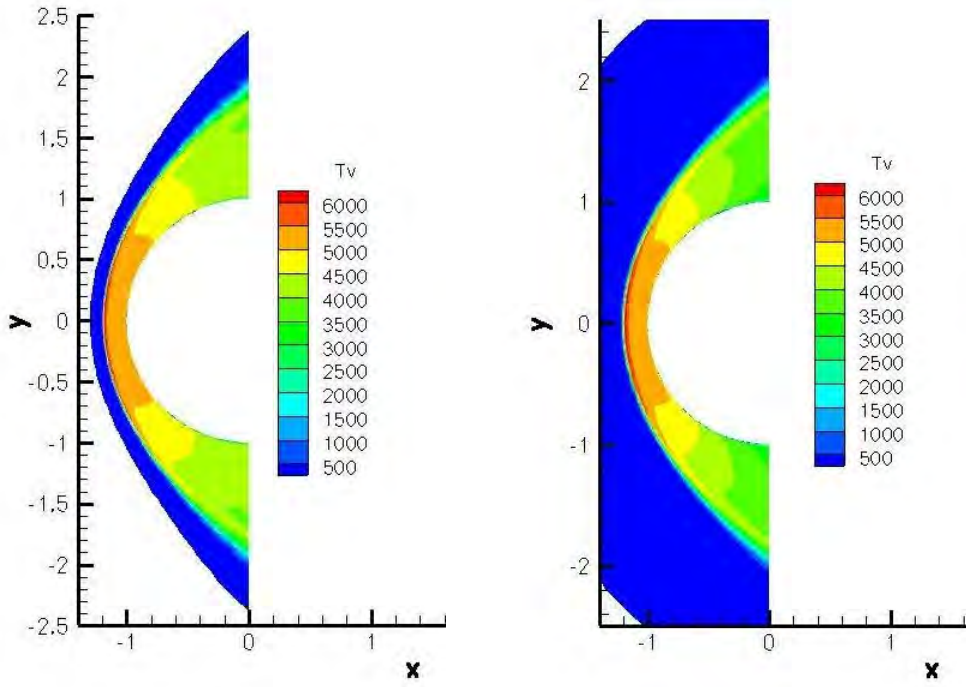

A MIG B US3D

Figure 6-19. Vibrational temperature contours for N_2 + O_2 case for both A) MIG and B) US3D. Both results compare very well to each other. Maximum temperature in MIG is 6300 K and in US3D is 6550 K, and the difference is again attributed to p-adaptivity as before explained.

Additionally, O_2 is seen to dissociate in the shock and the post-shock region, leading to formation of O. In the post-shock region, dissociation is prominent to a distance of 0.032 m away from the shock. In the rest of post-shock region, both the mass fractions of O_2 and O becomes almost constant, thus reaching chemical equilibrium. At the wall, which is fully catalytic having fixed temperatures of 500 K for both T and T_v, we find that O_2 and O go back to their freestream values. In comparison of MIG, and US3D, apart from the high rise in temperature observed in MIG, rest all values compare fairly well for both the codes.

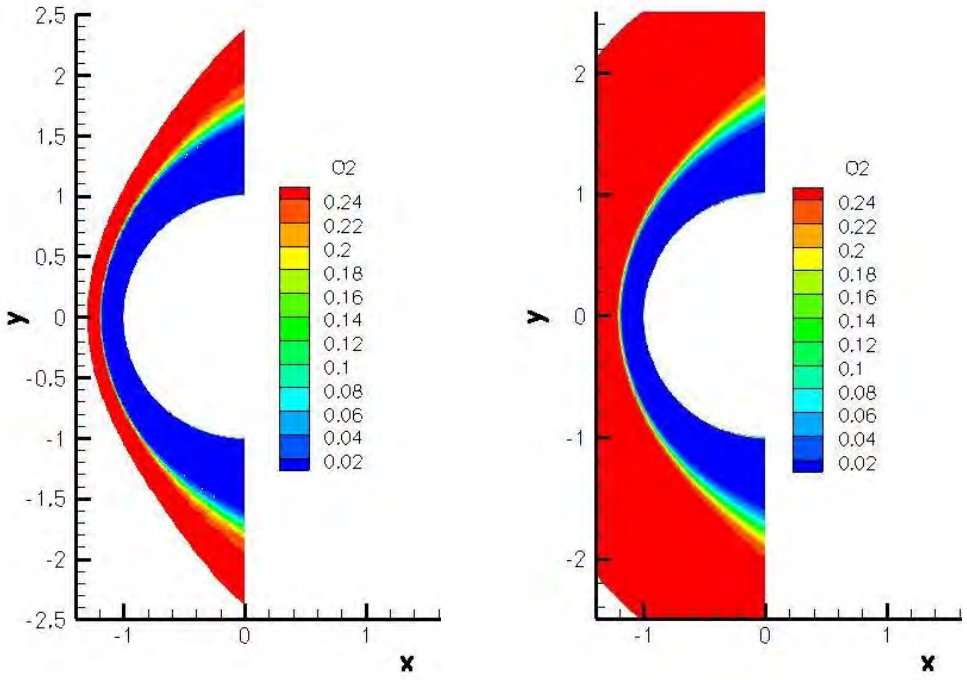

A MIG B US3D

Figure 6-20. Mass fraction contours of O_2 for N_2 + O_2 case for A) MIG and B) US3D. As noted in both cases, complete dissociation for O_2 occurs in the shock layer, as opposed to only partial dissociation in only O_2 case.

Next we present results for second test case; with N_2 + O_2 in freestream in mass fraction ratio of 0.7562:0.2438. Freestream temperature is 200 K, and the wall, which is fully catalytic is again at a fixed temperature of 500 K. For this also, we compare our results from MIG to those from US3D.

Temperature contours for N_2 + O_2 case are shown in Fig. (6-18) for both A) MIG and B) US3D. Both the results compare very well to each other. The maximum temperature in MIG is found to be 7700 K and in US3D to be 6500 K. This difference is due to p-adaptivity as has already been explained for the case of only O_2.

Contours for vibrational temperature also compare very well for MIG and US3D (see Fig. (6-19)). For T_v, maximum temperature in flow field for MIG is 6300 K and for US3D is 6550 K. Hence, the maximum values of vibrational temperature are much closer for

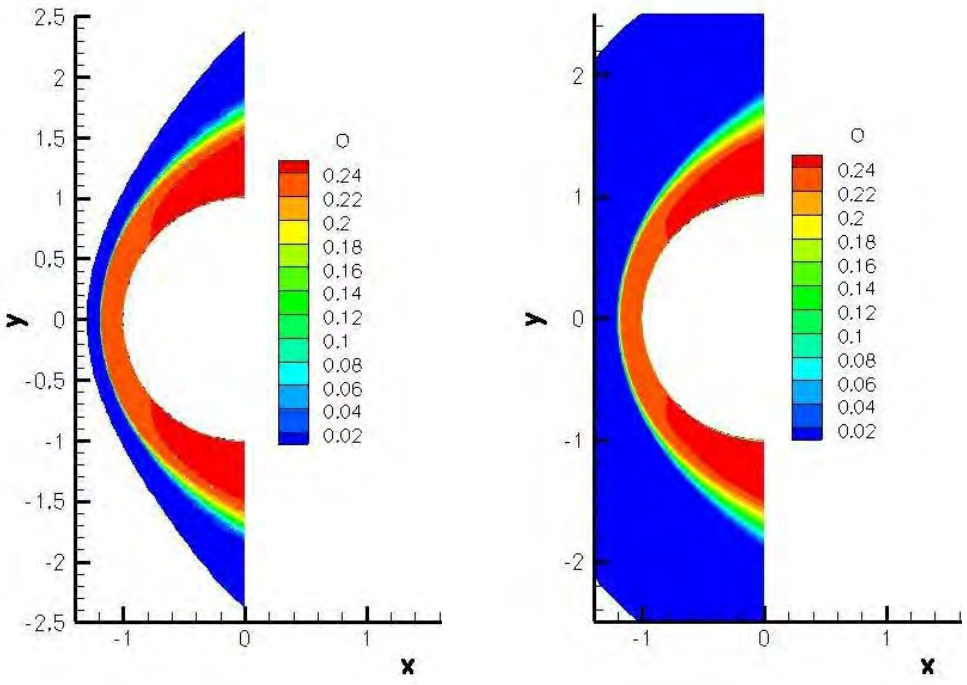

Figure 6-21. Mass fraction contours of O for N_2 + O_2 case for A) MIG and B) US3D. Maximum mass fraction for O, i.e. 0.2438 is found close to top and bottom regions of cylinder. This correlates to mass fraction of NO, in that the maximum O is observed when NO formed in the shock also dissociates into N and O giving extra O.

both the codes than it is for the maximum values of translational-rotational temperature. Hence, the difference between the two simulations can more certainly be attributed to difference in shock capturing approaches in both the codes.

Contours for mass fraction of O_2 are seen in Fig. (6-20), and again the excellent comparison is seen in both the codes. Complete dissociation of O_2 is seen in shock layer compared to only a partial dissociation of O_2 in the only O_2 case. This is explained by sensitivity of temperature contours and the shock standoff distance to the chemistry model. Results change significantly when the chemistry and thermal non-equilibrium models are turned on.

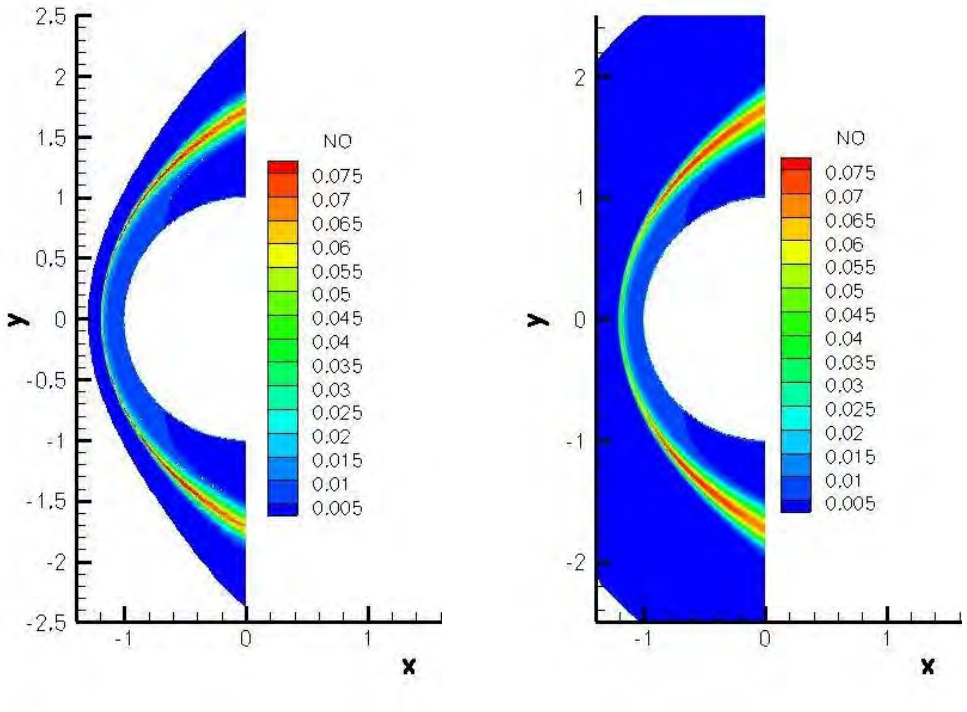

A MIG B US3D

Figure 6-22. Mass fraction contours of NO for N_2 + O_2 case for A) MIG and B) US3D. Maximum mass fraction for NO and also its production occurs in shock by combination of atomic N and O produced by dissociation reactions of N_2 and O_2. As the temperatures being maximum at shock drop down in the shock layer, NO (produced in shock) again dissociates into N and O.

Shock standoff distance, for only O_2 and N_2 + O_2 cases, are 0.15 m and 0.2 m respectively, in comparison to 0.4 m and 0.3 m for full thermo-chemical equilibrium and only thermal non-equilibrium. Due to higher temperatures observed in N_2 + O_2 case (6500 K maximum temperature in comparison to 5300 K for only O_2 case), complete dissociation of O_2 is observed. Dissociation of N_2 into N atoms is incomplete with maximum dissociation (of nearly 0.07 of total mass fraction, see Fig. (6-24)) occurring just after the shock. As we observed in the case of only O_2, the species are in thermo-chemical equilibrium in the shock layer at least close to stagnation region. This is due to increased value of density post-shock, that causes the species to equilibrate faster due to increased number of collisions.

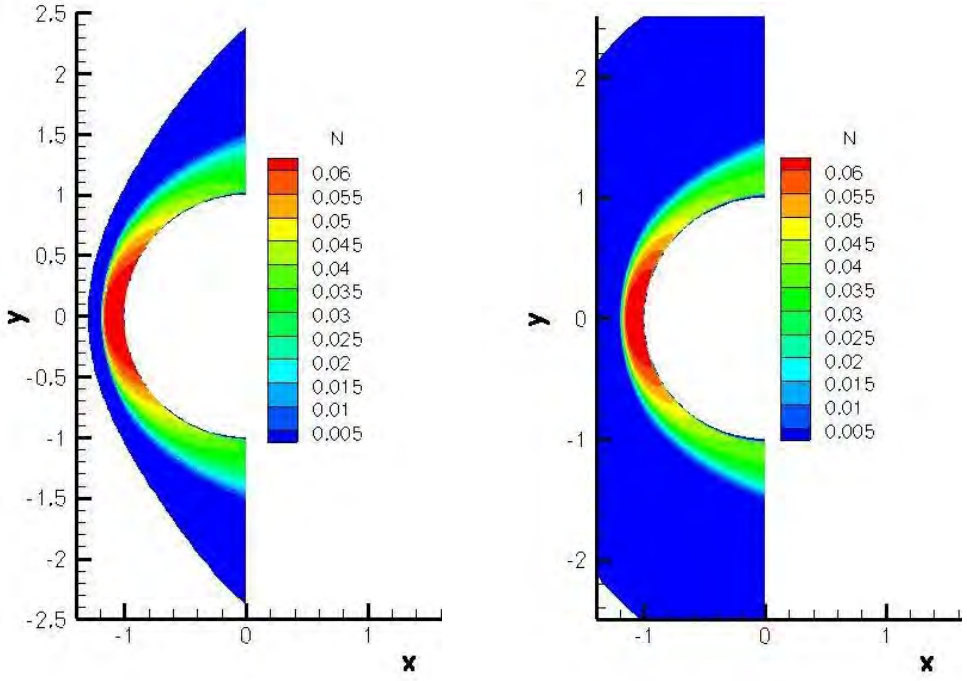

A MIG B US3D

Figure 6-23. Mass fraction contours of N for N_2 + O_2 case for A) MIG and B) US3D. Maximum mass fraction for N occurs close to stagnation region just after shock. N is formed by dissociation of N_2, and in shock combines with O to form NO.

A small portion of atomic nitrogen, N (produced by the dissociation), combines with atomic oxygen, O to form NO close to the shock region (see Fig. (6-22) and Fig. (6-25)). Away from shock, in the shock layer, the temperatures are not high enough to sustain NO which again dissociates into atomic N and O. Thus in the contours of N, we see the maximum value of mass fraction being just after the shock rather than in the shock.

As N_2 and O_2 continue to dissociate for some distance even after the shock, the temperature contours which have maximum in the shock, continue to drop unlike purely viscous case, where the temperatures remain almost constant after the shock.

As we go away from the stagnation line towards either the top or bottom of cylinder, temperature values decrease, and hence the amount of NO also decrease, which is produced in shock region, and it again dissociates to N and O, thus we see

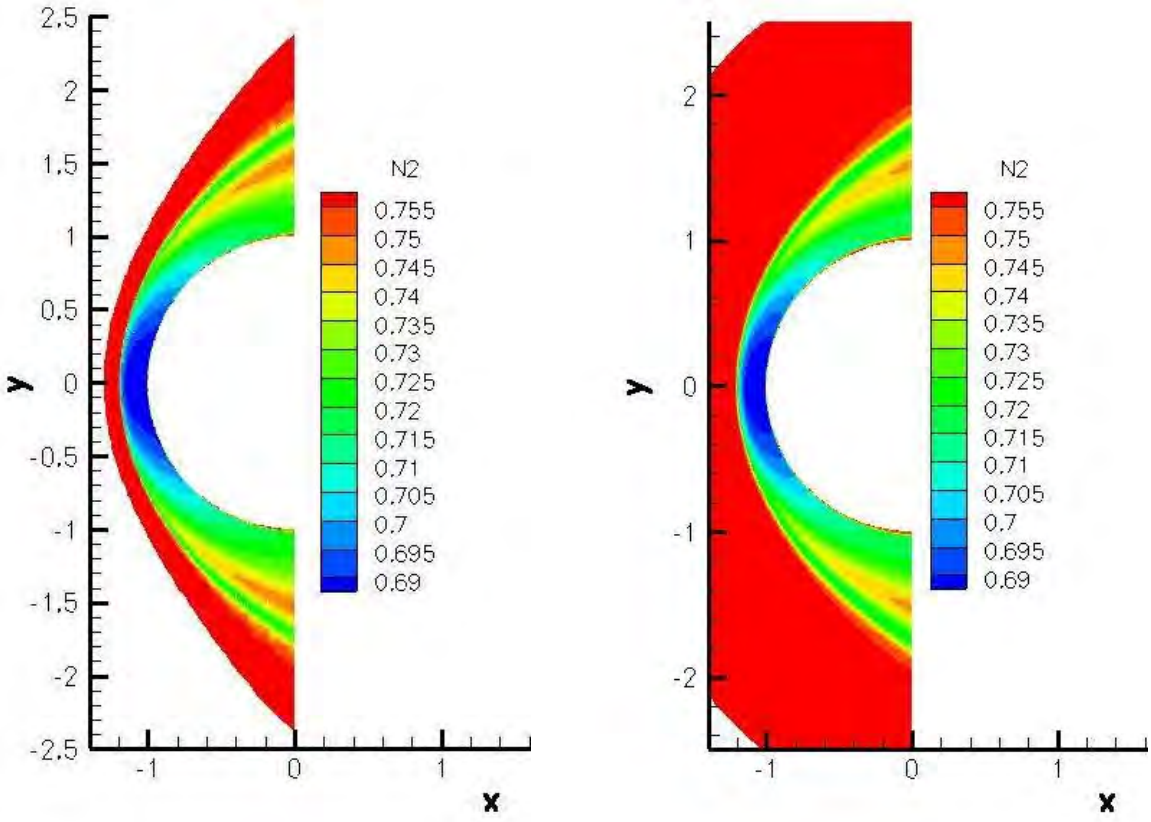

A MIG B US3D

Figure 6-24. Mass fraction contours of N_2 for N_2 + O_2 case for A) MIG and B) US3D. Maximum dissociation of N_2 occurs near stagnation region. Interestingly, we see increase in N_2 mass fraction just after the shock at top and bottom of the cylinder.

that maximum mass fraction of O is at top and bottom regions of cylinder, not near stagnation line.

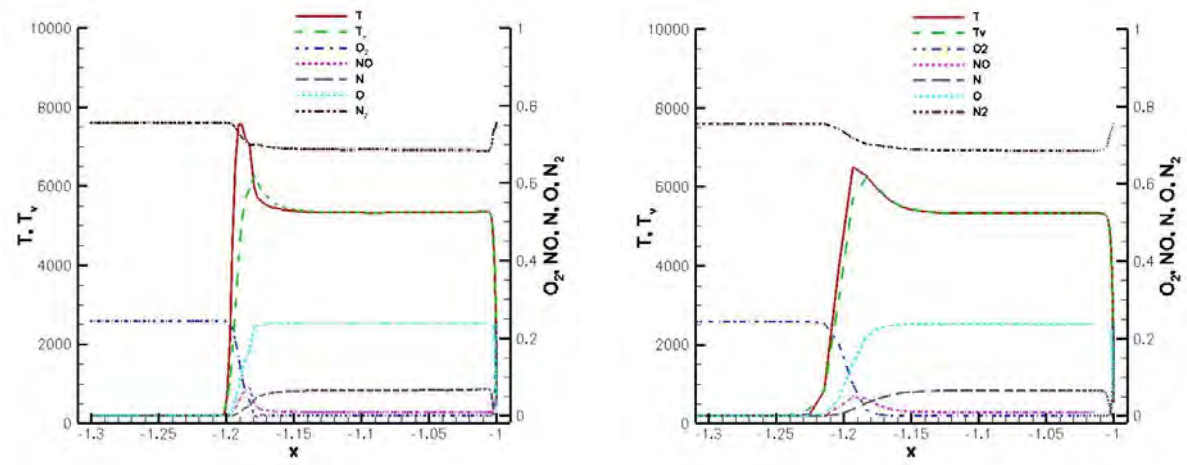

A MIG B US3D

Figure 6-25. Stagnation line plots for both temperatures, T and $\mathrm{T_v}$, and mass fractions of all the species for A) MIG and B) US3D. High temperature rise at the shock in MIG is observed relative to US3D. $\mathrm{N_2}$ dissociates only partially in the shock. Production of NO is seen only in shock, after which it again dissociates back to N and O.

CHAPTER 7
EFFECT OF PLASMA DBD ACTUATORS ON HYPERSONIC FLOW CASES

Active flow control is a very expanding topic of research, due to its vast industrial applications. Out of all flow control methods, like mechanical flaps, wall synthetic jets or MEMS; plasma based flow control is very promising. This is due to their robustness, simple design, low power consumption and real time flow control with high frequency [90].

Non-thermal plasmas are known to create maximum air flow speeds of 8 m/s (at 0.5 mm distance from wall) in a quiescent flow and able to provide effective flow control for freestream flow velocities up to 30 m/s. Air flow control can have many applications. E.g., by increasing the turbulence (with a wall jet), one can enhance the flow mixing in the separation region of the wing. Thus delaying the flow separation on the wing, one can increase the lift obtained. On the other hand, by decreasing turbulence, one can reduce the noise of an aerodynamic system.

In hypersonic flow control, plasma actuators have been successfully used along with magnetohydrodynamics [91]. In addition to this, the use of nano-pulsed DBD plasma actuators [92] has allowed significant shift (around 20 %) in distance of the detached bow shock from the cylinder. Both these cases add pressure perturbation to the flow.

In [91], via the use of direct current surface plasma discharge, electromagnetic perturbation is added to the flow that results in the growth of displacement thickness of the shear layer, being amplified by the pressure interaction. This mechanism depends on triggering the flow instability without requiring to add huge amount of power to ionize the flow. Hence, the power requirement of this device is low. This has been demonstrated to deflect the freestream flow of Mach 5, by an angle of 5°. This effect is expected to increase with the increase of incoming flow Mach number.

According to [91], DBD plasma actuators are most effective at bifurcation points in the flowfield, where the flow velocities are low ($\leq$ 30 m/s). However, an important feature of hypersonic flows is the strong inviscid-viscous interactions. Boundary layer in hypersonic flow is no longer negligible as it is in subsonic or supersonic flows. This large displacement thickness, in the boundary layer, displaces the incoming flow, thus producing outward flow deflection. This causes the compression waves to be produced, which coalesce into a shock wave. This shock wave then interacts with the boundary layer to close the interaction loop.

These inviscid-viscous interactions strengthen on the increase in Mach number of the incoming flow, hence this mechanism is exploited both in the case of adding electro-magnetic perturbation to the hypersonic flow (in [91]) and in the case of nano-pulsed discharge by adding a pressure perturbation in the shear layer of the flow (in [92]). The former plasma case has been applied to a flat plate and to the geometric cowl of scramjet.

The surface DBD plasma actuators depend on electrohydrodynamic acceleration of wall jet to actuate the flow near the wall. But, this becomes exceedingly difficult to achieve at high speeds, since it becomes excessively difficult (because of large power requirements) to maintain the high space charge density and high electric field in the discharge.

An alternative to this is sought in [93] wherein a series of high voltage nanosecond pulses (producing very high electric fields for a very short duration of time) are used to reattach the flow for Mach 0.85. In this case, the main mechanism of flow control is rapid localized heat generation, rather than electrohydrodynamic force in the case of micro-second pulsed DBD actuators [94]. In quiescent flow, this nanosecond pulsed DBD plasma actuator is known to produce shock waves ([93]).

It is interesting to note that the energy responsible for plasma breakdown in one pulse for nanosecond plasma (lasting 10 ns) and microsecond plasma (lasting 10 μs)

is almost same ([95]). Various methods of flow control, used for bow shock control in supersonic flows, like pulsed DC arced discharge, pulsed microwave discharge and laser optical breakdown, use thermal heat addition to reduce wave drag and surface heat transfer.

But, since the nanosecond pulsed plasma, applied to increase the shock stand-off distance temporarily, is in cold flow (T_∞ = 56 K); the heat loss due to increased shock distance is seen to be countered by the net heat added by the nano pulse. In fact, the $\mathrm{C_h}$ profiles increase by two orders of magnitude ([96]). It is not clear, if the same effect will be observed in the case of hypersonic flow over re-entry vehicles, wherein the maximum temperature in the flowfield is of order of 10,000 K? The maximum temperature of the flow-field in the case of [96] is 300 K.

Our main motive in the present work is to reduce the net surface heating coefficient, $\mathrm{C_h}$ at the surface of the vehicle. Nanosecond pulse, though promising to increase the shock stand-off distance, seems to add more heat during its duty cycle. Although, it is not clear if this will be beneficial for a re-entry vehicle or not.

Therefore as an alternative, we attempt to see the effect of micro-second pulsed DBD plasmas, wherein the power deposition is minimal (approximately 10 W/m^2 of the electrode).

As already seen in chapter 6, the boundary layer for hypersonic flows (at the stagnation point) is few millimeters. In fact, the flow has very low velocity close to the stagnation point. Hence, the localized body force of DBD plasma actuator can significantly affect the flow in this region, thus making significant changes in the $\mathrm{C_h}$ profile over the cylinder. We are interest in this application.

7.1 Effect of Plasma DBD Actuator on Surface Heating in Mach 17 Hypersonic Flow Over Cylinder

We look into the effect of micro-second pulsed DBD plasma actuators on hypersonic flows. As an example, we consider hypersonic flow over cylinder, with Mach number of

17 from chapter 6. The cylinder radius is 1 m. The body force as a result of plasma actuation is taken from [97] and applied at the stagnation point on the cylinder surface. We first note the effect of this actuation, on the heat transfer coefficient, $\mathrm{C_h}$, in order to enhance our understanding of the physics of this problem. Various designs for plasma actuators are then considered, by varying locations and polarity (i.e. direction of the force) of the plasma actuation.

We employ the grid given in Fig. (7-1) for these results and use DG methods along with slope limiter to capture the shock. This grid has 256 $\times$ 100 elements in the domain, where the 256 elements are uniformly distributed in the θ direction and 100 elements, with varying sizes, are distributed along the radial direction.

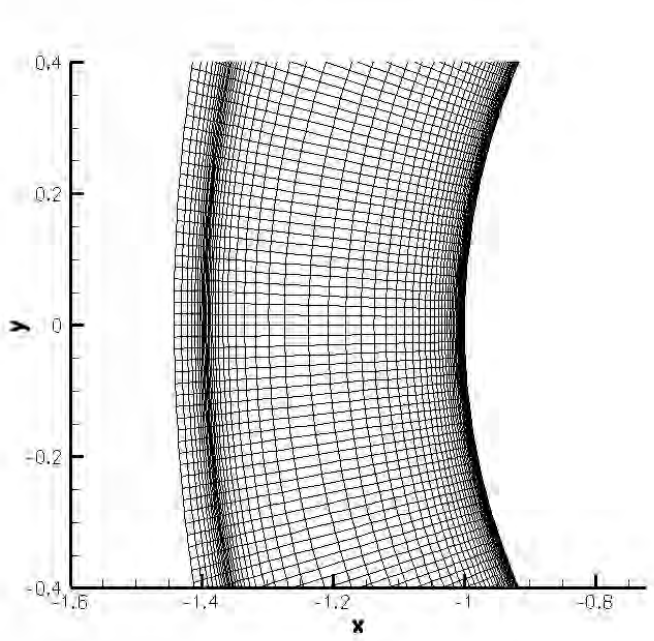

Figure 7-1. Mesh used for plasma actuation of hypersonic flow has 256 X 100 elements.

The body force distribution found based on first principles simulation of plasma discharge [97] is described as,

$$f_x = \frac{F_{x,0}}{\sqrt{{F_{x,0}}^2 + {F_{y,0}}^2}} \exp\left(- \left(\frac{(x - x_0) - (y - y_0)}{y - y_0 + y_b} \right)^2 - \beta_x (y - y_0)^2 \right) \quad (7\text{–}1)$$

$$f_y = \frac{F_{y,0}}{\sqrt{{F_{x,0}}^2 + {F_{y,0}}^2}} \exp\left(- \left(\frac{(x - x_0)}{y - y_0 + y_b} \right)^2 - \beta_y (y - y_0)^2 \right) \quad (7\text{–}2)$$

Here, $F_{x,0}$ = 2.6, $F_{y,0}$ = 2.0, β_x = 7.2 $\times$ 10^4, β_y = 9.0 $\times$ 10^5 and y_b = 0.00333. x_0 and y_0 represent the edge location of electrodes. This body force is integrated over the whole domain, and is multiplied by a factor to give average force distribution of approximately 10 kN/m^2.

This body force distribution, when applied at the stagnation point on the cylinder surface looks as given in Fig. (7-2).

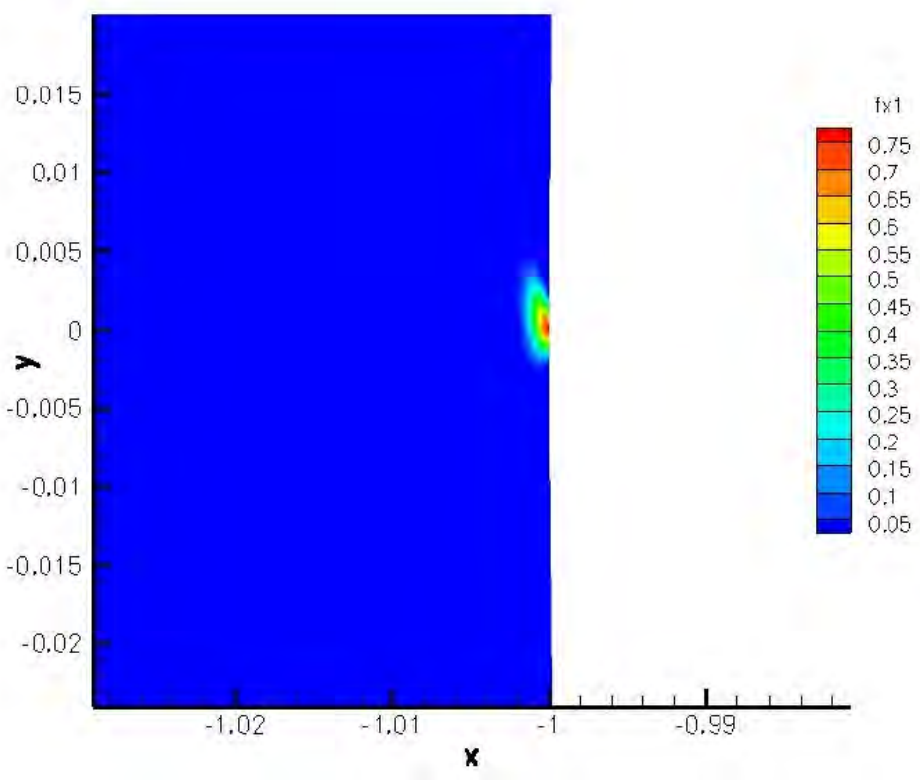

Figure 7-2. Plasma body force distribution in ′plasma1′ configuration, i.e. plasma actuator applied at the stagnation point with body force in +y-direction.

First, we present the results obtained on mesh without local refinement. Profiles for surface heat transfer coefficients, C_h, are shown for three different configurations of placement of DBD plasma actuators. ′plasma1′, refers to the plasma actuator placed at the stagnation point, with body force in the +y-direction; ′plasma2′ refers to two plasma actuators placed at 25 mm distance (measured along the circumference of the cylinder), away from the stagnation point. In this case, both plasma actuators apply body force away from each other, i.e. plasma actuator in positive part of y-axis, applies force in +y-direction and plasma actuator, in negative part of y-axis, applies force in y-direction. In the third configuration, i.e. ′plasma3′, the locations of plasma actuators is unchanged from ′plasma2′ configuration, but the directions of both forces are reversed so that both the forces act towards each other. The schematic in Fig. (7-3) illustrates the three configurations.

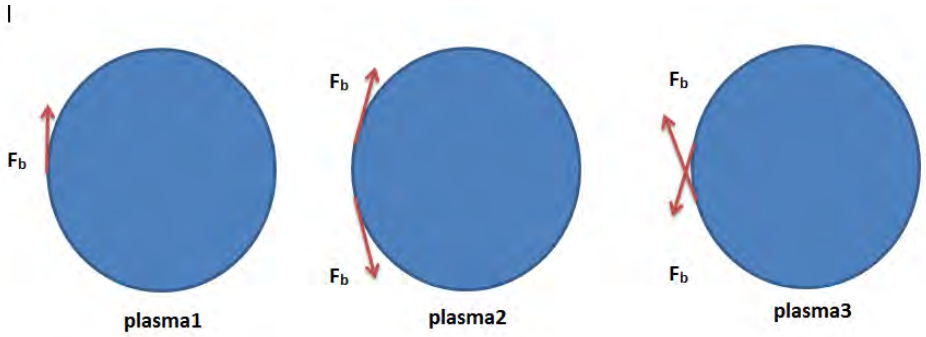

Figure 7-3. Three configurations for plasma DBD actuators. In first configuration, plasma actuator is applied at the stagnation point, with flow forcing in positive y-direction. Second and third configurations have same placements of the actuators, i.e. $\pm$ 25 mm from stagnation point along cylinder′ circumference, but with reversed flow forcing. Second configuration has forces pointing away from each other and third configuration has forces pointing towards each other.

The effect of these three configurations on the C_h profile is summarized in Fig. (7-4)

.

Plasma1 configuration leads to both increase and reduction of C_h profile along the surface of the cylinder. Maximum value of C_h of 0.00846 occurs at θ = -0.0136 (very

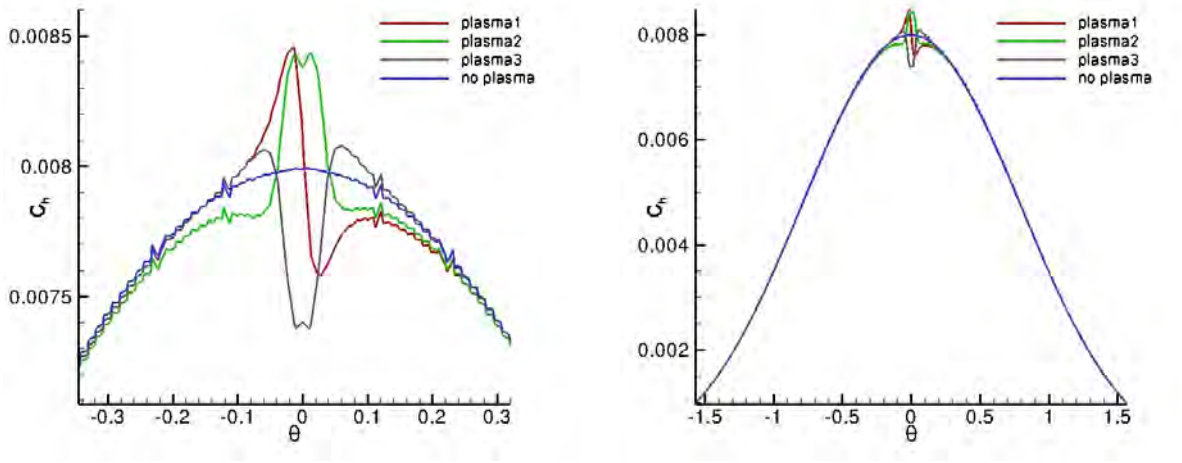

A Zoomed-in section

B Full plot

Figure 7-4. Effect of plasma actuation on the surface heat transfer coefficient, $\mathrm{C_h}$ of hypersonic flow over cylinder problem shown in (A) zoomed in section and in (B) full plot. The case of ′ no plasma ′, from MIG, compares well to $\mathrm{C_h}$ profile predicted from LAURA. The case of ′plasma stagnation pt′ corresponds to plasma1, ′plasma 50mm 2′ corresponds to plasma2, and ′plasma 50mm 3′ corresponds to plasma3. 50 mm is the distance (measured along cylinder circumference) between the plasma actuators in plasma2 and plasma3 configurations.

close to stagnation point), and minimum value of $\mathrm{C_h}$ of 0.00758 occurs at θ = 0.025. Since radius is 1 m, these locations correspond to -13.6 mm and 25 mm distance away from stagnation point.

Upon performing integration under the curve, we can see that the plasma actuator provides net cooling effect. Other two configurations, plasma2 and plasma3 are similar to moving the plasma′s effect on $\mathrm{C_h}$ profile (in plasma1) in $\pm$ 25 mm direction to the location of plasma actuator, and reversing the $\mathrm{C_h}$ profile based on the direction of plasma body force. Thus, the second and third configurations give overall heat transfer addition and reduction respectively.

To understand the flow physics, the effect of plasma actuator on the temperature and velocity profiles, near the wall (in direction normal to the wall), is analyzed, w.r.t. ′ no plasma ′. First, the effect of configuration1 is considered.

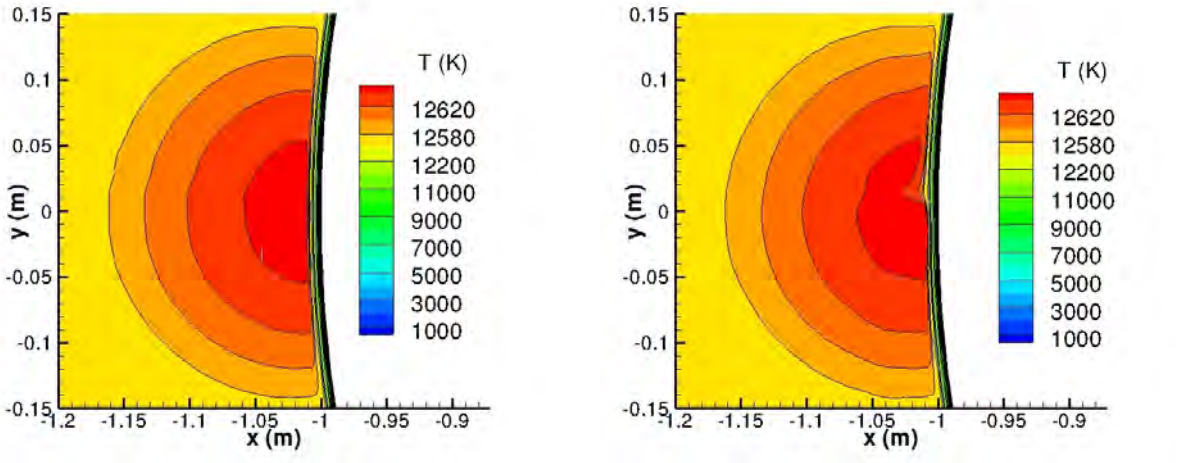

A Without plasma

B With plasma

Figure 7-5. Effect of no plasma vs plasma actuator in ′plasma1′ configuration on temperature contours close to the stagnation region of the cylinder.

The effect of actuator is easily seen in temperature contours, both with and without plasma (Fig. (7-5)). Visually, the temperature contours are moved closer to the cylinder surface for negative y-axis and away from the surface for positive y-axis, for ′plasma1′ relative to ′no plasma′ case. Thus, the actuator reduces the $\mathrm{C_h}$ value at about 25 mm distance downstream from its actual location, by strongly pushing the temperature contours away from the cylinder surface.

It can therefore be seen that the micro-second pulsed plasma DBD actuator, which are generally considered only appropriate for subsonic flows, have significant effect on hypersonic flows (near the boundary layer), in terms of heating. This is due to large thickness of boundary layer encountered in hypersonic flows, which results in low magnitude of velocities for a significant distance near the cylinder surface, and hence allows the plasma actuator to make some significant effect on the surface heating in hypersonic flow.

Next, we look at the temperature and velocity profiles (Fig. (7-6) and Fig. (7-7)), near the cylinder surface, as we move away from the wall in the normal direction.

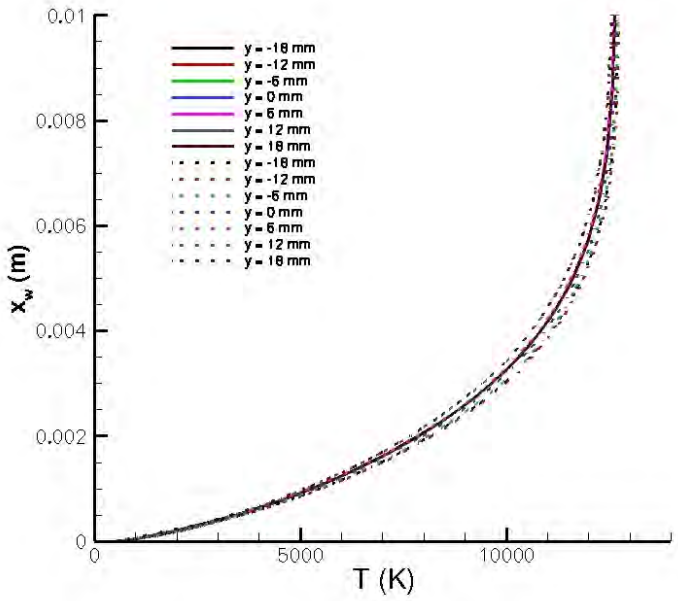

Figure 7-6. Temperature plots in the flow shown with distance in the flow from the wall, denoted as $\mathrm{x_w}$. Y locations correspond to the distances traveled along the cylinder surface in the positive or negative direction from the stagnation point. Solid lines refer to the results without plasma and dotted lines refer to the results with plasma (plasma1).

We notice from Fig. (7-6), that all the temperature profiles fall into a single curve for the ′no plasma′ case. For ′plasma1′ case, the temperature profiles are higher relative to the ′no plasma′ case for locations closer to the actuation point in the positive y-direction; and below the temperature profile for ′no plasma′ case for locations closer to the actuation point but in the negative y-direction. This corresponds to the increment and decrement observed in $\mathrm{C_h}$ profile in Fig. (7-4). From Fig. (7-5), we note that the maximum value of $\mathrm{C_h}$ is at -12.5 mm, close to -13.6 mm, seen in Fig. (7-4).

Velocity profiles in Fig. (7-7) indicate that there′s a significant increase of y-velocity, from 1 m/s to 8.5 m/s, at a distance of nearly 1mm away from cylinder surface at stagnation point. Thus, a strong flow velocity is actuated, which is why the actuator causes significant effect in the $\mathrm{C_h}$ value at the stagnation point, in the positive y-direction.

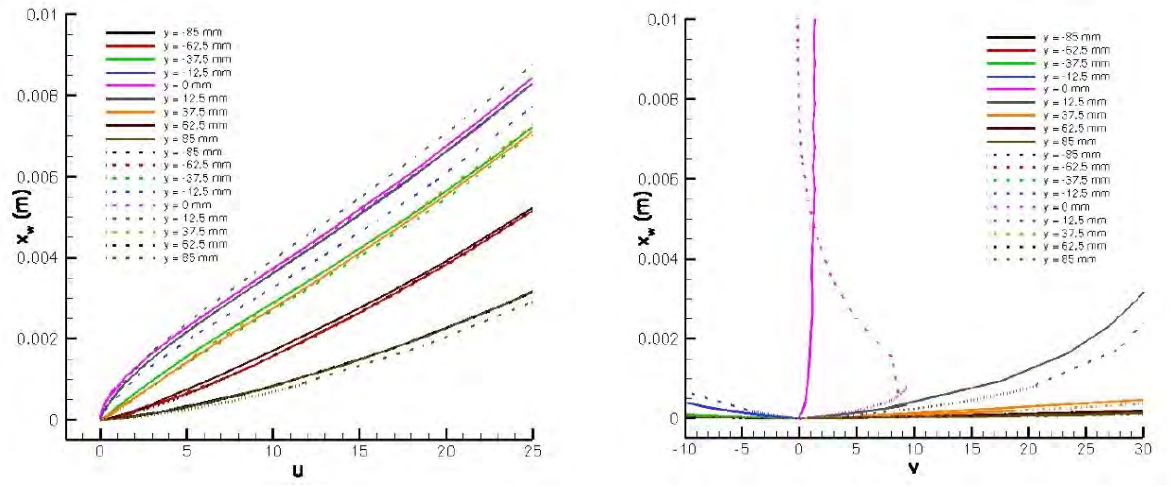

A X-velocity

B Y-velocity

Figure 7-7. X and Y velocity profiles shown with $\mathrm{x_w}$, the distance measured in the normal direction, away from the wall. Y-velocity is almost parallel to the cylinder surface, near the stagnation point, and is thus relevant to understand the cause of observed change in $\mathrm{C_h}$ value near stagnation point.

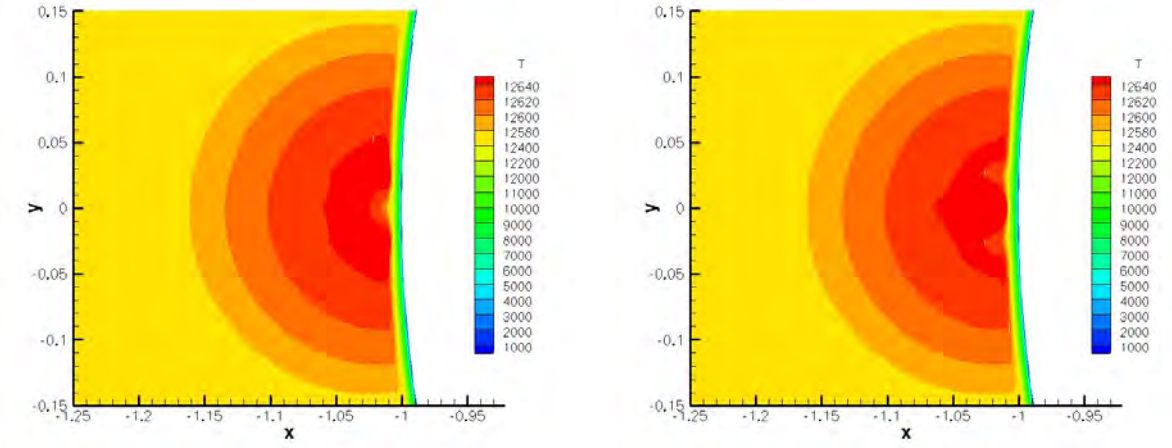

A plasma2

B plasma3

Figure 7-8. Temperature contours near stagnation region for two plasma actuators at 25 mm (w.r.t. stagnation point on cylinder surface), acting A) with body forces away from each other, i.e. plasma2 configuration and B) with body forces towards each other, i.e. plasma3 configuration.

Next we look at flows, with second and third configurations, with forces pointing away from each other (plasma2) and with forces towards each other (plasma3) respectively. The temperature contours close to the stagnation region are shown in Fig. (7-8). It is clearly seen that in ′plasma2′ configuration, the temperature contours are compressed relative to ′no plasma′ case, from y = - 50 mm to + 50 mm. Thus, for θ = -0.05 to 0.05, we see that $\mathrm{C_h}$ value for plasma2 configuration is higher than ′no plasma′ configuration. For rest of the region, $\mathrm{C_h}$ profile falls below the $\mathrm{C_h}$ profile for ′no plasma′ case.

Correspondingly for ′plasma3′ configuration, the temperature contours are pushed away from the cylinder wall, again from y = - 50 mm to + 50 mm, thus causing reduction in $\mathrm{C_h}$ value relative to ′no plasma′ case.

What causes the temperature contours to be pulled into and pushed away from the wall in plasma2 and plasma3 configurations respectively? We will try to understand this from the velocity schematic given in Fig. (7-9), for the ′plasma1′ configuration. Plasma body force induces a flow (shown in red) in the direction of the force. The oncoming flow (shown in blue) hits the cylinder surface (approximated by a flat wall in black).

Without the plasma body force, the flow has zero tangential velocity (along y-axis) a few mm distance away from the wall, and hence maximum value of $\mathrm{C_h}$ is experienced at the stagnation region. The flow induced, by the plasma, causes a leftward shift (from stagnation point) of the point of zero tangential velocity. This causes the maximum in $\mathrm{C_h}$ to shift slightly to the left in Fig. (7-4). The question, that arises, is why $\mathrm{C_h}$ profile shoots above the maximum value of $\mathrm{C_h}$ at the stagnation point for the ′no plasma′?

This is answered when looking closely (near the region of stagnation point), at the changes in velocity profiles, induced by the plasma in the ′plasma1′ configuration, relative to ′no plasma′ case in Fig. (7-10).

From Fig. (7-10), we notice that plasma actuator decelerates the flow (going in negative direction, to the left of the stagnation point), hence causing increased heating

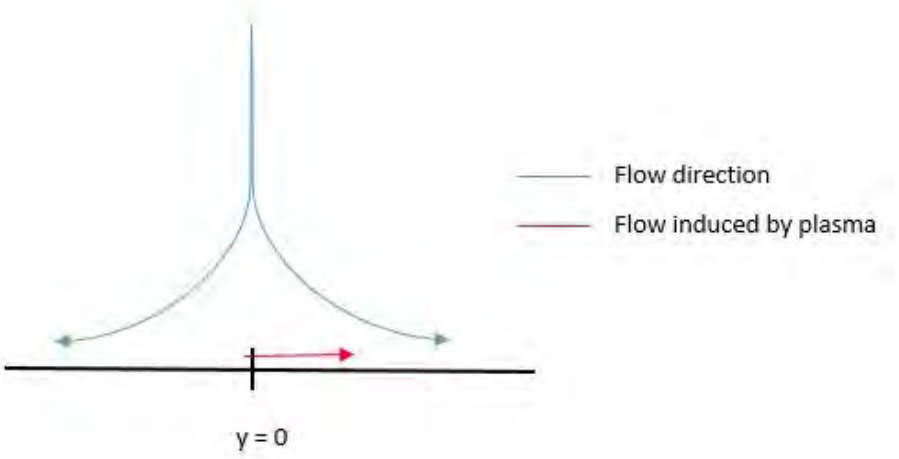

Figure 7-9. Schematic of flow induced (in red) by plasma body force with force direction in +y direction. The oncoming flow (in blue) hits the wall (in black). The cylinder surface close to the stagnation region can be approximated by a flat wall.

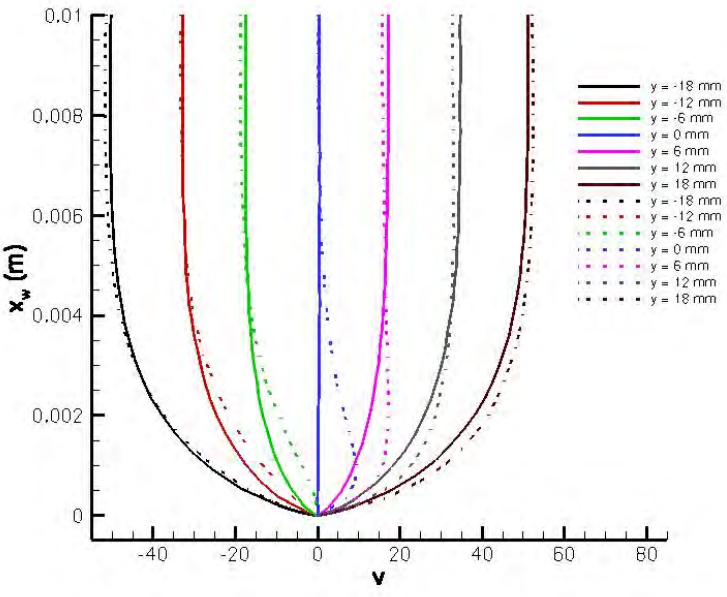

Figure 7-10. Y-velocity, v (m/s) (parallel to the cylinder wall) is generated for several locations close to the stagnation point, lying both to the left and the right. This is plotted for both with and without plasma actuators (solid lines represents the case without plasma actuator and dotted lines, the case with plasma actuator). This plot is for comparison of ′plasma1′ case to ′no plasma′ case.

at the surface, to the left of the stagnation point, and accelerates flow from stagnation point to approximately 18 mm to the right of the stagnation point, hence reducing heat transfer to that surface. Plasma actuator sucks in fluid at high temperature, from the bottom of the cylinder stagnation point and makes it flow over the cylinder surface to the top of the cylinder stagnation point. Thus, it increases the heat transfer to the bottom of the cylinder stagnation point, by pushing the high temperature fluid closer to the wall. It decreases the heat transfer to the top of the cylinder by generating a wall jet to the top of the cylinder, that pushes away the temperature contours from the wall.

Temperature profiles for plasma2 and plasma3 configurations in comparison to ′ no plasma ′ case, can be summarized in following way.

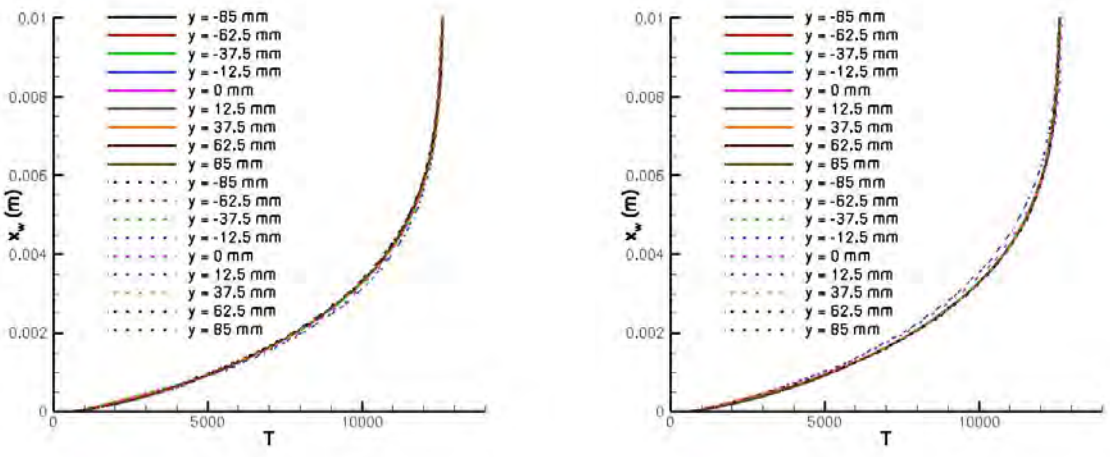

A plasma2 B plasma3

Figure 7-11. Temperature profiles for plasma2 and plasma3 configurations in comparison to ′no plasma′ case.

It can be seen above that temperature profiles for ′plasma2′ case, primarily lie below temperature profile for ′no plasma′ case and that for ′plasma3′ case, primarily lie above ′no plasma′ case, thus being consistent with higher and lower $\mathrm{C_h}$ profiles observed for ′plasma2′ and ′plasma3′ cases respectively in reference to ′no plasma′ case.

Same observation is also made in the velocity profiles for y-velocity, for ′plasma2′ and ′plasma3′ cases (see Fig. (7-12)). Here, the plasma DBD actuator located in positive y-axis, introduces a wall jet in the direction of the fluid flow in plasma2 configuration and in opposite direction of fluid flow in plasma3 configuration. By increasing the flow velocity next to wall, plasma actuator is able to entrain more of high temperature fluid, thus producing more surface heating for plasma2 configuration, and by decreasing the flow velocity next to wall, it is able to push the high temperature fluid away from the wall, thus reducing heating next to the wall for plasma3 configuration.

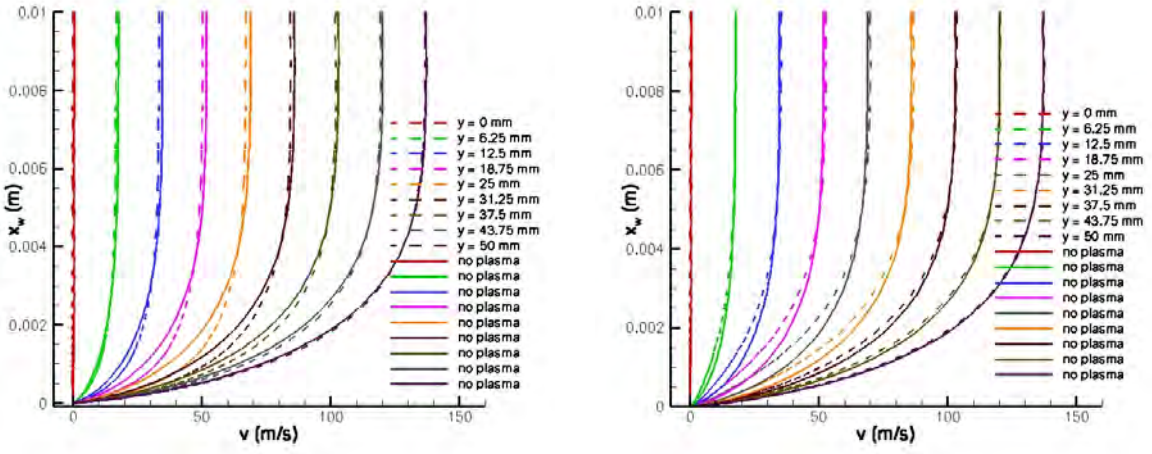

A plasma2 B plasma3

Figure 7-12. Y-velocity profiles for ′plasma2′ and ′plasma3′ configurationscd in comparison to ′no plasma′ case.

7.2 Effect of Plasma DBD Actuator on Surface Heating in Mach 17 Non-equilibrium Hypersonic Flow Over Cylinder

After successfully looking into the effect of plasma DBD actuator on the Mach 17 flow over hypersonic flow, we investigate its effect on a cylinder in hypersonic flow with thermo-chemical non-equilibrium. Applying the plasma actuators in the three configurations described in the section 7.1, we observe a similar effect on the surface heating in Fig. (7-13).

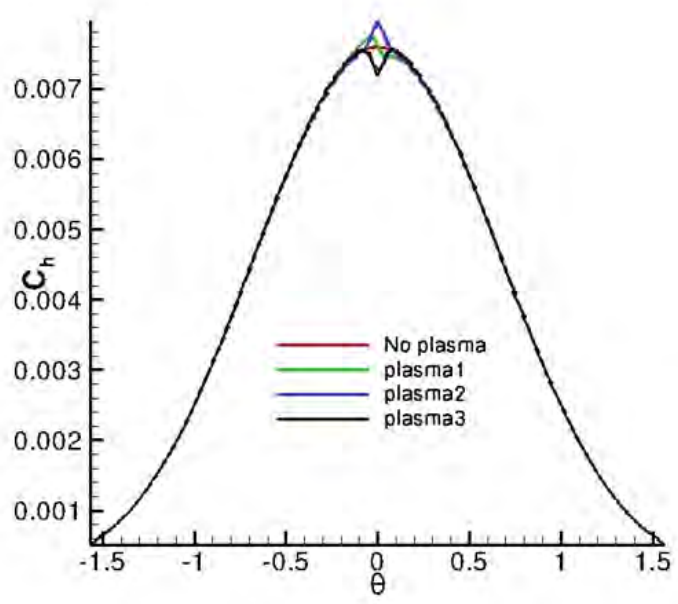

Figure 7-13. The effect of the plasma DBD actuator, on $\mathrm{C_h}$ profile for non-equilibrium hypersonic flow is shown. In reference to base case, with no plasma (shown in red), the plasma1 case gives both increase and decrease in $\mathrm{C_h}$ value, the plasma2 case gives overall increase in $\mathrm{C_h}$ value and the plasma3, as expected, gives overall reduction of heating.

When comparing plasma3 configuration to the base case, reduction of temperature gradient next to wall (at stagnation line) is observed (Fig. (7-14)). This is true for both translational-rotational temperature, T and vibrational temperature, $\mathrm{T_v}$. The effect is dominant to within 10 mm distance away from wall.

In addition to temperature profiles, the application of plasma DBD actuator is also seen to have effect on species mass fractions. This effect is not so pronounced for $\mathrm{O_2}$ and O, as can be seen in Fig. (7-15).

However, more significant effect is seen on stagnation line plots for N and NO (in Fig. (7-16)). The difference of plasma3 case, w.r.t. the base case is seen up to 25 mm distance away from the wall. In Fig. (7-16) A, we notice sudden reduction of N, close to the wall, for both with and without plasma actuator. This happens due to reduction in temperature, close to the wall (due to the boundary condition). At lower temperatures,

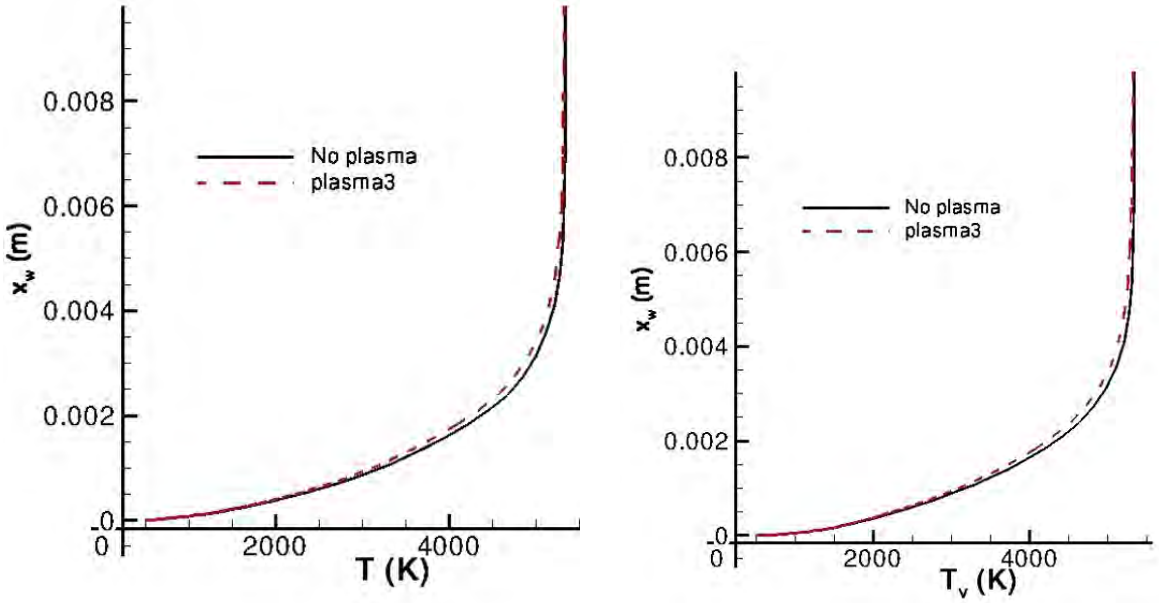

A plasma2 B plasma3

Figure 7-14. Effect of plasma3 configuration on stagnation line plots of T and $\mathrm{T_v}$ is shown next to the wall, in reference to ′no plasma′ case. Only a minor effect is seen in the temperature plots for distance up to 10 mm away from cylinder wall.

nitrogen can not sustain in the atomic form, and hence recombines to $\mathrm{N_2}$ (primarily) and NO near the wall. This recombination releases large amount of heating to the wall. A minor change in temperature, because of plasma, causes significant variation in mass fraction of N, up to distance of 25 mm away from wall.

For NO, there is increase in mass fraction, close to the wall (from 4 mm to 2 mm next to the wall). This is due to atomic N and O recombining into $\mathrm{N_2}$, $\mathrm{O_2}$ and NO. For distance of 2 mm away from the wall, even NO species vanishes due to the super-catalytic wall boundary condition. Hence a small peak for NO is observed in Fig. (7-16) B.

Plot of $\mathrm{N_2}$ in Fig. (7-17) shows that its mass fraction increases in two phases when approaching wall. From 30 mm to 2 mm distance from the wall, $\mathrm{N_2}$ monotonically increases, after which there is a dip in its mass fraction. This is due to mass fraction

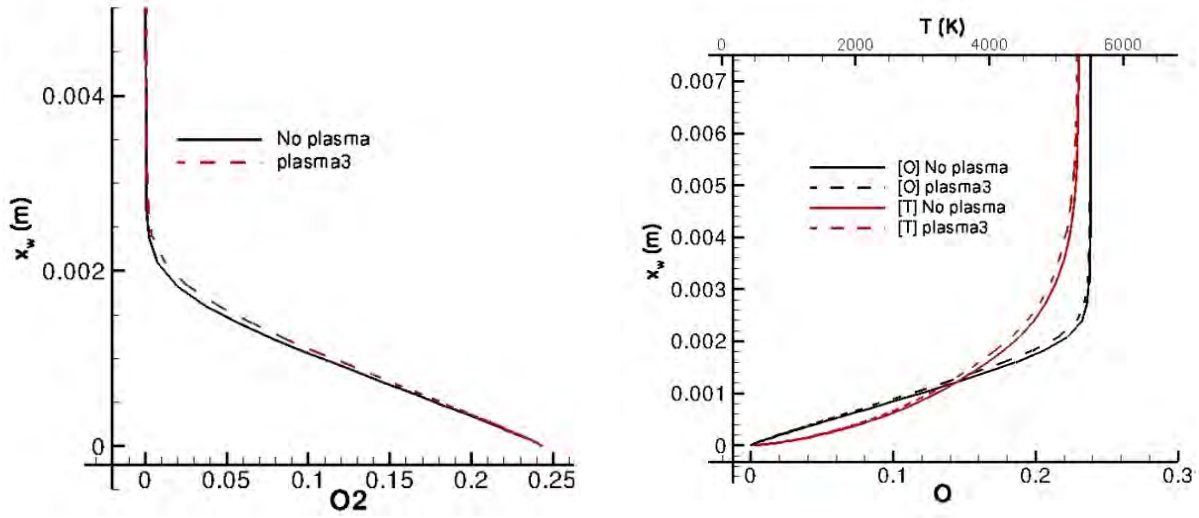

A plasma2 B plasma3

Figure 7-15. Effect of plasma3 configuration on stagnation line plots of O_2 and O, is shown next to the wall, in reference to ′no plasma′ case. Only a minor effect is seen in the plots for distance up to 6 mm away from cylinder wall.

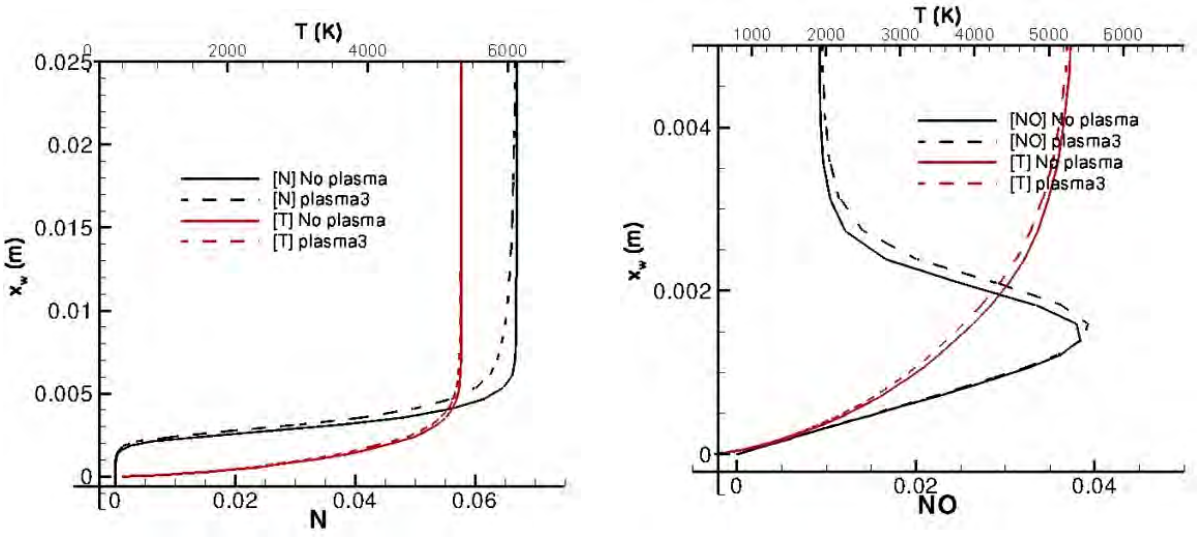

A plasma2 B plasma3

Figure 7-16. Effect of plasma3 configuration on stagnation line plots of N and NO, is shown next to the wall, with reference to ′no plasma′ case. Significant difference is noted in the mass fractions of N and NO, due to plasma DBD actuator in plasma3 configuration. For N, the effect is seen uptill 25 mm distance away from wall.

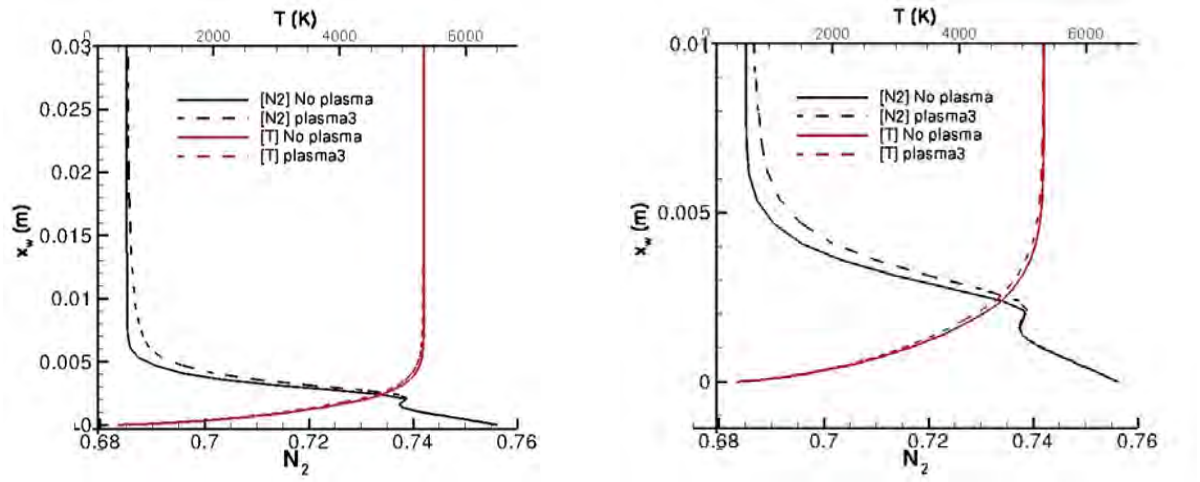

A plasma2 B plasma3

Figure 7-17. A) Effect of plasma3 configuration on stagnation line plot of N_2 near the wall, and its B) zoom-in section. A significant difference is seen in curves for N_2 up to 30 mm distance away from wall

of NO increasing at a distance of 2 mm close to wall. When NO start decreasing at approximately 1.5 mm distance away from wall, N_2 again begins to increase in its mass fraction. Thus, significant effect of plasma DBD actuators is noted on hypersonic flows, both with and without thermo-chemistry.

CHAPTER 8
CONCLUSION

In this work, we have successfully introduced discontinuous Galerkin (DG) methods to the fields of thermal ablation and hypersonic non-equilibrium flows. These two areas are characterized by highly non-linear, fully coupled and multi-physics problems. The challenges in thermal ablation include, unsteady flow of pyrolysis gases (which is a mixture of 14 gas species considered in chemical and thermodynamics equilibrium) flowing through a porous media, which is undergoing charring and ablation phenomena. For hypersonic flows with thermo-chemical non-equilibrium, the challenges are chemically reacting gas species (5 species model of N_2, O_2, NO, N and O was used) undergoing convection and diffusion processes in thermal non-equilibrium (we considered a two-temperature, T-T_v model).

Because of their complex governing equations, these problems are hard to analyze for their physics and thus difficult to debug as well. In addition, for an efficient solution process, a fully implicit method is indispensable. Without a fully implicit approach, the solution process is severely constrained with the time step restriction. This is due to high valued source terms occurring in both thermal ablation and hypersonic non-equilibrium flows. However, a fully implicit method requires the formulation of the jacobian matrices. This is a difficult task as the jacobian matrix is complex due to the complexity of the governing equations, and has to be re-tailored at the boundary for specific set of boundary conditions used. A small human error can significantly affect the convergence of the solution procedure. For this purpose, we implemented numerical evaluation of these jacobians, and carefully tailored them to the boundary conditions applied. We were able to get very good convergence rates for both problems, using CFL numbers of 10,000 and 5,000 for thermal ablation and hypersonic flow problems respectively. Herein, no approximations were assumed and the full set of governing equations were used.

We also demonstrated high-order accuracy and mesh convergence for the validation cases, shown in this work. Problems ranging from low speeds (M = 0.01), to moderate (M = 0.3, 0.38 and 0.5) and high speeds (M = 6, 10 and 17) were solved. In summary, we covered a wide range of flows varying from subsonic, transonic, supersonic and hypersonic flows.

In the field of hypersonic flows, both with and without thermo-chemistry, we demonstrated the application of r-p adaptivity method for capturing solutions with shock. With p = 0 used in the shock region, we captured shocks successfully without the use of slope limiters or artificial viscosity methods. r-adaptivity was used to selectively refine the elements in the shock, bringing in elements from outside the shock. Thus, extra number of elements, employed in the case of h-adaptivity, were not needed. This saves significant computational effort. Essentially, we successfully demonstrated the use of r-p adaptivity for hypersonic flows with inviscid, viscous and thermo-chemical non-equilibrium formulations. A good agreement for shock stand-off distance, surface heating coefficient and the temperature and species mass fractions was made for inviscid, viscous and non-equilibrium hypersonic flows respectively.

In addition to above, we also simulated the effect of micro-second pulsed, sinusoidal Dielectric Barrier Discharge (DBD) plasma actuators on the hypersonic flow over cylinder. A significant effect, on the heating on the cylinder surface, was noted. This has been possible due to the large boundary layer and small velocities, especially in the stagnation region, where the plasma actuators are able to actuate a wall jet close to cylinder surface. For the basic setting of the plasma actuator placed at the stagnation point of the cylinder, this wall jet pushes the fluid (close to the stagnation point) in the positive y-direction. This brings the high temperature gas, below and above the actuator, closer to and away from the cylinder surface respectively. Thus, the application of plasma actuator results in higher heating rate for surface below the stagnation point, and lower heating rate for surface above stagnation point.

In the two different configurations tried with two plasma actuators used on the cylinder surface at a distance of 50 mm from each other, the second configuration gives overall reduction in surface heating coefficient. Thus, we have demonstrated, that micro-second plasma DBD actuators, though conventionally thought of as being ineffective for high speed flows, do have significant effect on the heating distribution on the cylinder. We can work on more designs in future for even better performance of plasma DBD actuators for heating reduction in hypersonic flows.

The challenging area, that is yet unresolved, is the heating prediction for the hypersonic flow for locally refined mesh. The DG code is not free from residual effects coming from abruptly changing mesh elements, especially near stagnation line. Some residual differences between the surface heating plots, for locally refined mesh and the expected profile, are produced. This problem is, however, not unique to the DG methods or to the r-p adaptivity approach, but prevalent among all the methods (in the published literature). The results for surface heating predictions have, in general, been found to be very sensitive to the mesh.

In the field of thermal ablation, we find that much advancement in the understanding of the thermal ablation phenomena has occurred from the 1960′s, when the work in numerical simulation of thermal ablation began. Simulations at that time began with very simplifying assumptions, like thermally ablating media without any flow of pyrolysis gas being considered. CFD approximation methods were used to provide for net heating rates at the surface of the vehicle instead of solving flow outside the vehicle. At the same time, developments in CFD were also taking place, where full 3-D Navier Stokes was solved. Problem however, was the use of simple boundary conditions for CFD methods and simple governing equations for material thermal response, which did not take the unsteady nature of flow of pyrolysis gas within the porous ablating material. With the exception for Ahn et al and Dr Gosse′s work, the pyrolysis gas motion is still considered to be steady at a particular instant.

We have demonstrated capability to solve thermal ablation problems, with the unsteady flow of pyrolysis gas through the porous charring ablator, using DG methods, with high order accuracy. DG method, used specifically for thermal ablation problems, was 3^{rd} order accurate in space. For two test cases, namely TACOT test case from Ablation workshop and for the Langley arc-jet test sample, we have demonstrated accurate solution comparisons to the experimental results. The cases from Ahn et al, however do not match well with the experimental predictions. This is expected to be connected to the thermodynamic properties of pyrolysis gas in this case. The thermodynamic properties for the pyrolysis gas were provided in the two test cases (TACOT and Langley arc-jet case, where we accurately matched our results to the published and experiment), but not for Ahn et al., where we used CANTERA to generate thermodynamic properties for the gas.

We have even attempted to solve 2-D thermal ablation problem. In this we, however, ran into convergence issues, due to the condition number of the jacobian matrix being very high (approximately 10^{13}). This causes y-velocity to grow unboundedly (for a problem with flow only in x-direction) and become unstable. Therefore, our future step in the field of thermal ablation will be to resolve the convergence issue with the 2-D thermal ablation and run it in single framework with hypersonic flow.

Two alternatives to solving the 2-D thermal ablation problem, in case the problem still persists, are as follows. First option is to approximate 2-D thermally ablating geometry as a stack of 1-D grids aligned parallel to the normal at the exit of the 2-D geometry (where the pyrolysis gas leaves the 2D domain). Thus, we will attempt to run the Langley arc-jet test case in a loosely coupled fashion with the hypersonic flow solver. Second option is to use Darcy′s law to evaluate the velocity profile, based on pressure distribution inside the porous material. As already mentioned, many papers in literature for thermal ablation, do not solve for unsteady momentum equation, and use Darcy′s law instead. This approach is more stable, as it does not have the time term

for momentum equation in the Darcy′s law and can thus be used if the 2D unsteady momentum equation for the pyrolysis does not work.

If the single framework solution or the loosely coupled solution is successfully implemented, it will open, for us, new avenues for different types of multi-physics problems.

APPENDIX A
FLUID PROPERTIES

Table A-1. Blottner coefficients for species viscosity

Species	A_s	B_s	C_s
O_2	4.49290x10^{-2}	-8.26158x10^{-2}	-9.20195
NO	4.36378x10^{-2}	-3.35511x10^{-2}	-9.57674
N	1.15562x10^{-2}	6.031679x10^{-1}	-1.24327x10^{1}
O	2.03144x10^{-2}	4.29440x10^{-1}	-1.16031x10^{1}
N_2	2.68142x10^{-2}	83.17738x10^{-1}	-1.13156x10^{1}

Table A-2. Coefficients for forward reaction rates

Reaction	$C_{f,r,m}$	$\eta_{f,r,m}$	$\theta_{f,r,m}$
$N_2 + M \longleftrightarrow N + N + M$	3.70x10^{18}	-1.6	113,200
$O_2 + M \longleftrightarrow O + O + M$	2.75x10^{16}	-1	59,500
$NO + M \longleftrightarrow N + O + M$	2.30x10^{14}	-0.5	75,500
$N_2 + O \longleftrightarrow NO + N$	3.18x10^{10}	0.1	37,700
$NO + O \longleftrightarrow O_2 + N$	2.16x10^{5}	1.29	19,220

Table A-3. Equilibrium constant coefficients

Reaction	$A_{1,m}$	$A_{2,m}$	$A_{3,m}$	$A_{4,m}$	$A_{5,m}$
1	0.98499x10^{1}	-0.11314x10^{2}	-0.32028x10^{-2}	0.55205x10^{-4}	-0.63738x10^{-7}
2	0.88695x10^{1}	-0.53794x10^{1}	-0.88234x10^{-1}	0.47129x10^{-2}	-0.63470x10^{-4}
3	0.80072x10^{1}	-0.73520x10^{1}	-0.26707x10^{-1}	0.12446x10^{-2}	-0.15780x10^{-4}
4	0.86594x10^{1}	-0.71680x10^{1}	-0.24999	0.15237x10^{-1}	-0.21498x10^{-3}
5	0.88464x10^{1}	-0.41842x10^{1}	-0.37449	0.22172x10^{-1}	-0.31042x10^{-3}

APPENDIX B
BASIS FUNCTIONS

Table B-1. Basis functions for 2D discontinuous Galerkin

Basis/Order	1	2	3	4
1	1	1	1	1
1		-1 + 2x	-1 + 2x	-1 + 2x
1		-1 + 2y	-1 + 2y	-1 + 2y
1			$1 - 6x + 6x^2$	$1 - 6x + 6x^2$
1			$1 - 2y - 2x + 4xy$	$1 - 2y - 2x + 4xy$
1			$1 - 6y + 6y^2$	$1 - 6y + 6y^2$
1				$-1 + 12x - 30x^2 + 20x^3$
1				$-1 + 2y + 6x - 12xy - 6y^2 + 12xy^2$
1				$-1 + 6y - 6y^2 + 2x - 12xy + 12yx^2$
1				$-1 + 12y - 20y^2 + 20y^3$

REFERENCES

[1] Dec, J. A., Braun, R. D., and Lamb, B., "Ablative thermal response analysis using the finite element method," *Journal of Thermophysics and Heat Transfer*, Vol. 26, No. 2, 2012, pp. 201–212.

[2] Burgess, N. K., *An adaptive discontinuous Galerkin solver for aerodynamic flows*, Ph.D. thesis, University of Wyoming, 2011.

[3] Yoon, S., Gnoffo, P. A., White, J. A., and Thomas, J. L., "Computational challenges in hypersonic flow simulations," *AIAA Paper*, Vol. 4265, 2007, pp. 2007.

[4] Bhatia, A., Roy, S., and Gosse, R., "Pyrolysis gas flow in thermally ablating media using time-implicit discontinuous Galerkin methods," *49th AIAA Aerospace Sciences Meeting including the New Horizons Forum and Aerospace Exposition*, , No. AIAA 2011-145, 2011.

[5] Bhatia, A. and Roy, S., "Modeling the motion of pyrolysis gas through charring ablating material using Discontinuous Galerkin finite elements," *SIAM journal on numerical analysis*, , No. AIAA 2010-982, 2010.

[6] Bhatia, A., Roy, S., and Gosse, R., "2-D Hypersonic Non-equilibrium Flow Simulation using rp Adaptive Time-Implicit Discontinuous Galerkin Method," *51st AIAA Aerospace Sciences Meeting including the New Horizons Forum and Aerospace Exposition*, 2013.

[7] Sinha, K., "Computational Fluid Dynamics in Hypersonic Aerothermodynamics." *Defence Science Journal*, Vol. 60, No. 6, 2010.

[8] Gnoffo, P. A., "Updates to multi-dimensional flux reconstruction for hypersonic simulations on tetrahedral grids," *Proceedings of the 48th AIAA Aerospace Sciences Meeting*, 2010.

[9] Barter, G. E. and Darmofal, D. L., "Shock capturing with PDE-based artificial viscosity for DGFEM: Part I. Formulation," *Journal of Computational Physics*, Vol. 229, No. 5, 2010, pp. 1810–1827.

[10] Wang, L., *Techniques for High-Order Adaptive Discontinuous Galerkin Discretizations in Fluid Dynamics*, Ph.D. thesis, University of Wyoming, 2009.

[11] Gnoffo, P. A., "Planetary-Entry Gas Dynamics 1," *Annual Review of Fluid Mechanics*, Vol. 31, No. 1, 1999, pp. 459–494.

[12] Gosse, R., *Ablation Modeling of Electro-magnetically Launched Projectile for Access to Space*, Ph.D. thesis, University of Minnesota, Minnesota, WI, October 2007.

[13] Gogu, C., Matsumura, T., Haftka, R. T., and Rao, A. V., "Aeroassisted orbital transfer trajectory optimization considering thermal protection system mass," *Journal of Guidance, Control, and Dynamics*, Vol. 32, No. 3, 2009, pp. 927–938.

[14] Braun, R. D., "Aeroassist systems: An important element in NASA's new era of planetary exploration," *Journal of Spacecraft and Rockets*, Vol. 36, No. 3, 1999, pp. 297–297.

[15] Pitts, W. and Wakefield, R., "Performance of entry heat shields on Pioneer Venus probes," *Journal of Geophysical Research: Space Physics (1978–2012)*, Vol. 85, No. A13, 1980, pp. 8333–8337.

[16] Park, C. and Ahn, H.-K., "Stagnation-point heat transfer rates for Pioneer-Venus probes," *Journal of thermophysics and heat transfer*, Vol. 13, No. 1, 1999, pp. 33–41.

[17] Ahn, H.-K., Park, C., and Sawada, K., "Response of heatshield material at stagnation point of Pioneer-Venus probes," *Journal of thermophysics and heat transfer*, Vol. 16, No. 3, 2002, pp. 432–439.

[18] Seiff, A., Kirk, D. B., Young, R. E., Blanchard, R. C., Findlay, J. T., Kelly, G., and Sommer, S., "Measurements of thermal structure and thermal contrasts in the atmosphere of Venus and related dynamical observations: Results from the four Pioneer Venus probes," *Journal of Geophysical Research: Space Physics (1978–2012)*, Vol. 85, No. A13, 1980, pp. 7903–7933.

[19] Zhong, J., Ozawa, T., and Levin, D. A., "Modeling of Stardust Reentry Ablation Flows in the Near-Continuum Flight Regime," *AIAA journal*, Vol. 46, No. 10, 2008, pp. 2568–2581.

[20] Boyd, I. D., Zhong, J., Levin, D. A., and Jenniskens, P., "Flow and radiation analyses for stardust entry at high altitude," *AIAA Paper*, Vol. 1218, 2008.

[21] Ozawa, T., Zhong, J., Levin, D., Boger, D., and Wright, M., "Modeling of the stardust reentry flows with ionization in dsmc," *AIAA paper*, Vol. 611, 2007.

[22] Anderson, J. D., *Hypersonic and high temperature gas dynamics*, Aiaa, 2000.

[23] Ayasoufi, A., Rahmani, R., Cheng, G., Koomullil, R., and Neroorkar, K., "Numerical simulation of ablation for reentry vehicles," *9th AIAA/ASME Joint Thermophysics and Heat Transfer Conference*, 2006, pp. 5–8.

[24] Reynier, P., "Convective Blockage during Earth Re-entry. A review." 2008.

[25] R, T., "Thermal Diffusivity of POCO Graphite and Stainless Steel SRM 735-5," *Thermal Conductivity, Plenum Press*, Vol. 17, 1982, pp. 753–7621.

[26] Kendall, R., Rindal, R., and Bartlett, E., "Thermochemical ablation," *AIAA Paper*, Vol. 642, 1965, pp. 13–15.

[27] Moyer, C. B. and Rindal, R. A., "An analysis of the coupled chemically reacting boundary layer and charring ablator. Part 2- Finite difference solution for the in-depth response of charring materials considering surface chemical and energy balances(Computer program for finite difference equation analysis of in-depth response of materials exposed to high temperature environment)," 1968.

[28] Maruyama, S., Viskanta, R., and Aihara, T., "Active thermal protection system against intense irradiation," *Journal of Thermophysics and Heat Transfer*, Vol. 3, No. 4, 1989, pp. 389–394.

[29] Chen, Y.-K. and Milos, F. S., "Ablation and thermal response program for spacecraft heatshield analysis," *Journal of Spacecraft and Rockets*, Vol. 36, No. 3, 1999, pp. 475–483.

[30] POTTS, R., "Hybrid integral/quasi-steady solution of charring ablation," 1990.

[31] Potts, R. L., "Application of integral methods to ablation charring erosion-A review," *Journal of spacecraft and rockets*, Vol. 32, No. 2, 1995, pp. 200–209.

[32] Martin, A. and Boyd, I. D., "Simulation of pyrolysis gas within a thermal protection system," *40th AIAA Thermophysics Conference*, 2008, pp. 23–26.

[33] Amar, A. J., Blackwell, B. F., and Edwards, J., "Development and Verification of a One-Dimensional Ablation Code Including Pyrolysis Gas Flow," *Journal of Thermophysics and Heat Transfer*, Vol. 23, No. 1, 2009, pp. 59–71.

[34] Lachaud, J., Martin, A., Cozmuta, I., and Laub, B., "Ablation workshop test case - Version 1.1 - Feb. 2, 2011," 2011.

[35] Gaitonde, D. V., Visbal, M. R., and Roy, S., "A coupled approach for plasma-based flow control simulations of wing sections," *AIAA paper*, Vol. 1205, 2006, pp. 2006.

[36] Ahn, H.-K., Park, C., and Sawada, K., "Dynamics of pyrolysis gas in charring materials ablation," *36th Aerospace Sciences Meeting & Exhibit*, 1998.

[37] CANDLER, G. and MACCORMACK, R., "Hypersonic flow past 3-D configurations," *AIAA, Aerospace Sciences Meeting, 25 th, Reno, NV*, 1987, p. 1987.

[38] Chen, Y.-K., Henline, W., Stewart, D., and Candler, G., "Navier-Stokes solutions with surface catalysis for Martian atmospheric entry," *Journal of Spacecraft and Rockets*, Vol. 30, No. 1, 1993, pp. 32–42.

[39] Version, G., "3, The General Aerodynamic Simulation Program, Computational Flow Analysis Software for the Scientist and Engineer, User's Manual," *Aerosoft Co., Blacksburg*, 1996.

[40] Olynick, D. and Tam, T., "Trajectory-based validation of the shuttle heating environment," *Journal of spacecraft and rockets*, Vol. 34, No. 2, 1997, pp. 172–181.

[41] Blackwell, B., "Numerical prediction of one-dimensional ablation using a finite control volume procedure with exponential differencing," *Numerical Heat Transfer, Part A: Applications*, Vol. 14, No. 1, 1988, pp. 17–34.

[42] Blackwell, B. and Hogan, R., "One-dimensional ablation using Landau transformation and finite control volume procedure," *Journal of thermophysics and heat transfer*, Vol. 8, No. 2, 1994, pp. 282–287.

[43] Hogan, R., Blackwell, B., and Cochran, R., "Application of moving grid control volume finite element method to ablation problems," *Journal of thermophysics and heat transfer*, Vol. 10, No. 2, 1996, pp. 312–319.

[44] Martin, A. and Boyd, I. D., "Non-Darcian behavior of pyrolysis gas in a thermal protection system," *Journal of Thermophysics and Heat Transfer*, Vol. 24, No. 1, 2010, pp. 60–68.

[45] Scalabrin, L. C. and Boyd, I. D., "Numerical simulations of the FIRE-II convective and radiative heating rates," *AIAA Paper*, Vol. 4044, 2007, pp. 2007.

[46] Scalabrin, L. C., *Numerical simulation of weakly ionized hypersonic flow over reentry capsules*, Ph.D. thesis, The University of Michigan, 2007.

[47] Chen, Y.-K. and Milos, F., "Two-dimensional implicit thermal response and ablation program for charring materials," *Journal of Spacecraft and Rockets*, Vol. 38, No. 4, 2001, pp. 473–481.

[48] King, H., Muramoto, K., Murray, A., and Pronchick, S., "ABRES Shape Change Code (ASCC86): Technical Report and Users Manual," *Acurex Corporation, FR-86-24/ATD, Mt View, CA*, 1986.

[49] Chen, Y. and Milos, F., "Thermal Response Modeling System for a Mars Sample Return Vehicle," *Thermal and Fluid Analysis Workshop, NASA CP-2002-211783, Sept*, 2001.

[50] Manuals, M. and Volumes, A., "Marc Analysis Research Corporation," *Palo Alto, CA USA*, 1997.

[51] Hassan, B., Kuntz, D. W., and Potter, D. L., "Coupled fluid/thermal prediction of ablating hypersonic vehicles," *AIAA paper*, Vol. 168, 1998, pp. 1998.

[52] Kuntz, D. W., Hassan, B., and Potter, D. L., "Predictions of ablating hypersonic vehicles using an iterative coupled fluid/thermal approach," *Journal of Thermophysics and Heat Transfer*, Vol. 15, No. 2, 2001, pp. 129–139.

[53] Martin, A., Boyd, I. D., and Poggie, J., "Strongly coupled computation of material response and nonequilibrium flow for hypersonic ablation," *41th AIAA Thermophysics Conference*, 2009, pp. 22–25.

[54] Kitamura, K. and Shima, E., “Towards shock-stable and accurate hypersonic heating computations: A new pressure flux for AUSM-family schemes,” *Journal of Computational Physics*, Vol. 245, 2013, pp. 62–83.

[55] Barter, G. E., “Shock capturing with PDE-based artificial viscosity for an adaptive, higher-order discontinuous Galerkin finite element method,” Tech. rep., DTIC Document, 2008.

[56] Reed, W. H. and Hill, T., “Triangular Mesh Methods for the Neutron Transport Equation,” *Los Alamos Report LA-UR-73-479*, 1973.

[57] Cockburn, B., Lin, S.-Y., and Shu, C.-W., “TVB Runge-Kutta local projection discontinuous Galerkin finite element method for conservation laws III: one-dimensional systems,” *Journal of Computational Physics*, Vol. 84, No. 1, 1989, pp. 90–113.

[58] Cockburn, B. and Shu, C.-W., “TVB Runge-Kutta local projection discontinuous Galerkin finite element method for conservation laws. II. General framework,” *Mathematics of Computation*, Vol. 52, No. 186, 1989, pp. 411–435.

[59] Cockburn, B., Hou, S., and Shu, C.-W., “The Runge-Kutta local projection discontinuous Galerkin finite element method for conservation laws. IV. The multidimensional case,” *Mathematics of Computation*, Vol. 54, No. 190, 1990, pp. 545–581.

[60] Cockburn, B. and Shu, C.-W., “The Runge–Kutta discontinuous Galerkin method for conservation laws V: multidimensional systems,” *Journal of Computational Physics*, Vol. 141, No. 2, 1998, pp. 199–224.

[61] Cockburn, B. and Shu, C.-W., “The Runge-Kutta local projection P1-discontinuous Galerkin finite element method for scalar conservation laws,” *RAIRO Modél. Math. Anal. Numér*, Vol. 25, No. 3, 1991, pp. 337–361.

[62] Bassi, F. and Rebay, S., “A high-order accurate discontinuous finite element method for the numerical solution of the compressible Navier–Stokes equations,” *Journal of computational physics*, Vol. 131, No. 2, 1997, pp. 267–279.

[63] Cockburn, B. and Shu, C.-W., “The local discontinuous Galerkin method for time-dependent convection-diffusion systems,” *SIAM Journal on Numerical Analysis*, Vol. 35, No. 6, 1998, pp. 2440–2463.

[64] Bassi, F., Crivellini, A., Rebay, S., and Savini, M., “Discontinuous Galerkin solution of the Reynolds-averaged Navier–Stokes and¡ i¿ k¡/i¿–¡ i¿ ω¡/i¿ turbulence model equations,” *Computers & Fluids*, Vol. 34, No. 4, 2005, pp. 507–540.

[65] Douglas, J. and Dupont, T., “Interior penalty procedures for elliptic and parabolic Galerkin methods,” *Computing methods in applied sciences*, Springer, 1976, pp. 207–216.

[66] Peraire, J. and Persson, P.-O., "The compact discontinuous Galerkin (CDG) method for elliptic problems," *SIAM Journal on Scientific Computing*, Vol. 30, No. 4, 2008, pp. 1806–1824.

[67] Persson, P.-O. and Peraire, J., "Newton-GMRES preconditioning for discontinuous Galerkin discretizations of the Navier-Stokes equations," *SIAM Journal on Scientific Computing*, Vol. 30, No. 6, 2008, pp. 2709–2733.

[68] Nastase, C. R. and Mavriplis, D. J., "High-order discontinuous Galerkin methods using an¡ i¿ hp¡/i¿-multigrid approach," *Journal of Computational Physics*, Vol. 213, No. 1, 2006, pp. 330–357.

[69] Gopalakrishnan, J. and Kanschat, G., "A multilevel discontinuous Galerkin method," *Numerische Mathematik*, Vol. 95, No. 3, 2003, pp. 527–550.

[70] Fidkowski, K. J., Oliver, T. A., Lu, J., and Darmofal, D. L., "¡ i¿ p¡/i¿-Multigrid solution of high-order discontinuous Galerkin discretizations of the compressible Navier–Stokes equations," *Journal of Computational Physics*, Vol. 207, No. 1, 2005, pp. 92–113.

[71] Wilke, C., "A viscosity equation for gas mixtures," *The Journal of Chemical Physics*, Vol. 18, 1950, pp. 517.

[72] Blottner, F. G., Johnson, M., and Ellis, M., "CHEMICALLY REACTING VISCOUS FLOW PROGRAM FOR MULTI-COMPONENT GAS MIXTURES." Tech. rep., Sandia Labs., Albuquerque, N. Mex., 1971.

[73] Vincenti, W. G. and Kruger, C. H., "Introduction to physical gas dynamics," *Introduction to physical gas dynamics, by Vincenti, Walter Guido; Kruger, Charles H. New York, Wiley [1965]*, Vol. 1, 1965.

[74] PARK, C., "Assessment of two-temperature kinetic model for dissociating and weakly-ionizing nitrogen," 1986.

[75] McBride, B. J., Zehe, M. J., and Gordon, S., *NASA Glenn coefficients for calculating thermodynamic properties of individual species*, National Aeronautics and Space Administration, John H. Glenn Research Center at Lewis Field, 2002.

[76] Millikan, R. C. and White, D. R., "Systematics of vibrational relaxation," *The Journal of chemical physics*, Vol. 39, 1963, pp. 3209.

[77] Lax, P. D., "Weak solutions of nonlinear hyperbolic equations and their numerical computation," *Communications on Pure and Applied Mathematics*, Vol. 7, No. 1, 1954, pp. 159–193.

[78] Falgout, R., Cleary, A., Jones, J., Chow, E., Henson, V., Baldwin, C., Brown, P., Vassilevski, P., and Yang, U., "HYPRE: High Performance Preconditioners," *Users Manual. Version*, Vol. 1, No. 0, 2010.

[79] Persson, P.-O. and Peraire, J., “Sub-cell shock capturing for discontinuous Galerkin methods,” *AIAA paper*, Vol. 112, 2006, pp. 2006.

[80] Parmar, M., *Unsteady forces on a particle in compressible flows*, Ph.D. thesis, University of Florida, 2010.

[81] Bassi, F. and Rebay, S., “High-order accurate discontinuous finite element solution of the 2D Euler equations,” *Journal of Computational Physics*, Vol. 138, No. 2, 1997, pp. 251–285.

[82] Botta, N., “The inviscid transonic flow about a cylinder,” *Journal of Fluid Mechanics*, Vol. 301, 1995, pp. 225–250.

[83] Colella, P. and Glaz, H. M., “Efficient solution algorithms for the Riemann problem for real gases,” *Journal of Computational Physics*, Vol. 59, No. 2, 1985, pp. 264–289.

[84] D.L. Peterson, F. G. and Richardson, C., “Design and Performance of a Combined Convective and Radiative Heating Facility,” *AIAA Paper 71-255, San Antonio, Texas*, 1971.

[85] Goodwin, D., “Cantera users guide,” *Division of Engineering and Applied Science, California Institute of Technology, Pasadena, CA*, 2001.

[86] Philips, J., “ZunZun. com Online Curve Fitting and Surface Fitting Web Site,” 2011.

[87] Sykes, G. F., “Decomposition Characteristics of a Char-Forming Phenolic Polymer Used for Ablative Composites,” 1967.

[88] Sutton, K., “An Experimental Study of A Carbon-Phenolic Ablation Material,” , No. NASA-TN-D-5930, 1970.

[89] GNOFFO, P. and CHEATWOOD, F., “User’s Manual for the Langley Aerothermodynamic Upwind Relaxation Algorithm(LAURA),” 1996.

[90] Moreau, E., “Airflow control by non-thermal plasma actuators,” *Journal of Physics D: Applied Physics*, Vol. 40, No. 3, 2007, pp. 605.

[91] Shang, J. S., Kimmel, R. L., Menart, J. A., and Surzhikov, S. T., “Hypersonic flow control using surface plasma actuator,” *Journal of Propulsion and Power*, Vol. 24, No. 5, 2008, pp. 923–934.

[92] Nishihara, M., Takashima, K., Rich, J., and Adamovich, I., “Mach 5 bow shock control by a nanosecond pulse surface dielectric barrier discharge,” *Physics of Fluids (1994-present)*, Vol. 23, No. 6, 2011, pp. 066101.

[93] Roupassov, D., Nikipelov, A., Nudnova, M., and Starikovskii, A. Y., “Flow separation control by plasma actuator with nanosecond pulsed-periodic discharge,” *AIAA journal*, Vol. 47, No. 1, 2009, pp. 168–185.

[94] Riherd, M. and Roy, S., "Serpentine geometry plasma actuators for flow control," *Journal of Applied Physics*, Vol. 114, No. 8, 2013, pp. 083303.

[95] Kim, J.-H., Nishihara, M., Adamovich, I., Samimy, M., Gorbatov, S., and Pliavaka, F., "Development of localized arc filament RF plasma actuators for high-speed and high Reynolds number flow control," *Experiments in fluids*, Vol. 49, No. 2, 2010, pp. 497–511.

[96] Bisek, N. J., Poggie, J., Nishihara, M., and Adamovich, I., "Computational and Experimental Analysis of Mach 5 Air Flow over a Cylinder with a Nanosecond Pulse Discharge," *AIAA Paper*, Vol. 186, 2012, pp. 2012.

[97] Singh, K. P. and Roy, S., "Force approximation for a plasma actuator operating in atmospheric air," *Journal of Applied Physics*, Vol. 103, No. 1, 2008, pp. 013305.

BIOGRAPHICAL SKETCH

Ankush Bhatia was born in 1983 in Delhi, India. He earned his B. Tech. degree in Mechanical Engineering from Indian Institute of Technology, Delhi in 2006. During 2006-2007, he worked as a design engineer in Hindustan Petroleum Corporation Ltd. Since 2007, he has been working towards the doctorate here at the University of Florida under Dr. Subrata Roy. His research areas are thermal ablation, finite element and discontinuous Galerkin methods, and computational fluid dynamics (CFD).